Extending Attitude Estimation Capability for Agile Precision Target Tracking NanoSats

Hardware Characterisation, Configuration Selection, and Gyro-Stellar based Unscented Calibration Filter Synthesis

ALI NAWAZ

Faculty of Aerospace Engineering
Faculty of Mechanical, Maritime and Materials Engineering
Delft Center for Systems and Control, Delft University of Technology.

TUDelft   HYPERION TECHNOLOGIES   **DCSC**
Delft Center for Systems and Control

This page is intentionally left blank.

Extending Attitude Estimation Capability for
Agile Precision Target Tracking NanoSats

Hardware Characterisation, Configuration Selection, and Gyro-Stellar based Unscented Calibration Filter Synthesis

by

ALI NAWAZ

As part of the MSc thesis conducted at the Delft University of Technology.
In partial fulfilment of the requirements for
double MSc in Aerospace Engineering, and Systems & Control Engineering.
To be defended publicly on Friday, December 18, 2020 at 14:00.

An electronic version of this thesis is available at:
https://repository.tudelft.nl/islandora/search/?collection=education

TUDelft   HYPERION TECHNOLOGIES   DCSC
Delft Center for Systems and Control

This page is intentionally left blank.

Preface

The contents of this thesis work are intended for anyone with an interest in NanoSats, and agile precision pose estimation with MEMs rate gyros and NanoSat star trackers. The work presented here aims to capture the industry practices, and the attitude knowledge performance that can be expected across different mission phases of a NanoSat. This might also be of interest to precision payload designers, e.g. for preliminary sizing of laser communication terminal and optical ground station; or for aperture size and integration time definition of optical payloads.

Though space engineering is considered as a universal playground representing international collaboration across all societies around the world. Ironically, access to space engineering and sciences, remains dominated by selective few countries around the world. By employing COTS components, NanoSats aim to democratize the accessibility to space based science and research, by lowering the cost of entry for scientific communities around the world. This has been the driving factor for me to undertake a research in the direction of NanoSats. Control engineering is the hidden brain of any autonomous system; making precise systems from imprecise components. It was a natural step to focus on this aspect of NanoSats for this thesis work.

Given the scarcity of AOCS/GNC research opportunities for international students coming from nations with no space research program, I am grateful that I was allowed to extend this thesis work at Hyperion Technologies. Hyperion Technologies not only gave me a safe space to pursue my passion in AOCS, but also allowed me to chart out the future of in-house AOCS related developments outside of this thesis work. I am very grateful that Hyperion gave me the full flexibility to test and experiment with their systems such early in my career. I would like to thank dr. ir. Bert Monna for offering me working opportunity next to my thesis, which enabled me to partially fund this research work. I am grateful to have dr. ir. Steven Engelen as my supervisor; whose patience, optimism, calmness in the face of adversity, and passion for all things science often made failing a fun learning experience. I am glad that I shall continue working as an AOCS/GNC engineer at Hyperion Technologies, beyond this thesis work.

I would like to extend my gratitude to my academic thesis supervisors dr. ir. Erwin Mooij, and prof. dr. ir. Michel Verhaegen. Erwin taught me to stay focused on my research topic, and prevented my mind from constantly drifting away into other directions. This taught me to execute more, and speculate less; a lesson that I shall always remember. Prof. Michel, taught me to focus on principles over methods, for methods there are many but principles there are few. I would further like to thank dr. ir. Wouter van der Wal. I am delighted to have him as the chair of my thesis committee. The exposure that I got into NanoSats during my DSE project, played a role in allowing me to peak further into this topic for my MSc thesis.

Coming from a city with only 40% literacy rate, I had never imagined that my ambition would lead me here to obtaining not one but two master's degrees. I cannot express in words, how grateful I am to be given this opportunity, and for everyone who has supported me along this journey. I have tried to be resourceful wherever possible, but I am certain someone somewhere else given the right opportunity would have been more resourceful. This thesis work marks an end to my journey of MSc at TU Delft, but ignites a new journey of life long learning esp. in the domain of control engineering, for which I barely grasped the tip of the iceberg during my master's studies. Last but not the least, I would like to thank my family for consistently supporting me unconditionally. Any of this would not have been possible without their support.

Per aspera ad astra,
Ali Nawaz
December 04, 2020.
Delft, The Netherlands.

This page is intentionally left blank.

Contents

List of Symbols

Greek Symbols

β	Bias	[rad/s]
χ	Sigma points associated with the state vector	[-]
$\delta\rho$	Error quaternion vectorial element	[-]
δp	Error MRP	[-]
δq	Error quaternion	[-]
$\eta_\square$	Random white noise associated with $\square$	[-]
γ	Sigma points associated with the measurement vector	[-]
κ	State vector comprising of gyro misalignment and scale factors	[rad ppm]'
Ω	Discrete time quaternion propagation matrix	[-]
ω	True body angular rate	[rad/s]
$\bar{\sigma}$	Modified Rodrigues parameters (MRP)	[-]
Φ	State transition matrix	[-]
Π	State covariance scaling matrix	[-]
$\tilde{\Lambda}$	Symmetric scale factor matrix	[ppm]
ϑ	Eucleadian 2-norm of the innovation signal attitude	[rad]
ζ	State vector comprising of star tracker misalignment	[rad]
$\lambda_\square$	Symmetric scale factor	[ppm]
μ	Asymmetric scale factor	[ppm]
$\mu_\oplus$	Standard gravitational parameter of Earth (Tapley et al., 1996)	$3.986004415 \, 10^{14}$ [m^3 s^{-2}]
ϕ	Roll angle around X_{Body} axis	[rad]
Ψ	Yaw angle around Z_{Body} axis	[rad]
σ	Standard deviation	[-]
θ	Pitch angle around Y_{Body}	[rad]
$\theta_\square$	Euler attitude angle	[rad]

Latin Symbols

$\tilde{U}$	Asymmetric scale factor matrix	[ppm]
$\underline{q}$	Quaternion three element vector part	[-]
$\mathbf{C}$	Direction cosine matrix	[-]
$\mathbf{G_{DCM}}$	Skew symmetric matrix of $\mathbf{g_{DCM}}$ multiplied with $3n^2$	[rad/s]
$\mathbf{g_{DCM}}$	Vector with direction cosine matrix elements influencing gravity gradient	[-]

$\mathbf{h}$	Angular momentum	[kg m^2/s]
$\mathbf{J}$	NanoSat inertia matrix about the centre of mass	[kg m^2]
$\mathbf{K}$	Kalman gain matrix	[-]
$\mathbf{M}$	Simplified misalignment and scale factor matrix associated with gyro	[-]
$\mathbf{N}$	Window size for spectral analysis based covariance monitor	[-]
$\mathbf{n}$	Number of states in the filter	[-]
$\mathbf{n}$	Spacecraft mean motion	[rad/s]
$\mathbf{P}$	State covariance matrix	[-]
$\mathbf{Q}$	Process noise covariance matrix	[-]
$\mathbf{q}$	Quaternion four element vector	[-]
$\mathbf{R}$	Measurement noise covariance matrix	[-]
$\mathbf{r}$	Circular orbit radius from O_{ECI} to centre of mass of spacecraft	[m]
$\mathbf{S}$	Double-sided power spectral density	[unit^2/Hz]
$\mathbf{t}$	Torque vector	[Nm]
$\mathbf{v}$	Measurement noise	[-]
$\mathbf{W}$	Single-sided power spectral density	[unit^2/Hz]
$\mathbf{w}$	Process noise	[-]
$\mathbf{x}$	State vector	[-]
$\mathbf{y}$	Measurement vector	[-]

Operators

Δ_q	Quaternion discriminant
$\hat{\Box}$	Estimate
∇	Gradient operator
$\odot$	Quaternion or modified Rodrigues parameter multiplication operator
$\ominus$	Quaternion or modified Rodrigues parameter division operator
$\otimes$	Quaternion or modified Rodrigues parameter composition operator
$\Box^*$	Conjugate pair
$\Box^s$	Shadow set operator
$\Box_s$	Skew symmetric matrix operator
$\Box_t$	Quaternion transmutted matrix
$\tilde{\Box}$	Measured
c	Cosine of an angle
s	Sine of an angle
t	Tangent of an angle

Reference Frames and Coordinates

$\mathcal{F}_{\mathcal{B}}$	Body fixed reference frames

$\mathcal{F}_{\mathcal{I}}$	Inertial planetocentric reference frame	
$\mathcal{F}_{\mathcal{R}}$	Rotating planetocentric reference frame	
$\mathcal{F}_{\mathcal{V}}$	Vertical reference frame	
O	Origin of the reference frame	
X	X axis of the reference frame	
Y	Y axis of the reference frame	
Z	Z axis of the reference frame	

Subscipts and Superscripts

$\square^+$	Post update	
$\square^-$	Pre update	
$\square_k$	Variable at time instance k	
1	Yaw around X_{Body} axis	[rad]
2	Pitch around Y_{Body} axis	[rad]
3	Roll around Z_{Body} axis	[rad]
Body, b	Spacecraft body	
d	Desired	
dist	Disturbance	
e	Difference between desired and reference	
ECI	Earth centreed inertial	
g	Ideal gyroscope	
gm	Measured gyroscope	
grav	Gravity gradient	
LVLH	Local vertical local horizontal	
MA	Misalignment	
r	reference	
RW	Reaction wheel	
s1	Star tracker 1	
s2	Star tracker 2	
sc	Spacecraft	
ST	Star tracker	
u	Input	

This page is intentionally left blank.

List of Abbreviations

AKE	attitude knowledge error
ADCS	attitude determination and control subsystem
AODCS	attitude and orbit determination and control subsystem
ASF	asymmetric scale factor
CoM	centre of mass
COTS	commercial-off-the-shelf
CRP	classical Rodrigues parameters
DCM	direction cosine matrix
ECI	Earth centred inertial
ECEF	Earth centred Earth fixed
EKF	extended Kalman filter
FoV	field of view
GEO	geostationary Earth orbit
GNC	guidance, navigation and control
HPTAG	high performance triple axis gyro
IMU	inertial measurement unit
KF	Kalman filter
LCT	laser communication terminal
LEO	low Earth orbit
LoS	line of sight
LVLH	local vertical local horizontal
LPTAG	low performance triple axis gyro
MPSAG	medium performance single axis gyro
MA	misalignment
MEKF	multiplicative extended kalman filter
MEMS	micro electro-mechanical systems
MoI	moment of inertia
MRP	modified Rodrigues parameters
OGS	optical ground station
PSD	power spectral density
RMS	root mean square
RW	reaction wheel
SC	spacecraft
SMaP	size, mass and power
SO(3)	special orthogonal group
SF	scale factor
ST	star tracker
SSF	symmetric scale factor
UKF	unscented Kalman filter
USQUE	UnScented QUaternion Estimator

This page is intentionally left blank.

Motivation behind and the relevance of work undertaken as part of this thesis project is first outlined with the aid of Section 1.1. Section 1.2 will laydown the challenges and limitations associated with precision attitude estimation of agile NanoSats, and eventually introduce the potential solutions to them. Though calibration filters are moderately well studied subject; the need to revisit them, due to the unique hardware limitations, is further motivated. Current industrial practices and academic developments on the matter are discussed. Investigative routes that can lead to potential developments of current practices are proposed. The driving research question, and the corresponding research goals and objectives are captured in Section 1.3. Considering the time constraint on project duration, the scope of the research is narrowed down to focus solely on calibration filter and hardware characterisation utilising star tracker and gyros only. Reaction wheels are utilised to evaluate whether certain manoeuvres can be tracked by NanoSats.

1.1 | Research Motivation and Relevance of Work

NanoSats are becoming increasingly reliable, and capable of conducting complex scientific missions by virtue of advanced instruments on-board. Recent on-orbit demonstrations of ASTERIA (Arcsecond Space Telescope Enabling Research in Astrophysics) suggest that NanoSats are capable of precision photometry and exoplanet detection. This was made possible due to the recent developments in active optics and advances in three axis reaction wheel based active inertial pointing, leading to a pointing stability of 0.5 arcsec over a window of 20 minute (Smith et al., 2018). RainCube uses an active Ka-band radar to observe the evolution of weather systems and paving the way for increased temporal resolution (Tanelli et al., 2019). NanoSats are no longer limited to low Earth orbit (LEO); MarCO A and B became the first interplanetary NanoSats to relay telemetry of the near real-time descent of Insight lander. Insight's first picture of Mars was relayed to Earth by MarCO (Asmar and Matousek, 2016).

The data generated on board of these increasingly complex NanoSats is mismatched by their data downlink capabilities. Higher data transmission rates though achievable by means of radio frequency bands, comes at the disadvantage of higher power requirement, bigger antenna, and a much harder to obtain spectrum allocation on the much crowded radio frequency bands. RainCube for example collects 1.1TB/day at 25% duty cycle. However, with state-of-the-art RF (100 Mbps), from 600 km altitude $\approx$ 45 min of ground target tracking is achievable, only 30GB of data downlink is possible! As a result, most of these NanoSats rely heavily on on-board data compression, in case of RainCube compressing 1.1 TB to 200 MB (Robinson et al., 2019). This demonstrates how under-utilised the payload capabilities of NanoSat remains both in terms of data resolution and operational time. A potential solution to this ever growing need of higher data downlink rates from space, while maintaining lower power and volume, is to utilise a laser communication terminal (LCT) on-board. The fine beam of laser utilised by laser communication terminal, allows higher data transmission rates at a low power requirement by virtue of higher beam directionality. One such NanoSat based laser communication terminal is currently being developed by TNO in collaboration with Hyperion Technologies. The laser communication terminal under development features a 100 μrad fine laser beam, transmitting 1 Gbps of data rates, at a portable 30cm to 80cm ground telescope (Saathof et al., 2019). Despite the ground telescope constantly tracking the NanoSat, this requires the NanoSat to precisely track the ground telescope under agile slew conditions (Cahoy, 2018). This puts strict requirements on the NanoSat Attitude Determination and Control Subsystem (ADCS), which is the central focus of this thesis work.

Although precision inertial pointing has been achieved before with NanoSats, as seen with ASTERIA, agile precision ground target tracking expected of laser communication modules is something that has not been demonstrated before. Though OCSD (Optical Communications and Sensor Demonstration) from AeroCube corporations have claimed to have demonstrated momentary ground-station tracking error of 86.4 arcsec, with attitude knowledge error of 54 arcsec (1-σ), detailed results are not available (Rose et al., 2019). The laser communication module considered for this proposal requires an attitude knowledge of 20.63 arcsec and tracking accuracy of 1800 arcsec(1-σ) (Engelen, 2020a). Precision ground target tracking with Reaction Wheels(RW) is a multi-domain challenge (Cirillo et al., 2016), comprising of the following elements: 1. Actuator design, 2. Control design, 3. Sensor fusion 4. Micro vibration and propellant

sloshing 5. Orbit determination. The RW actuator disturbance introduced an attitude pointing error of 8 arcsec on the attitude pointing performance of ASTERIA (Shields et al., 2017). Similar performances are expected of RW-400.50 from Hyperion Technologies (Engelen, 2020a). Control design challenges depend on the system limitations, especially on the sensor and actuator limitations. Thus characterisation of sensor and actuator limitation is considered as part of the proposed planning. GNSS offered by Hyperion Technologies can provide orbit knowledge of <8m, leading to a tracking knowledge error of 4.125 arcsec (1-σ) from 400km orbital altitude (Engelen, 2020a). Propellant sloshing induced effects is beyond the scope of the proposal. Rigid body rotational dynamics are considered for preliminary considerations. This leaves us with sensor fusion, which is considered to be the most challenging aspect of precision NanoSat, as it relies on utilisation of miniaturised sensors (Yoon et al., 2017). Precision attitude estimation thus forms the central focus of this thesis work.

The challenges associated with the precision attitude knowledge estimation for NanoSat laser communication terminal, can be broadly split in two core segments: 1.) Terrestrial target tracking manoeuvre induced limitations 2.) NanoSat hardware dominated limitations. Typical to the precision attitude determination is the use of star trackers and gyros. A star tracker is a camera that provides long term stable attitude knowledge at low sample rates, and gyros provide short term stable attitude rate knowledge with high sampling rate. These sensors when fused together with a filter, facilitate stable high sampling rates of attitude knowledge (Bayard, 2010, Winkler, 2011). As outlined by (Marlow and Cahoy, 2016), slew rates as high as 1.5 deg/s are expected from LEO NanoSats tracking optical ground station. A sample ground station tracking manoeuvre from 600km altitude (Chen et al., 2000a) in Figure 1.1, shows that it violates the star tracker slew rate capabilities of ST200 and ST400 from Hyperion Technologies (Engelen, 2020a). From a mission planning point of view, on board trajectory optimization as presented in (Magner and Zee, 2018) can lead to increased availability of star trackers. However, high slew rates at high precision still prevail. Thus the focus of this research will be restrained to the NanoSat hardware dominated limitations, and calibration filter development to provide the required precision attitude knowledge during an optical ground station tracking manoeuvre, which can be extended to agile precision target tracking missions in general.

1.2 | Literature Review and Proposed Investigation Direction

The objective of this Section is to signify the differences in attitude knowledge estimation between steady-state inertially pointed and terrestrial target tracking missions that undergo agile slew manoeuvres. In light of that, recent precision pointing and tracking missions, along with the underlying sensor suite and filter schemes are discussed. Strategies utilised by traditional satellites for precision attitude determination under agile conditions is discussed. Limitation of the current precision pointing/tracking NanoSat missions are discussed. Challenges associated with direct implementation of traditional agile attitude determination and calibration techniques, on hardware constrained NanoSats are discussed. Potential solutions to the challenges are presented. The section concludes with a potential choice of calibration filter, in combination with sensor and actuator suites to extend the existing attitude knowledge estimation and calibration of agile terrestrial target tracking NanoSats.
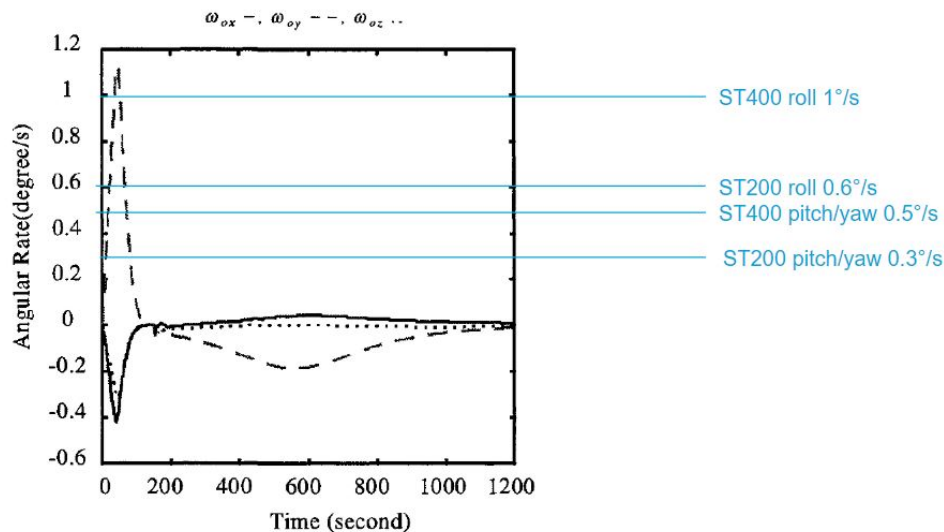
Figure 1.1: *Ground-station tracking slew from 600km altitude. Adapted from (Chen et al., 2000a).*

Recent precision pointing NanoSat mission have mostly been inertially pointed. This includes MinXSS, ASTERIA (world's most precisely pointed NanoSat), and BRITE. All of which utilised 6/7 state variants of Extended Kalman Filter (EKF) (Hegel, 2018). BRITE relied solely on star trackers for precision attitude and attitude rate estimation, to avoid the noise introduced by miniaturised rate gyros (Sarda et al., 2014). The laser communication terminal under development requires precision attitude knowledge requirement of 20.63 arcsec (1σ) under agile slew manoeuvre of 1.5 deg/s. Better attitude knowledge acquisition precision results in better attitude control accuracy, which leads to better final pointing/tracking performance; this leads to finer beamwidth of laser that requires transmission to a ground station. Finer the beamwidth of a laser beam, more energy and hence higher data-rates can be transmitted to a ground terminal. Given optimal stars in the Field of View (FoV) and 5 Hz of sample rate, the star tracker attitude solution has a consistent offset of 1.5/5 = 0.3 degrees. And to satisfy 20.63 arcsec attitude sampling at 1.5 deg/s, the gyros must be sampled at (1.5/(20.63/3600))·2 = 523.5 Hz to satisfy the Nyquist criterion, and meet the desired attitude resolution. Under agile conditions sampling gyros at high rates, and passing them through a low-pass low-delay anti-aliasing filter to meet the desired attitude knowledge is common to traditional satellites (Lam et al., 2003). This brief analysis demonstrates that for the expected conditions, both MEMS gyro and star tracker must be utilised. Besides this, star tracker blinding under agile slew manoeuvres, or Earth-limb/Moon/Sun/low stars in the FoV is very common. Under such momentary blinding conditions, satellites typically rely on the gyro's dead reckoning capabilities.

Contrary to traditional satellites, NanoSatellites do not have access to fibre optic gyro (FOG)/hemisphere resonance gyros (HRG) due to their size, weight and power (SWaP) limitations. MEMS gyro noise can be classified into angle quantization (AQ), angle flicker noise (AFN), angle random walk (ARW), rate flicker noise (RFN), rate random walk (RRW) and rate ramp (RR). Of these, ARW is an indicator of the long term gyro solution stability, and the most dominant source of noise at low freq (Pittelkau, 2010). ARW for MEMS gyro is a factor of 10-100x worse than FOG/HRG (Yoon et al., 2017). One possibility of reducing MEMS gyro noise is to utilise a cluster of gyros. It is a well known statistical fact that averaging n uncorrelated homogenous sensors with noise σ, leads to a performance of $\frac{\sigma}{\sqrt{n}}$, and if the gyro clusters are correlated this performance can be improved further (Xue et al., 2012). Though this strategy leads to improved MEMS gyro solution with regards to random noise, however the systematic errors associated with the system: misalignment, symmetric and asymmetric scale factors are not compensated for. The ill-effects of attitude estimation without calibrating for misalignment, symmetric, and asymmetric scale factor were presented in (Pittelkau, 2001). In the absence of calibration for these deterministic parameters, the performance of traditional 6/7 state Kalman filtering scheme for attitude estimation degrades significantly under agile tracking conditions expected of laser communication terminals. Pittelkau further outlined in his survey of on-board implementation and the developments of calibration algorithms; that star tracker sample rates will increase from 20 to 100 Hz in the future, which are expected to improve the performance of gyro-less attitude control systems. However, improved accuracy and sampling rates of star-trackers will not displace gyros in cases where low noise, low latency, and wide bandwidth are required. Low latency is clearly important for high precision agile slew manoeuvres. Previous on-board real-time calibration applied to larger class of satellites included Spitzer, Cassini, and ICESAT. Draper inertial stellar compass demonstrated the feasibility of an EKF based calibration filter with MEMS gyros and star tracker (Pittelkau, 2007).

Given that both NanoSat star tracker and MEMS gyro cluster are required to meet the desired attitude knowledge performance specification; the next challenge is to find alternative solutions that minimize the MEMS gyro cluster size and its corresponding impact on the calibration filter solution times. One such solution is witnessed in (Yoon et al., 2017), where to facilitate gyroless attitude estimation, reaction wheel hall-sensors are utilised. With the aid of reaction wheel hall sensors, the filter calibration states might be extended to include reaction wheel misalignment, reaction wheel and NanoSat moment of inertia, wheel speeds, and unmodelled disturbance torque. Most reaction wheels are flown as momentum wheels, esp. for precision missions, to avoid zero-wheel crossings that reduce reaction wheel life time, and significantly impact the attitude pointing precision. At such momentum offset conditions reaction wheel hall sensors have significant samples, 8 to 24 per wheel rotation for RW400 (Engelen, 2019), and unlike star trackers do not undergo blinding. Utilising these hall sensor readings has the potential to improve the attitude estimation and calibration performance, and leading to the reduction of large cluster size of MEMS gyros.

Though nominal orbital manoeuvres are sufficient, calibration manoeuvres might be necessary for persistence of excitation and dynamic observability of the calibration parameters (Pittelkau, 2005a). Corkscrew manoeuvre traditional to larger class of satellites might not be feasible for NanoSat applications due to the limited boresight performance, as a result, a 6U NanoSat rigid body simulator is developed considering reaction wheel torque response delays. Since the calibration filter update rate is limited to the star tracker solution update rate, in between the star tracker solution update, gyro only dead-reckoning or reaction-wheel and gyro fused dead-reckoning in combination with
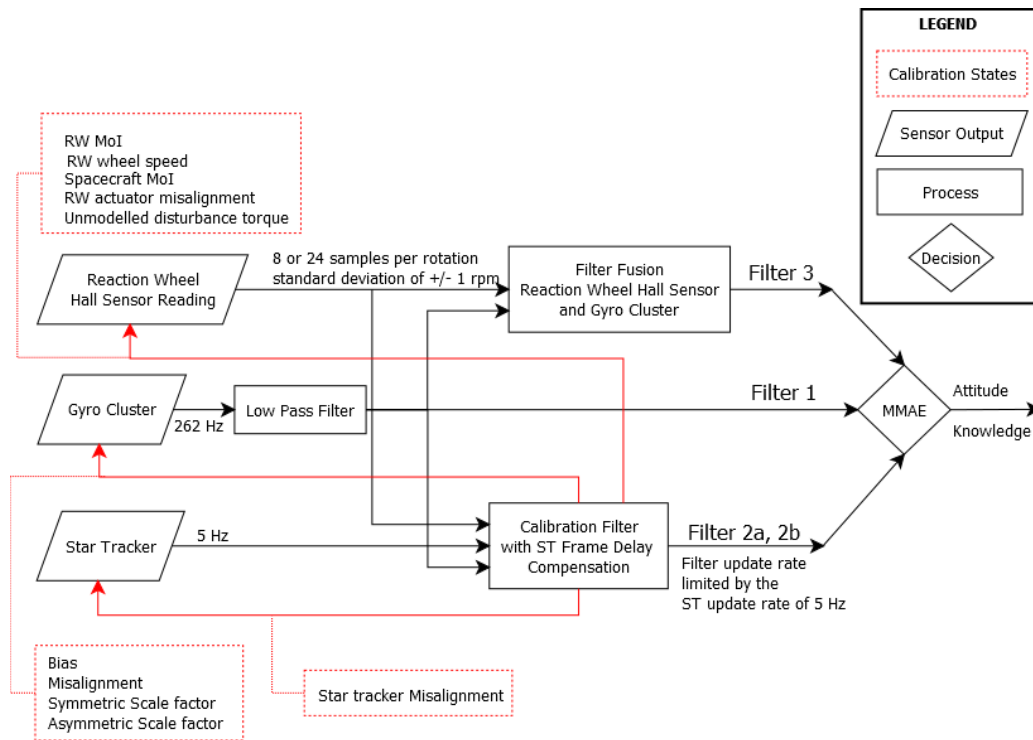
Figure 1.2: *Overview of the general proposed calibration and precision attitude estimation filter, capable of supporting the high precision and high attitude knowledge solution update rate requirement for agile NanoSat laser communication terminals.*

the calibration parameters from previous filter update is proposed. In light of that a Multi-Model Adaptive Estimator (MMAE) scheme as outlined in (Lam and Crassidis, 2007), can be utilised to compensate for the low star tracker solution update rate, and provide the attitude control loop and the laser communication terminal with higher rate of attitude knowledge estimates. An overview of the proposed scheme is presented with the aid of Figure 1.2. Depending on the availability of the sensor suite, different filter outputs are utilised to provide the attitude knowledge estimate required by the Laser Communication Terminal/AOCS unit. Filter 1, utilises a low pass filter on the averaged gyro cluster output to provide attitude knowledge based on dead-reckoning. This is activated when both reaction wheel hall sensor and star tracker output are unavailable. In the absence of star trackers, Filter 3 fuses the reaction wheel hall sensor and gyro output reading in-combination with the rotational dynamics and kinematics to provide the desired attitude knowledge. Filter 2b, fuses reaction wheel hall sensor, gyro, and star tracker output to provide the attitude knowledge. And Filter 2a, fuses star trackers and MEMs gyro cluster to provide the required attitude knowledge. Due to time constraint of the proposed project, the scope of the project is limited to Filter 2a utilising MEMS gyro cluster and star trackers.

In the presence of star tracker solution delays and lower solution update rates, it is necessary to be able to propagate over longer time duration. An Unscented Kalman Filter based calibration filter has shown promise in faster convergence and robustness of solution, especially for longer propagation durations, over EKF variants as seen in (Lai et al., 2003). For larger class of satellites with better hardware, it has been argued in (Pittelkau, 2007) that UKF might require 4 times the computational power of EKF. However, recent developments in NanoSat onboard computer suggest such computational requirements is not problematic (Engelen, 2019). However, lighter variants of UKF, e.g. Single Propagated UKF in (Biswas et al., 2018), have demonstrated equal robustness, faster convergence, and solution update rate, when applied for 6/7 state filtering processes on CubeSats. In the face of computational adversities, these lighter alternatives are worth investigating for application to calibration filters.

To conclude, this segment of the research plan aimed at stressing the need to revisit calibration filters, under the limitations imposed by NanoSat hardware, to meet the attitude knowledge requirements expected of laser communication terminal. Limitations imposed by NanoSat hardware under agile slewing operations were discussed; and a general scheme based on four underlying filters operating upon the availability of sensor suite was presented. The scope of the proposed research plan is narrowed down to focus on calibration filter associated with MEMS gyro

cluster and NanoSat star trackers. Four different types of MEMS rate gyros and a variant of NanoSat star tracker will be characterised and modelled in collaboration with Hyperion Technologies. Physical steady state attitude error noise floor of different configurations of gyro-stellar combinations arising out of these sensor combinations will be analysed. Gyro-stellar configurations will be chosen, based on attitude error noise Power Spectral Density, such that they meet the attitude knowledge requirement expected by NanoSat laser communication terminal. UKF based calibration filter will be synthesised to calibrate for deterministic error sources, required to meet the attitude knowledge requirements under non-ideal sensor alignment and scale factor conditions. Calibration manoeuvres shall be investigated to facilitate persistent-excitation/observability of deterministic error states. Capability of NanoSat reaction wheels to track these manoeuvres shall be investigated by testing the torque input-output response of reaction wheels, in collaboration with Hyperion Technologies. The conducted research will provide insight into the current attitude knowledge estimation and calibration capabilities of NanoSats under agile operational conditions, and lay down the foundation for the generalised four filter based scheme outlined earlier in this section. The conducted research shall further outline the limitation of regular 6/7 state UKF based attitude estimator (USQUE), in the presence of sensor misalignment and scale factor, for different manoeuvre profiles. Furthermore performance of an USQUE based calibration filter, under such operational conditions will be evaluated.

1.3 | Research Question(s), Aims/Objectives and Sub-goals

Sections 1.1 and 1.2, meticulously laid down the necessity of investigating the precision attitude estimation challenges of agile precision terrestrial target tracking NanoSats bounded by sensor and actuator limitations. The research question central to this proposal is presented in Section 1.3.1, while the corresponding project goal is captured in Section 1.3.2.

1.3.1 | Research Question(s)

In order to meet the objective of providing an attitude knowledge of 20.63 arcsec (1σ) for NanoSat laser communication terminal, under terrestrial targeting tracking applications with agile slew rates upto 1.5 deg/s, the following research question is formulated:

> How can we extend the attitude knowledge estimation capabilities of agile precision target tracking NanoSats, by virtue of calibration filters utilising NanoSat MEMS rate gyro cluster and star trackers as sensing elements?

This core research question can lead to the following sub-questions:

1. How well can the relevant performance parameters of MEMS rate gyro clusters and NanoSat star tracker be characterised, and modelled?

2. What configuration and sampling rate of NanoSat star tracker and MEMS rate gyro cluster will lead to minimal attitude estimation error from a steady state random noise power spectral density standpoint?

3. What is the attitude knowledge performance of a regular attitude and bias estimator, for steady state and agile manoeuvres in the presence of sensor misalignment, scale factors and slew-rate induced star tracker drop out?

4. How well can a calibration filter provide attitude knowledge, for steady state and agile manoeuvres in the presence of sensor misalignment, scale factors and slew-rate induced star tracker drop out?

5. How do calibration manoeuvres impact the convergence of calibration parameters?

6. How is the calibration filter parameter estimation and convergence performance impacted by degraded MEMS rate gyros?

1.3.2 | Research Objective

The research questions in the previous section can lead to the following main objective for the research to be undertaken:

> The objective of the research project is to investigate the attitude knowledge estimation and calibration capabilities of agile terrestrial target tracking NanoSats, in particular enable the strict body attitude knowledge requirement expected of NanoSat laser communication terminal under agile slew rates, by characterising a cluster of MEMS rate gyros and NanoSat star trackers, and testing the performance of the calibration filter convergence for attitude knowledge and calibration parameter estimation for different gyro-stellar configu-

rations.

The above presented research objectives can be further divided into five research sub-goals.

Sub-Goal 1: Characterise, model and verify NanoSat MEMS rate gyros and star trackers for configuration selection by steady state random noise power spectral density analysis.

Sub-Goal 2: Develop a rigid body NanoSat simulator with actuator considerations to simulate calibration and ground target tracking manoeuvres, while facilitating sensor output readings corrupted by random and deterministic noise sources.

Sub-Goal 3: Demonstrate the attitude knowledge performance degradation of a 6/7 state Unscented attitude and gyro bias estimator, in the presence of sensor misalignment, scale factor and slew-rate induced star tracker dropouts.

Sub-Goal 4: Evaluate the attitude knowledge performance of an Unscented calibration filter for the chosen gyro-stellar configurations, in the presence of sensor misalignment, scale factor and slew-rate induced star tracker dropouts.

Sub-Goal 5: Evaluate the sensitivity and parameter convergence of the synthesised Unscented calibration filter, with regards to sensor degradation and calibration manoeuvres.

The novelty of the proposal, lies in the synthesis of calibration filter for precision attitude knowledge estimation of a hardware-constrained agile terrestrial target tracking NanoSat. The primary focus is thus on the characterisation and modelling of different types of MEMS rate gyros, NanoSat star tracker, and reaction wheels; which is made possible by the hardware support of Hyperion Technologies. Based on the hardware characterisation, different configuration of MEMS gyro cluster and star tracker will be chosen for utilisation in a UKF based calibration filter. As discussed earlier in Section 1.2, calibration filters, in general, have proven their precision attitude estimation capability in traditional agile satellites by virtue of deterministic error source calibration. This work shall investigate their applicability and significance with regards to NanoSat hardware.

Sensor misalignments are common to all satellites. Even when sensor alignments are calibrated optically with a Master Reference Cube (MRC) on ground, launch vibrations and thermal expansions can lead to sensor misalignments. Under inertial/steady pointing conditions, gyro misalignment and scale factor is captured as a linear combination under the estimated gyro bias. However under agile/target tracking conditions, performance of a steady state attitude estimation filter is expected to degrade significantly due to the presence of uncalibrated sensor misalignment and scale factors. This is especially true for NanoSats. Due to low volume, and low cost entry point to space, often times an MRC is not utilised for on ground calibration of sensor misalignments. Furthermore, MEMS rate gyros on NanoSat PCBs(Printed Circuit Boards) are auto-picked and placed, which can easily introduce sensor misalignments in the order of degrees. A calibration filter is investigated, to fuse the heterogeneous configuration of sensors and provide the necessary calibration thereof. This, in general, enables increased autonomy of satellites, and reduces the efforts of calibration on ground, and during satellite commissioning phase.

1.4 | **Thesis Outline**

A visual overview of the tasks undertaken as part of the thesis work, is outlined with the aid of Figure 1.3. First, the specifications of the hardware under consideration, and the corresponding mission overview and requirement is defined in Chapter 2. Sensors configurations are selected, characterised, modelled and verified in Chapter 3. A rigid body NanoSat simulator is developed in Chapter 4, with sensor and actuator limitations under consideration. Calibration and ground target tracking manoeuvres are synthesized, and the output of the rigid body NanoSat simulator in the presence of sensor disturbances, misalignment and scale factors is presented. Chapter 5 presents the algorithm for UnScented QUaternion Estimator (USQUE), and USQUE based calibration filter. Performance of the developed filters, is discussed in Chapter 6. Conclusions and recommendations are presented in Chapter 7.
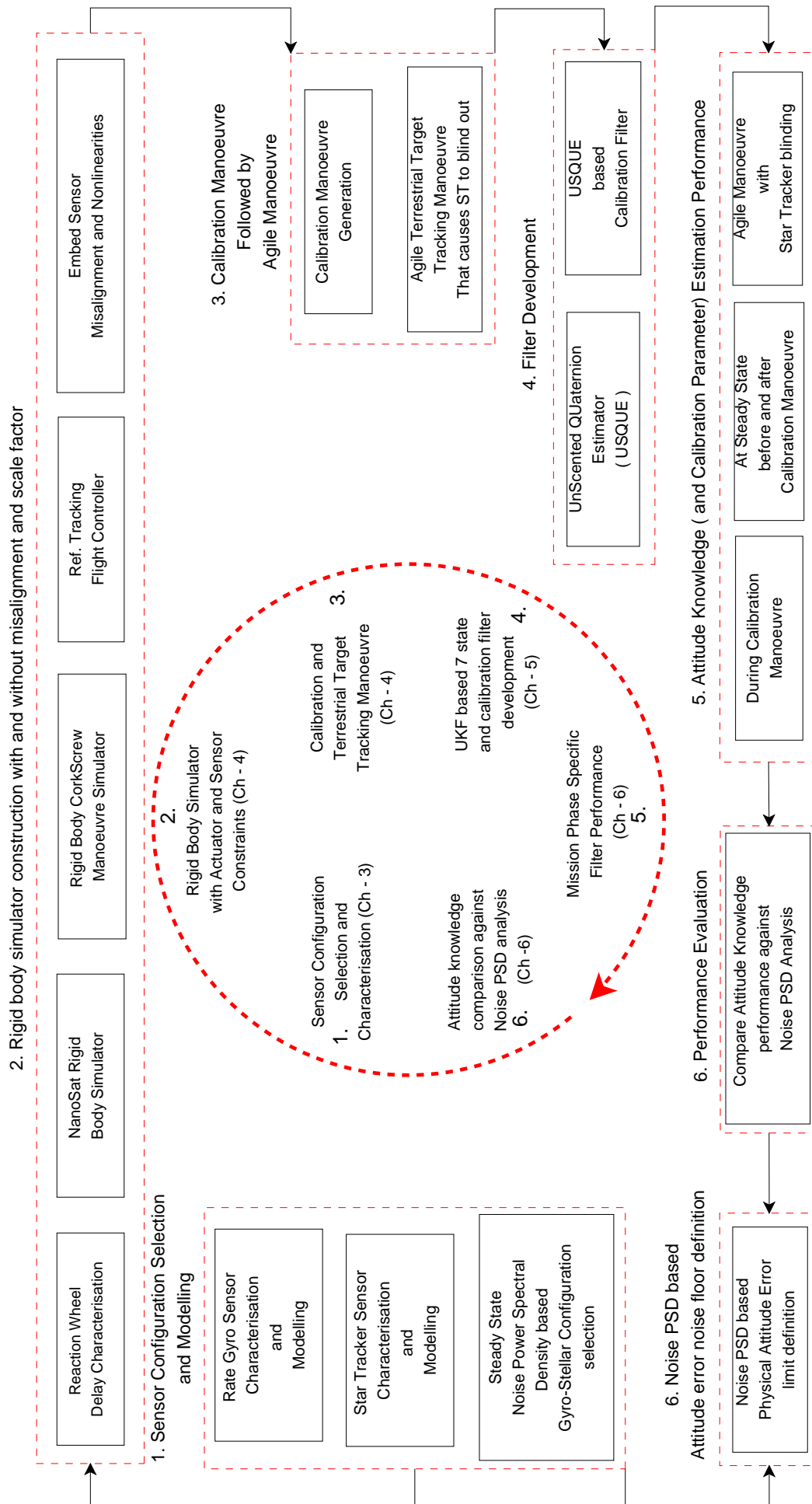
Figure 1.3: *Overview of the elements undertaken as part of the thesis project.*

This page is intentionally left blank.

Mission and Hardware Overview

The following sections aim at presenting an overview of a representative agile mission, and the relevant hardware under consideration. Section 2.1 provides an overview of the mission, and the corresponding attitude requirements. Section 2.2 presents an overview of the hardware under consideration for this thesis work, and the underlying hardware specifications.

2.1 | Mission Overview and Requirements

A representative agile precision target tracking mission is captured with the aid of Figure 2.1, where a laser communication terminal is utilised as the payload. The objective of the NanoSat mission is to track an Optical Ground Station (OGS), and downlink data with a laser communication terminal. The Optical Ground Station under consideration is expected to be portable and have a diameter of 30-80 cm for laser beam reception. The laser communication terminal under consideration has a Full-Width-Half-Maximum beamwidth of 100 μrad, which enables a data transmission rate of 1 Gbps at a slant range of 1000 km. In order to meet such high data throughput, via such a narrow beamwidth, the NanoSat must follow strict body pointing requirements. In order to ensure data transmission under agile slewing conditions, the optical ground station further tracks the NanoSat with an uplink beacon. As demonstrated by Step 2, in Figure 2.1, the OGS actively seeks the downlink beacon, beamed by the laser communication terminal. The laser communication terminal seeks the uplink beacon, transmitted by the OGS. Once the NanoSat detects the uplink beacon, it latches onto the uplink beacon with a Fine Steering Mirror (FSM) as shown by Step 3. The uplink beacon further boosts the attitude knowledge of the NanoSat. Until this step, the NanoSat is expected to facilitate the attitude pointing requirements expected of the laser communication terminal.

In order to meet the above presented mission objectives, relevant requirements are presented with the aid of Table 2.1, 2.2. The requirements are defined with a unique identifier. The nomenclature utilised to define the requirements follow the following template:

$$\underbrace{\textbf{V}}_{\text{type}}\text{REQ} - \overbrace{\textbf{WW}}^{\text{depth}} - \underbrace{\textbf{XX}}_{\text{(sub)system}} - \overbrace{\textbf{YY}}^{\text{depth of (sub)system (optional)}} - \underbrace{\textbf{ZZ}}_{\text{Category (optional)}} - \overbrace{\textit{A.B}}^{\text{number}}$$

Here, **V** defines the type of requirement. It can be either a functional (F), performance (P), or constraint (C) requirement. Functional requirements define the function that needs to be done in order to accomplish the mission
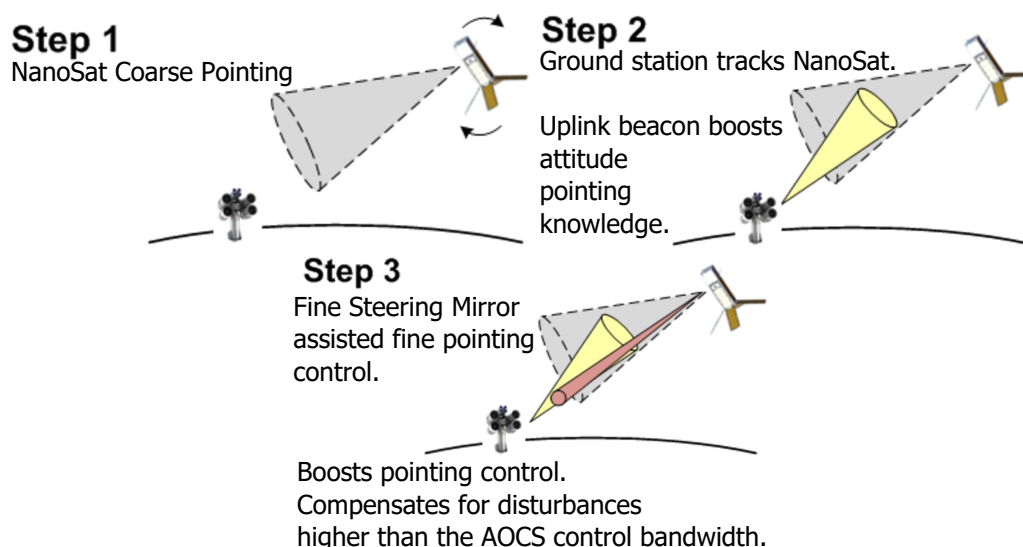
Figure 2.1: *Architecture for pointing of NanoSat featuring Laser Communication Terminal. Adapted from (Cahoy, 2018).*

Table 2.1: *Preliminary requirements associated with the ADCS unit, relevant for achieving the mission objectives of NanoSat laser communication terminal.*

ID	Requirement	Rationale
Mission design		
CREQ-M-SC-1	The NanoSat shall have a volume of 6U (30cm x 20cm x 10cm).	Deployer induced
CREQ-M-SC-2	The NanoSat shall have a maximum total mass of 12kg.	Launcher/Deployer induced
CREQ-M-SC-3	The NanoSat shall have a maximum principal mass moment of inertia of diag(0.025, 0.05, 0.065) kg.m^2	Based on uniform mass and volume
FREQ-M-SC-C-1	The NanoSat shall be able to meet the pointing requirement expected from all mission phases	Payload driven
FREQ-M-SC-ADCS-N-1	The NanoSat shall be able to meet the attitude knowledge requirement expected from all mission phases	Payload driven
CREQ-M-SC-4	The NanoSat shall have a nominal operational altitude in the range 300-600 km	Mission driven
CREQ-M-SC-5	The NanoSat shall be in a quasi-polar LEO, with inclination of 92°	Relevant for guidance
NanoSat design		
FREQ-S-ADCS-C-A-1	The NanoSat shall have one reaction wheel per body axis for three axis active attitude control.	Mission driven
FREQ-S-ADCS-N-S-1	The NanoSat shall have at least 2 star trackers for precision attitude knowledge measurement.	Avoiding occultation Improving attitude knowledge
FREQ-S-ADCS-N-S-2	The NanoSat shall have TBD MEMS rate gyros for attitude rate measurement.	Sensor fusion and ST calibration (See Ch-3)
Guidance		
FREQ-S-ADCS-SW-G-1	The NanoSat guidance system shall be able to generate calibration manoeuvres.	Calibration driven
FREQ-S-ADCS-SW-G-2	The NanoSat guidance system shall be able to generate terrestrial ground target tracking manoeuvres	Data downlink driven Earth observation driven
FREQ-S-ADCS-SW-G-3	The NanoSat guidance system shall be able to generate inertial pointing manoeuvres.	Optical payload driven
Navigation		
PREQ-SS-ADCS-SW-N-1	The NanoSat state estimator shall run at 5 Hz	Slew rate driven
PREQ-SS-ADCS-SW-S-1	The star tracker shall provide attitude knowledge with an update rate of 5 Hz.	ST hardware driven
PREQ-SS-ADCS-SW-S-2	MEMS rate gyros shall operate at TBD Hz.	Manufacturer specific (See Table 3.3)
PREQ-SS-ADCS-SW-S-3	MEMS rate gyros shall provide attitude rate knowledge at 5 Hz.	Slew rate driven
FREQ-SS-ADCS-SW-N-1	The state estimator shall provide attitude knowledge in the event of no star tracker knowledge update.	Payload driven
FREQ-SS-ADCS-SW-N-2	The state estimator shall be capable of operating under asynchronous gyro-stellar sensor inputs	Payload driven
PREQ-SS-ADCS-SW-N-2	The NanoSat state estimator shall provide an absolute attitude knowledge error bound of 20.63 arcsec(1 σ) with respect to the inertial reference frame, across all mission phases	Payload driven
PREQ-SS-ADCS-SW-N-3	The calibration filter shall operate at 5 Hz.	ST update rate driven
PREQ-SS-ADCS-SW-S-4	The calibration filter shall calibrate the star tracker misalignments to an accuracy of TBD arcsec	undefined
PREQ-SS-ADCS-SW-S-5	The calibration filter shall calibrate the gyro misalignments to an accuracy of TBD arsec	undefined
PREQ-SS-ADCS-SW-S-6	The calibration filter shall calibrate the gyro scale factors to an accuracy of TBD ppm	undefined
Control		
PREQ-S-ADCS-C-1	The NanoSat control system shall be able to track calibration manoeuvre with a maximum absolute pointing error of 1800 arcsec(1 σ) in the inertial reference frame.	Based on mission pointing requirement
PREQ-S-ADCS-C-2	The NanoSat attitude control system shall be able to track a reference ground station attitude with a maximum absolute pointing error of 1800 arcsec(1 σ) in the inertial reference frame.	LCT induced
PREQ-S-ADCS-C-3	The NanoSat attitude control system shall be to track other guidance signals with a maximum absolute pointing error of 1800 arcsec(1 σ) in the inertial reference frame.	Payload induced

objectives. Performance requirements define how well the system needs to perform the functions. Constraints are requirements that cannot be traded off with respect to cost, schedule, or performance (Prof. Olivier de Weck, 2009). Character **WW** represents whether the requirement is a mission (M), system (S), or subsystem (SS) requirement. **XX** represents the acronym of the system or subsystem under consideration. For instance, SC= spacecraft, and ADCS = attitude determination and control system. **YY** defines the item of (sub)system under consideration, for instance G= guidance, N= navigation, C= control, SW= onboard software, and SIM= simulator. **ZZ** identifies the category of item, for instance G= guidance, N= navigation, C = control, S= sensor, and A= actuator. Finally, *A* defines the requirement number, and *B* identifies a sub-requirement.

Table 2.2: *Preliminary simulation requirements associated with the ADCS unit, relevant for achieving the mission objectives of NanoSat laser communication terminal.*

ID	Requirement	Rationale
	Simulation	
PREQ-SS-ADCS-SIM-S-1	At steady state conditions, 1σ standard deviation obtained from MEMS rate gyro simulator output noise PSD shall not exceed the 1σ standard deviation obtained from Allan-variance based noise PSD by a factor of 1.001	See Table 3.13, and 3.14
PREQ-SS-ADCS-SIM-S-2	At steady state conditions, difference between 1σ standard deviation obtained from low-pass filtered gyro output noise PSD and Allan-variance based noise PSD shall not exceed more than a factor of 1.01	See Table 3.15
PREQ-SS-ADCS-SIM-S-3	At steady state, 1σ standard deviation of the star tracker noise PSD simulator, shall not exceed the analytical 1σ standard deviation by a factor of 1.01	See Table 3.16
FREQ-SS-ADCS-SIM-S-1	Rigid body simulator shall be capable of generating attitude signal as seen by the star tracker	Input for filter
FREQ-SS-ADCS-SIM-S-2	Rigid body simulator shall be capable of generating attitude rate signal as seen by the gyro	Input for filter
FREQ-SS-ADCS-SIM-S-3	Rigid body simulator shall be able to map gyro-stellar misalignment and scale factors in the respective sensor body frames.	Input for filter
FREQ-SS-ADCS-SIM-S-4	Rigid body simulator shall be able to generate gyro-stellar output under the influence of misalignments and scale factors	Input for filter
FREQ-S-ADCS-SIM-G-1.A	The rigid body NanoSat simulator shall be able to generate representative guidance maneouvres.	Evaluation of filter performance
FREQ-SS-ADCS-SIM-G-1.B	Initial steady state and calibration manoeuvre shall be simulated with a kinematics based simulator.	Input for filter
FREQ-SS-ADCS-SIM-G-1.C	Phase B of the manoeuvre shall comprise of pre-ground target tracking manoeuvre, agile ground target tracking manoeuvre, and target tracking manoeuvre.	Filter performance across different mission phases
CREQ-SS-ADCS-SIM-A-1.A	Reaction wheel torque limit shall be saturated at 0.17 mNm for tracking Phase B manoeuvre	See Section 4.4.1
FREQ-SS-ADCS-SIM-A-1.B	Reaction wheel torque input-output delay shall be considered for tracking Phase B manoeuvre	See Section 4.4.1
PREQ-SS-ADCS-SIM-C-1	Phase B manoeuvre shall be tracked with a worst case accuracy of 1800 arcsec (1σ).	See Figures C.5, and C.6

Table 2.3: *Overview of star tracker performances from Hyperion Technologies (Engelen, 2020a).*

Hyperion Technologies Star Tracker		
Performance		
ST200	*Value*	*Units*
Absolute attitude determination accuracy (pitch, yaw)	30	arcseconds (3σ) [1] [2]
Absolute attitude determination accuracy (roll)	200	arcseconds (3σ)
Update rate	5	Hz
Maximum slew rate (tip/tilt)	>0.3	°/s
Minimum slew rate (roll)	>0.6	°/s

2.2 | Hardware Under Consideration

Given the above presented mission overview and expected attitude knowledge requirement, the objective of this thesis work is evaluate whether such strict attitude knowledge requirements can be met by NanoSat hardware, in the first place. It is still unclear whether the presented requirements are feasible for NanoSats for the mission profile discussed. In light of this, the first objective of this thesis work is to characterise and procure hardware. Later the characterised hardware parameters are utilised to construct models, to be facilitate inputs for relevant algorithms.

Since the thesis work is extended at Hyperion Technologies, hardware from Hyperion Technologies is utilised wherever applicable. A variant of integrated-Attitude Determination and Control Subsystem-400, presented with the aid of Figure2.2a, is utilised for this thesis work. Instead of the one star tracker in the current model, 2 star trackers are included to enable precision pointing and tracking, and avoid occultation of the star trackers. ST200 series of star trackers, as presented in Figure 2.2b, are utilised for this thesis work. Performance specification of the star trackers is provided with the aid of Table 2.3. RW-400.50 series of reaction wheels, as presented in Figure 2.2c, is utilised for this thesis assignment. Specifications for RW-400.50 is presented with the aid of Table 2.4. Detailed analysis of the relevant reaction wheel parameters for rigid body NanoSat simulator development is presented in Section 4.4.1. CUBECAT laser communication terminal which is used as a reference payload for agile terrestrial target tracking NanoSat missions is presented with the aid of Figure 2.3. Corresponding specifications are presented with the aid of Table 2.5.

(a) *Integrated ADCS, iADCS-400.*

(b) *ST200 star tracker.*

(c) *RW-400.50 reaction wheel series.*

Figure 2.2: *ADCS hardware components developed Hyperion Technologies, that are taken into consideration for this thesis work (Engelen, 2020a).*

Table 2.4: *Reaction wheel system performance overview (Engelen, 2020a).*

	HT RW400 [Mean] (Engelen, 2019)	HT RW400 [σ] (Engelen, 2019)	HT RW400 [3σ] (Engelen, 2019)
Max. Momentum Storage [mNms]	15, 30, 50	15, 30, 50	15, 30, 50
Max. Torque [mNm]	12	12	12
Max rotation speed [rpm]	6000	6000	6000
Control accuracy [% target of rpm]	+/- 1	+/- 1	+/- 1
Static Imbalance [$\mathrm{g\ mm}$] *(Fine)	0.0007	0.0003	0.0016
Dynamic Imbalance [$\mathrm{g\ mm^2}$] *(Fine)	1.7	1.3	5.6

Table 2.5: *Performance specifications of CubeCAT laser communication terminal from Hyperion Technologies (Engelen, 2020a).*

CubeCAT laser communication terminal (LCT)[3]		
	Value	*Units*
Performance		
Raw data rate modes (downlink)	100/300/1000	Mbps
Raw data rate (uplink)	200	kbps
On-board buffer size	>64	GB
Maximum slant range	1000	km
Host satellite platform constraints		
Pointing accuracy	<8.7/ 0.5/ 1800	mrad/ deg/ arcsec (3σ)
Low-frequency vibration velocity (<20Hz)	<2.445	mrad/s (3σ)
High frequency vibration/jitter amplitude (>20Hz)	<15/0.86/3.1	μ rad/mdeg/arcsec (3σ)
Pointing knowledge error	<0.3/17.2/61.9	mrad/ mdeg/ arcsec (3σ)
Dimension		
Outer Dimensions	96 x 96 x 96	mm
Mass	<1.33	kg

An overview of the MEMS rate gyros characterised as part of this thesis work is presented with the aid of Figure 2.4. Due to confidentiality concerns, vendor names are not presented here. Detailed characterisation of all gyros is discussed in Chapter 3.

---

[1]Single axis 3 sigma definition (Presented values): `https://bit.ly/31bM5Lr`
[2]Multi axis 3 sigma definition: Ch-7.2.2.2 of (Wertz, 2001)
[3]Hyperion Technologies LCT: `https://hyperiontechnologies.nl/wp-content/uploads/2019/05/HT-LC400-V1.1_Flyer.pdf`

Figure 2.3: *CUBECAT laser communication terminal from Hyperion Technologies (Engelen, 2020a).*
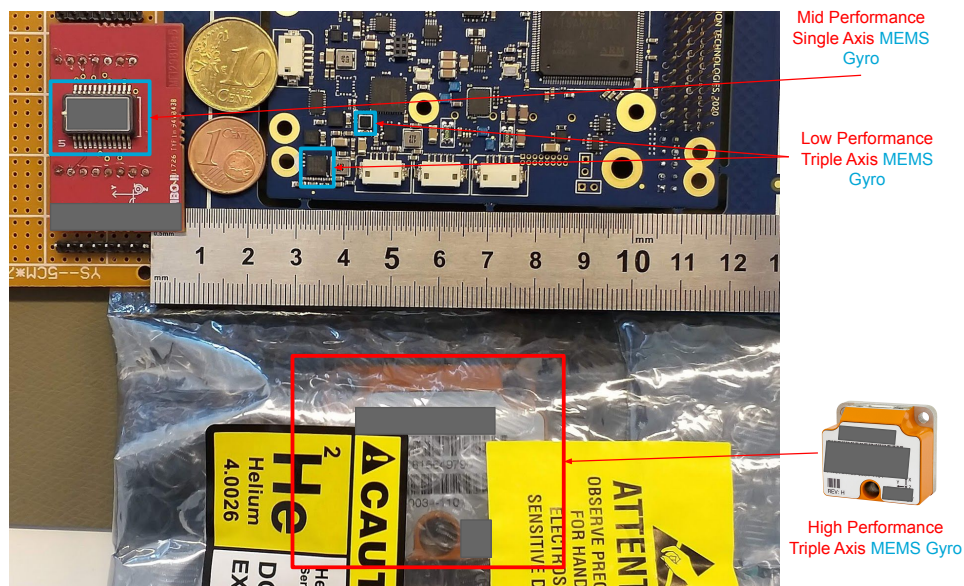
Figure 2.4: *Overview of the four different variants of MEMS rate gyros considered as part of this thesis work. Current Low Performance Triple Axis MEMS rate gyros on iADCS-400, in combination with High Performance Triple Axis and Medium Performance Single Axis MEMS rate gyro considered for future developments (Engelen, 2020b).*

This page is intentionally left blank.

Sensor Characterisation and Configuration Selection

3.1 | Methodology

This chapter serves three core objectives. The first objective of this chapter is to outline the characteristic parameters of the sensors utilised for the calibration filter. Section 3.2 is aimed at defining the stochastic and systematic parameters of a MEMS gyro. Mechanisms to model and represent these parameters for the calibration filter synthesis process is further discussed. The second objective of this chapter is to characterise these sensor specific parameters to facilitate appropriate selection of sensor configuration to meet the desired attitude knowledge estimation requirement. In that regard, Section 3.3 first outlines the sensors utilised and their respective characteristic properties. Allan-Variance and noise Power Spectral Density (PSD) analysis is conducted on singular sensor units to facilitate configuration selection. Gyro-stellar noise power density hybridisation is conducted on the noise PSD of independent MEMS gyro sensor units, along with 7 different homogenous and heterogeneous configurations. Based on this, the gyro-stellar configuration is selected for the calibration filter. The objective of the calibration filter is to identify the systematic noise sources and meet the physical noise density limits. The final objective of this chapter is to present and verify a gyroscope simulator, that captures the noise density behaviour of the chosen gyros. This verified stochastic gyro noise model is utilised to read out the rigid body NanoSat angular rates. This is presented with the aid of Section 3.4. Low pass filters are synthesised in Section 3.5 to subsample the MEMS rate gyros. Subsampled gyro output is further verified. Star tracker noise model is defined and verified in Section 3.6. Outcome of the chapter is summarised in Section 3.7.

3.2 | Gyroscope Parameters

The errors associated with rate gyros, can be classified into stochastic and systematic errors. And overview of the stochastic noise parameters is presented in Section 3.2.1, similarly an overview of the systematic error parameters is presented in Section 3.2.3. Modelling of stochastic noise parameters in presented in Section 3.2.2. Modelling of systematic error parameters is presented in Section 3.2.4. Section 3.2.5 captures the gyro sense axes parametrisation utilised for the UKF based calibration filter.

3.2.1 | Stochastic Noise Parameters

Typical gyro noise parameters can be segmented into six different types, which taken together captures the gyro noise behaviour. These include angular random walk (ARW), angle quantization (AQ), angle flicker noise (AFN), rate flicker noise (RFN)/bias instability (B)/pink rate noise, rate random walk (RRW), rate ramp (RR). Among these, angular random walk, rate random walk, rate flicker noise (Bias Instability) are commonly observed in case of MEMS rate gyros. For low performance MEMS rate gyro, in addition to the aforementioned rate ramp and angle quantization noise can be further observed.

A brief description of the stochastic noise errors is presented here. For further details interested readers are referred to (IEEE Std 647-2006, 2006, IEEE Std 952-1997, 2008, Pittelkau, 2010).

- **Angular random walk (ARW)** $[°/\sqrt{h}]$: Angle random walk can be expressed with the help of Farenkopf's gyro model (Lai et al., 2003):

$$\tilde{\boldsymbol{\omega}}(t) = \boldsymbol{\omega}(t) + \boldsymbol{\beta}(t) + \boldsymbol{\eta}_v(t) \tag{3.1a}$$

$$\dot{\boldsymbol{\beta}}(t) = \boldsymbol{\eta}_u(t) \tag{3.1b}$$

Here, $\tilde{\boldsymbol{\omega}}$ is the attitude rate measured by the gyro. $\boldsymbol{\eta}_v$ and $\boldsymbol{\eta}_u$ are independent zero-mean Gaussian white noise processes with

$$E\left\{\boldsymbol{\eta}_v(t)\boldsymbol{\eta}_v(\tau)\right\}^T = \boldsymbol{I}_{3\times3}\boldsymbol{\sigma_v}^2\delta(t - \tau) \tag{3.2a}$$

$$E\left\{\boldsymbol{\eta}_u(t)\boldsymbol{\eta}_u(\tau)\right\}^T = \boldsymbol{I}_{3\times3}\boldsymbol{\sigma_u}^2\delta(t - \tau) \tag{3.2b}$$

$\boldsymbol{\eta}_v$ represents a zero-mean Gaussian white noise in the angular rate, leading to a random walk in the angle, the Angular Random Walk (ARW). $\boldsymbol{\beta(t)}$ is the gyro bias.

○ **Rate random walk (RRW)** [$\circ/h^{3/2}$]: $\boldsymbol{\eta}_u$ represents a zero-mean Gaussian white noise in the angular acceleration, leading to a random walk behaviour in the angular rate, the Rate Random Walk (RRW)

○ **Rate flicker noise (RFN) /bias instability** [$°/h$]: Flicker noise processes are characterised by a power spectral density (PSD) that decreases as $1/\boldsymbol{f}^\gamma$, with increasing frequency $\boldsymbol{f}$ and a constant slope γ. Flicker noise sets the gyro noise floor, and is as a result the limiting factor in attitude estimation performance. Rate flicker noise is also known as bias instability, which should not be confused with bias, which are both called drift. Integrated RFN is the Angle Flicker Noise (AFN). Until the work of (Pittelkau, 2013), RRW was used for attitude determination instead of the bias instability/RFN. This results in a sub-optimal filter design, especially in the case of low cost MEMS gyros. Sub-optimality can be seen from the general Allan Variance/ PSD plots in Figure 3.1. However, for the sake of simplicity, this work will focus on the model presented in Equation (3.1). Interested readers, are referred to (Pittelkau, 2013) for attitude determination with flicker noise gyro model.

○ **Rate ramp** [$°/h^2$]: It is a phenomena, which very much like RRW manifests itself at longer propagation times/ lower frequencies, but with a higher noise contribution than RRW as observed in AV/PSD plot in Figure 3.1. It is rather dominant for low cost MEMS gyro for long finite time intervals and is more systematic than random in nature. Since it was only observed in the very low-cost low-performance MEMS gyros, which was later discarded during the configuration selection process. It is only considered during gyro noise characterisation and configuration selection process, and not included in the gyro models.

○ **Quantization noise** [$°$]: Some consider it as a part of systematic error (Grewal et al., 2007), while others characterise them as part of the random noise associated with the digital read out of the gyro signal. Nevertheless, it is a very low frequency behaviour. It was observed only in the case of low cost MEMS gyro characterisation, and is considered only for PSD characterisation and gyro configuration selection procedure. Since the gyros selected for the configuration, do not demonstrate this quantization noise effect, at least not a level that it is considered significant, it is not considered as part of the gyro model.

3.2.2 | Stochastic Noise Modelling

The gyro noise parameters presented in Section 3.2.1, are characterised with the aid of Allan Variance or Power Spectral Density analysis. Inclusion of dynamic calibration of the noise, as outlined in (Lam et al., 2004), as part of the calibration filter is beyond the scope of this work. Direct PSD analysis on gyro data is a very time consuming process, as time series dataset is collected over 18hr. Alternatively, a very common industrial practice is to conduct an Allan Variance analysis on the gyro test data (Lam et al., 2003). Analytic relations between Allan Variance and the corresponding PSD alternative, facilitate a faster conversion of the extracted characteristic parameters into PSD plots for further analysis. PSD analysis for noise characterisation is a widely applied, simple, yet powerful approach for noise induced disturbance evaluation. Gyro noise characteristic parameters extracted from Allan Variance analysis alone is enough to be included in the gyro models described in Equations 3.1 and 3.2, and to initiate the calibration filter. However, for gyro sample rate selection, gyro dead-reckoning performance evaluation, gyro noise reduction by averaging, gyro-stellar sensor fusion behaviour analysis, and gyro-stellar configuration selection, PSD analysis is valuable. Furthermore, noise density PSD of the simulated gyro output must match with the Allan-Variance based noise density PSD.

Figure 3.1 (Pittelkau, 2010) visually captures the relation between Allan Variance and PSD equivalence. While Tables 3.1 and 3.2 capture the gyro noise sources and their corresponding τ and frequency domain properties for Allan Variance and PSD analysis (IEEE Std 647-2006, 2006, IEEE Std 952-1997, 2008).

3.2.3 | Systematic Error Parameters

Systematic gyro errors are modelled separately from the stochastic gyro errors. These errors can be calibrated and compensated for. A brief overview of the common input/output errors are presented with the aid of Figure 3.3 (Grewal et al., 2007). Systematic errors taken together with the stochastic errors form the total sensor errors. In combination with the gyro specific systematic errors; launch-vibration/thermal-distortion/placement induced misalignment of gyro sense axes is further considered to be part of the systematic error.

The systematic error sources in Figure 3.3, can be defined as the following (Grewal et al., 2007):

○ **Bias**: Any nonzero sensor output when the input is zero

○ **Scale factor error**: Results from ageing or manufacturing tolerances of gyros.

○ **Nonlinearity**: Present in most sensors to some degree.
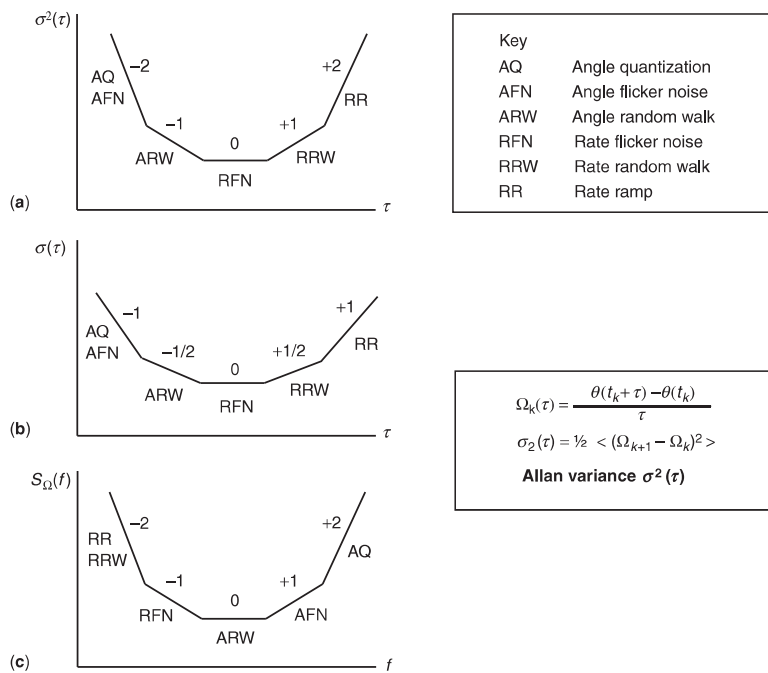
Figure 3.1: *Gyro performance metric a.) Allan Variance b.) Allan Standard Deviation c.) Power Spectral Density (Pittelkau, 2010).*
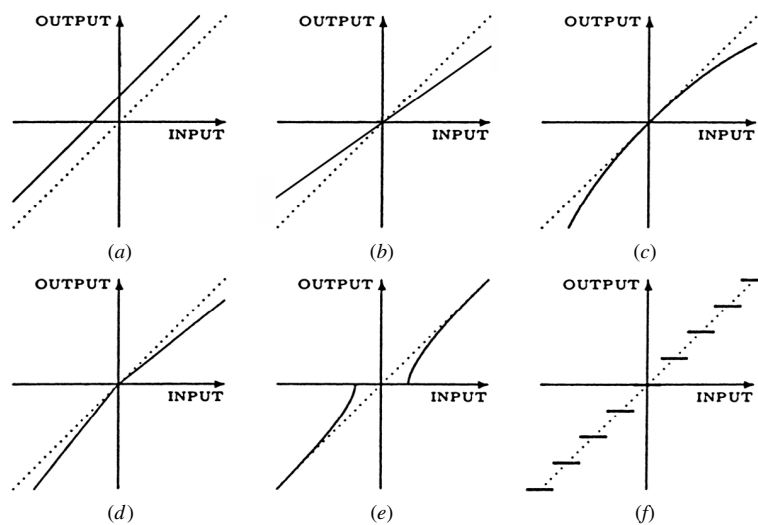
Figure 3.2: *Common input/output error types a.) bias b.) scale factor c.) non-linearity d.) ±asymmetry e.) deadzone and f.) quantisation (Grewal et al., 2007).*

○ **Scale factor sign asymmetry**: Arises often from the mismatched push-pull amplifiers.

○ **Deadzone**: This is due to mechanical stiction or locking (for a Ring Laser Gyro).

○ **Quantization error**: Inherent to all digitized systems. It may not be zero-mean when the input is held constant, as it could be under calibration conditions.

3.2.4 | Systematic Error Modelling

As observed in (Pittelkau, 2007), bias, scale factor (symmetrical and asymmetrical), and misalignment are modelled as part of the calibration filter synthesis. As they form the most dominant systematic error sources. First the definition of scale factors is presented, and later the process of modelling misalignment is presented. To conclude this section on gyro modelling, the gyro model utilised by the calibration filter and the one used for observability analysis of calibration parameters further presented.

Table 3.1: *Gyro noise and drift processes in frequency domain (IEEE Std 952-1997, 2008).*

Stochastic model contributor				Asymptotic properties PSD $S(f)$		
Nomenclature	Equivalent white noise input		Other name	θ	Ω	$S_\Omega(f)$
	Generic	This Std				
White angle	N_θ^2	Φ^2	Angle measurement noise	0	+2	$(2\pi f)^2 \phi^2$
Angle quantization	—	Q^2	White angle energy spectrum	0	+2	$\frac{4Q^2}{\tau} \sin^2 \pi f \tau$
Flicker angle	$N_{F\theta}^2$	—	Pink angle noise	–1	+1	$2\pi f N_{F\theta}^2$
Angle random walk, white rate noise	N_Ω^2	N^2	Reg angle noise	–2	0	N^2
Rate quantization	—	—	Discrete white rate noise or white rate energy spectral density	–2	0	—
Bias instability	$N_{F\Omega}^2$	B^2	Pink rate noise	–3	–1	$\frac{B^2}{2\pi f}$
Markov rate	$N_{c\Omega}^2$	q^2	Correlated drift rate	–2, –4	0, –2	$\frac{(q_c \tau_c)^2}{1 + (2\pi f \tau_c)^2}$
Rate random walk	N_Ω^2	K^2	Red rate noise	–4	–2	$\frac{K^2}{(2\pi f)^2}$
Ramp instability	$N_{F\Omega}^2$	R^2	Pink angular acceleration noise	–5	–3	$\frac{R^2}{(2\pi f)^3}$
Random bias	$\Omega(0)$	B_0^2	Bias or fixed draft	See Note 2	See Note 2	$B_0^2 \delta(f)$
Random ramp	$\dot\Omega(0)$	R_0^2	Rate ramp	See Note 2	See Note 2	—
Periodic rate	Ω_0	—	Harmonic	Discrete spectra	Discrete spectra	$\frac{1}{2}\Omega_0^2 \delta(f - f_0)$

NOTES
1—Mod σ—Modified Allan variance
2—Remove by regression or by filtering

Scale Factor

Scale factor can be divided into symmetric, asymmetric, and non-linear scale factor as captured with the aid of Figure 3.3. However, as discussed in (Pittelkau, 2007), symmetric and asymmetric scale factors are the ones that form part of the calibration filter as they strongly influence the attitude estimation error. While for observability analysis a linearized version of gyro model is utilised which assumes linear combination of symmetric and asymmetric scale factors. Observability of asymmetric scale factors and bias can be dealt with separately (Pittelkau, 2005b). Scale factor errors are considered to be of additive in nature. As seen in Figure 3.3, symmetric scale factor (SSF) is identical for both positive and negative angular rate measurements. While asymmetric scale factor (ASF) depends on the sign of the angular rate measurements. For simplification, the symmetric scale factor is taken as a constant s for each of the gyro sense axis. While, the asymmetric scale factor can be written as: $\mu \operatorname{sgn}(\omega^g)$. Here ω^g is the sensed angular rate. Thus with both of the scale factors combined the gyro scale factor model for a single sense axis can be expressed as:

$$\tilde\omega = (1 + \lambda + \mu \operatorname{sgn}(\omega^g)) \omega^g + b + \eta_v \tag{3.3}$$

For multiple sense axes, in matrix formulation this can be expressed as:

$$\tilde{\boldsymbol{\omega}} = (\mathbf{I} + \tilde{\boldsymbol{\Lambda}} + \tilde{\mathbf{U}})\boldsymbol{\omega^g} + \mathbf{b} + \boldsymbol{\eta_v} \tag{3.4}$$

Table 3.2: *Gyro noise and drift processes in time domain continued from Table 3.1 (IEEE Std 952-1997, 2008).*

θ	Ω	$\sigma_\Omega^2(\tau)$
		Asymptotic properties **Allan variance** σ(t)
−1/2	−1, (−3/2) See Note 1	$\dfrac{3\Phi^2}{\tau^2} f_n$
0	−1	$\dfrac{3Q^2}{\tau^2}$
0	−1	$\dfrac{N_{F\theta}^2}{2\pi\tau^2}[3(2 + \ln 2\pi f_n \tau) - \ln 2]$
+1/2	−1/2	$\dfrac{N^2}{\tau}$
+1	0	—
+1	0	$\dfrac{2B^2 \ln 2}{\pi}$
+1 1/2, +1/2	+1/2, −1/2	$\dfrac{(q_c T_c)^2}{\tau}\left[1 - \dfrac{T_c}{2\tau}\left(3 - 4e^{-\frac{\tau}{T_c}} + e^{-\frac{2\tau}{T_c}}\right)\right]$
+1 1/2	+1/2	$\dfrac{K^2 \tau}{3}$
+2	+1	—
See Note 2	See Note 2	—
See Note 2	See Note 2	$\dfrac{R_0^2 \tau^2}{2}$
See Note 2	See Note 2	$\Omega_0^2\left[\dfrac{\sin^2 \pi f_0 \tau}{\pi f_0 \tau}\right]$

NOTES
1—Mod σ—Modified Allan variance
2—Remove by regression or by filtering

Nonlinear scale factors can be modelled by a polynomial, exponential or the expression presented in Equation (3.5) (Grewal et al., 2007).

$$z_{\text{input}} = \sum_{i=0}^{N} a_i z_{\text{output}}^i \tag{3.5}$$

Here, a_0 is the bias and a_1 the scale factor. The polynomial input-output model is linear in the calibration parameters, so they can still be calibrated using a system of linear equations similar to scale factor and bias. However, the non-linearities may not be observable and stationary. It is proposed by (Pittelkau, 2007) that an equally effective and more efficient way would be to model non-linearities as rate dependent processes. As with most calibration filters, (Pittelkau, 2002) captured the asymmetric non-linearities as part of the rate white-noise η_v. This is the preferred approach for the calibration filter.

(a) Types of scale factor error   (b) Deviation from ideal 1:1 transfer function
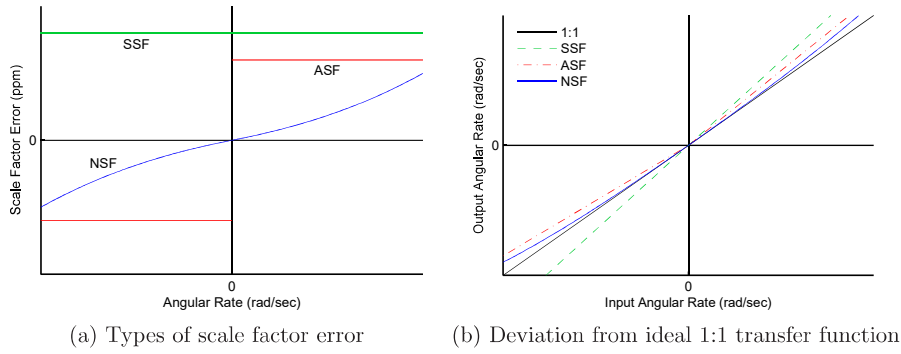
Figure 3.3: *Illustration of scale factor error. Symmetric, asymmetric and nonlinear (Pittelkau, 2007).*

(a) First Generation SIRU   (b) Second Generation SIRU

(c) Skewed Pair of IMUs   (d) Parallel Pair of IMUs
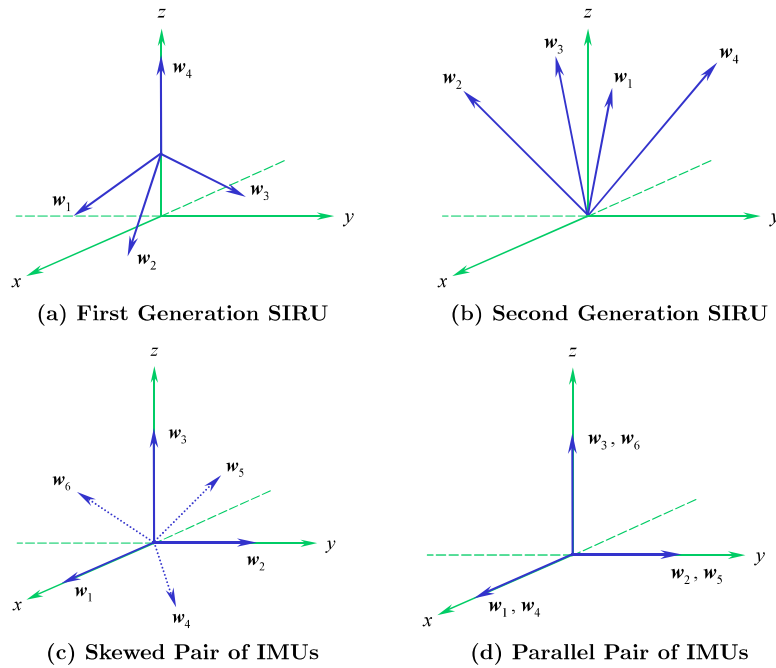
Figure 3.4: *Redundant IMU configurations (Pittelkau, 2004).*

Misalignment

When it comes to misalignment, there are two general ways of misalignment definition that is often utilised by calibration filters in the literature: 1.) Euler parametrisation 2.) Rotation vector parametrisation (Pittelkau, 2007). Euler parametrisation is based on the azimuth and elevation angle definition of the gyro sense axis. Though Euler parametrisation has been utilized by multiple calibration filters in the literature, it was demonstrated in (Pittelkau, 2007) that the azimuth angle can become very sensitive to the elevation angle and other perturbations, as the elevation angle reaches $\pm 90°$. Especially under these conditions the azimuth angle cannot be estimated. Interested readers are referred to (Pittelkau, 2007) for further details. Calibration filter to be developed here, relies on the rotation vector parametrisation.

Redundant Inertial Measurement Units (RIMU)

Before rotational vector parametrisation is defined, it is important to define what is meant by Redundant Inertial Measurement Units (RIMU). A RIMU is an IMU that has more than three angular rate sense axes ($n > 3$). The redundancy is defined in the sense of angular rate measurement (Pittelkau, 2004). Optimal configuration of these sense axes are based on Platonic solids (Pittelkau, 2005a). Some commonly used configurations of RIMU is presented with the aid of Figure 3.4. Due to volume constraints imposed by NanoSat ADCS, parallel pair of IMUs is the central focus of this thesis work.

Rotation Vector Model Parametrisation
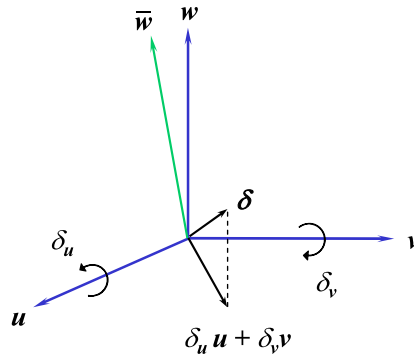
Figure 3.5: *Gyro misalignment definition ([Pittelkau, 2004]).*

A general RIMU misalignment model based on small-angle rotation vector is presented with the aid of Figure 3.5 ([Pittelkau, 2004]). Here, $\boldsymbol{w}_i$ is the nominal gyro sense axis, $\overline{\boldsymbol{w}}_i$ is the true gyro sense axis, and $\boldsymbol{\delta}_i$ is the small angle rotation vector. The angular rate about the ith gyro axis, ω_i^g, presented earlier in Equation (3.3) is given by the projection of the body angular rate ω^b onto that axis:

$$\boldsymbol{\omega}_i^{\mathbf{g}} = \overline{\boldsymbol{w}}_i \cdot \boldsymbol{\omega}^{\mathbf{b}} = \overline{\boldsymbol{w}}_i^T \boldsymbol{\omega}^{\mathbf{b}} \tag{3.6}$$

Since, only the nominal vector $\boldsymbol{w}_i$ is known. This can be related to the true vectors by small angle transformations ([Pittelkau, 2004]):

$$\overline{\boldsymbol{w}}_i = \left(\boldsymbol{I} + [\delta_i \times]\right) \boldsymbol{w}_i = \boldsymbol{w}_i - [\boldsymbol{w}_i \times] \delta_i \tag{3.7}$$

Here, δ_i is the small angle rotation vector. Any component of δ_i has no effect in the direction of the nominal gyro sense axis $\boldsymbol{w}_i$. Thus, δ_i has the minimal parametrisation:

$$\delta_i = \delta_{\boldsymbol{u}i} \boldsymbol{u}_i - \delta_{\boldsymbol{v}i} \boldsymbol{v}_i \tag{3.8}$$

Here, the vectors $\boldsymbol{u}_i$, $\boldsymbol{v}_i$, and $\boldsymbol{w}_i$ are a mutually orthogonal triad such that $\boldsymbol{u}_i = -\boldsymbol{w}_i \times \boldsymbol{v}_i$ and $\boldsymbol{v}_i = \boldsymbol{w}_i \times \boldsymbol{u}_i$. And, δ_{ui} and δ_{vi} are small angle rotations about u_i and v_i. The minus sign in Equation (3.8) is chosen for convenience of derivations. Utilising Equations 3.7 and 3.8 the misalignment model can be expressed as ([Pittelkau, 2004]):

$$\overline{\boldsymbol{w}}_i = \boldsymbol{w}_i - \delta_{\boldsymbol{u}i} \boldsymbol{v}_i - \delta_{\boldsymbol{v}i} \boldsymbol{u}_i \tag{3.9}$$

Here, the vectors u_i and v_i can be computed by applying the QR decomposition to either $[w_i \times]$, $I - w_i w_i^T$ or $\begin{bmatrix} w_i & 0 & 0 \end{bmatrix}$. The vectors from Q factor are then selected to ensure that $\begin{bmatrix} \boldsymbol{u}_i & \boldsymbol{v}_i & \boldsymbol{w}_i \end{bmatrix}$ forms a right-handed triad. The choice of $\boldsymbol{u}_i$ and $\boldsymbol{v}_i$ is not unique, but once chosen they should not be changed ([Pittelkau, 2007]). For n gyro sense axes, this formulation can be written in matrix notation as:

$$\boldsymbol{U} = \begin{bmatrix} \boldsymbol{u}_1 & \boldsymbol{u}_2 & \cdots & \boldsymbol{u}_n \end{bmatrix} \quad \boldsymbol{V} = \begin{bmatrix} \boldsymbol{v}_1 & \boldsymbol{v}_2 & \cdots & \boldsymbol{v}_n \end{bmatrix} \quad \boldsymbol{W} = \begin{bmatrix} \boldsymbol{w}_1 & \boldsymbol{w}_2 & \cdots & \boldsymbol{w}_n \end{bmatrix} \tag{3.10a}$$

Consequently the misalignment model for n gyro sense axes, can be expressed as:

$$\begin{pmatrix} \omega_1^{\mathbf{g}} \\ \omega_2^{\mathbf{g}} \\ \vdots \\ \omega_n^{\mathbf{g}} \end{pmatrix} = \begin{bmatrix} \boldsymbol{w}_1^T \\ \boldsymbol{w}_2^T \\ \vdots \\ \boldsymbol{w}_n^T \end{bmatrix} \boldsymbol{\omega}^{\mathbf{b}} - \begin{bmatrix} \omega^{\mathbf{b}} \cdot \boldsymbol{v}_1 & 0 & 0 & 0 \\ 0 & \omega^{\mathbf{b}} \cdot \boldsymbol{v}_2 & \cdots & 0 \\ \vdots & \vdots & \ddots & \vdots \\ 0 & 0 & \cdots & \omega^{\mathbf{b}} \cdot \boldsymbol{v}_n \end{bmatrix} \begin{pmatrix} \delta_{u1} \\ \delta_{u2} \\ \vdots \\ \delta_{un} \end{pmatrix} - \cdots$$

$$\cdots \begin{bmatrix} \omega^{\mathbf{b}} \cdot u_1 & 0 & \cdots & 0 \\ 0 & \omega^{\mathbf{b}} \cdot u_2 & \cdots & 0 \\ \vdots & \vdots & \ddots & \vdots \\ 0 & 0 & \cdots & \omega^{\mathbf{b}} \cdot u_n \end{bmatrix} \begin{pmatrix} \delta_{v1} \\ \delta_{v2} \\ \vdots \\ \delta_{vn} \end{pmatrix} \tag{3.10b}$$

In compact notation,

$$\boldsymbol{\omega}^{\mathbf{g}} = \boldsymbol{W}^T \boldsymbol{\omega}^{\mathbf{b}} - \boldsymbol{C}_{\boldsymbol{v}}\left(\boldsymbol{\omega}^{\mathbf{b}}\right) \boldsymbol{\delta}_{\boldsymbol{u}} - \boldsymbol{C}_{\boldsymbol{u}}\left(\boldsymbol{\omega}^{\mathbf{b}}\right) \boldsymbol{\delta}_{\boldsymbol{v}}$$
$$= \boldsymbol{W}^T \boldsymbol{\omega}^{\mathbf{b}} - \boldsymbol{C}_{\mathbf{g}}\left(\boldsymbol{\omega}^{\mathbf{b}}\right) \boldsymbol{\delta}_{\mathbf{g}} \tag{3.10c}$$

Where,

$$\boldsymbol{C}_{\mathbf{g}} = \begin{bmatrix} \boldsymbol{C}_{\boldsymbol{v}} & \boldsymbol{C}_{\boldsymbol{u}} \end{bmatrix} \text{ and } \boldsymbol{\delta}_{\mathbf{g}} = \begin{bmatrix} \delta_u \\ \delta_v \end{bmatrix} \tag{3.10d}$$

Here, $\boldsymbol{\delta}_u$ and $\boldsymbol{\delta}_v$, is the vector for small angle misalignment. $\boldsymbol{\delta_u} = [\delta_{u1}, \delta_{u2}, \ldots, \delta_{un}]^T$ and $\boldsymbol{\delta_v} = [\delta_{v1}, \delta_{v2}, \ldots, \delta_{vn}]^T$. Derivations for larger angles, for the chosen gyro-stellar configuration is presented with the aid of Section 4.7.2. However, a linearized model is often utilised for calibration filters, as a result the choice for the calibration filter under consideration.

Augmented RIMU Systematic Gyro Error Measurement Model

Now that the individual scale factor and misalignment models are defined, the misalignment model in Equation (3.10d) can be substituted into Equation (3.4), to get a general systematic gyro error model relating the measured angular rate $\boldsymbol{\omega_{gm}}$:

$$\boldsymbol{\omega_{gm}} = \tilde{\omega} = (\mathbf{I} - \tilde{\boldsymbol{\Lambda}} - \tilde{\mathbf{U}})\boldsymbol{\omega^g} + \mathbf{b} + \boldsymbol{\eta_v} \tag{3.11a}$$

$$\boldsymbol{\omega_{gm}} = \tilde{\omega} = (\mathbf{I} - \tilde{\boldsymbol{\Lambda}} - \tilde{\mathbf{U}})\left(\boldsymbol{W}^T\boldsymbol{\omega}^{\mathrm{b}} - \boldsymbol{C_v}\left(\boldsymbol{\omega}^{\mathrm{b}}\right)\boldsymbol{\delta_u} - \boldsymbol{C_u}\left(\boldsymbol{\omega}^{\mathrm{b}}\right)\boldsymbol{\delta_v}\right) + \mathbf{b} + \boldsymbol{\eta_v} \tag{3.11b}$$

In compact form combining all the misalignments this can be expressed as (Pittelkau, 2002, 2001):

$$\boldsymbol{\omega_{gm}} = \tilde{\boldsymbol{\omega}} = (\mathbf{I} - \tilde{\boldsymbol{\Lambda}} - \tilde{\mathbf{U}})\left(\boldsymbol{I} - \tilde{\boldsymbol{\Delta}}\right)\boldsymbol{T^b_{g_o}}\boldsymbol{\omega}^{\mathrm{b}} + \mathbf{b} + \boldsymbol{\eta_v} \tag{3.11c}$$

Here, $\boldsymbol{T^b_{g_o}}$ is the transformation matrix describing the nominal orientation of the gyro reference $\boldsymbol{g_o}$ with respect to the body coordinate system b. $\tilde{\boldsymbol{\Lambda}} = \mathrm{diag}\left[\lambda_x, \lambda_y, \lambda_z\right]$ is a matrix of symmetric scale factor errors. $\tilde{\boldsymbol{U}} = \mathrm{diag}\left[\mu_x\,\mathrm{sign}\left(\omega_x\right), \mu_y\,\mathrm{sign}\left(\omega_y\right), \mu_z\,\mathrm{sign}\left(\omega_z\right)\right]$ is a matrix of asymmetric scale factor errors. $\boldsymbol{I} - \tilde{\boldsymbol{\Delta}}$ is a non-orthogonal small angle misalignment matrix.

In the body frame, this true angular rate can be expressed as:

$$\boldsymbol{\omega_b} = \mathbf{T^b_{g_o}}(\mathbf{I} - \tilde{\boldsymbol{\Delta}})^{-1}(\mathbf{I} - \tilde{\boldsymbol{\Lambda}} - \tilde{\mathbf{U}})^{-1}\left(\boldsymbol{\omega_{gm}} + \mathbf{b_g} + \boldsymbol{\eta_v}\right) \tag{3.12}$$

Since the misalignment and scale factors are small, the true angular rate can be further simplified to (Pittelkau, 2002):

$$\begin{aligned}
\boldsymbol{\omega_b} &= T^b_{g_o}(I - \tilde{\boldsymbol{\Delta}})^{-1}(I - \tilde{\boldsymbol{\Lambda}} - \tilde{U})^{-1}\left(\boldsymbol{\omega}_{\mathrm{gm}} + \boldsymbol{b}_g + \boldsymbol{\eta_v}\right) \\
&= T^b_{go}(I + \boldsymbol{\Delta})(I + \boldsymbol{\Lambda} + U)\left(\boldsymbol{\omega}_{\mathrm{gm}} + \boldsymbol{b}_g + \boldsymbol{\eta_v}\right) \\
&\simeq T^b_{g_o}(I + \boldsymbol{\Delta} + \boldsymbol{\Lambda} + U)\left(\boldsymbol{\omega}_{\mathrm{gm}} + \boldsymbol{b}_g + \boldsymbol{\eta_v}\right)
\end{aligned} \tag{3.13}$$

Note that, $\boldsymbol{\Delta} \simeq \tilde{\boldsymbol{\Delta}}, \boldsymbol{\Lambda} \simeq \tilde{\boldsymbol{\Lambda}}$, and $U \simeq \tilde{U}$ because the misalignments and scale factors are small. Sometimes the above presented Equation can be further simplified by defining $M = \boldsymbol{\Delta} + \boldsymbol{\Lambda} + U$:

$$\boldsymbol{\omega_b} = T^b_{g_o}(I + M)\left(\boldsymbol{\omega}_{\mathrm{gm}} + \boldsymbol{b}_g + \boldsymbol{\eta_v}\right) \tag{3.14}$$

When it comes to observability analysis, a modified version of the misalignment/scale factor model presented in Equation (3.13) is often utilised. This is presented as follows:

$$\acute{\boldsymbol{w}}_i = (1 - \lambda_i - s_i\mu_i)\,\overline{\boldsymbol{w}}_i = (1 - \lambda_i - s_i\mu_i)\left(\boldsymbol{w}_i - \delta_{\boldsymbol{u}i}\boldsymbol{v}_i - \delta_{\boldsymbol{v}i}\boldsymbol{u}_i\right) \tag{3.15a}$$

$$\begin{aligned}
\acute{\boldsymbol{w}}_i &= (1 - \lambda_i)\left(\boldsymbol{w}_i - \delta_{\boldsymbol{u}i}\boldsymbol{v}_i - \delta_{\boldsymbol{v}i}\boldsymbol{u}_i\right) \\
&\simeq \boldsymbol{w}_i - \lambda_i\boldsymbol{w}_i - \delta_{\boldsymbol{u}i}\boldsymbol{v}_i - \delta_{\boldsymbol{v}i}\boldsymbol{u}_i
\end{aligned} \tag{3.15b}$$

This is not meant to be used in the calibration filter, but only utilised for observability analysis purposes. This model excludes asymmetric scale factor, otherwise unless if the asymmetric scale factors are small they cannot be modelled as constant parameters. Bias and asymmetric scale factor are treated separately for observability considerations (Pittelkau, 2005b). The linearized model used for asymmetric scale factor observability analysis is presented as follows:

$$\acute{\boldsymbol{w}}_i = (1 - \lambda_i - s_i\mu_i)\,\overline{\boldsymbol{w}}_i = (1 - \lambda_i - s_i\mu_i)\left(\boldsymbol{w}_i - \delta_{\boldsymbol{u}i}\boldsymbol{v}_i - \delta_{\boldsymbol{v}i}\boldsymbol{u}_i\right) \tag{3.16a}$$

$$\acute{\boldsymbol{w}}_i = \boldsymbol{w}_i - \lambda_i\boldsymbol{w}_i - s_i\mu_i\boldsymbol{w}_i - \delta_{\boldsymbol{u}i}\boldsymbol{v}_i - \delta_{\boldsymbol{v}i}\boldsymbol{u}_i \tag{3.16b}$$

Where, $s_i = \mathrm{sign}\left(\omega^g_i\right)$.

3.2.5 | Three Gyro Sense Axes Parametrisation for Unscented Kalman Calibration Filter

This section defines the gyroscope model utilised for the baseline unscented calibration filter (Lai et al., 2003). By temporarily defining $\bar{\omega} = (I + \Lambda + U)(\tilde{\omega} - \beta - \eta_v)$, right hand side of Equation (3.13) with misalignment can be expressed as:

$$(I + \Delta)\bar{\omega} = \begin{bmatrix} 1 & -\delta_{xz} & \delta_{xy} \\ \delta_{xz} & 1 & 0 \\ -\delta_{xy} & 0 & 1 \end{bmatrix} \begin{pmatrix} \bar{\omega}_x \\ 0 \\ 0 \end{pmatrix} + \begin{bmatrix} 1 & -\delta_{yz} & 0 \\ \delta_{yz} & 1 & -\delta_{yx} \\ 0 & \delta_{yx} & 1 \end{bmatrix} \begin{pmatrix} 0 \\ \bar{\omega}_y \\ 0 \end{pmatrix} + \dots$$

$$\dots \begin{bmatrix} 1 & 0 & \delta_{zy} \\ 0 & 1 & -\delta_{zx} \\ -\delta_{zy} & \delta_{zx} & 1 \end{bmatrix} \begin{pmatrix} 0 \\ 0 \\ \bar{\omega}_z \end{pmatrix} \tag{3.17a}$$

$$(I + \Delta)\bar{\omega} = \begin{bmatrix} 1 & -\delta_{yz} & \delta_{zy} \\ \delta_{xz} & 1 & -\delta_{zx} \\ -\delta_{xy} & \delta_{yx} & 1 \end{bmatrix} \bar{\omega} \tag{3.17b}$$

As outlined in (Pittelkau, 2007), one of the attitude sensors or the IMU has to be chosen as the body reference sensor, so that the misalignments are fully observable. The calibration filter which is the central focus of this thesis work, is a relative misalignment calibration filter (Pittelkau, 2002). The calibrated misalignment is then relative to the reference sensor. As discussed in (Pittelkau, 2007) three degrees of freedom of attitude are unobservable if all attitude sensors and IMU are parametrized with rotational misalignment vectors. As a result, a misalignment vector decomposition is conducted with the aid of QR factorisation to split the misalignment into orthogonal (with Q, also known as rotational) and non-orthogonal (with R) misalignment components. This results in 3 orthogonal/rotational misalignment parameters that can be eliminated to achieve full observability of calibration states. A general overview of misalignment decomposition into rotational and non-orthogonal elements is outlined in (Pittelkau, 2004, 2005b). Here an example is shown for three axis gyro, which will be used for baseline calibration filter development. Though star trackers are the most accurate attitude knowledge sensors on board of a NanoSat, it is not preferred as the reference sensor. Star tracker solution update failure under high slew rates and occultation, and the low star tracker update rates, means that the filter can be left with unobservable misalignments and potential divergence. Reconfiguring the filter and starting again every time the star tracker is lost, results in a shift in the estimated attitude. To improve reliability, autonomy and convergence times, IMUs are chosen as the reference sensors.

The matrix $I + \Delta$ can be factored such that $I + \Delta = \mathcal{Q}\mathcal{R}$. Here, $\mathcal{Q}$ is orthogonal and $\mathcal{R}$ is upper triangular. Since the misalignment angles are small, the matrix $\mathcal{Q}$ can be approximated by a small-angle transformation $I + [\delta \times]$ and $\mathcal{R}$ by the three non-orthogonal misalignment angles ξ_x, ξ_y, and ξ_z. Based on this, Equation (5.64) can be factorised as (Lai et al., 2003):

$$I + \Delta = (I + [\delta \times])\mathcal{R} = \begin{bmatrix} 1 & -\delta_z & \delta_y \\ \delta_z & 1 & -\delta_x \\ -\delta_y & \delta_x & 1 \end{bmatrix} \begin{bmatrix} 1 & \xi_z & -\xi_y \\ 0 & 1 & \xi_x \\ 0 & 0 & 1 \end{bmatrix} \simeq \begin{bmatrix} 1 & -(\delta_z - \xi_z) & \delta_y - \xi_y \\ \delta_z & 1 & -(\delta_x - \xi_x) \\ -\delta_y & \delta_x & 1 \end{bmatrix}$$
$$\tag{3.18}$$

Comparing the misalignment elements in Equations 3.18 with that in 5.64, the orthogonal(rotational) and non-orthogonal misalignments can be expressed in terms of the general misalignments as:

$$\delta_x = \delta_{yx}, \quad \xi_x = \delta_{yx} - \delta_{zx} \tag{3.19a}$$

$$\delta_y = \delta_{xy}, \quad \xi_y = \delta_{xy} - \delta_{zy} \tag{3.19b}$$

$$\delta_z = \delta_{xz}, \quad \xi_z = \delta_{xz} - \delta_{yz} \tag{3.19c}$$

A special advantage of separating orthogonal (rotational) and nonorthogonal misalignments in the IMU is that the orthogonal (rotational) misalignments are generally large and time varying, where as the nonorthogonal misalignment are generally small and nearly constant (Pittelkau, 2007). This alternative means of parametrisation helps remove the orthogonal misalignment, when three axis gyro is utilised as a reference sensor. Setting the orthogonal misalignment δ to zero ($\delta_x = \delta_y = \delta_z = 0$) gives $I + \Delta = \mathcal{R}$. This further leads to the following simplifications:

$$\begin{aligned} \xi_x &= -\delta_{zx} \\ \xi_y &= \delta_{zy} \\ \xi_z &= -\delta_{yz} \end{aligned} \tag{3.20}$$

This removes three unobservable degrees of freedom of attitude and defines the gyro as the reference sensor. Noting that $\boldsymbol{U}(\boldsymbol{\omega}) = \left(\mu_x\left|\omega_x\right|, \mu_y\left|\omega_y\right|, \mu_z\left|\omega_z\right|\right)^T$ in Equation (3.13), the following expression can be derived for the angular rate in the NanoSat body frame (Pittelkau, 2002):

$$\boldsymbol{\omega}_b = \boldsymbol{T}_{g_o}^b \boldsymbol{\omega}_{\mathrm{gm}} + \boldsymbol{T}_{g_o}^b (\boldsymbol{I} + \boldsymbol{\Delta} + \boldsymbol{\Lambda} + \boldsymbol{U}) (b_g + \boldsymbol{\eta}_v) + \dots$$

$$\dots \boldsymbol{T}_{g_o}^b \times \begin{bmatrix} 0 & -\omega_z & \omega_y & \omega_x & 0 & 0 & |\omega_x| & 0 & 0 \\ \omega_z & 0 & 0 & 0 & \omega_y & 0 & 0 & |\omega_y| & 0 \\ 0 & 0 & 0 & 0 & 0 & \omega_z & 0 & 0 & |\omega_z| \end{bmatrix} \begin{pmatrix} \xi_x \\ \xi_y \\ \xi_z \\ \lambda_x \\ \lambda_y \\ \lambda_z \\ \mu_x \\ \mu_y \\ \mu_z \end{pmatrix} \tag{3.21a}$$

$$\simeq \boldsymbol{T}_{g_o}^b \boldsymbol{\omega}_{\mathrm{gm}} + \boldsymbol{T}_{g_o}^b b_g + \boldsymbol{T}_{g_o}^b \boldsymbol{\Omega}_g \delta_g + \boldsymbol{T}_{g_o}^b \boldsymbol{\eta}_v \tag{3.21b}$$

To get the expression for angular velocity estimate, $\hat{\boldsymbol{\omega}}$, in the baseline (Lai et al., 2003) the following simplifications can be made. By defining $\breve{\boldsymbol{\omega}} = \tilde{\boldsymbol{\omega}} - \boldsymbol{\beta}$, note that $\boldsymbol{\omega}_{gm} - \tilde{\boldsymbol{\omega}}$, The above equation can be expressed as:

$$\boldsymbol{\omega} = \boldsymbol{T}_{g_0}^b (\boldsymbol{I} + \boldsymbol{\Delta} + \boldsymbol{\Lambda} + \boldsymbol{U}) (\breve{\boldsymbol{\omega}} - \boldsymbol{\eta}_v) \tag{3.22a}$$

$$= \boldsymbol{T}_{g_0}^b \breve{\boldsymbol{\omega}} - \boldsymbol{T}_{g_0}^b (\boldsymbol{I} + \boldsymbol{\Delta} + \boldsymbol{\Lambda} + \boldsymbol{U}) \boldsymbol{\eta}_v + \boldsymbol{T}_{g_0}^b (\boldsymbol{\Delta} + \boldsymbol{\Lambda} + \boldsymbol{U}) \breve{\boldsymbol{\omega}} \tag{3.22b}$$

$$= \boldsymbol{T}_{g_0}^b \breve{\boldsymbol{\omega}} - \boldsymbol{T}_{g_0}^b (\boldsymbol{I} + \boldsymbol{\Delta} + \boldsymbol{\Lambda} + \boldsymbol{U}) \boldsymbol{\eta}_v + \dots$$

$$\dots \boldsymbol{T}_{g_0}^b \times \begin{bmatrix} 0 & \breve{\omega}_z & \breve{\omega}_y & \breve{\omega}_x & 0 & 0 & |\breve{\omega}_x| & 0 & 0 \\ \breve{\omega}_z & 0 & 0 & 0 & \breve{\omega}_y & 0 & 0 & |\breve{\omega}_y| & 0 \\ 0 & 0 & 0 & 0 & 0 & \breve{\omega}_z & 0 & 0 & |\breve{\omega}_z| \end{bmatrix} \times \begin{pmatrix} \xi_x \\ \xi_y \\ \xi_z \\ \lambda_x \\ \lambda_y \\ \lambda_z \\ \mu_x \\ \mu_y \\ \mu_z \end{pmatrix} \tag{3.22c}$$

$$= \boldsymbol{T}_{g_0}^b \breve{\boldsymbol{\omega}} + \boldsymbol{T}_{g_0}^b \boldsymbol{\Omega}_g \boldsymbol{\kappa} - \boldsymbol{T}_{g_0}^b (\boldsymbol{I} + \boldsymbol{\Delta} + \boldsymbol{\Lambda} + \boldsymbol{U}) \boldsymbol{\eta}_v \tag{3.22d}$$

Here $\boldsymbol{\Omega}_g$ and $\boldsymbol{\kappa}$ correspond to the previous matrix of gyro measurement, and vector of gyro misalignment and scale factor errors. Thus, the angular velocity estimate is:

$$\hat{\boldsymbol{\omega}} = \boldsymbol{T}_{b,g_0} \breve{\boldsymbol{\omega}} + \boldsymbol{T}_{b,g_0} \hat{\boldsymbol{\Omega}}_g \hat{\boldsymbol{\kappa}} \tag{3.23}$$

Here, the hats correspond to their respective estimated values. And $\breve{\boldsymbol{\omega}}$ is a function of both the uncompensated, measured gyro rate $\tilde{\boldsymbol{\omega}}$, and the estimated gyro bias $\tilde{\boldsymbol{\beta}}$ (Lai et al., 2003).

3.3 | Noise Power Spectral Density based Configuration Selection

This section facilitates MEMS gyro configuration selection from a power spectral density standpoint. Section 3.3.1 specifies the star tracker and four different gyro types considered as part of this analysis. Gyro noise parameters are characterised in Section 3.3.3. Gyro-Stellar sensor configurations are analysed and selected in Section 3.3.4.

3.3.1 | MEMS Gyro and NanoSat Star Tracker Choices

For the analysis on gyro-stellar configuration selection that follow the remnant of this chapter, three different variants of gyros were selected. Due to confidentiality concerns, the exact manufacturers of these components could not be specified in this thesis work. However, relevant specification parameters are presented here. Three different variants of MEMS gyros are selected for analysis: 1.) High Performance Triple Axis Gyro (HPTAG) 2.) Medium Performance Single Axis Gyro (MPSAG) 3.) Low Performance Triple Axis Gyro (LPTAG). Parameters required for PSD and Allan-Deviation analysis are tabulated with the aid of Table 3.3. The use of Fiber Optic Gyros is a common practice for agile precision tracking missions. Due to Size, Weight and Power constraints they are not utilised on NanoSats. However for the sake of completion, characteristic parameters of micro-Fiber Optic Gyro, μFOG-3U [1], is also presented.

Table 3.3: *MEMS gyroscope specific parameters for the three variants of MEMS gyroscopes chosen, and the micro-Fiber Optic Gyro for reference.*

Parameter	Quantization		Angular Random Walk		Bias Instability		Rate Random Walk		Sampling Frequency
Nomenclature, Units	$Q, [\degree]$	$Q, [rad]$	$N, [\degree/\sqrt{(h)}]$	$N, [rad/\sqrt{s}]$	$B, [\degree/h]$	$B, [rad/s]$	$K, [\degree/h^{3/2}]$	$K, [rad/s^{3/2}]$	$[Hz]$
Gyroscope									
MEMS High Performance Triple Sense Axis Gyro	-	-	0.15	4.36e-05	0.31	1.52e-06	0.57	4.57e-08	2000
MEMS Mid Performance Single Sense Axis Gyro	-	-	0.33	9.70e-05	3.01	1.46e-05	18.07	1.46e-06	2300
MEMS Low Performance Triple Sense Axis Gyro	5.61e-04	9.80e-06	0.47	1.37e-04	31.30	1.52e-04	692.82	5.60e-05	1600
LITEF μFORS-3U/-3UC Single Sense Axis Gyro	-	-	0.08	2.33e-05	0.05	2.42e-07	-	-	1000

Since this thesis work is extended at Hyperion Technologies, ST200 class of star tracker is chosen for estimating the attitude knowledge. Parameters specific to the performance of ST200 star tracker are presented with the aid of Table 2.3. Since the boresight performance of star tracker is much lower compared to the pitch and yaw performance, it is often a common practice to fly two orthogonal star trackers to get roll performance similar to pitch and yaw performance. Furthermore, two star trackers provide redundancy against occultation effects.

3.3.2 | Gyro Characteristic Parameter Extraction and Simulator: Verification & Validation Scheme

The following sections will focus on extracting the relevant gyro characteristic parameters from Allan-Deviation plots of four different types of MEMS rate gyros. The extracted parameters are later utilised to simulate gyro Allan-Deviation, single sided attitude rate, and attitude error noise Power Spectral Density behaviour. Based on the analysed gyro noise power spectral densities, gyro-stellar hybridization is conducted for 7 configurations of gyros, to facilitate selection of the configuration that shall accommodate the desired attitude knowledge requirement. Later in Section 3.4, a gyro simulator is constructed to facilitate sensing of the appropriate spacecraft body rate.

To facilitate accurate gyro parameter characterisation, and representative gyro simulator, the verification and validation scheme outlined in Figure 3.6 is utilised through out the following sections. First the gyro characteristic parameters are extracted from the gyro Allan-Deviation plots. Slopes of the Allan-Deviation plots, which uniquely represent the presence of a certain noise source, are verified against the expected theoretical Allan-Deviation noise plots. The extracted characteristic parameters, in combination with the analytical relations presented by IEEE Std 647-2006 (2006), are utilised to reconstruct the Allan-Deviation plots. This is verified and validated against the Allan-Deviation plots provided by the manufacturers. The steps undertaken so far, ensure the appropriate extraction of characteristic gyro parameters from the Allan-Deviation analysis provided by the manufacturers.

Once the characteristic parameters are extracted, based on the relations outlined in IEEE Std 647-2006 (2006), single sided attitude rate and attitude error noise PSD are constructed. The slopes of the single sided attitude rate and attitude error noise PSD are verified against the expected theoretical slopes. This step ensures a verified analytical noise PSD for the extracted gyro characteristic parameters. At steady state, the noise PSD of the gyro output should match this analytical attitude rate noise PSD.

A gyro simulator is constructed based on the gyro noise parameters characterised from Allan-Deviation analysis. The gyro simulator is run for 25,000s at zero angular rate input. Fourier transform is conducted on the gyro output, to attain single sided attitude rate PSD. This is verified against the analytical attitude rate noise PSD.

3.3.3 | Gyro Allan-Deviation and Power Spectral Density Analysis

MEMS Gyro Choices and Allan-Variance Analysis

As outlined earlier in Section 3.2.2, Allan-Deviation is the standard approach to characterise MEMS gyro noise parameters. Allan-Deviation for Medium Performance Single Axis Gyro (MP-SAG) and High Performance Triple Axis Gyro (HP-TAG) were provided by the manufacturers, and is presented with the aid of Figures 3.7 and 3.8. MPSAG was sampled at 2000Hz and HPTAG was sampled at 2300 Hz. These sampling rates are important to reconstruct the gyro models in the rigid body NanoSat simulator. Characteristic rate gyro noise parameters can be extracted from these

---

[1]Northrop Grumman LITEF - μFORS 3U https://northropgrumman.litef.com/fileadmin/downloads/Datenblaetter/Datenblatt_uFors-3U_-3UC_-6U_-6UC.pdf
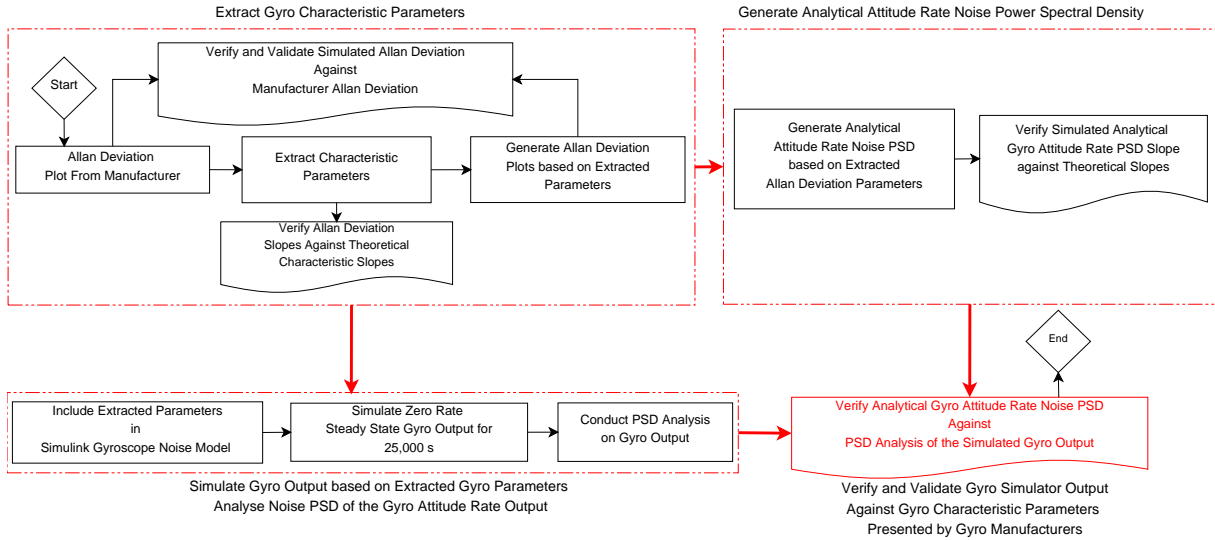
Figure 3.6: *Schematic overview of MEMS rate gyro parameter characterisation, simulator development, verification and validation process.*
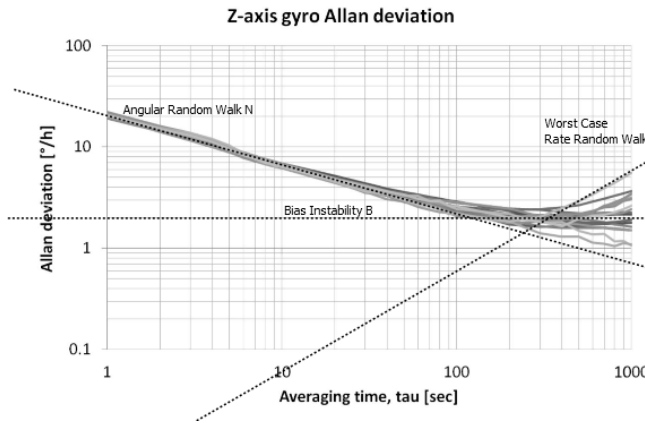
Figure 3.7: *Gyro Attitude Rate Allan-Deviation for Medium Performance Single Axis Gyro (Engelen, 2020b).*
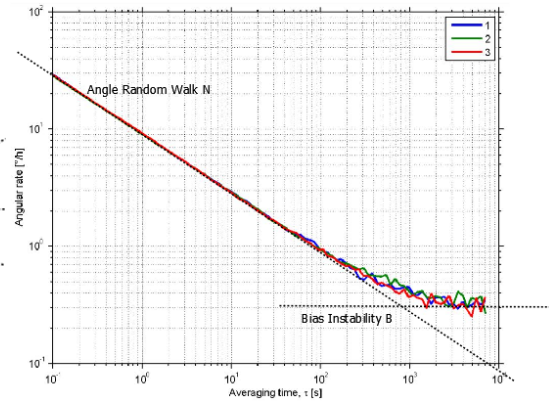
Figure 3.8: *Gyro Attitude Rate Allan-Deviation for High Performance Triple Axis Gyro (Engelen, 2020b).*

Table 3.4: *Characteristic gyro stochastic noise relations for most commonly observed Allan-Deviation parameters.*

Parameter	Quantization	Angular Random Walk	Bias Instability	Rate Random Walk
Nomenclature, Units	**Q, [$°$]**	**N, [$°/\sqrt{(h)}$]**	**B, [$°/h$]**	**K, [$°/h^{3/2}$]**
Double-sided attitude rate PSD [$(°/s)^2/Hz$]	$\frac{4Q^2}{\tau}\sin^2 \pi f\tau$	N^2	$\frac{B^2}{2\pi f}$	$\frac{K^2}{(2\pi f)^2}$
Allan Variance $\sigma_\Omega^2(\tau)$ [$(°/h)^2$]	$\frac{3Q^2}{\tau^2}$	$\frac{N^2}{\tau}$	$\frac{2B^2\ln 2}{\pi}$	$\frac{K^2\tau}{3}$
Allan Standard Deviation $\sigma_\Omega(\tau)$ [$°/h$]	$\frac{\sqrt{3}Q}{\tau}$	$\frac{N}{\sqrt{\tau}}$	$B\sqrt{\frac{2\ln 2}{\pi}}$	$K\sqrt{\frac{\tau}{3}}$
Nomenclature, Units	**Q, [rad]**	**N, [$rad/\sqrt{s}$]**	**B, [rad/s]**	**K, [$rad/s^{3/2}$]**
Allan Standard Deviation $\sigma_\Omega(\tau)$ [rad/s]	$\frac{\sqrt{3}Q}{\tau}\cdot\frac{180\cdot 3600}{\pi}$	$\frac{N}{\sqrt{\tau}}\cdot\frac{180\cdot 3600}{\pi}$	$B\sqrt{\frac{2\ln 2}{\pi}}\cdot\frac{180\cdot 3600}{\pi}$	$K\sqrt{\frac{\tau}{3}}\cdot\frac{180\cdot 3600}{\pi}$
Parameter Specific Description for Allan Standard Deviation for τ measured in [s], and Allan Standard Deviation [$°/h$]	$\sigma\cdot\frac{\pi}{180\cdot 3600}\frac{\tau}{\sqrt{3}}$	$\sigma\cdot\frac{\pi}{180\cdot 3600}\sqrt{\tau}$	$\sigma\cdot\frac{\pi}{180\cdot 3600}\cdot\sqrt{\frac{\pi}{2ln2}}$	$\sigma\cdot\frac{\pi}{180\cdot 3600}\cdot\sqrt{\frac{3}{\tau}}$

Allan-Deviation plots utilising the Allan-Variance relations presented earlier in Table 3.2. Relevant Allan-Variance and PSD parametric relations are re-tabulated in Table 3.4. The corresponding gryo parametric values are presented with the aid of Table 3.3. Each of the noise sources contributing to the total gyro stochastic noise has a unique slope in the Allan-Variance as shown earlier with Figure 3.1. Characteristic parametric slopes in Figures 3.7 and 3.8 were matched against the ideal slopes presented in Figure 3.1. The percentage difference of all the MEMS rate gyro slopes from the ideal slopes are presented in Table 3.5. When it comes to High Performance Triple Axis Gyro, the Rate Random Walk is not observed in the Allan-Deviation plot presented in Figure 3.8. Neither it was specified by

the manufacturer. Thus it was constructed analytically. From Figure 3.1 it can be observed that Bias Instability (or Rate Flicker Noise, RFN, $^\circ$) has a zero slope in the Allan-Variance plot. While Angular Random Walk (ARW, $^\circ/\sqrt{hr}$) and Rate Random Walk (RRW, $^\circ/h/\sqrt{h}$) have slope of identical magnitudes but negative values. When the Angular Random Walk (ARW) and Rate Random Walk (RRW) slopes intersect with the Bias Instability (RFN) floor the following relation can be assumed for total gyro noise variance:

$$\sigma_{tot}(\tau)^2 = \sigma_{ARW}(\tau)^2 + \sigma_{RRW}(\tau)^2 = \sigma_{RFN}(\tau)^2 \tag{3.24}$$

Utilising the Allan-Variance relations presented in Table 3.4, the above presented relations can be expanded as follows:

$$\sigma_{tot}(\tau)^2 = \frac{N^2}{\tau} + \frac{K^2\tau}{3} = \frac{2B^2\ln 2}{\pi} \tag{3.25}$$

Let, the time at which the ARW slope N intersects the RRW slope K, below the bias instability line B can be denoted by τ_1. The standard deviation at this point $\sigma_{tot}(\tau_1)$ is equivalent to bias instability:

$$\sigma_{tot}(\tau_1)^2 = 2 \cdot \left(N \cdot \tau_1^{-\frac{1}{2}}\right)^2 = \frac{2 \cdot B^2\ln(2)}{\pi} \tag{3.26}$$

The unknown time constant at which this takes place be expressed as:

$$\tau_1 = \frac{\pi \cdot N^2}{B^2\ln 2} \tag{3.27}$$

Substituting Equation (3.27) in 3.25, leads to the following relation:

$$K = \frac{\sqrt{3}\ln 2 B^2}{\pi N} \tag{3.28}$$

The above results in conservative estimates, however in the same order of magnitude. For MEMS gyro the Allan-Deviation characteristic parameters do change over their life time. Gyro Allan-Deviation for Low Performance Triple Axis gyros are typically not provided by the manufacturers, especially due to high unit performance variability. As a result Allan-Deviation of two different types of gyros with similar performance specifications were provided by Hyperion Technologies. The tests were conducted under static conditions for 18 hours, with temperature variability of 4 degree Celsius. Both of the gyros were sampled at 1600Hz. Long term gyro sampled data shows low frequency behaviour. Low frequency gyro behaviour is very important to characterise the MEMS rate gyro dead-reckoning behaviour. However, for the application of gyro-stellar hybridisation it is irrelevant as the star tracker is sampled at 5 Hz. Allan-Deviation analysis was conducted on partial and full dataset, as denoted respectively by partial run and full run. Figures 3.9 and 3.10 demonstrate the Allan-Deviation behaviour for partial and full run of Type 1 sensor of LPTAG class. Similarly, Figures 3.11 and 3.12 capture the Allan-Deviation for partial and full run for Type 2 sensor of LPTAG class.

For both type 1 and 2 of low performance triple axis gyro, the worst axis is chosen as the representation for all axes. When it comes to Allan-Deviation analysis for LPTAG gyro, two new phenomena were observed. For the full 18 hour dataset, Rate Ramp (RR) was observed which is due to the long time series dataset capable of capturing the low frequency behaviour. And Angle Quantization (AQ) was also observed at high frequencies. Similar to the case of MPSAG and HPTAG, the Allan-Variance characteristic parameters are determined utilising the relations presented in Table 3.2, and are summarised in Table 3.4. Parametric slopes of the presented Allan-Variance plots are compared against theoretical Allan-Variance slopes in Figure 3.1. %-difference from the theoretical slope value is presented with the aid of Table 3.5. These offsets can be denoted partly due to the temperature deviations during the data logging process, and the fact that Allan-Deviation is a generalised overview of true noise PSD. However, it is important to note that these %-differences do not have a significant impact on the final noise PSD, as outlined later in the following subsections.

Noise Power Spectral Density from Allan Variance

Now that the characteristic gyro Allan-Deviation slope parameters are extracted, the Allan-Deviation slopes are simulated utilising the relations provided in Table 3.2.. Simulated Allan-Deviation plots for MPSAG and HPTAG are presented with the aid of Figures 3.13 and 3.14. Since the underlying noise processes of gyros can be considered as random noise processes of different origins, assuming that these processes are independent, the individual Allan-Variance characteristic slopes can be combined together utilising the following expression:

$$\sigma_{\text{total}}^2 = \sigma_{\text{ARW}}^2(\tau) + \sigma_{\text{Q}}^2(\tau) + \sigma_{\text{RFN}}^2(\tau) + \sigma_{\text{RRW}}^2(\tau) + \sigma_{\text{RR}}^2(\tau) + \dots \tag{3.29}$$
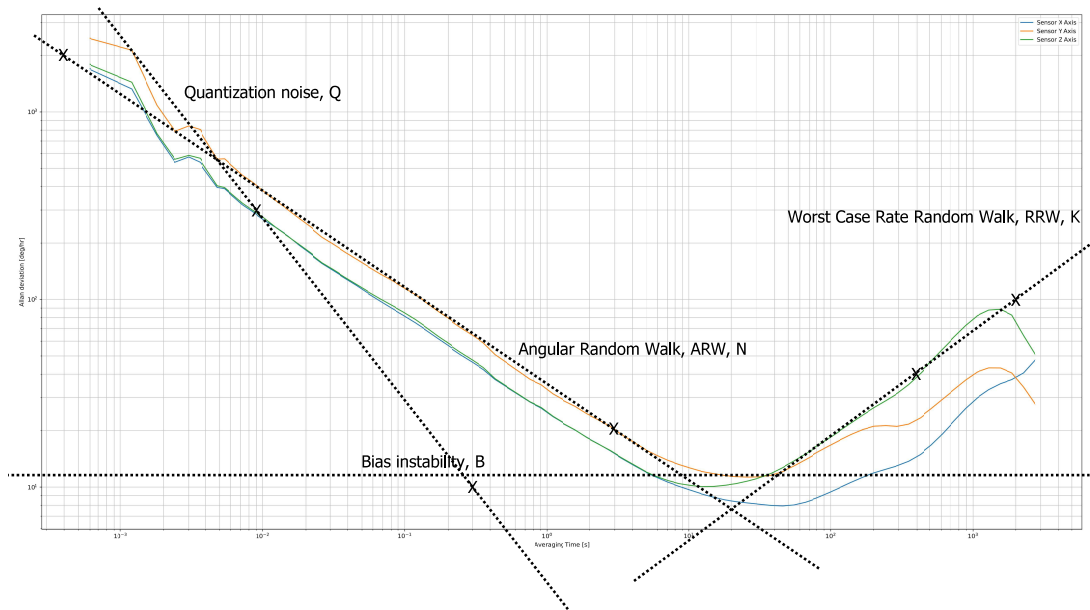
Figure 3.9: *Gyro Attitude Rate Allan-Deviation for Low Performance Triple Axis Gyro Type 1 for partial dataset (Engelen, 2020b).*
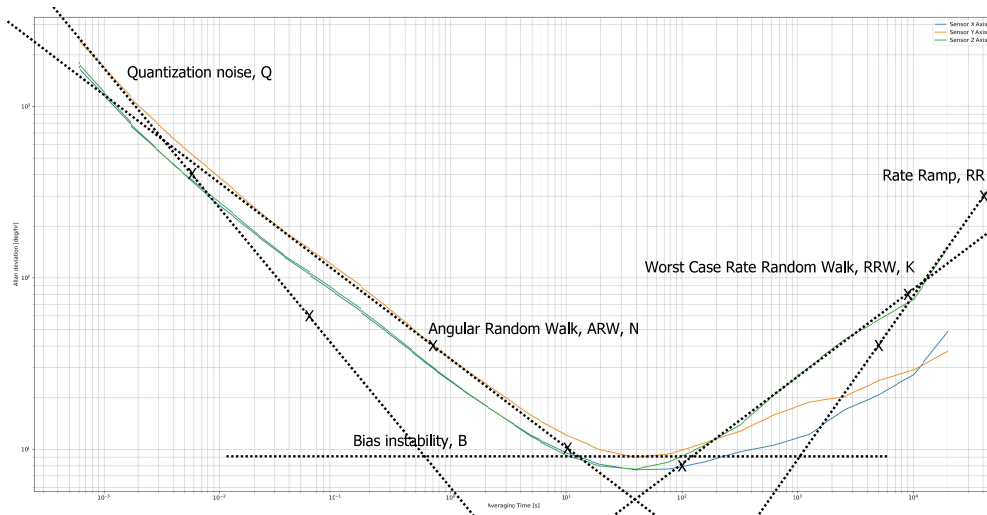
Figure 3.10: *Gyro Attitude Rate Allan-Deviation for Low Performance Triple Axis Gyro Type 1 for full dataset (Engelen, 2020b).*

Table 3.5: *Percentage difference in parametric Allan-Deviation slopes for Low Performance Triple Axis Gyro (LPTAG), Medium Performance Single Axis Gyro (MPSAG), and High Performance Triple Axis Gyro (HPTAG), compared against expected theoretical slopes.*

%-Difference from nominal value	Quantization Slope	Angular Random Walk Slope	Rate Random Walk Slope	Rate Ramp Slope
LPTAG Sensor 1 partial run	4.44%	1.60%	6.93%	-
LPTAG Sensor 1 full run	17.6%	2.13%	1.17%	3.1%
LPTAG Sensor 2 partial run	7.27%	2.55%	2.37%	-
LPTAG Sensor 2 full run	4.05%	4.57%	14.37%	7.92%
MPSAG	-	4.62%	2.51%	-
HPTAG	-	0.41%	-	-

The corresponding single sided attitude rate PSDs can be generated utilising the relations outlined in Tables 3.1 and 3.4. Please note that the relations provided in the tables represent double sided PSD. For single sided PSD, the relations must be multiplied with 2. Details on the underlying mathematics of PSD is presented with the aid of Appendix B. Since the underlying gyro noise processes can be considered as random noise processes of different
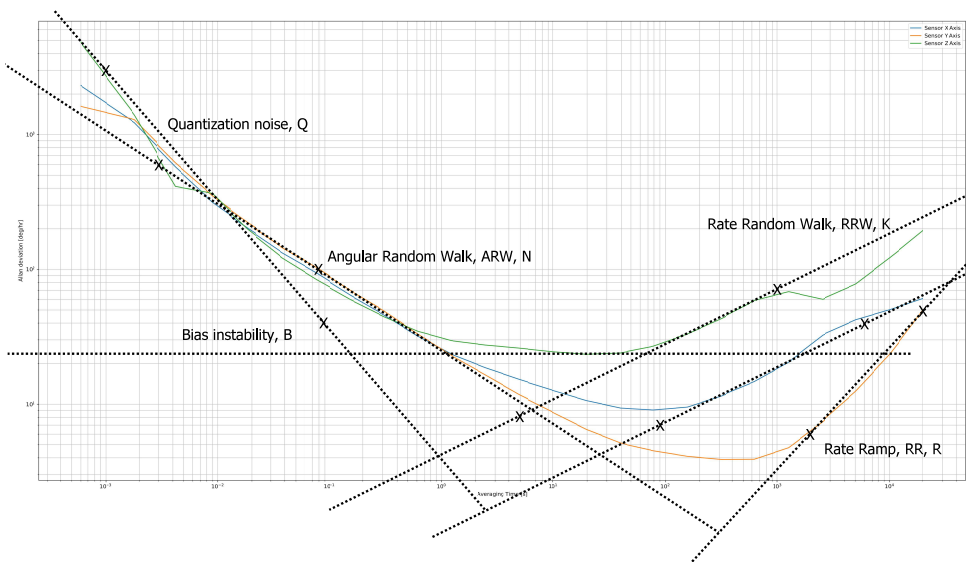
Figure 3.11: *Gyro Attitude Rate Allan-Deviation for Low Performance Triple Axis Gyro Type 2 for partial dataset (Engelen, 2020b).*
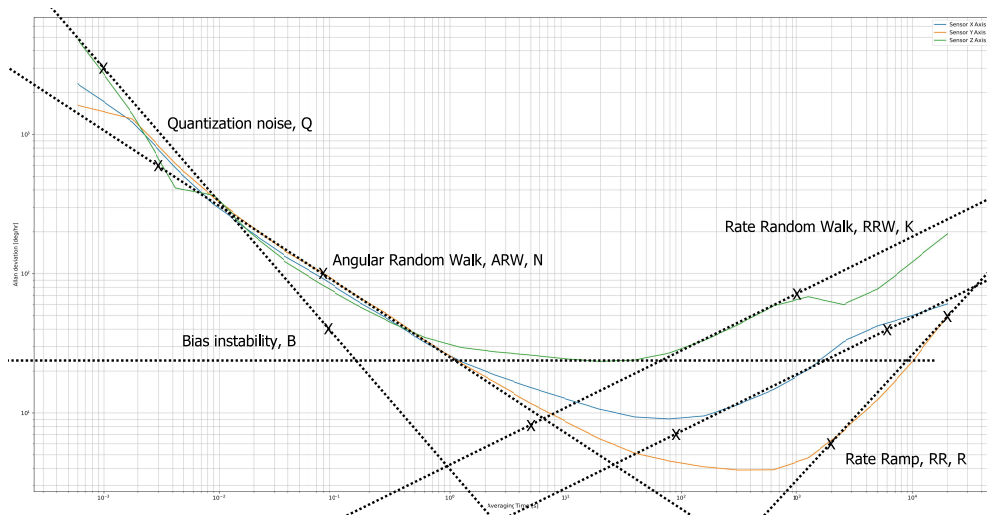
Figure 3.12: *Gyro Attitude Rate Allan-Deviation for Low Performance Triple Axis Gyro Type 2 for full dataset (Engelen, 2020b).*

origins, assuming that that these processes are independent the combined PSD can be expressed as (IEEE Std 647-2006, 2006):

$$PSD_{total} = PSD_{RRW} + PSD_{ARW} + PSD_{RFN} + PSD_{RR} + PSD_Q \ldots \tag{3.30}$$

Utilising the characteristic gyro noise parameters presented in Table 3.3, in combination with the analytical attitude rate PSD and Allan-Deviation relations presented in Table 3.4, Allan-Deviation and single sided attitude rate/error PSD can be constructed. Figure 3.15 presents the single sided attitude rate PSD for MPSAG. The attitude rate single sided PSD for HPTAG is presented with the aid of Figure 3.16. Corresponding attitude error single sided PSD is presented with the aid of Figures 3.17 and 3.18. The rate PSD is related to the angle PSD through the following expression (IEEE Std 647-2006, 2006):

$$S_\Omega(2\pi f) = (2\pi f)^2 S_\theta(2\pi f) \tag{3.31}$$

Similarly, Figure 3.19 presents the simulated Allan-Deviation for LPTAG. Corresponding single sided attitude rate PSDs are presented with the aid of Figure 3.20. Consequent attitude error single sided PSD is presented with the aid of Figure 3.21. Clearly partial run from sensor 2 demonstrates the highest noise density. As a result sensor two, partial run is chosen as the LPTAG sensor for configuration analysis. Figure 3.22 presents the characteristic elements that facilitate in the reconstruction of the Allan-Deviation of the chosen LPTAG. While Figures 3.23 and 3.24 represent the
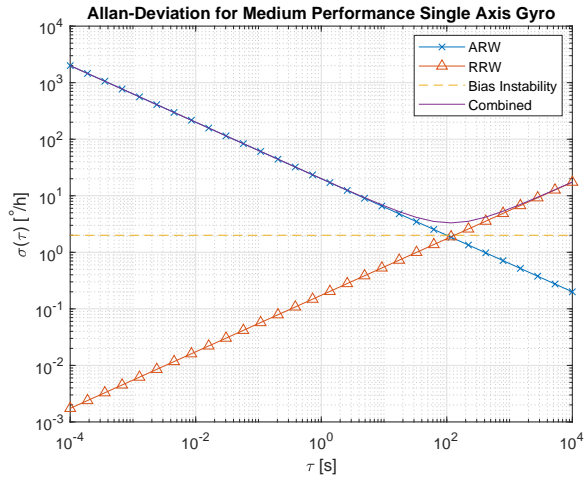
Figure 3.13: *Gyro attitude rate Allan-Deviation for MPSAG.*
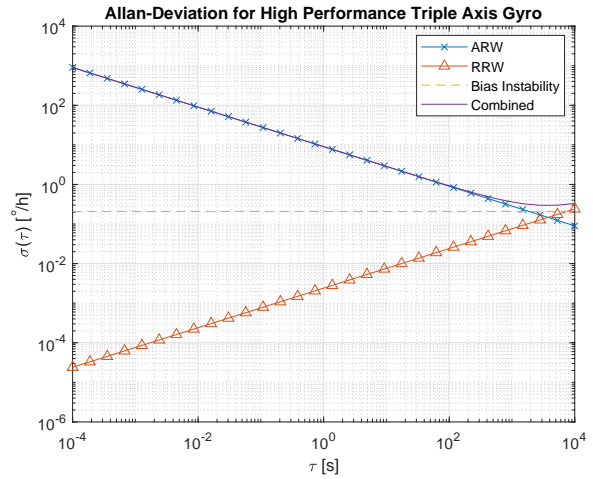
Figure 3.14: *Gyro attitude rate Allan-Deviation for HPTAG.*
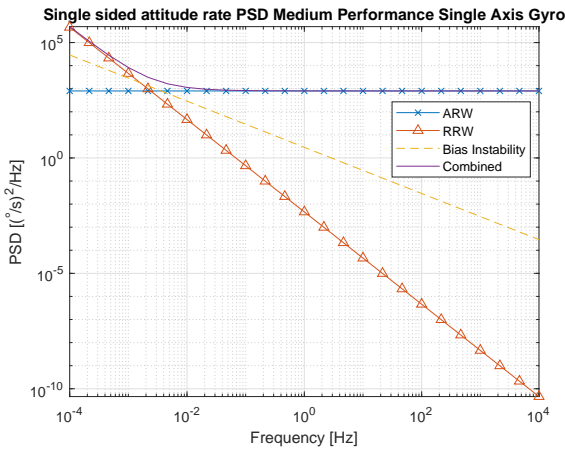
Figure 3.15: *Gyro attitude rate single sided PSD for MPSAG.*
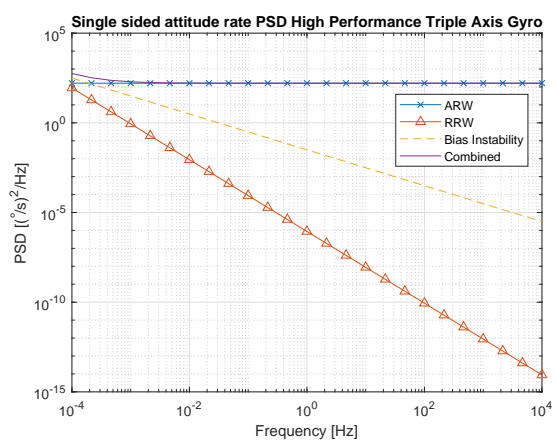
Figure 3.16: *Gyro attitude rate single sided PSD for HPTAG.*
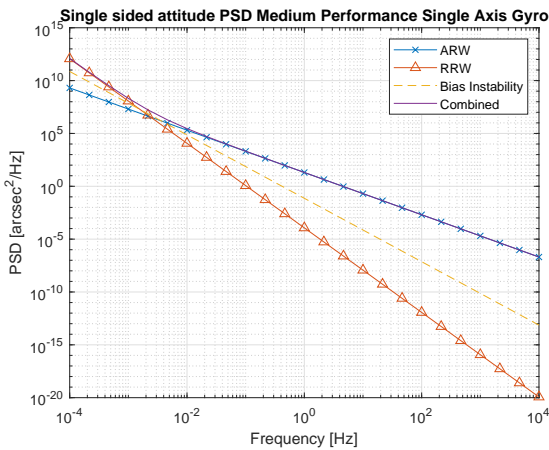
Figure 3.17: *Gyro attitude error single sided PSD for MPSAG.*
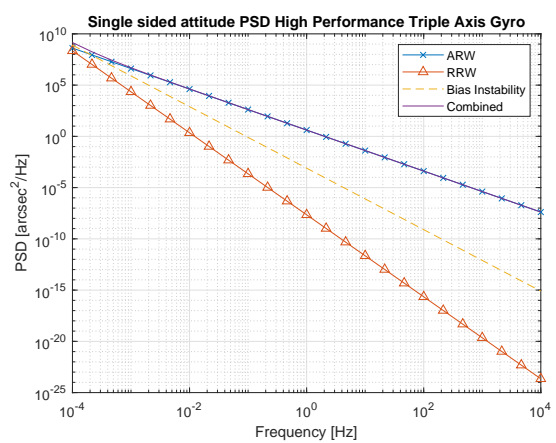
Figure 3.18: *Gyro attitude error single sided PSD for HPTAG.*

characteristic elements that constitute the single sided attitude rate and attitude error PSD for the chosen LPTAG. Slopes for all of the above presented PSD plots are verified to match against the theoretical slopes presented earlier in Tables 3.1.
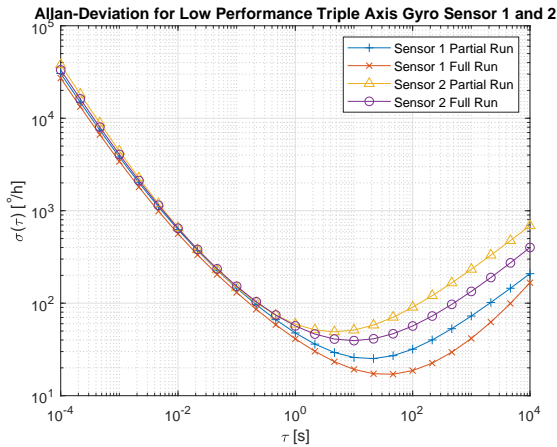
Figure 3.19: *Gyro Allan-Deviation for two different sensor types and run times of LPTAG.*
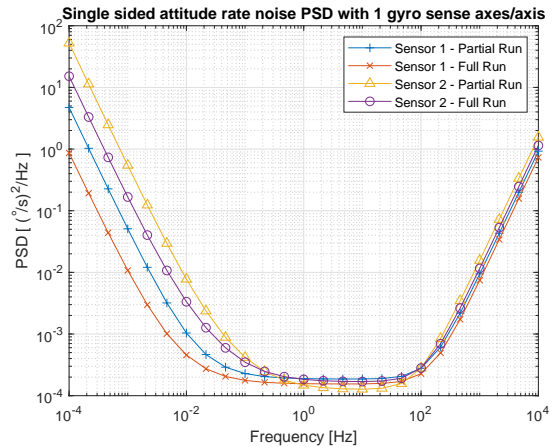
Figure 3.20: *Gyro attitude rate PSD for two different sensor types and run times of LPTAG.*
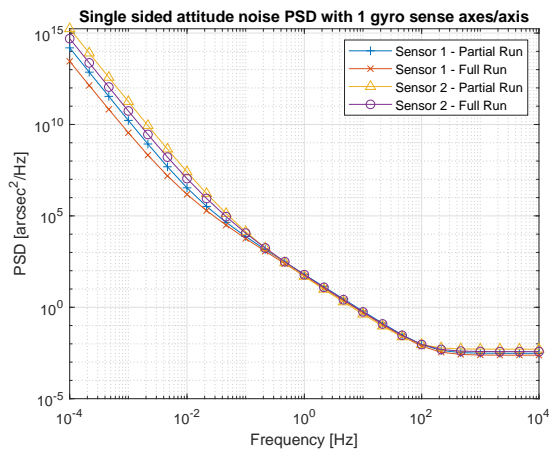
Figure 3.21: *Gyro attitude error PSD for two different sensor types and run times of LPTAG.*
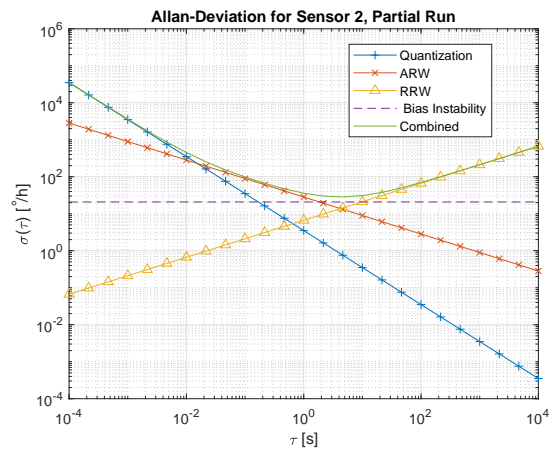
Figure 3.22: *Gyro Allan-Deviation for the chosen LPTAG sensor.*
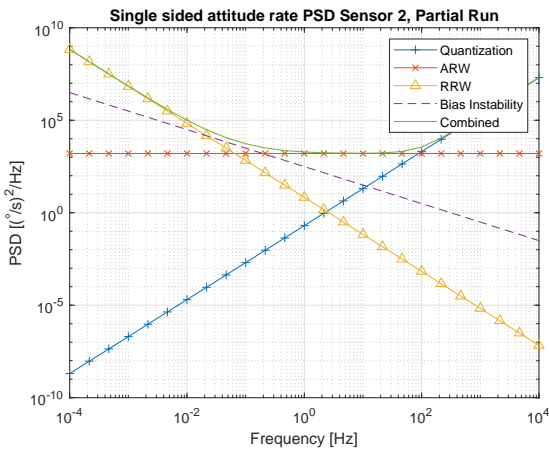
Figure 3.23: *Gyro attitude rate PSD for the chosen LPTAG sensor.*
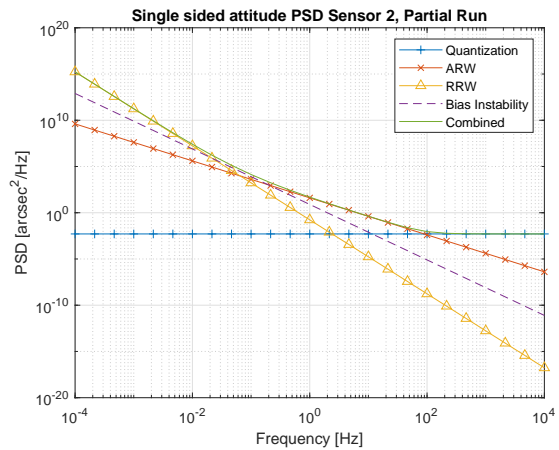
Figure 3.24: *Gyro attitude error PSD for the chosen LPTAG sensor.*

3.3.4 | Gyro-Stellar Sensor Hybridisation based Configuration Selection

Now that the individual gyro noise densities are characterised by virtue of Allan-Deviation and Power Spectral Density based analysis; the physical attitude knowledge estimation performance limit of a gyro-stellar sensor fusion process
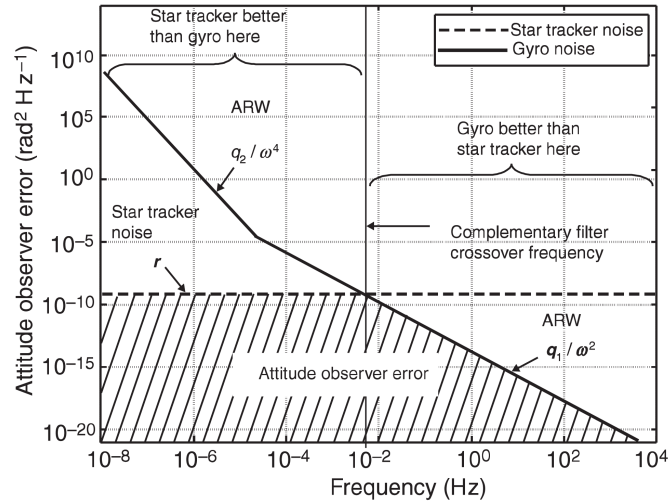
Figure 3.25: *Attitude knowlege error from single-sided gyro-stellar noise PSD with a simple complementary filter (Bayard, 2010).*

Table 3.6: *MEMS gyroscope distribution overview for different configurations.*

Configuration	No. of HPTAG	No. of MPSAG	No. of LPTAG	No. of sense axes/axis	Total number of Sense Axes
1	-	9	-	3	9
2	-	-	24	24	72
3	1	3	-	2	6
4	1	3	3	5	15
5	-	3	3	4	12
6	-	6	-	2	6
7	2	-	-	2	6

can be obtained by noise density analysis. This is important to accommodate quantitative selection of configuration of gyroscope and star trackers. It is a well established statistical fact, that for n homogeneous uncorrelated sensors with noise σ, by virtue of averaging, the combined noise can be reduced to $\frac{\sigma}{\sqrt{n}}$ (Xue et al., 2012). The use of a gyro cluster further adds redundancy to the system in the event of gyro failures which is more so common for COTS MEMS gyro, which are less radiation tolerant compared to the traditional space classified Hemisphere Resonance Gyros or Fiber Optic Gyros. Though this strategy of gyro clustering leads to improved MEMS gyro solution with regards to random noise, however the systematic errors associated with the system: misalignment, symmetric and asymmetric scale factors are not compensated for. The ill-effects of attitude estimation without calibrating for misalignment, symmetric, and asymmetric scale factor were presented in (Pittelkau, 2001). The objective the calibration filter is to remove these systematic errors, so that one is left with the stochastic noise error inherent to the sensors. As a result, noise PSD based gyro-stellar hybridisation as presented by Figure 3.25 is utilised to enable appropriate sensor configuration selection for the calibration filter. The underlying notion is that the area under attitude error noise PSD is equivalent to the variance as outlined by Equation (B.18a). Attitude error by virtue of gyro-stellar stochastic noise processes is the standard deviation obtained from this variance. Once the systematic gyro-stellar errors are removed, the attitude observer error can be extracted for gyro-stellar hybridisation process by the shaded area presented in Figure 3.25.

Seven different combinations of gyro configurations, arising out of the three chosen gyro types, were analysed in combination with one and two ST200 star trackers. Underlying elements of the configurations are presented with the aid of Table 3.6. It is important to note that all configurations are stacked on a plane, thus the sense axes are parallel to the Euler 3-2-1 axes. This is equivalent to the parallel sense axes presented earlier in Figure 3.4. For homogeneous sensor configurations, single gyro PSD is divided by n parallel sense axes. Since variance is represented by the area under the PSD curve. For heterogenous configurations, a weighted average is taken, weighted by the number of sense axes. The expressions are outlined as follows:

$$PSD_{homogeneous\ total} = \frac{PSD_{single\ gyro}}{n} \tag{3.32a}$$

$$PSD_{heterogeneous\ total} = \frac{n_1 \cdot PSD_1 + \ldots + n_n \cdot PSD_n}{n_{total}^2} \tag{3.32b}$$
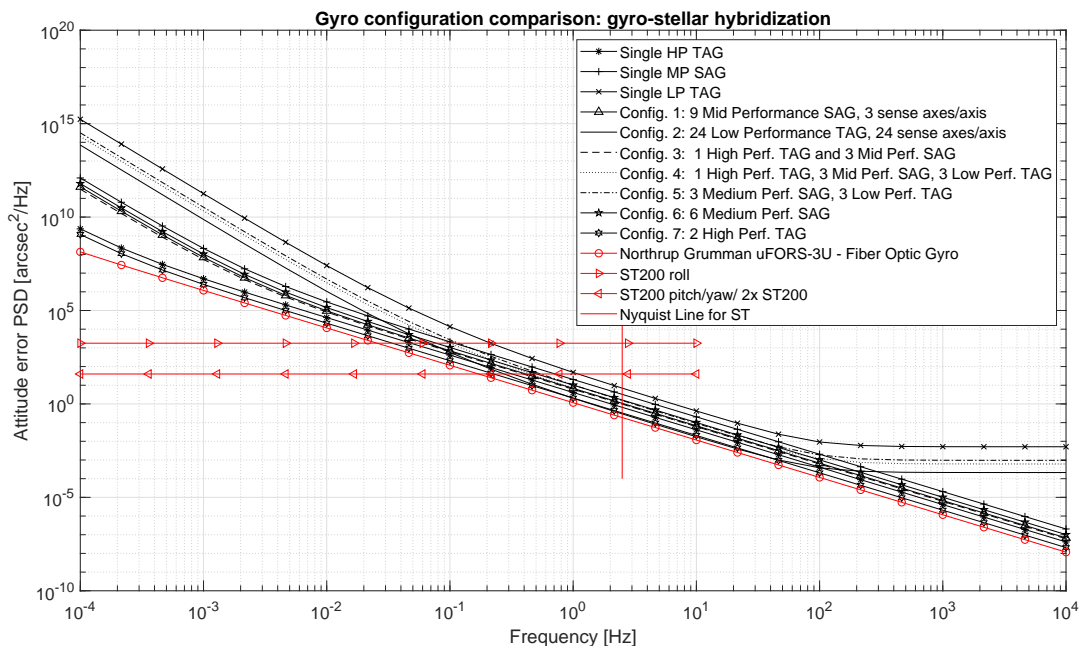
Figure 3.26: *Single-sided attitude error PSD for gyro-stellar configuration selection.*

Table 3.7: *Configuration specific frequency ranges of star tracker used for gyro-stellar hybridisation.*

Configurations	Star Tracker Frequency Range (Roll)		Star Tracker Frequency Range (Pitch/Yaw)	
	Lower Bound [Hz]	Upper Bound [Hz]	Lower Bound [Hz]	Upper Bound [Hz]
1 LPTAG	0	0.214	0	1.01
1 MPSAG	0	0.109	0	0.714
1 HPTAG	0	0.0481	0	0.320
1 uFOG	0	0.0256	0	0.171
Configuration 1	0	0.0634	0	0.413
Configuration 2	0	0.0677	0	0.274
Configuration 3	0	0.0600	0	0.392
Configuration 4	0	0.100	0	0.450
Configuration 5	0	0.117	0	0.542
Configuration 6	0	0.077	0	0.505
Configuration 7	0	0.0341	0	0.227

The star tracker PSD is assumed to have a uniform distribution bandlimited by the Nyquist frequency of the star tracker sampling rate of 5 Hz. This means that the area under the star tracker attitude error PSD between 0 Hz and 2.5 Hz should amount to the 1σ variance of the star tracker presented in Table 2.3. The upper bound on single sided attitude error PSD is chosen such that, the area under the single sided attitude error PSD until the Nyquist sampling rate of the star tracker represents the variance of the star tracker provided in Table 2.3. When two orthogonal star trackers are utilised, the roll performance resembles the pitch/yaw performance. Attitude error single sided PSD distribution for all the configurations is presented with the aid of Figure 3.26. Singular gyro performance is also presented in combination with the configurations. Since most satellites rely on Fiber Optic Gyro for agile slew manoeuvres, due to their high performance, behaviour of a representative micro-Fiber Optic Gyro, μFOG-3U [2], is also presented. The gyro-stellar hybridisation frequency is the frequency beyond which gyro measurements become relevant (Cirillo et al., 2016). This hybridisation frequency for all the configurations are presented as frequency upper bounds in Table 3.7. Utilising the hybridisation frequencies in Table 3.7, different upper limits are set on the gyro sampling rate to obtain the overall attitude knowledge error. Since the star tracker is sampled at 5 Hz, first attempt is to sample the gyros at 5 Hz. The expected gyro-stellar attitude knowledge is presented with the aid of Table 3.8. However, it is important to note that the systems needs to satisfy 20.63 arcsec (1σ) attitude knowledge requirement under a slew rate of 1.5 deg/s. The requirement on angular acceleration is not made available, otherwise an optimal upper bound on gyro sampling rate must consider both the angular rate and angular acceleration. In order to

---

[2]Northrop Grumman LITEF - μFORS 3U https://northropgrumman.litef.com/fileadmin/downloads/Datenblaetter/Datenblatt_uFors-3U_-3UC_-6U_-6UC.pdf

Table 3.8: *Gyro-stellar hybridisation based attitude estimation performance limit from a noise power spectral density standpoint, for different gyro sampling rates. This does not account for systematic gyro errors.*

Attitude Knowledge Error Overview [Star Tracker at 5 Hz, Gyro at 5 Hz]	Gyro-Stellar Hybridization [arcsec] ST200 pitch/yaw 2x ST200	ST200 roll	Attitude Knowledge Error Overview [Star Tracker at 5 Hz, Gyro at 523.5095 Hz]	Gyro-Stellar Hybridization [arcsec] ST200 pitch/yaw 2x ST200	ST200 roll
Single LPTAG Single Axis	11.83071	34.22362	Single LPTAG Single Axis	11.83071	34.22362
Single MP-SAG Single Axis	9.86330	26.87321	Single MP-SAG Single Axis	9.86330	26.87321
Single HP-TAG Single Axis	6.75440	17.77620	Single HP-TAG Single Axis	6.75440	17.77620
Single uFOG - SAG Single Axis	5.15458	13.39566	Single uFOG - SAG Single Axis	5.15458	13.39566
Configuration 1: 9x MPSAG 3 sense axes/axis	7.35274	19.74366	Configuration 1: 9x MPSAG 3 sense axes/axis	7.63379	19.84870
Configuration 2: 24x LPTAG 24 sense axes/axis	5.63425	18.02742	Configuration 2: 24x LPTAG 24 sense axes/axis	5.75972	18.06980
Configuration 3: 1x HPTAG, 3xMPSAG 2 sense axes/axis	7.08160	18.98122	Configuration 3: 1x HPTAG, 3xMPSAG 2 sense axes/axis	7.34856	19.08114
Configuration 4: 1x HPTAG, 3x MPSAG, 3x LPTAG 5 sense axes/axis	7.55980	22.56822	Configuration 4: 1x HPTAG, 3x MPSAG, 3x LPTAG 5 sense axes/axis	7.84940	22.67577
Configuration 5: 3x MPSAG, 3x LPTAG 4 sense axes/axis	8.75182	25.88257	Configuration 5: 3x MPSAG, 3x LPTAG 4 sense axes/axis	9.10965	26.01492
Configuration 6: 6xMPSAG 2 sense axes/axis	8.52377	22.89829	Configuration 6: 6xMPSAG 2 sense axes/axis	8.86798	23.02693
Configuration 7: 2xHPTAG 2 sense axes/axis	5.76883	15.07867	Configuration 7: 2xHPTAG 2 sense axes/axis	5.87297	15.11867

Table 3.9: *Gyro-stellar hybridisation based attitude estimation performance limit from a noise power spectral density standpoint, for different gyro sampled at 2000Hz. This does not account for systematic gyro errors.*

Attitude Knowledge Error Overview [Star Tracker at 5 Hz, Gyro at 2000 Hz]	Gyro-Stellar Hybridization [arcsec] ST200 pitch/yaw 2x ST200	ST200 roll
Single LPTAG Single Axis	13.46602	34.87940
Single MP-SAG Single Axis	10.46612	27.09527
Single HP-TAG Single Axis	6.93462	17.84494
Single uFOG - SAG Single Axis	5.21962	13.42080
Configuration 1: 9x MPSAG 3 sense axes/axis	7.63518	19.84924
Configuration 2: 24x LPTAG 24 sense axes/axis	5.80457	18.08542
Configuration 3: 1x HPTAG, 3xMPSAG 2 sense axes/axis	7.34988	19.08165
Configuration 4: 1x HPTAG, 3x MPSAG, 3x LPTAG 5 sense axes/axis	7.93717	22.70988
Configuration 5: 3x MPSAG, 3x LPTAG 4 sense axes/axis	9.22061	26.05788
Configuration 6: 6xMPSAG 2 sense axes/axis	8.86968	23.02759
Configuration 7: 2xHPTAG 2 sense axes/axis	5.87349	15.11887

guarantee a sampling resolution of 20.63 arcsec (1σ) at a slew rate of 1.5 deg/s, while meeting the Nyquist sampling criteria the gyros should be sampled at $f_s = 2 \cdot \frac{1}{\frac{20.63}{3600} \frac{1}{1.5}}$ = 523.5095Hz. When the gyros are sampled at this rate, the attitude knowledge error obtained are presented in Table 3.8. Green shaded boxes indicate that the attitude knowledge requirement of 20.63 arcsec (1σ) is met. Often times MEMS gyros are sampled at kHz level to minimise the resonances associated with clock frequencies. Most of the gyros considered for the analysis are sampled on average at 2000Hz. Later the gyro samples are sub-sampled appropriately to meet the filter update rates. Table 3.9 captures the attitude error arising out of gyro-stellar hybridisation process. In theory, the high frequency gyro output can be sub-sampled with a low-pass anti-aliasing filter to meet the 5Hz calibration filter update rate requirements, with `sinc` filter for instance. However, an ideal `sinc` filter introduces infinite time delay in practice. Comparing the gyro-stellar hybridisation performances in Tables 3.8 and 3.9 it is clear that a simple low pass filter with low delay is sufficient, since the noise introduced by high frequency sampling does not significantly contribute to the overall attitude knowledge error. Green shaded boxes indicate that the attitude knowledge requirement of 20.63 arcsec (1σ) is met. From the gyro-stellar hybridisation presented in Tables 3.8 and 3.9 it is evident that in the case that 2 star
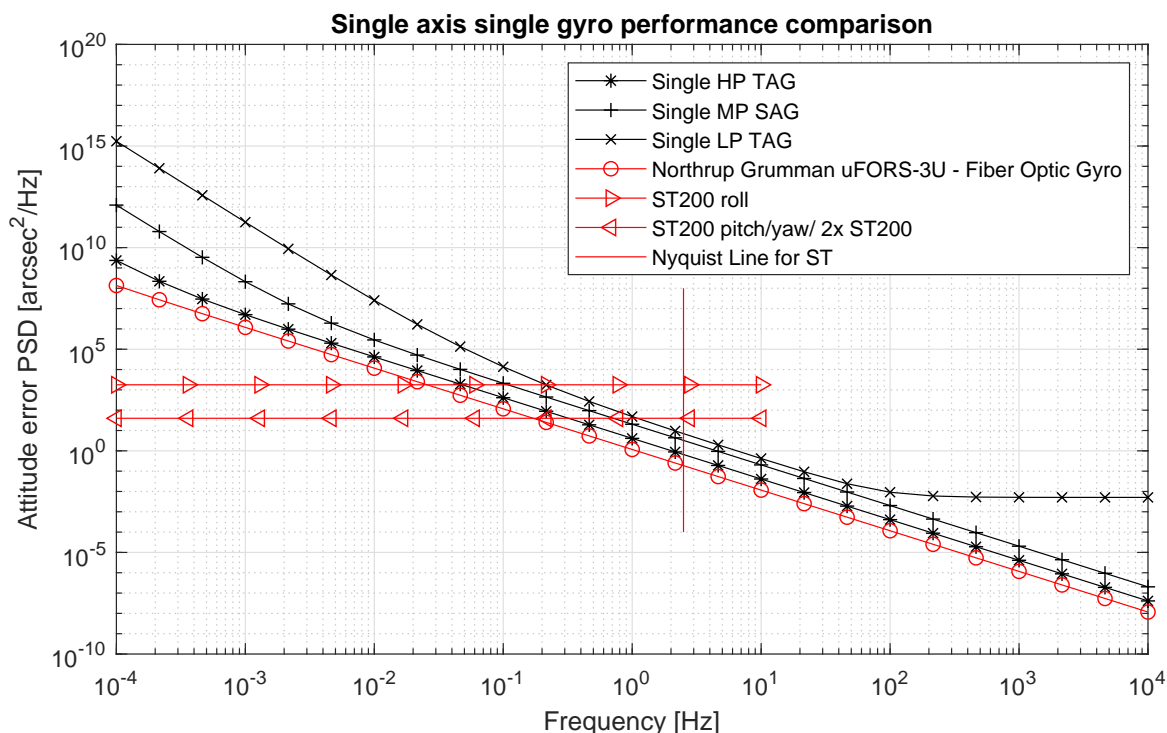
Figure 3.27: *Attitude error single sided PSD overview for single gyro units and star tracker.*
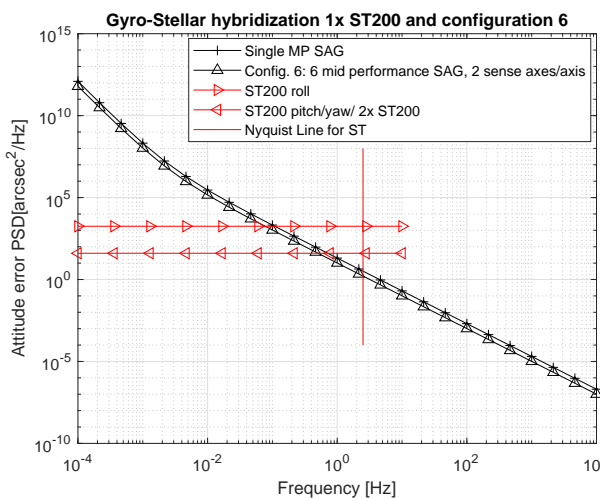
Figure 3.28: *Attitude error single sided PSD overview for configuration 6.*
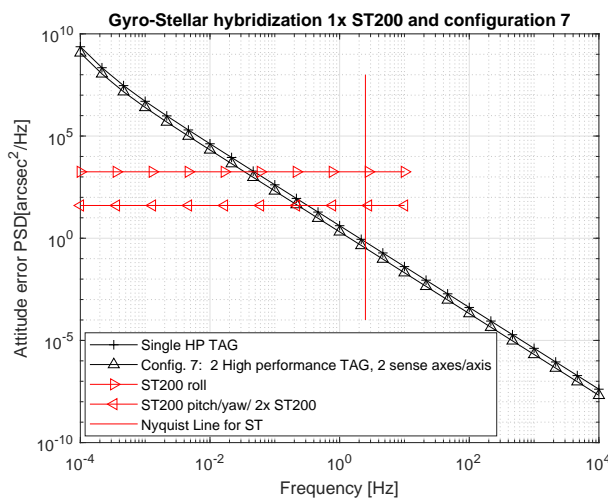
Figure 3.29: *Attitude error single sided PSD overview for configuration 7.*

trackers are utilised, 3 MPSAG or 1 LPTAG or 1 HPTAG is sufficient to meet the attitude knowledge requirements, given that the systematic errors are removed by virtue of a calibration filter. Since MEMS gyro performances are sensitive to radiation effects, LPTAG is excluded from analysis. Three MPSAG and one HPTAG is considered for the calibration filter analysis. Since the calibration filter considered as part of this thesis work is a relative misalignment calibration filter, often times three rotational misalignments are discarded to ensure observability of the calibration states. As discussed earlier in Section 3.2.5, all the misalignments are calibrated with respect to gyro as a result three rotational misalignment from gyros are always discarded for full observability. In light of that, if the three gyro sense axes are not sufficient to meet the attitude knowledge requirements, configurations 6 and 7 will be investigated. Since both of these configurations offer 2 sense axes/axis and 6 sense axes in total. To conclude this section on configuration choices, Figure 3.27 presents the attitude error noise density overview for single unit gyros and star tracker. While Figures 3.28 and 3.29 outlines that for configurations 6 and 7.

Table 3.10: *Gyro dead reckoning performances for gyro sampled at 5 Hz and star tracker sampled at 5 Hz. With [Q] = Qualified, [MP] = Moderate Performance, and [UQ] = Unqualified.*

Attitude Knowledge Error Overview	Dead Reckoning [arcsec]				
	30s	1.5 min	3 min	5 min	10 min
Single LPTAG Single Axis	72.4412 [UQ]	166.4634 [UQ]	429.0284 [UQ]	1206.8554 [UQ]	3589.5789 [UQ]
Single MP-SAG Single Axis	24.3748 [MP]	36.8921 [UQ]	57.5941 [UQ]	96.1094 [UQ]	181.2845 [UQ]
Single HP-TAG Single Axis	10.7187 [Q]	15.7989 [Q]	23.2934 [MP]	34.4500 [UQ]	51.3619 [UQ]
Single uFOG - SAG Single Axis	5.7099 [Q]	8.4048 [Q]	12.3555 [Q]	18.1570 [Q]	26.6933 [UQ]
Configuration 1: 9x MPSAG 3 sense axes/axis	14.0728 [Q]	21.2997 [MP]	33.2520 [UQ]	55.4888 [UQ]	104.6646 [UQ]
Configuration 2: 24x LPTAG 24 sense axes/axis	14.7870 [Q]	33.9792 [UQ]	87.5751 [UQ]	246.3483 [UQ]	732.7197 [UQ]
Configuration 3: 1x HPTAG, 3xMPSAG 2 sense axes/axis	13.3137 [Q]	20.0663 [Q]	31.0629 [UQ]	51.0471 [UQ]	94.2018 [UQ]
Configuration 4: 1x HPTAG, 3x MPSAG, 3x LPTAG 5 sense axes/axis	25.6532 MP]	58.2205 [UQ]	149.1383 [UQ]	418.5653 [UQ]	1244.0374 [UQ]
Configuration 5: 3x MPSAG, 3x LPTAG 4 sense axes/axis	31.9544 [UQ]	72.6684 [UQ]	186.3319 [UQ]	523.1358 [UQ]	1554.9938 [UQ]
Configuration 6: 6xMPSAG 2 sense axes/axis	17.2356 [Q]	26.0867 [MP]	40.72552 [UQ]	67.9596 [UQ]	128.1875 [UQ]
Configuration 7: 2xHPTAG 2 sense axes/axis	7.5793 [Q]	11.1715 [Q]	16.4709 [Q]	24.3598 [MP]	36.3184 [UQ]

Table 3.11: *Gyro dead reckoning performances for gyro sampled at 523.5095 Hz and star tracker sampled at 5 Hz. With [Q] = Qualified, [MP] = Moderate Performance, and [UQ] = Unqualified.*

Attitude Knowledge Error Overview	Dead Reckoning [arcsec]				
	30s	1.5 min	3 min	5 min	10 min
Single LPTAG Single Axis	72.4412 [UQ]	166.4634 [UQ]	429.0284 [UQ]	1206.8554 [UQ]	3589.5789 [UQ]
Single MP-SAG Single Axis	24.3748 [MP]	36.8921 [UQ]	57.5941 [UQ]	96.1094 [UQ]	181.2845 [UQ]
Single HP-TAG Single Axis	10.7187 [Q]	15.7989 [Q]	23.2934 [MP]	34.4500 [UQ]	51.3619 [UQ]
Single uFOG - SAG Single Axis	5.7099 [Q]	8.4048 [Q]	12.3555 [Q]	18.1570 [Q]	26.6933 [UQ]
Configuration 1: 9x MPSAG 3 sense axes/axis	14.1397 [Q]	21.3439 [MP]	33.2803 [UQ]	55.5058 [UQ]	104.6736 [UQ]
Configuration 2: 24x LPTAG 24 sense axes/axis	14.8067 [Q]	33.9877 [UQ]	87.5784 [UQ]	246.3495 [UQ]	732.7201 [UQ]
Configuration 3: 1x HPTAG, 3xMPSAG 2 sense axes/axis	13.3775 [Q]	20.1087 [Q]	31.0902 [UQ]	51.0637 [UQ]	94.2109 [UQ]
Configuration 4: 1x HPTAG, 3x MPSAG, 3x LPTAG 5 sense axes/axis	25.6912 [MP]	58.2373 [UQ]	149.1448 [UQ]	418.5676 [UQ]	1244.0382 [UQ]
Configuration 5: 3x MPSAG, 3x LPTAG 4 sense axes/axis	32.0008 [UQ]	72.6889 [UQ]	186.3399 [UQ]	523.1386 [UQ]	1554.9948 [UQ]
Configuration 6: 6xMPSAG 2 sense axes/axis	17.3175 [Q]	26.1409 [MP]	40.7599 [UQ]	67.9805 [UQ]	128.1985 [UQ]
Configuration 7: 2xHPTAG 2 sense axes/axis	7.6170 [Q]	11.1972 [Q]	16.4883 [Q]	24.3716 [MP]	36.3263 [UQ]

For the sake of completion, Tables 3.10 - 3.12 represent the dead-reckoning performances for different gyros and configuration combinations. Figure 3.30 presents an overview of all the gyros and different configurations, in combination with the dead reckoning frequency lines for gyro only attitude propagation. Open-loop gyro only attitude knowledge estimation that meet the 20.63 arcsec (1σ) requirement are labelled as Qualified [Q]. Ones which stay within 30 arcsec (1σ) are labelled as Moderate Performing [MP]. While the ones that exceed the 30 arcsec (1σ) limit are marked as Unqualified [UQ]. Since calibration filters are event based filters, where the event is dependent on the star tracker update, in-between the star tracker update the system has to rely on the previous calibration filter update and the gyro dead-reckoned attitude knowledge. This is especially true in the events when the star tracker has slower update rate which surpasses the propagation update rate of the calibration filter.

3.4 | MEMS Gyroscope Noise Generation and Verification

Now that the gyro noise characteristics are defined and the configurations are chosen, the objective of this segment is to develop gyro models with noise behaviour that capture the noise behaviour defined by the Allan-Variance analysis. In order to do so, an ideal gyro model is defined. The ideal gyro model is superimposed with random noise non-idealities. The gyro model is later simulated for a certain duration, single sided attitude rate and attitude error PSD is extracted from the simulated output. The output PSD is verified against Allan-Variance based gyro PSD. Figure A.1 in Appendix A presents the Simulink model of the gyro. While Figure 3.31 presents a simplified overview of the gyro noise model. MEMS rate gyros are driven by an oscillating mass or a tuning fork, which oscillates at a

Table 3.12: *Gyro dead reckoning performances for gyro sampled at 2000 Hz and star tracker sampled at 5 Hz. With [Q] = Qualified, [MP] = Moderate Performance, and [UQ] = Unqualified.*

Attitude Knowledge Error Overview	Dead Reckoning [arcsec]				
	30s	1.5 min	3 min	5 min	10 min
Single LPTAG	72.5568	166.5137	429.0479	1206.8623	3589.5812
Single Axis	[UQ]	[UQ]	[UQ]	[UQ]	[UQ]
Single MP-SAG	24.4913	36.9692	57.6435	96.1391	181.3002
Single Axis	[MP]	[UQ]	[UQ]	[UQ]	[UQ]
Single HP-TAG	10.7724	15.8354	23.3182	34.4667	51.3732
Single Axis	[Q]	[Q]	[MP]	[UQ]	[UQ]
Single uFOG - SAG	5.7385	8.4243	12.3687	18.1660	26.6994
Single Axis	[Q]	[Q]	[Q]	[Q]	[UQ]
Configuration 1: 9x MPSAG	14.1400	21.3442	33.2805	55.5059	104.674
3 sense axes/axis	[Q]	[MP]	[UQ]	[UQ]	[UQ]
Configuration 2: 24x LPTAG	14.8106	33.9895	87.5790	246.3497	732.7202
24 sense axes/axis	[Q]	[UQ]	[UQ]	[UQ]	[UQ]
Configuration 3: 1x HPTAG, 3xMPSAG	13.3778	20.1089	31.0904	51.0638	94.2109
2 sense axes/axis	[Q]	[Q]	[UQ]	[UQ]	[UQ]
Configuration 4: 1x HPTAG, 3x MPSAG, 3x LPTAG	25.6977	58.2402	149.1459	418.5680	1244.0383
5 sense axes/axis	[MP]	[UQ]	[UQ]	[UQ]	[UQ]
Configuration 5: 3x MPSAG, 3x LPTAG	32.00906	72.6925	186.3413	523.1391	1554.9950
4 sense axes/axis	[UQ]	[UQ]	[UQ]	[UQ]	[UQ]
Configuration 6: 6xMPSAG	17.31794	26.14116	40.76012	67.9806	128.1986
2 sense axes/axis	[Q]	[MP]	[UQ]	[UQ]	[UQ]
Configuration 7: 2xHPTAG	7.6172	11.1973	16.4884	24.3717	36.3263
2 sense axes/axis	[Q]	[Q]	[Q]	[MP]	[UQ]

Figure 3.30: *Single-sided attitude error PSD for gyro dead reckoning behaviour analysis for single gyro units and corresponding configurations.*

much higher frequency than the rates at which they are sampled. For the MPSAG and HPTAG under consideration, the natural frequency of the vibrating mass is 8000 Hz. A damping coefficient of $\frac{\sqrt{2}}{2}$ is assumed and the MEMS rate gyro dynamics is modelled as a second order transfer function. MEMS rate gyros also come with a built-in Low Pass Anti-Aliasing Filter to support sampling at lower frequencies. This is not activated for gyro verification, as the Allan-Deviation provided by the manufactures are outputs at 2000 Hz for MPSAG and 2300 Hz for HPTAG respectively. Angular Random Walk (ARW) is modelled as a band-limited white noise, where the maximum and minimum frequency bound of the double sided PSD is defined by the sampling frequency of the gyro. The height of the double sided PSD is defined by N^2. Rate Random Walk (RRW) is a brown noise behaviour that scales down with $1/f^2$ in the frequency domain. This equivalent to integrating the white noise output with $\frac{1}{s}$, since transfer function input-output is squared to capture the input-output PSD relation as demonstrated by Equation (B.15) in Section B. RRW is also modelled primarily as a band-limited white noise with the height of the double sided PSD defined by K^2. However, RRW is a pink noise behaviour which scales down with $1/f$ in the frequency domain. This leads to an irrational transfer function of the form $\frac{1}{\sqrt{s}}$ in the Laplace domain. Since the spectrum is not rational it cannot be simply created using standard linear system theory and differential equation models to simulate it in the time domain. However, they can be approximated within given frequency bands of interests.

Pink noise shaping filters can be modelled both as a digital filter in z-domain, or as a continuous time in the s-domain. The following first aims at constructing a pink noise shaping filter based on power series expansion of backward Euler scheme defined as: $s = \frac{z-1}{zh}$. For backward Euler scheme, $\forall$ stable Continuous Time $\rightarrow$ stable Discrete Time, and $\exists$ unstable Continuous Time $\rightarrow$ stable Discrete Time. The method presented here can be extended to forward difference scheme $\left(s = \frac{z-1}{h}\right)$ or Tustin/bilinear approximation $\left(s = \frac{2z-1}{hz+1}\right)$. Forwarded differences are not recommended, since $\forall$ unstable Continuous Time$\rightarrow$ unstable Discrete Time, and $\exists$ stable Continuous Time $\rightarrow$ unstable Discrete Time. Furthermore, it is not suitable for applications to causal problems. Tustin on the other hand is recommended over backward Euler scheme; since $\forall$ unstable Continuous Time$\rightarrow$ unstable Discrete Time, and $\forall$ stable Continuous Time $\rightarrow$ stable Discrete Time. Both backward Euler scheme and Tustin based pink noise shaping filter can be easily expanded with a power series expansion. As power series expansion usually leads to higher order of filters, continued fraction expansion as presented by Chen et al. (2003), or Muir recursion is preferred for lower order of filters. However, series expansions or iterative schemes often lead to the lack of authority in the selection of the frequency region of interest. Continued fractional expansion schemes exist in continuous time domain as well, but similar problems of higher filter order, non-linear phase behaviour, and lack of fitting exist. However, curve fitting or identification techniques in the continuous time domain provide better authority over the frequency region of interest. Furthermore, it results in lower filter order compared to the digital alternative. There are different ways in which continuous time rational transfer functions can replicate the behaviour of fractional order irrational transfer function. Some of these methods are presented by Vinagre et al. (2000). Section 3.4.2 presents Oustaloup's method for approximating fractional order irrational transfer function. Oustaloup's method is preferred, due to lower shaping filter order, better authority over frequency region selection, linear phase behaviour and a better fit of gyro bias instability.

3.4.1 | Digital Pink Noise Shaping Filter based on Backward Difference

Pink noise is a fractional representation of the brown noise process, the latter being a rational transfer function of a simple integrator. Brown noise is given as the integral of the white noise, whose impulse response function is the unit step function:

$$H_{Brown\ Noise}(s) = \frac{1}{s} \tag{3.33}$$

Pink noise is simply a fractional estimate of the above presented impulse response function, with α=1:

$$H_{Pink\ Noise}(s) = \frac{1}{s^{\frac{\alpha}{2}}} \tag{3.34}$$

Since the gyro is run at a digital time step, the z-transform of Brown noise in backward difference scheme can be expressed as:

$$H_{Brown\ Noise}(z) = \frac{1}{1 - z^{-1}} \tag{3.35}$$

Corresponding Pink noise can be expressed as:

$$H_{Pink\ Noise}(z) = \frac{1}{(1 - z^{-1})^{\frac{\alpha}{2}}} \tag{3.36}$$
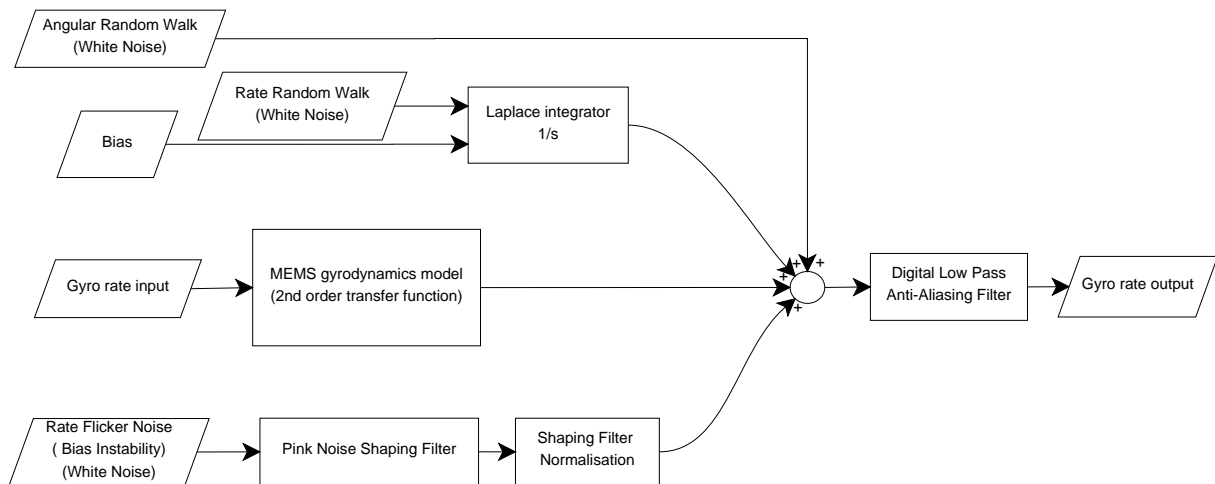
Figure 3.31: *Overview of the gyro noise model, for reading out rigid body simulator attitude rates.*
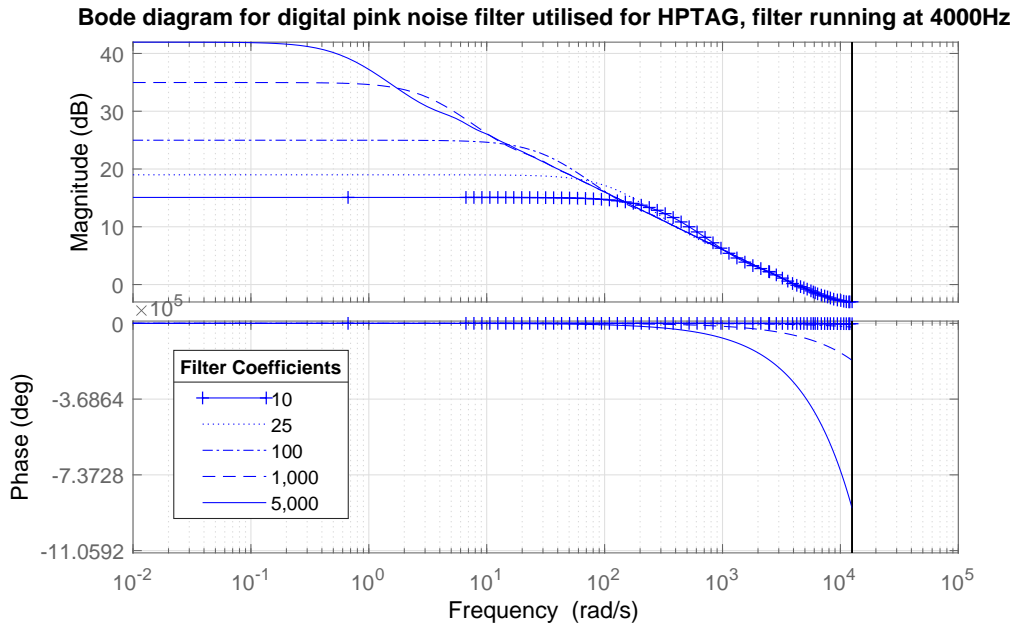
Figure 3.32: *Magnitude and phase bode plot for the varying order of filter coefficients of backward scheme based on power series expansion for HPTAG bias instability approximation.*

The denominator of the pink noise filter can be easily expanded by binomial series. Power series for a function f defined by $f(x) = (1 + x)^\alpha$, with $\alpha \in \mathbb{C}$ an arbitrary complex number, can be defined as:

$$(1 + x)^\alpha = \sum_{k=0}^{\infty} \binom{\alpha}{k} x^k \tag{3.37a}$$

$$(1 + x)^\alpha = 1 + \alpha x + \frac{\alpha(\alpha - 1)}{2!} x^2 + \cdots \tag{3.37b}$$

Using the above presented power series expansion, the denominator of the pink noise filter presented in Equation (3.36) can be expanded as:

$$H(z) = \frac{1}{1 - \frac{\alpha}{2} z^{-1} - \frac{\frac{\alpha}{2}\left(1 - \frac{\alpha}{2}\right)}{2!} z^{-2} + \cdots} \tag{3.38}$$

The above expansion of the transfer function is equivalent to a recursive auto-regressive filter of the form(Kasdin, 1995):

$$x_n = -a_1 x_{n-1} - a_2 x_{n-2} - a_3 x_{n+3} - \cdots + w_n \tag{3.39}$$

The filter coefficients can be easily found from an iterative formula similar to that for the Moving Average case:

$$\begin{aligned} a_0 &= 1 \\ a_k &= \left(k - 1 - \frac{a}{2}\right) \frac{a_k - 1}{k} \end{aligned} \tag{3.40}$$

The above presented filter can be easily implemented to obtain time domain pink noise behaviour, and can be scaled to accommodate any noise that scales down with the behaviour $\frac{1}{f^\alpha}$. For pink noise, α = 1. The pink noise filter is driven by band-limited white noise with amplitude B^2. Magnitude and phase Bode plot for varying order of pink noise filter based on backward difference is presented with the aid of Figures 3.32 and 3.33. For increasing order of filter, magnitudes at lower frequencies better match the pink noise behaviour. However, this comes at an expensive penalty of increasingly non-linear phase behaviour at higher frequencies. Similar phase behaviour is expected of Tustin based series expansion to fit the irrational transfer function. Figure 3.34 demonstrates the poles of the pink noise shaping filter, based on increasing order of the filter coefficients. All poles lie inside the unit circle, and are hence stable. With increasing filter coefficients the poles move closer to the edges of the unit circle, which might lead to ringing effect. The effectiveness of the above presented filter in capturing the pink noise behaviour is presented with the aid of Figures 3.35 and 3.36. In order to scale the filter output with respect to the expected analytic behaviour, the linear part of the filter was focused upon. The filter was scaled such that the square root of the area
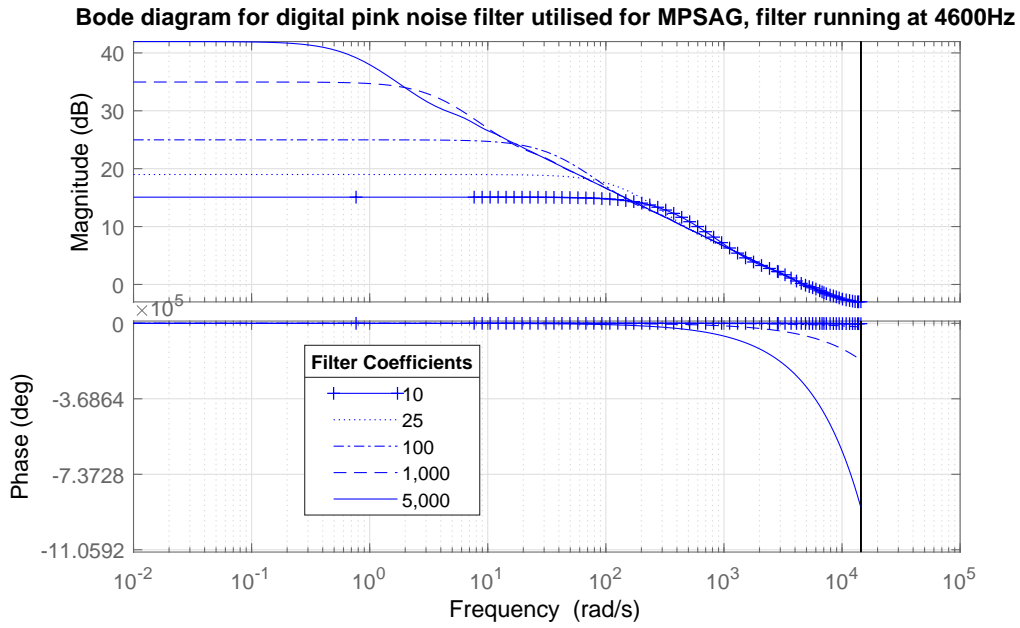
Figure 3.33: *Magnitude and phase bode plot for the varying order of filter coefficients of backward scheme based on power series expansion for MPSAG bias instability approximation.*
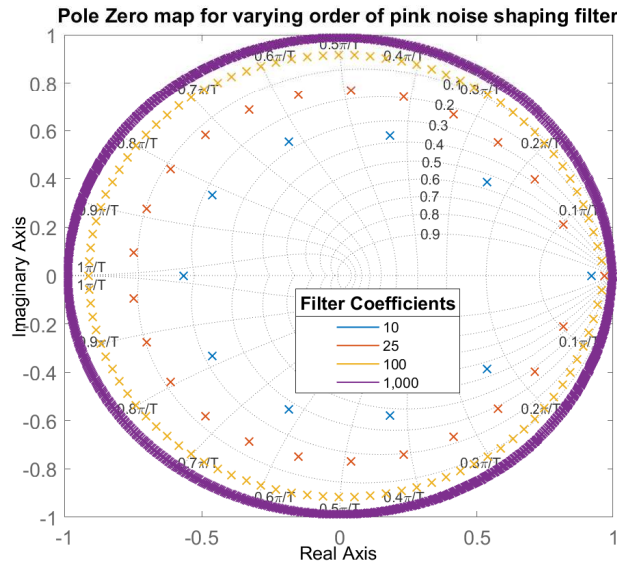
Figure 3.34: *Pole zero map for varying pink noise filter order based on power series expansion of backward difference scheme.*

under the PSD output of the filter in the linear region, would match the square root of the area under the analytical slope of the filter in the same frequency region.

$$\sigma_{filter\ output} \cdot k_{output\ scaling} = \sigma_{analytic\ behaviour} \tag{3.41}$$

The magnitude of $k_{output\ scaling}$ can either be multiplied after the filter output, alternatively it can be squared and multiplied with the underlying driving white noise to get the appropriate scaling. As expected, increasing the filter coefficients enables a better approximation of the irrational transfer function, however, it comes at the expense of delay introduced, and the beyond a certain point more and more filter coefficients are required to better capture the low frequency pink noise behaviour. Since, the star tracker runs at 5 Hz, below 2.5 Hz, the response becomes
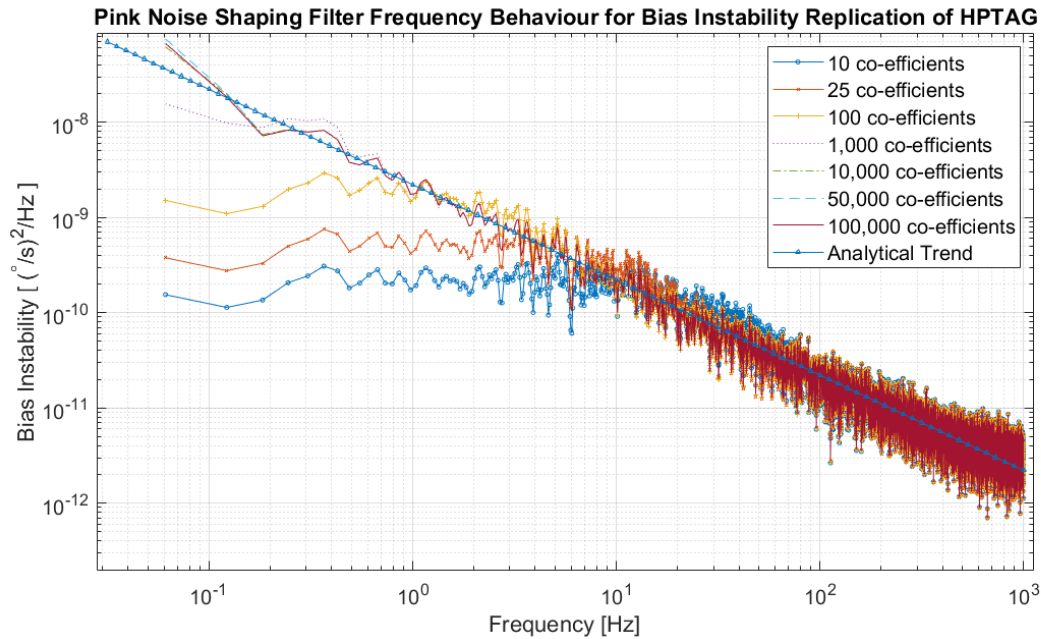
Figure 3.35: *Pink noise shaping filter frequency domain noise PSD behaviour for different co-efficient sizes k, based on power series expansion of backward difference scheme.*
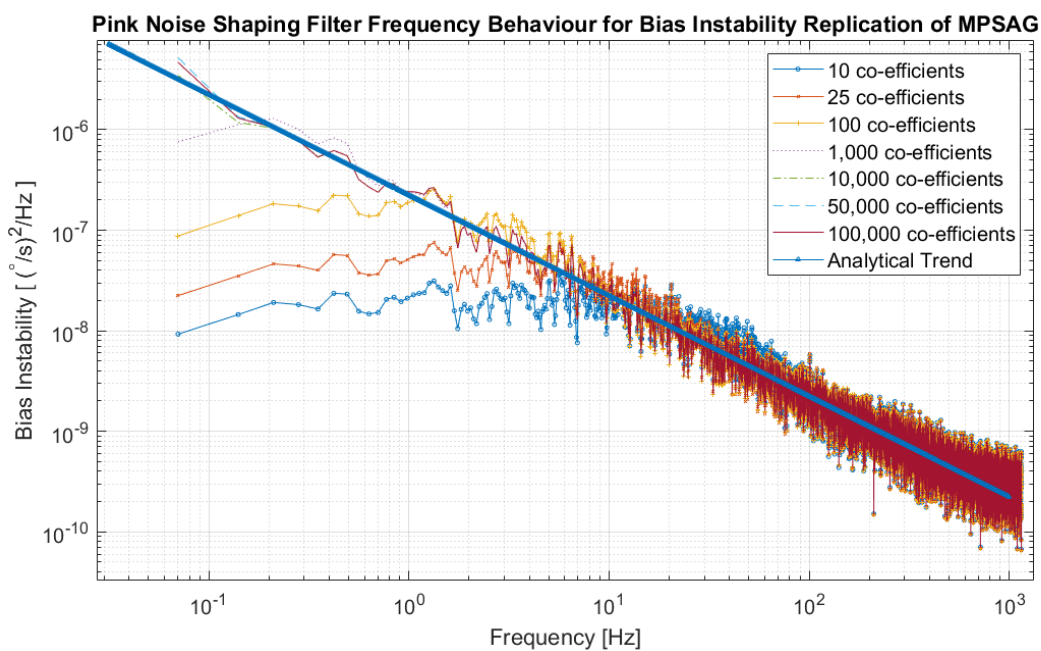
Figure 3.36: *Pink noise shaping filter noise PSD behaviour for different co-efficient sizes k, based on power series expansion of backward difference scheme.*

less relevant unless of course the gyro performs dead-reckoning. The differences in performance, with regards to the variance of noise density, is minimal between k = 1000 and k = 100,000. As a result k = 1000 is utilised for the pink noise filter synthesised in this work, to capture the low frequency behaviour well enough. It is well suited for real time noise generation. The accuracy of this pink noise filter in capturing the gyro bias instability is discussed further when the gyro models are verified.

Now that the gyro noise generation process is discussed, the gyro noise model is simulated and the corresponding output is verified. To verify the MPSAG and HPTAG gyro model, the gyro noise simulator was run to simulate the gyro

Verification of Noise PSD Behaviour for Medium Performance Single Axis Gyro. Simulation Time = 25000s, Overlap % = 80, Windows = 10
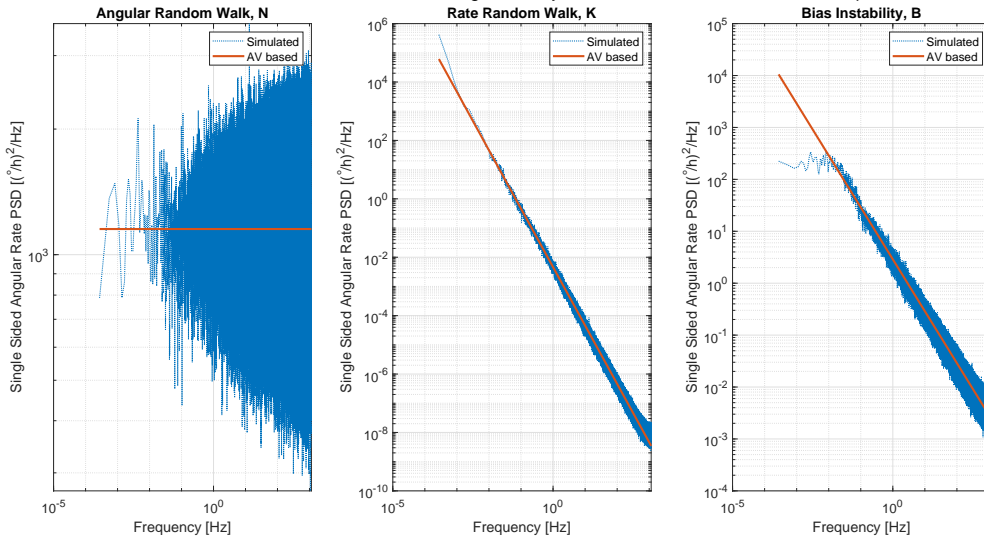
Figure 3.37: *Noise PSD behaviour verification of the individual gyro noise elements for Medium Performance Single Axis Gyro, based on power series expansion of backward difference scheme.*
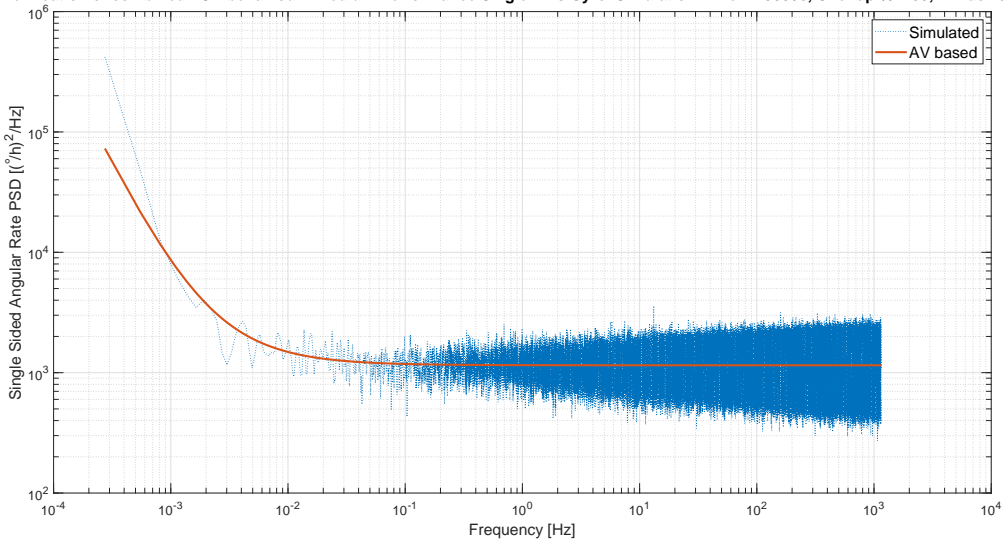
Figure 3.38: *Noise PSD behaviour verification of the gyro output with all noise elements combined for Medium Performance Single Axis Gyro, based on power series expansion of backward difference scheme.*

noise for 25,000 s (in simulation time, not equivalent to real time). PSD analysis was conducted on the individual characteristic gyro noise module output to verify the individual gyro noise elements. Later the the combined gyro noise output was verified against the Allan-Deviation characterised by the single sided attitude error PSD. Figure 3.37 represents the gyro noise behaviour for individual noise element; while Figure 3.38 represents the combined behaviour of the Medium Performance Single Axis Gyro.

Figure 3.39 represents the gyro noise behaviour for individual noise element; while Figure 3.40 represents the combined behaviour of the High Performance Triple Axis Gyro. Discrete Fourier Transform was conducted on the gyro output to obtain the gyro output PSD plots presented above. A brief discussion on DFT and the underlying scheme is presented in Appendix B. For MPSAG the data was sampled at 2,300 Hz and for HPTAG the data was sampled at 2,000 Hz. The simulation time was set to 25,000 s, this resulted in 2,300·25,000 = 57,500,000 data points for MPSAG and 2,000·25,000 = 50,000,000 data points for HPTAG. With 10 windows, each segment of window provides 2500s of time series. Overlapping was observed to have very little effect on variance of generated PSD curves. The next power of 2

Verification of Noise PSD Behaviour for High Performance Triple Axis Gyro. Simulation Time = 25000s, Overlap % = 80, Windows = 10
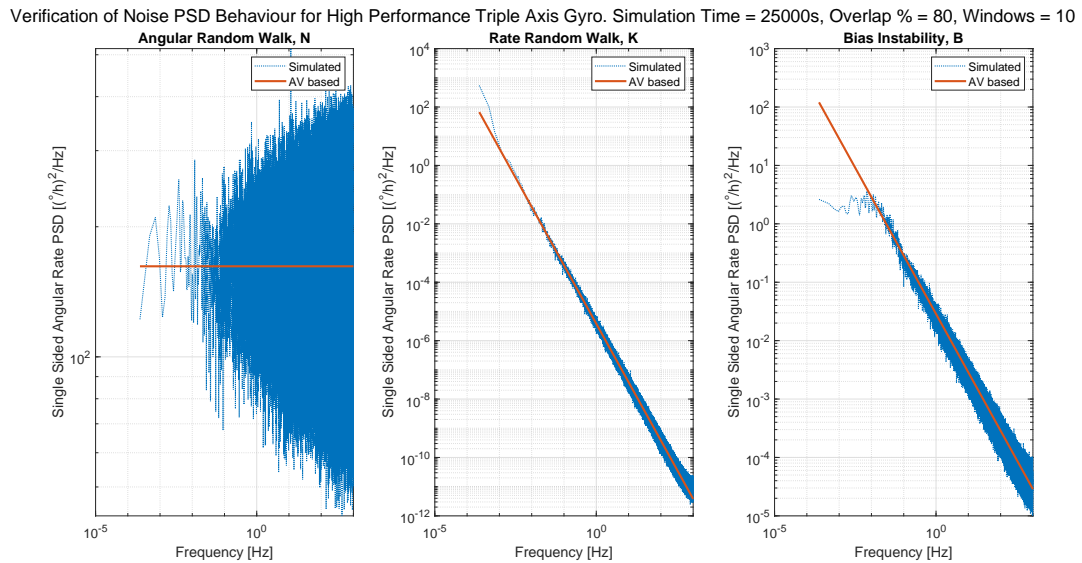
Figure 3.39: *Noise PSD behaviour verification of the individual gyro noise elements for High Performance Triple Axis Gyro, based on power series expansion of backward difference scheme.*
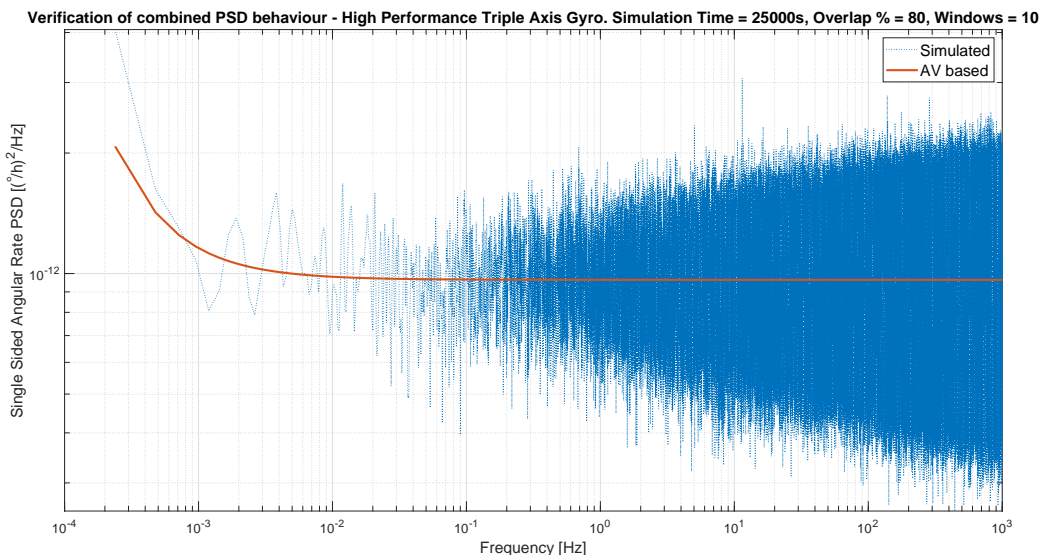
Figure 3.40: *Noise PSD behaviour verification of the gyro output with all noise elements combined for High Performance Triple Axis Gyro, based on power series expansion of backward difference scheme.*

greater than the length of the window segments is utilised to generate the PSD curves. The noisy dataset is by virtue of shorter run times, which in turn effects the number of data points available in a given window. From the above it can be visually verified that the PSD curves of the gyro output matches the analytic trend. To quantify the accuracy of the gyro output, one can evaluate the standard deviation denoted by the square root of the area underneath the PSD curves. Standard deviation of the simulated, and analytic trend are analysed over the frequency range 10^{-4} Hz and 10^{3} Hz. The results are presented in Table 3.13. The simulated and analytic gyro rate output PSD are off by a factor of 1.00014 for MPSAG and 1.00010 for HPTAG. Alternatively, the observed %-difference between simulated and analytic gyro rate output noise PSD is 0.0125% for MPSAG and 0.0179% for HPTAG. The gyro simulator is verified and validated, in accordance with the scheme outlined in Section 3.3.2.

3.4.2 | Continuous Time Pink Noise Shaping Filter based on Oustaloup's Method

The objective here is to replicate the processes outlined in Section 3.4.1, but in continuous time with Oustaloup's method. In order to approximate the pure fractional derivative term s^{γ}, $0 \leq \gamma \leq 1$ ensuring that the magnitude

Table 3.13: *Analytic and simulated standard deviation of the attitude rate noise PSD between the frequency range 10^{-4} Hz and 10^3 Hz with backward difference power series expansion based pink noise shaping filter.*

Standard Deviation [$^\circ/s$] Frequency Range [10^{-4} to 10^3 Hz]	Angular Random Walk ARW	Random Rate Walk RRW	Rate Flicker Noise RFN	Combined
Simulated MPSAG	0.31976	0.00246	0.00168	0.31977
Analytical MPSAG	0.31972	0.00122	0.00185	0.31973
Factor Offset	1.00012	2.02524	0.91038	1.00014
Simulated HPTAG	0.11182	8.68317e-05	1.6143e-04	0.11182
Analytical HPTAG	0.11180	3.75207e-05	1.8406e-04	0.11180
Factor Offset	1.00010	2.31423	0.87706	1.00010
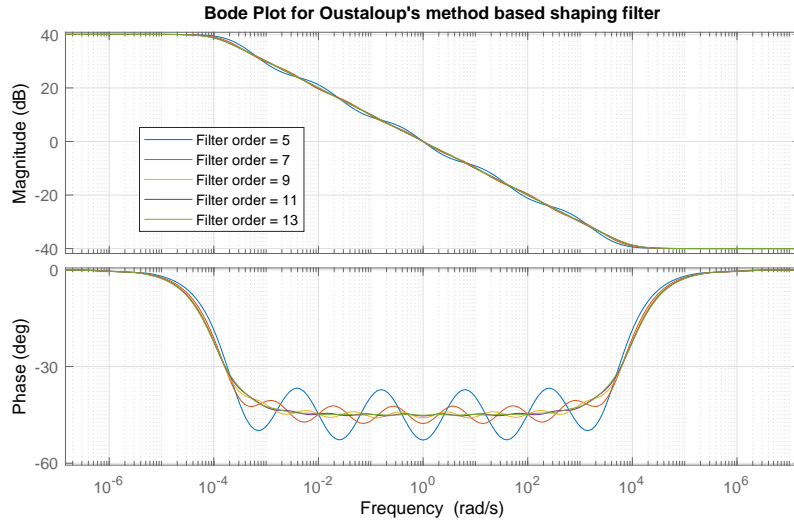
Figure 3.41: *Bode magnitude and phase response for pink noise filter behaviour approximation with Oustaloup's method.*

response fits within the frequency range (ω_b, ω_h), Oustaloup's method can be expressed as:

$$G_{f,\gamma}(s) = K \prod_{k=-N}^{N} \frac{s + \omega'_k}{s + \omega_k} \qquad (3.42)$$

In the above expression, the poles, zeros, and gains can be evaluated utilising the following:

$$\omega'_k = \omega_b \left(\frac{\omega_h}{\omega_b}\right)^{\frac{k+N+\frac{1}{2}(1-\gamma)}{2N+1}} \qquad (3.43a)$$

$$\omega_k = \omega_b \left(\frac{\omega_h}{\omega_b}\right)^{\frac{k+N+\frac{1}{2}(1+\gamma)}{2N+1}} \qquad (3.43b)$$

$$K = \omega_h^{\gamma} \qquad (3.43c)$$

Here, k = -N, . . ., N. The above expression leads to a pink noise shaping filter of order 2·N + 1. The above presented filter is synthesised for N = 2 to 6, resulting in filters with orders 5 to 13. Bode magnitude and phase plot for varying the order of the shaping filter is presented with the aid of Figure 3.41. Poles and zeros of the synthesized filter, all lie in the left half plane on the real axis as observed in Figures 3.42 and 3.43. As observed in Figure 3.41, for N = 3 (filter order 7), the magnitude response reaches a linear behaviour capable of approximating the pink noise. However, the phase behaviour remains oscillatory. The phase reaches linear behaviour in the frequency region of interest for filter orders 11 and 13. Bias-instability pink noise output PSD for varying orders of shaping filter for MPSAG and HPTAG MEMS rate gyro is presented with the aid of Figures 3.44 and 3.45.

Oustaloup's filter of order 13 is chosen to shape bias instability for simulating the gyro simulator. Corresponding rational transfer function to approximate the irrational fractional order pink noise transfer function in the frequency
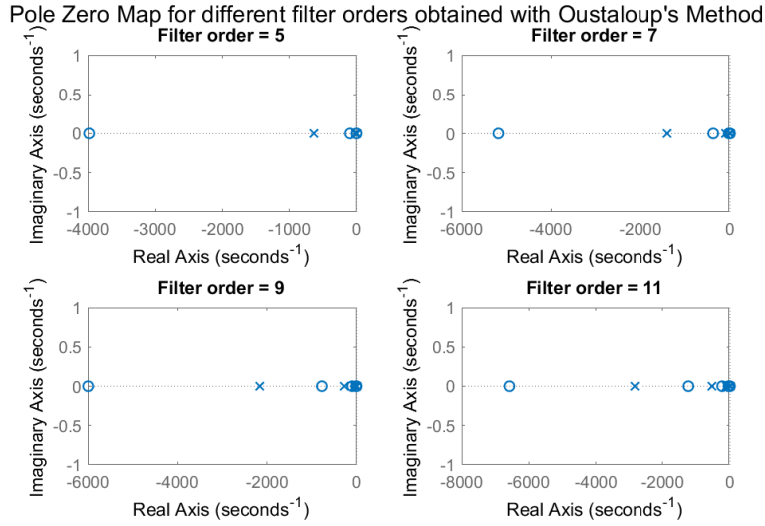
Figure 3.42: *Pole zero map for pink noise shaping filter of orders 5, 7, 9, and 11 with Oustaloup's method.*
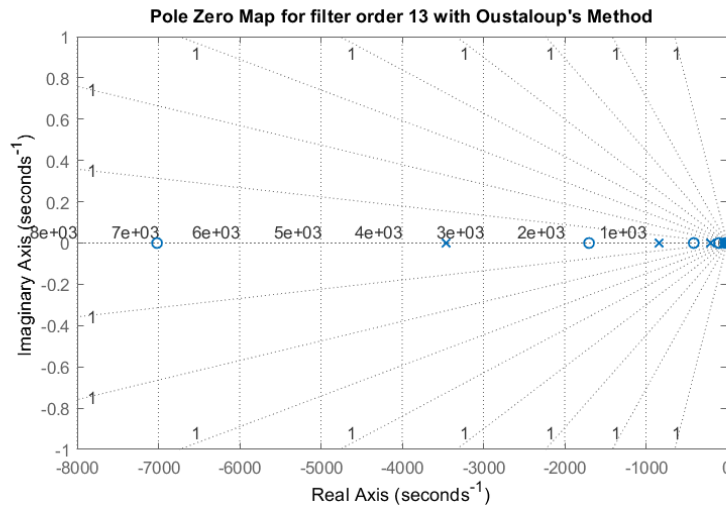
Figure 3.43: *Pole zero map for pink noise shaping filter of order 13 with Oustaloup's method.*

region of interest is given by:

$$G_{13,-\frac{1}{2}}(s) = \frac{s^{13} + 9263s^{12} + 1.674e07s^{11} + 7.005e09s^{10} + 7.03e11s^9 + 1.706e13s^8 + 1.003e14s^7}{100s^{13} + 4.561e05s^{12} + 4.059e08s^{11} + 8.363e10s^{10} + 4.132e12s^9 + 4.937e13s^8 + 1.429e14s^7}$$

$$\cdots \frac{+1.429e14s^6 + 4.937e13s^5 + 4.132e12s^4 + 8.363e10s^3 + 4.059e08s^2 + 4.561e05s + 100}{+1.003e14s^6 + 1.706e13s^5 + 7.03e11s^4 + 7.005e09s^3 + 1.674e07s^2 + 9263s + 1}$$

(3.44)

The driving input to the filter is band-limited white noise of magnitude B^2, bounded by the respective gyro sampling rates. For MPSAG the gyro output is sampled at 2300 Hz, and for HPTAG the gyro output is sampled at 2000 Hz. The gyro simulator is run for 25,000s at steady state. Single sided attitude rate PSD is conducted on the gyro output. Figure 3.46 demonstrates the combined gyro output single-sided attitude rate noise PSD for MPSAG; stacked against the analytical single sided attitude rate noise PSD. Figure 3.47 demonstrates the combined gyro output single-sided attitude rate noise PSD for HPTAG; stacked against the analytical single sided attitude rate noise PSD. From the above it can be visually verified that the PSD curves of the gyro output matches the analytic trend. To quantify the accuracy of the gyro output, one can evaluate the standard deviation denoted by the square root of the area underneath the PSD curves. Standard deviation of the simulated, and analytic trend are analysed over the frequency range 10^{-4} Hz and 10^3 Hz. The results are presented in Table 3.14. The simulated and analytic gyro rate output PSD are off by a factor of 1.0000745 for MPSAG and 1.000082 for HPTAG. Alternatively, the observed %-difference between simulated and analytic gyro rate output noise PSD is 0.0088% for MPSAG and 0.0126% for HPTAG. Clearly the continuous time pink noise shaping filter, performs significantly better than the backward scheme power series expansion based

Table 3.14: *Analytic and simulated standard deviation of the attitude rate noise PSD between the frequency range 10^{-4} Hz and 10^3 Hz with pink noise shaping filter based on Oustaloup's method with filter order 13.*

Standard Deviation [$°/s$] Frequency Range [10^{-4} Hz to 10^3 Hz]	Angular Random Walk ARW	Random Rate Walk RRW	Rate Flicker Noise RFN	Combined
Simulated MPSAG	0.45219	0.0016577	0.0018522	0.45220
Analytical MPSAG	0.45216	0.0012168	0.0018472	0.45216
Factor Offset	1.0000736	1.36237	1.00266	1.0000745
Simulated HPTAG	0.15813	5.64609e-05	1.83843e-04	0.15813
Analytical HPTAG	0.15811	3.75207e-05	1.84062e-04	0.15811
Factor Offset	1.000083	1.50479	0.99881	1.000083

digital filter. The gyro simulator is verified and validated, in accordance with the scheme outlined in Section 3.3.2.
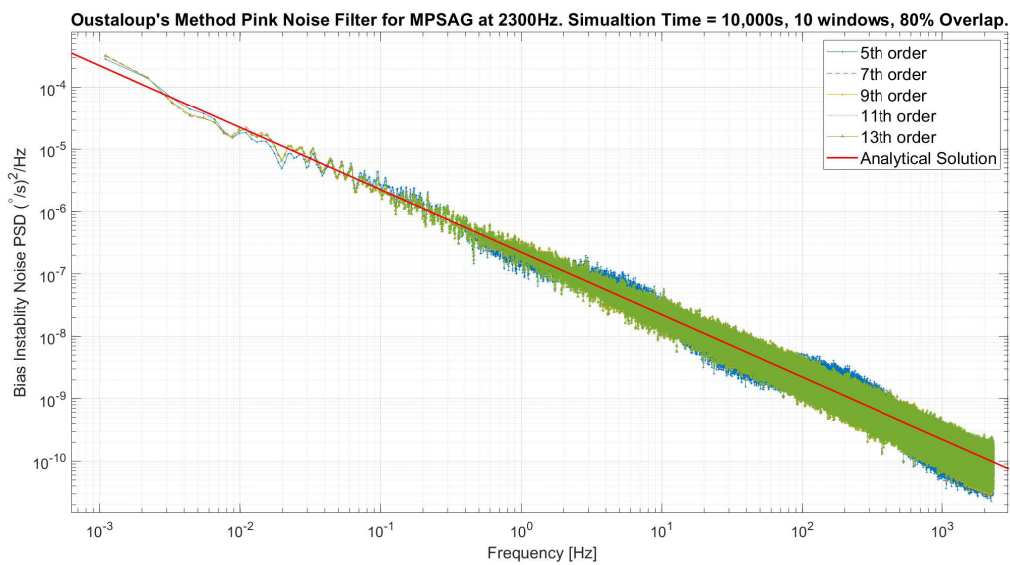
Figure 3.44: *Bias instability PSD behaviour of MPSAG with Oustaloup's method.*
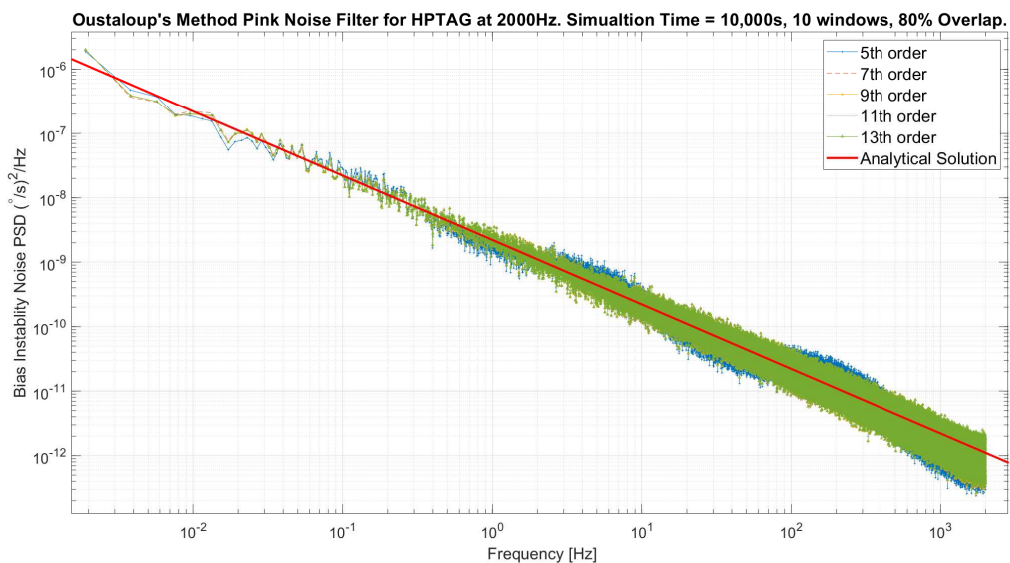
Figure 3.45: *Bias instability PSD behaviour of HPTAG with Oustaloup's method.*
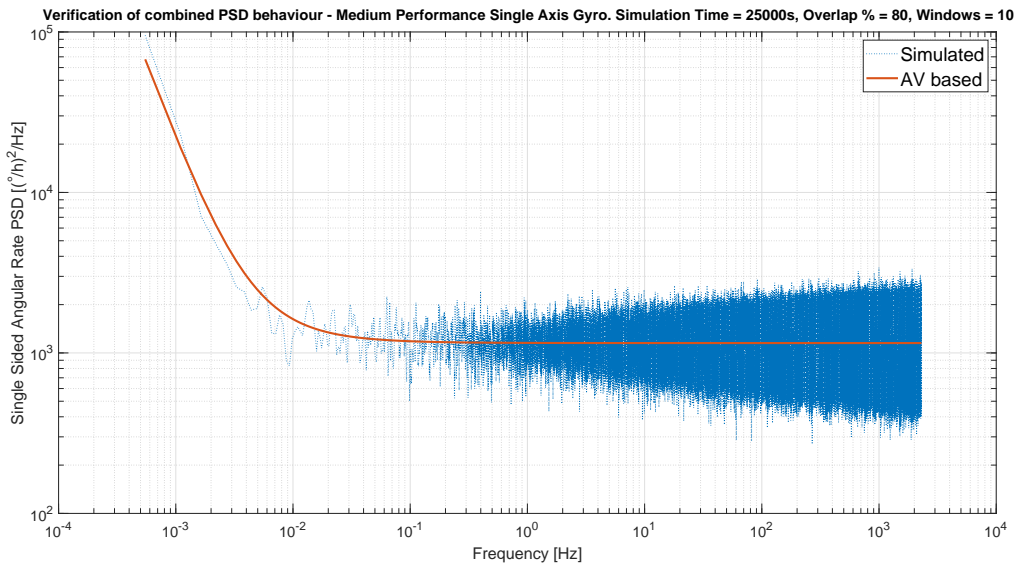
Figure 3.46: *Noise PSD behaviour verification of the gyro output with all noise elements combined for Mid Performance Single Axis Gyro with Oustaloup's method for bias instability.*
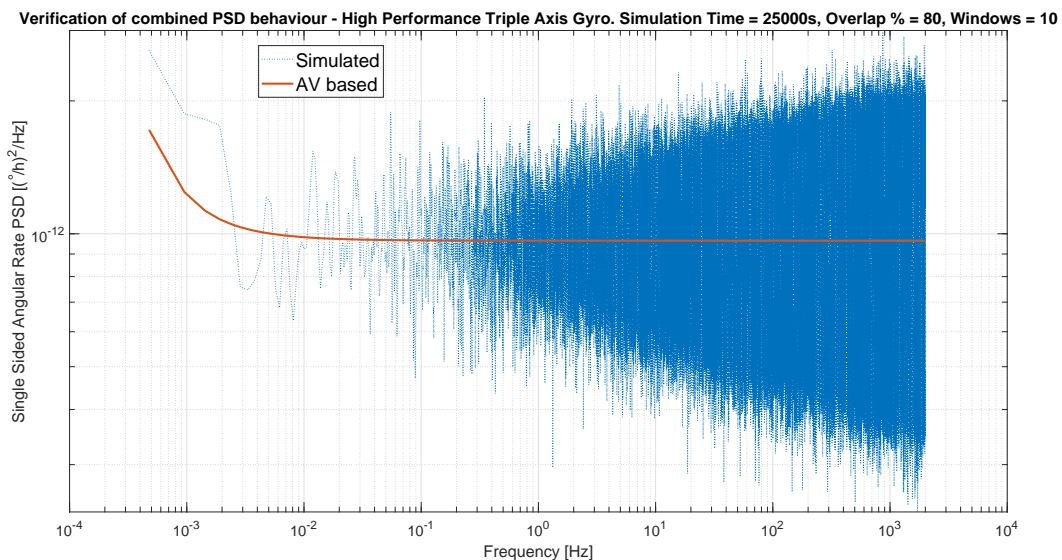
Figure 3.47: *Noise PSD behaviour verification of the gyro output with all noise elements combined for High Performance Triple Axis Gyro with Oustaloup's method for bias instability.*

3.5 | **Subsampling Gyro Output**

Running the calibration filter at the operational rate of the MEMS gyros is unreasonable, since the manoeuvres that a satellite undergoes are of significantly lower frequencies. An angular rate of 3 deg/s, represents a rate of change of angular motion at 0.0083Hz. While the internal operational frequency of HPTAG is 2000Hz and that of MPSAG is 2300Hz. As a consequence it is important to subsample the gyros with a filter that introduces little noise after the cut-off frequency of interest. Ideally, a sinc filter would result in perfect signal upto the cut-off frequency of interest; however, in practice it is non-causal and has infinite delay. As a consequence, Butterworth and Legendre-Papoulis filters are investigated. Normalized polynomials for a Butterworth filter can be expressed as:

$$H(s) = \frac{G_0}{B_n(a)}, \text{ where } a = \frac{s}{\omega_c} \tag{3.45a}$$

G_0 denotes the DC gain, and ω_c the cut-off frequency. While the even and odd polynomials can be expressed as:

$$B_n(s) = \prod_{k=1}^{\frac{n}{2}} \left[s^2 - 2s \cos \left(\frac{2k + n - 1}{2n} \pi \right) + 1 \right] \quad n = \text{ even} \tag{3.45b}$$

$$B_n(s) = (s + 1) \prod_{k=1}^{\frac{n-1}{2}} \left[s^2 - 2s \cos \left(\frac{2k + n - 1}{2n} \pi \right) + 1 \right] \quad n = \text{ odd} \tag{3.45c}$$

Utilising the above expressions, third and fourth order Butterworth filter can be expressed as:

$$H_{B3}(s) = \frac{1}{\left(\frac{s}{\omega_c} + 1 \right) \left(\left(\frac{s}{\omega_c} \right)^2 + \frac{s}{\omega_c} + 1 \right)} \tag{3.46a}$$

$$H_{B4}(s) = \frac{1}{\left(\left(\frac{s}{\omega_c} \right)^2 + 0.7654 \frac{s}{\omega_c} + 1 \right) \left(\left(\frac{s}{\omega_c} \right)^2 + 1.8478 \frac{s}{\omega_c} + 1 \right)} \tag{3.46b}$$

Similarly, Legendre-Papoulis (Optimal-"L") Filter (Bond, 2011) is characterised by Legendre Polynomials. Legendre polynomial functions of the first kind can be expressed as:

$$P_0(x) = 1 \quad \text{for i = 0} \tag{3.47a}$$

$$P_1(x) = x \quad \text{for i = 1} \tag{3.47b}$$

$$P_i(x) = \frac{(2 \cdot i - 1) \cdot x \cdot P_{i-1}(x) - (i - 1) \cdot P_{i-2}(x)}{i} \quad \text{otherwise} \tag{3.47c}$$

Above presented Legendre polynomial of the first kind can be used as a basis for Optimal-"L" filter polynomials, L_n, which is not the same as the Legendre Polynomials from which they are derived. For odd L_n polynomial:

$$L_n \left(\omega_n^2 \right) = \int_{-1}^{2 \cdot \omega_n - 1} \left(\sum_{i=0}^{k} a_i \cdot P_i(x) \right)^2 dx \tag{3.48a}$$

$$a_i \triangleq \frac{2 \cdot i + 1}{\sqrt{2} \cdot (k + 1)}, \quad \text{where } k = \frac{n - 1}{2} \tag{3.48b}$$

Here $\omega_n \triangleq \frac{\omega}{\omega_{3\text{dB}}}$, where $\omega_{3\text{dB}} = 2 \cdot \pi \cdot f_{3\text{dB}}$. For even L_n polynomial:

$$L_n \left(\omega_n^2 \right) = \int_{-1}^{2 \cdot \omega_n - 1} (x + 1) \cdot \left(\sum_{i=0}^{k} a_i \cdot P_i(x) \right)^2 dx \tag{3.49a}$$

$$a_i \triangleq \frac{2 \cdot i + 1}{\sqrt{(k + 1) \cdot (k + 2)}}, \quad \text{where, i is even. 0 otherwise. And } k = \frac{n - 2}{2} \tag{3.49b}$$

Magnitude response of any low-pass, all pole filter is given by:

$$M(\omega) = \frac{K_0}{\sqrt{1 + f \left(\omega^2 \right)}} \tag{3.50}$$

L_n polynomials form the desired filters from the rational function:

$$M^2(\omega) = \frac{1}{1 + L_n \left(\omega^2 \right)} \tag{3.51}$$

Here, n is the filter order. Magnitude squared function can be translated to the s-plane utilising the following relations $s = j\omega$, $s^2 = -\omega^2$. This leads to the following filter transfer function that can be utilised to construct Legendre-Papoulis filter:

$$h \left(s^2 \right) = H(s)H(-s) = \frac{1}{1 + L_n \left(-s^2 \right)} \tag{3.52}$$
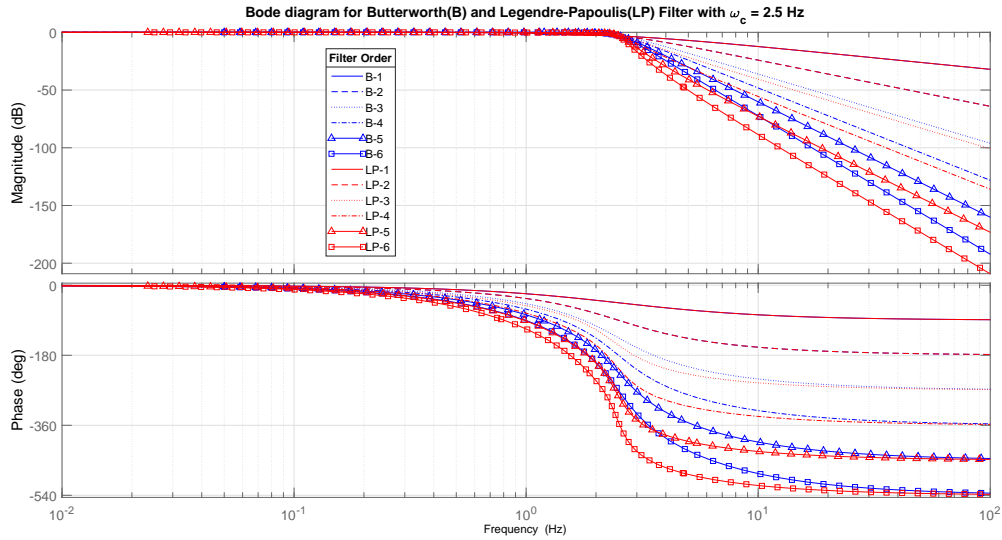
Figure 3.48: *Bode diagram comparison for Legendre-Papoulis and Butterworth filter, with cut-off frequency at ω_c = 2.5 Hz. Legendre-Papoulis demonstrates steeper roll-off after the cut-off frequency and low phase distortion.*

Table 3.15: *Verification of gyro output noise PSD with low pass filter, compared against analytical Allan-Variance based gyro rate output noise PSD.*

Combined Gyro Noise Standard Deviation [$^\circ/s$] Frequency Range [$6.10 \cdot 10^{-4}$ Hz to 2.5 Hz] Filter cut-off frequency at 2.5 Hz	Order 1	Order 2	Order 3	Order 4	Order 5	Order 6
Analytical MPSAG sampled at 2300 Hz			0.0	1499		
Simulated MPSAG with Butterworth Filter Sampled at 5 Hz	0.01890	0.01596	0.01548	0.01537	0.01533	0.01487
Factor offset	1.2609	1.0646	1.0328	1.0256	1.0229	0.9917
Simulated MPSAG with Legendre-Papoulis Filter Sampled at 5 Hz	0.01890	0.01596	0.01505	0.01501	0.01486	0.01487
Factor offset	1.2609	1.0646	1.0042	1.0016	0.9912	0.9917

Utilising the above expressions, third and fourth order Optimum-"L" filter can be expressed as:

$$H_{LP3}(s) = \frac{1}{\left(\frac{s}{\omega_c} + 0.6203\right) \cdot \left(\left(\frac{s}{\omega_c}\right)^2 + 0.6904 \cdot \frac{s}{\omega_c} + 0.9308\right)} \tag{3.53a}$$

$$H_{LP4}(s) = \frac{1}{\left(\left(\frac{s}{\omega_c}\right)^2 + 1.0994 \cdot \frac{s}{\omega_c} + 0.4308\right) \cdot \left(\left(\frac{s}{\omega_c}\right)^2 + 0.4634 \cdot \frac{s}{\omega_c} + 0.9477\right)} \tag{3.53b}$$

Figure 3.48 compares the Bode plots magnitude and phase response for Legendre-Papoulis and Butterworth filter, with cut-off frequency of ω_c = 2.5 Hz. For verification of the gyro signal after subsampling with the above synthesized low pass filters, a PSD based approach is chosen. Gyro signal output of the MPSAG gyro is passed through low pass filters, and later PSD of the subsampled gyro signal is compared against the ideal PSD slope obtained earlier with the Allan-Variance analysis. Figure 3.49, demonstrates that both Butterworth and Legendre-Papoulis, has near-identical performance. First and second order low pass filters distort the signal noise spectrum. While third order onward, both Butterworth and Legendre-Papoulis filters can be utilised. Table 3.15, summarises the verification of the quantitative metrics of the sub-sampled gyro noise processes. A pole-zero map of the third and fourth order Butterworth and Legendre-Papoulis filter is presented with the aid of Figure 3.50. Underlying filter expressions were presented earlier with the aid of Equations (3.46) and (3.53). A fourth order Legendre-Papoulis filter is utilised for filtering the signals, as it has both a relatively steeper roll-off after the cut-off frequency, and lower phase distortion.

In order to evaluate the impact of gyro sampling rate on the attitude filter output, the gyro output is subsampled at 5Hz and 100Hz. Previous analysis explained the gyro subsampling of 5Hz with a cut-off of 2.5Hz. Similarly, a 4th order

Single Sided Angular Rate PSD Behaviour with Legendre-Papoulis and Butterworth Low Pass Filter, ω_c= 2.5 Hz
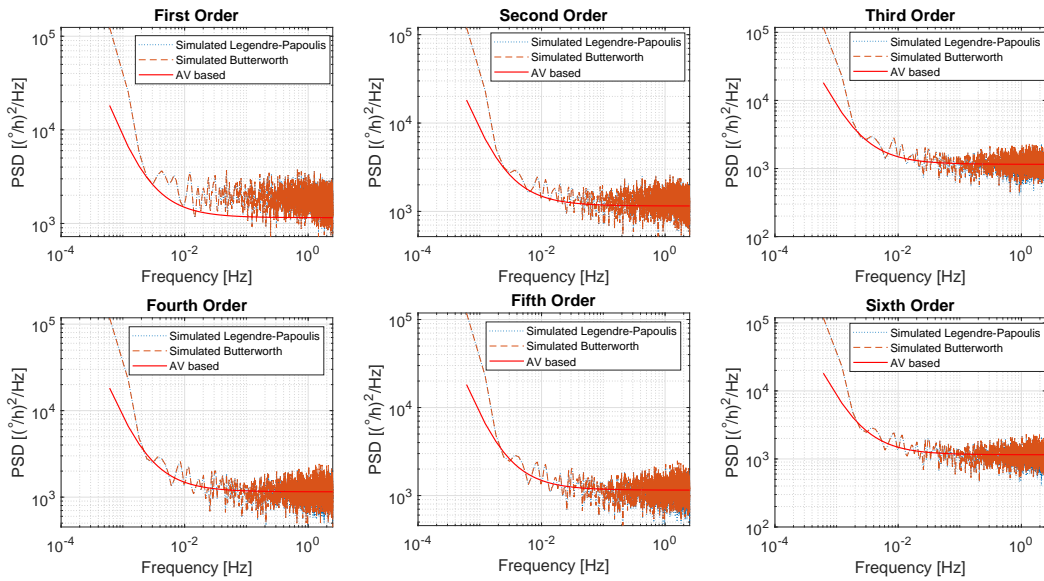
Figure 3.49: *Single sided attitude rate PSD for Mid Performance Single Axis Gyro (MPSAG) after sub-sampling at 5Hz with Legendre-Papoulis and Butterworth low pass filters with cut-off frequency at ω_c= 2.5 Hz. Gyro simulator run at 4600 Hz, for a simulation time of 10,000s, Gyro sampled at 2300 Hz. PSD is conducted with 10 windows, and 80% overlap between window segments.*

Figure 3.50: *Pole zero map comparing 3rd and 4th order Butterworth and Legendre-Papoulis (Optimum-"L") low pass filter.*

Legendre-Papoulis filter with a cut-off frequency ω_c at 50Hz is employed to sub-sample the gyros to 100Hz.Figure 3.51 visually verifies the gyro output noise PSD against the expected PSD constructed based on Allan Variance analysis.
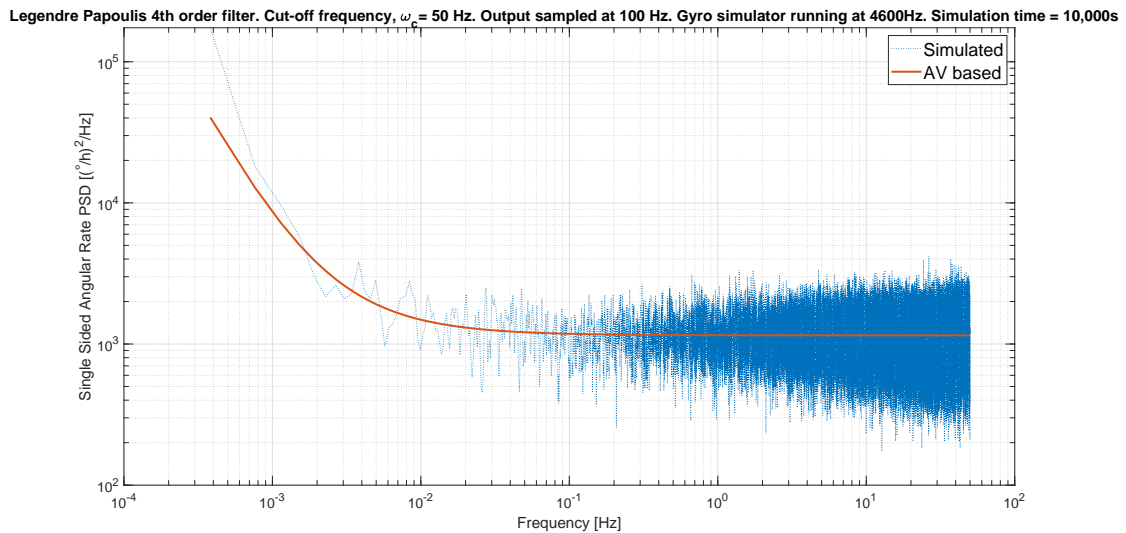
Figure 3.51: *Single sided attitude rate noise PSD for MPSAG after sub-sampling with Legendre-Papoulis Filter of 4th order, verified against the expected attitude rate noise PSD based on Allan-Variance analysis. The filter is synthesized with a cut-off frequency of 50Hz, and the gyro output is sampled at 100Hz. The gyro simulator is run for 10,000s at 2x2300Hz, to capture gyro operational dynamics at 2300Hz.*
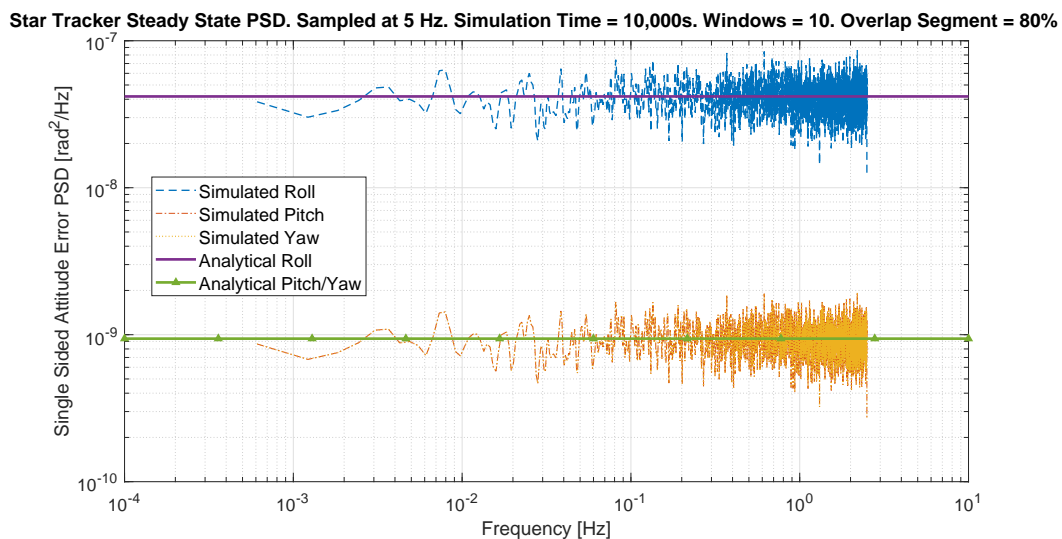
Figure 3.52: *PSD verification of the simplified ST200 star tracker simulator compared against the expected analytical ST200 PSD.*

3.6 | **Star Tracker Sensor Noise Model Definition and Verification**

ST200 from Hyperion Technologies is utilised for the attitude knowledge acquisition. Star tracker is a complex system, characterisation of which is beyond the scope of this thesis work. Simplified assumptions are made to model the star tracker noise behaviour. Star tracker noise is modelled with uniform band-limited white-noise; such that the area under the star tracker single-sided attitude noise PSD upto the Nyquist frequency of the star tracker sampling rate, matches the 1σ attitude error as presented earlier in Table 2.3. Noise is added on the nominal Euler321, Yaw-Pitch-Roll angles, before parameterising the Euler 321 coordinates into quaternion coordinates. Star tracker quaternion output is then fed into the attitude estimator. Figure 3.52 provides verification of the star tracker steady-steady Euler output noise single-sided PSD, against the expected uniform distribution to match the 1σ attitude error. Table 3.16 quantifies the expected output noise PSD against the observed noise PSD for verification.

Table 3.16: *Verification of expected analytical standard deviation of ST200 star tracker, and standard deviation obtained from PSD on simulated time series.*

ST200 sampled at 5 Hz Nyquist Frequency at 2.5 Hz	Roll [rad, 1σ]	Pitch/Yaw [rad, 1σ]
Analytical standard deviation	3.2321e-04	4.8481e-05
Simulated PSD based standard deviation	3.2270e-04	4.8406e-05
Factor offset	1.0016	1.0016
Percentage offset	0.1560	0.1560

3.7 | Summary and Conclusions

This chapter focused on three core segments: 1. Defining and characterising all possible sensor induced error sources. In that regard, the random noise errors that establish the physical noise floor of the chosen sensors are analysed in a decoupled manner from the systematic errors that the calibration filter is expected to observe and eliminate. Models for rate gyro random noise errors are presented. Systematic gyro error models, for utilisation in a calibration filter, are derived.

2. Random noise errors are characterised for four different types of MEMS rate gyros by Allan-Variance analysis. Seven different MEMS gyro cluster configurations are presented, aimed at reducing the random noise error floor. Attitude error noise floor of gyro-stellar hybridisation and gyro only dead-reckoning, in the event of star tracker loss and in between calibration filter updates, is analysed by virtue of single sided attitude error PSD analysis.

3. Noise models for the chosen gyros are simulated and verified against PSD curves analytically derived earlier from Allan-Variance analysis. In that regard, a digital filter based on power series expansion of backward scheme, and a continuous time rational transfer function based on Oustaloup's method is investigated to capture the bias instability of the gyros. These gyro noise models can be implemented on the rigid body NanoSat simulator, to simulate the noisy gyro angular rate output. This noisy gyro output is superimposed with systematic errors before feeding it into the calibration filter.

Based on the analysis presented in this segment, two main configurations are of primary interest to meet the expected attitude knowledge requirements under agile slewing conditions: three Medium Performance Single Axis Gyros (MPSAG) with two ST200 NanoSat class of star trackers; and one High Performance Triple Axis Gyro (HPTAG) with two ST200 NanoSat class of star trackers. Two star trackers are necessary to avoid occulation effects, and to compensate for the low performance boresight which is typical for NanoSat class of star trackers. It was observed that if the the High Performance Triple Axis Gyro is calibrated for systematic errors, the physical noise floor alone can easily satisfy the attitude knowledge requirement under dead-reckoning mode in the event of star loss at 1.5 minute benchmark. However for MPSAG, this is well below 30 seconds. Nevertheless, calibration filter proposed is a relative calibration filter. To ensure full observability of the calibration states, three rotational misalignment of the reference sensor is discarded. Gyros are often chosen as the main reference sensors due to the high availability and no occultation losses. As a consequence, three gyro sense axes proposed as the preliminary choice of interest might not deliver the required attitude knowledge performance. As a secondary choice of interest, Configuration 6 (which is comprised of six MPSAG and two NanoSat star trackers, 2 sense axes/axis) and Configuration 7 (which is comprised of two HPTAG and two NanoSat star trackers, 2 sense axes/axis) are proposed. Secondary configuration choices are expected to provide better attitude knowledge output by lowering the physical noise floor. Even if the three rotational misalignment calibration states are discarded from gyro sense axis for observability considerations, the other three gyro rotational misalignments for the remaining three gyro sense axes are observed. This shall allow the calibration filter to meet the expected attitude knowledge performances. Furthermore, this facilitates system redundancy and the capability of fault-tolerance by tracking scale factor errors with calibration filters. However, the increased gyro cluster size comes at the expense of increased power consumption and higher calibration filter computational burden.

Rigid Body NanoSat Simulator

The objective of this chapter is to lay down the framework that enables generation of attitude and angular rate motion required for calibration manoeuvre, and ground target tracking. In that regard, this chapter can be split into three distinctive segments: The first segment is aimed at outlining the mathematical fundamentals required to construct the rigid body simulator, sensor models, and kinematic relations in the filter. The second segment is dedicated to outlining the rigid body simulator and its underlying working principles. Manoeuvres for calibration, and ground target tracking are further discussed. The third segment is dedicated to defining the sensor models used to read out attitude/attitude rate, and finally the output generated by rigid body simulator that is fed into the filters synthesized in Chapter 5.

First the coordinate frames involved in synthesizing the flight kinematics and dynamics are defined in Section 4.1. Though perceptually Euler-321, otherwise known as Yaw-Pitch-Roll, is favourable for coordinate parametrisation; mathematically it poses limitations associated with continuous tracking. As a consequence Section 4.2 aims at defining the different coordinate parametrisations utilised to compensate for the deficiency imposed by other forms of parametrisations. Section 4.3 aims at presenting the rigid body kinematics and dynamics in different coordinate parametrisations.

A brief overview of the rigid body flight controller synthesized in MRP parametrisation is presented in Appendix C. Calibration and ground target tracking manoeuvres are defined in Section 4.5. Reaction wheel torque output capability, and the consequent torque input-output delay relation is established in Section 4.4; to evaluate the feasibility of tracking ground station with the controllers synthesised and limitations imposed by the reaction wheels. Interface of the rigid body simulator and the calibration filter is discussed in Section 4.6.

Sensor models utilised to read out the ideal signals, is described in Section 4.7. Attitude and attitude rate output signal generated by the rigid body simulator, for use as filter input, is discussed in Section 4.8.

4.1 | Coordinate Reference Frame

The objective of this section is to lay down the respective coordinate frameworks required to formulate the kinematics and dynamics of a spacecraft orbiting a central body in space. In order to express and manipulate the orientation of a satellite, different frames of references are required to derive flight kinematics and dynamics. This section aims at outlining the coordinate reference frames involved in the formulation of a ground-station tracking problem. For modelling the attitude of a body in orbit around Earth, there are four main frames of references involved: Earth centred inertial reference frame (ECI, $\mathcal{F}_\mathcal{I}$), local vertical local horizontal reference frame (LVLH, $\mathcal{F}_\mathcal{V}$), and the spacecraft body reference frame ($\mathcal{F}_\mathcal{B}$). If the flight controller is tracking a ground-station at a given latitude and longitude then Earth centred Earth fixed or rotating planetocentric frame of reference (ECEF, $\mathcal{F}_\mathcal{R}$) is used to generate the guidance laws. It is important to note that all coordinate systems used for this project are right handed coordinate systems. An inertial reference frame is a frame in which Newton's laws of motion are valid. Any frame moving with constant velocity and without rotation w.r.t. to an inertial reference frame is also inertial (Goldstein, 1980).

Earth Centred Earth Fixed ECEF

A geocentric coordinate system fixed to the rotation Earth results in a body-fixed (BF) or International Terrestial Reference Frame (ITRF) coordinate system. The origin is at the centre of Earth and the axes are realised by the adopted coordinates of defining stations on the Earth's surface. Because the stations are affected by plate tectonic motion ($\approx$cm/yr), ITRF is estimated regularly. Confusion might exist since ITRF is often known as ECEF. The term "Earth-fixed" describes a terrestrial reference system whose net global orientation remains unchanged over time with respect to the crust of the Earth. The U.S. Air Force Space Command has historically reserved the term "Earth-Fixed Greenwich frame, EFG" for the (rotating) pseudo-body fixed frame (no polar motion), and used "Earth-centred rotating, ECR" to describe the Earth-fixed ITRF, ECEF (Vallado, 2013). Axes of ECEF are aligned with the International
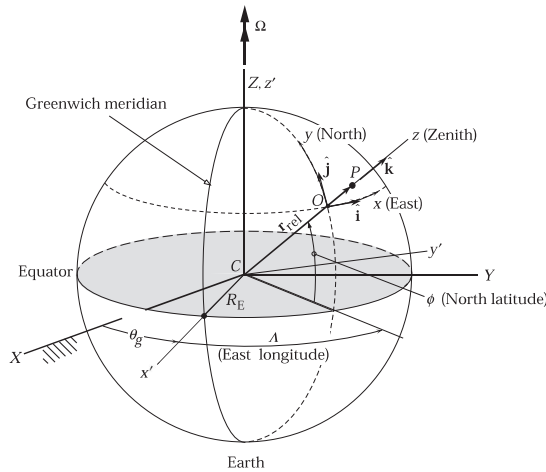
Figure 4.1: *Earth centred Inertial reference frame indicated by XYZ.*
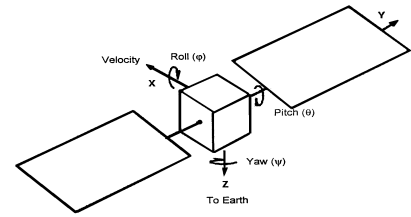
Figure 4.2: *Spacecraft body reference frame definition.*

Reference Pole (IRP) and International Reference Meridian (IRM), these are fixed with respect to the Earth's surface. The z-axis points to the true north, which is not co-incident with the Earth's instantaneous rotational axis. This leads to slight wobbling known as polar motion. The x-axis intersects the 0° latitude(equator) and 0° longitude (prime meridian, Greenwich) (Vallado, 2013). This makes the ECEF rotate with the Earth, hence coordinates of a fixed point on the surface of the Earth do not change wrt the ECEF (Montenbruck et al., 2000) (DoD WGS84, 2000). This coordinate frame is important for generating guidance law for ground-station tracking (Chen et al., 2000a).

Earth Centred Inertial ECI

Earth centred Inertial reference frame $\mathcal{F}_{\mathcal{I}}$ is a pseudo or quasi inertial coordinate frame where the main influence of non-inertial acceleration is due to the gravitational acceleration between the Sun and the Earth. Nevertheless, for most applications involving spacecraft orbiting Earth, it can be used as the inertial reference frame. ECI is one of the most common, yet the most confusing coordinate frames of reference (Vallado, 2013). There are five different types of often used ECI reference frames, namely J2000[1], M50, Geocentric Celestial Reference Frame (GCRF), Mean of Date (MOD) frame and True Equator - Mean Equinox (TEME). For satellite attitude control often J2000 ECI and TEME ECI is used. For J2000 ECI the origin O_{ECI} is placed at the centre of Earth. X_{ECI} lies in the equatorial plane along the intersection with the ecliptic plane towards the direction of the Sun's apparent motion ascending node. This direction is also known as the direction of Aries or Vernal Equinox. TEME ECI is used for the NORAD two line elements, it does not use the conventional mean equinox. It is used when orbits are propagated with the aid of SGP4 orbit propagator. Conversion between J2000 and TEME can be found in (Vallado, 2013). For further information interested readers are referred to (Mazzini, 2016) (Meeus, 1998) (Goldstein, 1980). Figure 4.1 outlines the Earth centred Inertial reference frame. Since this is the inertial reference frame, it is of core importance for generating guidance law, and tracking the motion of remaining frames of reference. It is also used to define LVLH frame, and the gravity gradient torque direction on the spacecraft dynamics.

Local Vertical Local Horizontal LVLH

Local Vertical and Local Horizontal coordinate frame is centred at the CoM of the spacecraft, which in this case coincides with origin of the $\mathcal{F}_{\mathcal{B}}$. The LVLH frame is outlined with the aid of Figure 4.3, in conjunction with $\mathcal{F}_{\mathcal{B}}$ and $\mathcal{F}_{\mathcal{I}}$. The X-Z plane of the coordinate system lies in the orbit ecliptic, while the Y axis points is $\perp$ the orbit ecliptic in line with the right hand coordinate system. Y axis is $\parallel$ the angular momentum vector of the orbit. The LVLH frame has a mean motion equivalent to the orbital period of the spacecraft orbiting the planet(Markley and Crassidis, 2014). This frame of reference is important for gravity gradient torque implementation. LVLH is also the frame with respect to which the angular displacement of the spacecraft body axis are controlled for Nadir pointing satellite mission.

Spacecraft Body Reference Frame

There are two ways of looking at the spacecraft body fixed reference frame. The first one is in line with Sylvester's law of inertia, such that the origin of the frame is placed that the centre of Mass (CoM) and the axes aligned with

---

[1]The epoch J2000 corresponds to January 1, 2000 at 11:58:55.816 UTC
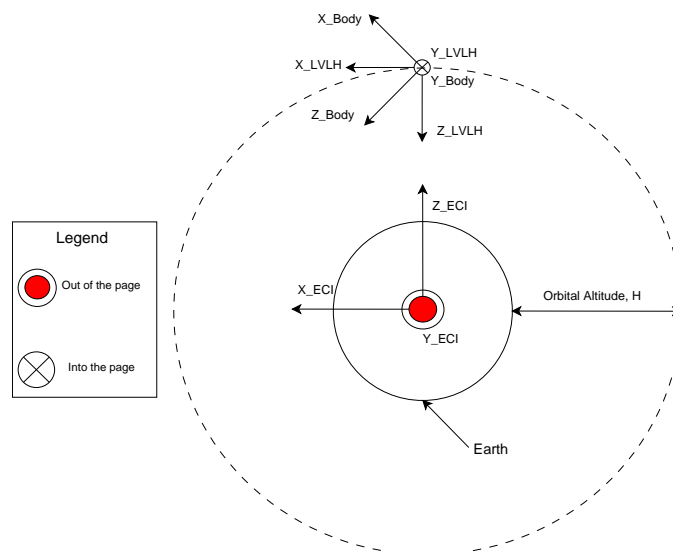
Figure 4.3: *LVLH frame in collaboration with ECI and spacecraft body reference frame.*

the principal axes of inertia. The second form is aligned with the spacecraft body axis such that, if the spacecraft is perfectly nadir pointing and undergoing a circular orbit, the nadir axis is the Z axis, the velocity of the spacecraft is along X axis, and Y axis is perpendicular to X and Z axis. The origin O_{Body} is at the CoM of the spacecraft. *"Assumption: Both the body frames outlined here are equivalent, i.e. the spacecraft has a Moment of Inertia (MoI) in the form of inertia tensor."*. Figure 4.2 outlines the spacecraft body axis (Chu, 2018). Figure 4.3 outlines $\mathcal{F}_{\mathcal{B}}$, in conjunction with $\mathcal{F}_{\mathcal{V}}$ and $\mathcal{F}_{\mathcal{I}}$. Flight controllers are usually designed in the spacecraft body fixed reference frame. All control actions and internal/external disturbance torques on the spacecraft are applied in $\mathcal{F}_{\mathcal{B}}$.

4.2 | Coordinate Parametrisation

The objective of this section is to provide an overview of the different types of coordinate parametrisations involved in describing the orientation, in turn the kinematics and dynamics of a satellite in space. Transformations from one type of coordinate parametrisation to another type, and the justifications for the use and limitations of different form of parametrisations are further outlined. A summary of the different type of parametrisations and their properties are presented in Table 4.1. First the Euler parameters are described for orientation representation. Later the notion of Directional Cosine Matrix (DCM), also known as Special Orthogonal SO(3) group is introduced. To avoid singularities in the Euler kinematic representation of the satellite attitude in orbit, quaternions are introduced. quaternions provide a good solution for avoiding singularities, however they impose limitations on continuous attitude estimation and tracking. This is of concern for large attitude slew manoeuvres, when the "unwinding phenomena" is encountered (Chaturvedi et al., 2011). Finally to facilitate continuous large attitude manoeuvres, Modified Rodrigues Parameters (MRP) are presented.

4.2.1 | Definitions

Euler Angles

Euler angles are the most commonly used attitude angles. They describe the orientation of one reference frame with respect to another frame. The underlying basis of Euler rotations is to undergo sequential rotations around each axis to achieve a desired orientation. There are twelve possible rotation sequences, divided into two groups *Proper Euler angles* and *Trait-Bryan angles*. It is the Euler 3-2-1 rotation sequence that is mostly used for spacecraft and aircraft attitude determination and control problems. The rotation sequence is also known as the Yaw (Ψ)-Pitch(θ)-Roll(ϕ) sequence. Where yaw is the motion around Z_{Body} axis, pitch is the motion around Y_{Body} axis and roll is the motion around X_{Body} axis. Different literature refer to the θ parameters differently. Some refer to [θ_1, θ_2, θ_3] as the Yaw-Pitch-Roll sequence, while others refer them to Roll-Pitch-Yaw sequence. For the derivations outlined in this report the nomenclature outlined in Table 4.2 is used. Euler 3-1-3 angles is asymmetric set, while Euler 3-2-1 is a symmetric set. The former, though quite common in the aerospace domain, is mostly used by astronomers to define the orientation of planetary orbital planes relative to Earth orbital planes (Schaub and Junkins, 2002). For brevity elements of Euler 3-2-1 sequences that influence the spacecraft orientation problem are discussed here.

For Euler rotations between two reference frames with coinciding centres of origin, the Direction Cosine Matrix (DCM)

Table 4.1: *Summary of different coordinate parametrisation (Bandyopadhyay et al., 2015, Chaturvedi et al., 2011).*

Attitude Representation	Range, Transformation	Global?	Unique?
Euler Angles	$\phi, \theta, \psi \in [-\pi, \pi]$	No. Singularity at $\theta = \pm\pi/2$	No.
Euler Axis of Rotation and Angle	$e \in \mathbb{S}^2, \Phi \in [-\pi, \pi]$	Yes	No. $e^S = -e$ $\Phi^S = 2\pi - \Phi$
Quaternions	$\boldsymbol{\beta} \in \mathbb{S}^3$ $\beta_i = e_i \sin\frac{\Phi}{2}, i \in \{1,2,3\}$ $\beta_4 = \cos\frac{\Phi}{2}$	Yes	No. $\left(\boldsymbol{\beta}^S = -\boldsymbol{\beta}\right)$
Classical Rodrigues Parameters (CRP)	$\boldsymbol{\sigma} \in \mathbb{R}^3$ $\boldsymbol{\sigma} = \boldsymbol{e} \tan\frac{\Phi}{2}$	No. Singularity at $\Phi = \pm\pi$	Yes
Modified Rodrigues Parameters (MRP)	$\boldsymbol{q} \in \mathbb{R}^3$ $\boldsymbol{q} = \boldsymbol{e} \tan\frac{\Phi}{4}$	No. Singularity at $\Phi = 2\pi$	No. $\boldsymbol{q}^S =$ $-e \tan\frac{2\pi - \Phi}{4}$
Rotation Matrix SO(3) or DCM	$\boldsymbol{R} \in \mathbb{R}^{3 \times 3}$ $\boldsymbol{R}\boldsymbol{R}^T = \mathbf{I}, \boldsymbol{R}^T\boldsymbol{R} = \mathbf{I}$ $\det(\boldsymbol{R}) = 1$	Yes	Yes

is of core interest for defining the kinematics and dynamics of spacecraft problem. DCM corresponding to the Euler 3-2-1 rotation sequence is outlined with the aid of Equation (4.1). DCM are also known as Special Orthogonal group or SO(3).

$$\mathbf{C}(\theta) = R_X(\theta_1) \cdot R_Y(\theta_2) \cdot R_Z(\theta_3) \tag{4.1a}$$

$$R_X(\theta_1) = \begin{bmatrix} 1 & 0 & 0 \\ 0 & \mathbf{c}\theta_1 & \mathbf{s}\theta_1 \\ 0 & -\mathbf{s}\theta_1 & \mathbf{c}\theta_1 \end{bmatrix} \tag{4.1b}$$

$$R_Y(\theta_2) = \begin{bmatrix} \mathbf{c}\theta_2 & 0 & -\mathbf{s}\theta_2 \\ 0 & 1 & 0 \\ \mathbf{s}\theta_2 & 0 & \mathbf{c}\theta_2 \end{bmatrix} \tag{4.1c}$$

$$R_Z(\theta_3) = \begin{bmatrix} \mathbf{c}\theta_3 & \mathbf{s}\theta_3 & 0 \\ -\mathbf{s}\theta_3 & \mathbf{c}\theta_3 & 0 \\ 0 & 0 & 1 \end{bmatrix} \tag{4.1d}$$

Thus the DCM matrix for Euler 3-2-1 sequence is:

$$\mathbf{C}(\theta) = \begin{bmatrix} \mathbf{c}\theta_2\mathbf{c}\theta_3 & \mathbf{c}\theta_2\mathbf{s}\theta_3 & -\mathbf{s}\theta_2 \\ \mathbf{s}\theta_1\mathbf{s}\theta_2\mathbf{c}\theta_3 - \mathbf{c}\theta_1\mathbf{s}\theta_3 & \mathbf{s}\theta_1\mathbf{s}\theta_2\mathbf{s}\theta_3 + \mathbf{c}\theta_1\mathbf{c}\theta_3 & \mathbf{s}\theta_1\mathbf{c}\theta_2 \\ \mathbf{c}\theta_1\mathbf{s}\theta_2\mathbf{c}\theta_3 + \mathbf{s}\theta_1\mathbf{s}\theta_3 & \mathbf{c}\theta_1\mathbf{s}\theta_2\mathbf{s}\theta_3 - \mathbf{s}\theta_1\mathbf{c}\theta_3 & \mathbf{c}\theta_1\mathbf{c}\theta_2 \end{bmatrix} \tag{4.1e}$$

$$\mathbf{C}(\theta) = \begin{bmatrix} C_{11} & C_{12} & C_{13} \\ C_{21} & C_{22} & C_{23} \\ C_{31} & C_{32} & C_{33} \end{bmatrix} \tag{4.1f}$$

Quaternion

Quaternions were introduced in spaceflight kinematics to avoid singularities seen by kinematics in Euler representation. Quaternion representation is global but not unique. To visualize quaternions, one has to understand the principle of "eigen axis rotation" and "Euler's formula".

Table 4.2: *Table outlining the definition of Euler 3-2-1 sequences under consideration.*

Axis of rotation	Nomenclature	θ nomenclature
X_{Body}	Roll - ϕ	θ_1
Y_{Body}	Pitch - θ	θ_2
Z_{Body}	Yaw - Ψ	θ_3

Previous section outlined Euler rotations as sequential rotation i.e. a rotation is conducted around each axis sequentially to achieve a desired orientation. However Euler sequential rotations can also be performed by a single rotation in physical space, this captures the notion of Euler eigen axis. Imagine a case of three rotations (yaw-pitch-roll) performed by a body in inertial space. In case of Euler, the body will first rotate around Z axis, followed by rotation around the new Y axis and finally a rotation around the new X axis. However in case of Euler's eigen axis rotation, there is an axis somewhere in the body, a single rotation around this axis would achieve the same final orientation result. This single rotation around the eigen axis to change the orientation of a rigid body is both the time and energy optimal attitude manoeuvre. Interested readers can visualise it further using Stanford's Euler Rotation Theorem visualisation [(2)].

Euler's formula, as shown in Equation ([4.2]), facilitates rotation of a vector in a 2D plane (X - axis real number, Y - axis imaginary number). For a vector (x + y ·i) in the 2D plane, a rotation of the vector by θ degrees, is simply the multiplication of the Euler's formula with the vector.

$$e^{i\theta} = \cos\theta + i \cdot \sin\theta \tag{4.2}$$

Euler's formula for rotation can be extended to three dimensional spaces. quaternions capture this rotation in a four number coordinate system. A scalar part and a vector part. The scalar part is connected to the rotation around the eigenaxis, often denoted as q_0 or q_4 in the literature. While the vector part of quaternions, $[q_1, q_2, q_3]^T$, outline a unit vector in the direction of eigen axis of rotation. This is outlined with the aid of Equation ([4.3]). Furthermore, quaternion coordinates are restricted to move on the surface of a unit sphere, this defines the unity constraint in quaternions representation of spacecraft attitude problem.

$$q_1 = e_1 \cdot \sin\frac{\theta}{2} \tag{4.3a}$$

$$q_2 = e_2 \cdot \sin\frac{\theta}{2} \tag{4.3b}$$

$$q_3 = e_3 \cdot \sin\frac{\theta}{2} \tag{4.3c}$$

$$q_4 = \cos\frac{\theta}{2} \tag{4.3d}$$

$$\mathbf{q} \cdot \mathbf{q}^T = 1 \tag{4.3e}$$

Relation between Euler and quaternion is presented with the aid of Equation ([4.4]).

$$\begin{pmatrix} q_1 \\ q_2 \\ q_3 \\ q_4 \end{pmatrix} = \begin{pmatrix} \mathbf{s}\frac{\theta_1}{2}\mathbf{c}\frac{\theta_2}{2}\mathbf{c}\frac{\theta_3}{2} - \mathbf{c}\frac{\theta_1}{2}\mathbf{s}\frac{\theta_2}{2}\mathbf{s}\frac{\theta_3}{2} \\ \mathbf{c}\frac{\theta_1}{2}\mathbf{s}\frac{\theta_2}{2}\mathbf{c}\frac{\theta_3}{2} + \mathbf{s}\frac{\theta_1}{2}\mathbf{c}\frac{\theta_2}{2}\mathbf{s}\frac{\theta_3}{2} \\ \mathbf{c}\frac{\theta_1}{2}\mathbf{c}\frac{\theta_2}{2}\mathbf{s}\frac{\theta_3}{2} - \mathbf{s}\frac{\theta_1}{2}\mathbf{s}\frac{\theta_2}{2}\mathbf{c}\frac{\theta_3}{2} \\ \mathbf{c}\frac{\theta_1}{2}\mathbf{c}\frac{\theta_2}{2}\mathbf{c}\frac{\theta_3}{2} + \mathbf{s}\frac{\theta_1}{2}\mathbf{s}\frac{\theta_2}{2}\mathbf{s}\frac{\theta_3}{2} \end{pmatrix} \tag{4.4}$$

For visualisation one might be interested in converting quaternions back to Euler 3-2-1 rotation sequence. This can be achieved with the aid of Equation ([4.5]) ([Blanco], 2013). However, one must note that this has clipping effect at 180°. A quaternion discriminant is defined as:

$$\Delta_q = q_4 q_2 - q_1 q_3 \tag{4.5a}$$

When, $|\Delta_q| < \frac{1}{2}$

$$\theta_1 = \tan^{-1}\frac{2 \cdot (q_2 \cdot q_3 + q_1 \cdot q_4)}{q_4 \cdot q_4 - q_1 \cdot q_1 - q_2 \cdot q_2 + q_3 \cdot q_3} \tag{4.5b}$$

$$\theta_2 = -2\sin^{-1}(q_1 \cdot q_3 - q_2 \cdot q_4) \tag{4.5c}$$

$$\theta_3 = 2\tan^{-1}\frac{(q_1 \cdot q_2 + q_3 \cdot q_4)}{q_4 \cdot q_4 + q_1 \cdot q_1 - q_2 \cdot q_2 - q_3 \cdot q_3} \tag{4.5d}$$

While, for $|\Delta| \approx \frac{1}{2}$ and, $\Delta_q = \frac{-1}{2}$

$$\theta_3 = 2\tan^{-1}\left(\frac{q_1}{q_4}\right), \quad \theta_2 = -\pi/2, \quad \theta_1 = 0 \tag{4.5e}$$

[(2)]Visualisation Euler eigen axis rotation: https://web.stanford.edu/~ajdunl2/so3/so3.html

While, for $|\Delta| \approx \frac{1}{2}$ and, $\Delta_q = \frac{1}{2}$

$$\theta_3 = -2\tan^{-1}\left(\frac{q_1}{q_4}\right), \quad \theta_2 = \pi/2, \quad \theta_1 = 0 \tag{4.5f}$$

Euler's formula when extended to three dimension can be seen as rotations with quaternions. Where to rotate vector $\mathbf{p}$, through angle θ, to a new orientation $\mathbf{p}'$, the sequence outlined in Equation (4.6) is followed.

$$\mathbf{p}' = \mathbf{q} \cdot \mathbf{p} \cdot \mathbf{q}^{-1} \tag{4.6a}$$

$$\mathbf{q} = e^{\frac{\theta}{2}(e_1\bar{i} + e_2\bar{j} + e_3\bar{k})} = \cos\frac{\theta}{2} + \sin\frac{\theta}{2} \cdot (e_1 \cdot \bar{i} + e_1 \cdot \bar{j} + e_1 \cdot \bar{k}) \tag{4.6b}$$

$$\mathbf{q}^{-1} = e^{-\frac{\theta}{2}(e_1\bar{i} + e_2\bar{j} + e_3\bar{k})} = \cos\frac{\theta}{2} - \sin\frac{\theta}{2} \cdot (e_1 \cdot \bar{i} + e_1 \cdot \bar{j} + e_1 \cdot \bar{k}) \tag{4.6c}$$

Here, $\mathbf{q}^{-1}$ = $\mathbf{q}^*$, is the quaternion conjugate pair or inverse quaternion. This is equivalent to inverse rotation. The notion of inverse quaternion being equivalent to conjugate quaternion, is only true for unit quaternions. The unit quaternion rotation expressed in Equation (4.6) can be expressed in terms of a matrix rotation. This leads to the DCM representation in terms of quaternions. DCM in terms of unit quaternion, $\mathbf{C}(\mathbf{q})$, can be expressed as (Wie, 1998):

$$\mathbf{C}(\mathbf{q}) = \begin{bmatrix} 1 - 2\left(q_2^2 + q_3^2\right) & 2\left(q_1q_2 + q_3q_4\right) & 2\left(q_1q_3 - q_2q_4\right) \\ 2\left(q_2q_1 - q_3q_4\right) & 1 - 2\left(q_1^2 + q_3^2\right) & 2\left(q_2q_3 + q_1q_4\right) \\ 2\left(q_3q_1 + q_2q_4\right) & 2\left(q_3q_2 - q_1q_4\right) & 1 - 2\left(q_1^2 + q_2^2\right) \end{bmatrix} \tag{4.7}$$

The $\mathbf{C}(\mathbf{q})$ presented in Equation (4.7) facilitates the unit quaternion rotation described in Equation (4.6). This is described with the aid of Equation (4.2.1). Note that the description of $\mathbf{C}(\mathbf{q})$ presented here is only valid for unit quaternions. This is not equivalent to the general quaternion rotation matrix. Unlike unit quaternion, general quaternion does not follow the unit norm constraint on quaternion vector. Further information on general quaternion definitions and algebra is well summarised in (Diebel, 2006, Shoemake, Shuster, 1993, Trawny and Roumeliotis, 2005).

$$\mathbf{p}' = \mathbf{q} \cdot \mathbf{p} \cdot \mathbf{q}^{-1} \tag{4.8}$$

$$\mathbf{p}' = \mathbf{C}(\mathbf{q}) \cdot \mathbf{p} \tag{4.9}$$

If $\mathbf{C}(\theta)$ is available, unit quaternion can be extracted from it with the aid of Equation (4.10). Further a compressed form of DCM in quaternion is expressed in Equation (4.10) (Wie, 1998).

$$\underline{\mathbf{q}} = \begin{pmatrix} q_1 \\ q_2 \\ q_3 \end{pmatrix}, \quad \mathbf{Q_s} = \begin{bmatrix} 0 & -q_3 & q_2 \\ q_3 & 0 & -q_1 \\ -q_2 & q_1 & 0 \end{bmatrix} \tag{4.10a}$$

Here $\underline{q}$ is the quaternion vector part and $\mathbf{Q_s}$ is the quaternion vector skew symmetric matrix.

$$\mathbf{C}(\underline{\mathbf{q}}, q_4) = \left(q_4^2 - \underline{\mathbf{q}}^T\underline{\mathbf{q}}\right)I + 2\underline{\mathbf{q}}\underline{\mathbf{q}}^T - 2q_4\mathbf{Q_s} \tag{4.10b}$$

$$q_4 = \pm\frac{1}{2}\sqrt{C_{11} + C_{22} + C_{33} + 1}, \text{ for } 0 \leq \theta \leq \pi \tag{4.10c}$$

$$\underline{\mathbf{q}} = \frac{1}{4q_4}\begin{pmatrix} C_{23} - C_{32} \\ C_{31} - C_{13} \\ C_{12} - C_{21} \end{pmatrix}, \text{ if } q_4 \neq 0 \tag{4.10d}$$

Errors in quaternions are expressed in terms of the rotation required to achieve a desired quaternion orientation. Quaternion multiplication rule in matrix form, or quaternion transmuted matrix, is used to estimate the quaternion errors or relative quaternion attitude vectors. A quick overview of combining two successive quaternion rotations, from $\mathbf{q}$ to $\mathbf{q}'$ to $\mathbf{q}''$, is outlined with the aid of Equation (4.11). The following transformation is achieved via quaternion multiplication rule in matrix form:

$$\begin{pmatrix} q_1 \\ q_2 \\ q_3 \\ q_4 \end{pmatrix} = \begin{bmatrix} q_4'' & q_3'' & -q_2'' & q_1'' \\ -q_3'' & q_4'' & q_1'' & q_2'' \\ q_2'' & -q_1'' & q_4'' & q_3'' \\ -q_1'' & -q_2'' & -q_3'' & q_4'' \end{bmatrix}\begin{pmatrix} q_1' \\ q_2' \\ q_3' \\ q_4' \end{pmatrix} \tag{4.11a}$$

While the following transformation is achieved via quaternion transmuted matrix, $\mathbf{Q}$.

$$
\begin{pmatrix} q_1 \\ q_2 \\ q_3 \\ q_4 \end{pmatrix} = \begin{bmatrix} q'_4 & -q'_3 & q'_2 & q'_1 \\ q'_3 & q'_4 & -q'_1 & q'_2 \\ -q'_2 & q'_1 & q'_4 & q'_3 \\ -q'_1 & -q'_2 & -q'_3 & q'_4 \end{bmatrix} \begin{pmatrix} q''_1 \\ q''_2 \\ q''_3 \\ q''_4 \end{pmatrix}
\tag{4.11b}
$$

For the sake of completion, quaternion composition and multiplication operation is introduced in Equation (4.12). Underlying definition of composition operator $\otimes$, and multiplication operator $\odot$ follow from Equation (4.11).

$$
C(\mathbf{q}'') = C(\mathbf{q}') \cdot C(\mathbf{q})
\tag{4.12a}
$$

The above is equivalent to (Shuster, 1993):

$$
\mathbf{q}'' = \mathbf{q}' \otimes \mathbf{q} = \begin{pmatrix} q_4\underline{\mathbf{q}}' + q'_4\underline{\mathbf{q}} - \underline{\mathbf{q}}' \times \underline{\mathbf{q}} \\ q_4 q'_4 - \underline{\mathbf{q}}^T \underline{\mathbf{q}}' \end{pmatrix} \equiv \mathbf{q} \odot \mathbf{q}'
\tag{4.12b}
$$

$$
\begin{pmatrix} q''_1 \\ q''_2 \\ q''_3 \\ q''_4 \end{pmatrix} = \begin{bmatrix} q'_4 & -q'_3 & q'_2 & q'_1 \\ q'_3 & q'_4 & -q'_1 & q'_2 \\ -q'_2 & q'_1 & q'_4 & q'_3 \\ -q'_1 & -q'_2 & -q'_3 & q'_4 \end{bmatrix}^T \begin{pmatrix} q_1 \\ q_2 \\ q_3 \\ q_4 \end{pmatrix}
\tag{4.12c}
$$

Since both the quaternion transmuted matrix, $\mathbf{Q}_t$, and quaternion matrix multiplications form are orthonormal matrices, $\mathbf{Q}_t^{-1} = \mathbf{Q}_t^T$. This leads to the definition of quaternion error outlined in Equation (4.13).

$$
\begin{pmatrix} q_{1e} \\ q_{2e} \\ q_{3e} \\ q_{4e} \end{pmatrix} = \begin{bmatrix} q_{4r} & q_{3r} & -q_{2r} & -q_{1r} \\ -q_{3r} & q_{4r} & q_{1r} & -q_{2r} \\ q_{2r} & -q_{1r} & q_{4r} & -q_{3r} \\ q_{1r} & q_{2r} & q_{3r} & q_{4r} \end{bmatrix} \begin{pmatrix} q_1 \\ q_2 \\ q_3 \\ q_4 \end{pmatrix}
\tag{4.13}
$$

Here, subscript r indicated the reference or commanded orientation. Subscript e the error, and no subscripts mean the current state of orientation. The above is known as the quaternion multiplication rule. Alternatively it can also be expressed with the aid of quaternion transmutted matrix $\mathbf{Q}_t$. To complete this section on quaternion mathematics, quaternion division is introduced with the aid of Equation (4.14).

$$
\mathbf{q} = \mathbf{q}'' \ominus \mathbf{q}
\tag{4.14a}
$$

This is related to quaternion multiplication and composition operator with $\mathbf{q}^{-1}$

$$
\mathbf{q} = \mathbf{q}'' \ominus \mathbf{q}' = \mathbf{q}'^{-1} \otimes \mathbf{q}'' = \mathbf{q}'' \odot \mathbf{q}'^{-1} = \begin{pmatrix} c - q''_4\underline{\mathbf{q}}' + q'_4\underline{\mathbf{q}}'' + \underline{\mathbf{q}}' \times \underline{\mathbf{q}}'' \\ q''_4 q'_4 + \underline{\mathbf{q}}''^T \underline{\mathbf{q}}' \end{pmatrix}
\tag{4.14b}
$$

Modified Rodrigues Parameters

Modified Rodrigues Parameters or MRPs were introduced to spacecraft attitude kinematics to facilitate the application of continuous attitude tracking. MRPs are defined by adding 1 to the denominator of the definition of Classical Rogridues Parameters, CRP. MRPs are defined in Equation (4.15).

$$
\sigma = \frac{\underline{\mathbf{q}}}{1 + q_4}
\tag{4.15a}
$$

$$
\sigma = \begin{pmatrix} \sigma_1 \\ \sigma_2 \\ \sigma_3 \end{pmatrix}
\tag{4.15b}
$$

The inverse quaternion equivalent of MRP is the shadow set:

$$
\sigma^s = \frac{-\sigma}{|\sigma|^2} = \frac{-\underline{\mathbf{q}}}{1 - q_4}
\tag{4.15c}
$$

DCM in terms of MRPs are expressed with the aid of Equation (4.16), interested readers can find the derivations in (Schaub and Junkins, 2002) (Chu, 2018).

$$\mathbf{C}(\sigma) = \frac{1}{(1+\sigma^2)^2} \begin{bmatrix} (1+\sigma^2)^2 - 8\sigma_2^2 - 8\sigma_3^2 & 8\sigma_1\sigma_2 + 4\sigma_3(1-\sigma^2) & 8\sigma_1\sigma_3 + 4\sigma_2(1-\sigma^2) \\ 8\sigma_2\sigma_1 + 4\sigma_3(1-\sigma^2) & (1+\sigma^2)^2 - 8\sigma_1^2 - 8\sigma_3^2 & 8\sigma_2\sigma_3 + 4\sigma_1(1-\sigma^2) \\ 8\sigma_3\sigma_1 + 4\sigma_2(1-\sigma^2) & 8\sigma_3\sigma_2 + 4\sigma_1(1-\sigma^2) & (1+\sigma^2)^2 - 8\sigma_1^2 - 8\sigma_2^2 \end{bmatrix} \tag{4.16a}$$

In compact form this can expanded as (Shuster, 1993)

$$\sigma = \begin{pmatrix} \sigma_1 \\ \sigma_2 \\ \sigma_3 \end{pmatrix} , \sigma_s = \begin{bmatrix} 0 & -\sigma_3 & \sigma_2 \\ \sigma_3 & 0 & -\sigma_1 \\ -\sigma_2 & \sigma_1 & 0 \end{bmatrix} \tag{4.16b}$$

$$\mathbf{C}(\sigma) = I - \frac{4(1-|\sigma|^2)}{(1+|\sigma|^2)^2}\sigma_s + \frac{8}{(1+|\sigma|^2)^2}\sigma_s^2 \tag{4.16c}$$

MRP algebra is similar to the algebraic notations outlined for quaternions in the previous section. For the sake of brevity, detailed explanations are avoided and the final algebraic notations are presented here. Interested readers can find detailed derivations and explanations in (Shuster, 1993). MRP algebra is summarised with the aid of Equation (4.17). MRP composition, multiplication and division operation (Shuster, 1993):

$$\sigma = (-\sigma') \otimes \sigma'' = \sigma'' \odot (-\sigma') = \sigma'' \ominus \sigma' = \frac{(1-|\sigma'|^2)\sigma'' - (1-|\sigma''|^2)\sigma' + 2\sigma_s'\sigma''}{1 + |\sigma''|^2 |\sigma'|^2 + 2\sigma''^T \sigma'} \tag{4.17}$$

Using the MRP algebraic expressions outlined in Equation (4.17), MRP error or relative attitude is derived in Equation (4.18)

$$\sigma_r = \sigma \odot \sigma_e = \sigma_e \otimes \sigma = \sigma \ominus -\sigma_e \tag{4.18a}$$

$$\sigma_e = \sigma_r \otimes (-\sigma) \tag{4.18b}$$

From Equation (4.17) the following can be deduced

$$\sigma'' = \sigma' \otimes \sigma \tag{4.18c}$$

$$\sigma'' = \frac{(1-|\sigma|^2)\sigma' + (1-|\sigma'|^2)\sigma - 2\sigma' \times \sigma}{1 + |\sigma'|^2|\sigma|^2 - 2\sigma' \cdot \sigma} \tag{4.18d}$$

Using the above, MRP error can be estimated using:

$$\sigma_e = \frac{(1-|\sigma|^2)\sigma_r - (1-|\sigma_r|^2)\sigma + 2\sigma \times \sigma_r}{1 + |\sigma|^2 |\sigma_r|^2 + 2\sigma^T \sigma_r} \tag{4.18e}$$

4.2.2 | Choice of Parametrisation

The thesis work presented here utilises all forms of parametrisations presented in the Section above. Transformation to-and-from Euler-321 is conducted wherever necessary. For steady-state and calibration manoeuvre tracking kinematics simulator, quaternion is utilised for internal mathematics. Rigid body NanoSat dynamics, kinematics, and controller is synthesised by utilising MRP in combination with its shadow set to facilitate ground target tracking. Gyro and Star Tracker misalignments are defined with Euler321 rotation matrices. Star tracker noise is added in Euler-321, later converted to quaternions as star tracker output, to preserve the unity norm while maintaining the error metrics defined by the manufacturer. Though the filter takes input attitude as quaternion, and outputs the attitude in quaternion, internal mathematics are conducted in MRP to avoid violating the unity norm constraint associated with unit quaternions. The relations presented in the Section above, are used consistently to

4.3 | **Rigid Body Rotational Kinematics and Dynamics**

The objective of this section is to derive rigid body rotational kinematics and dynamics of a NanoSat in different parametrisations.

4.3.1 | Euler

The kinematics and dynamics presented here are in $\mathcal{F}_\mathcal{B}$ for Euler 3-2-1 sequence. Gravity gradient torque included in the dynamics expression makes the assumption that the satellite is in circular orbit.

Dynamics

Before presenting the definition of rigid body rotational dynamics of the spacecraft, a brief insight into the derivation is provided. Angular momentum of a rigid body spacecraft about $\mathcal{F}_\mathcal{B}$ at the CoM is $\mathbf{H} = J\omega|_{\mathcal{F}_\mathcal{B}}$. Fundamentals of dynamics state that $\dot{\mathbf{H}}$ is equivalent to the external moment of force (torque), $\boldsymbol{t}$ acting on the CoM of the rigid body spacecraft. Application of transport theorem and noting that for a rigid body spacecraft $\boldsymbol{J}$ does not change over time, one can get the expression outlined in Equation (4.19) (Wie, 1998). Subscript and superscript B and N indicate $\mathcal{F}_\mathcal{B}$ and $\mathcal{F}_\mathcal{N}$ respectively.

$$\boldsymbol{t} = \left.\frac{d\mathbf{H}}{dt}\right|_B + \omega^{B/N} \times \mathbf{H} \tag{4.19a}$$

In the following, $\omega = \omega^{B/N}$ is used for simplicity.

$$\boldsymbol{t} = \boldsymbol{J} \cdot \left.\frac{d\omega}{dt}\right|_N + \omega \times \boldsymbol{J} \cdot \omega = \boldsymbol{J} \cdot \dot{\omega} + \omega \times \boldsymbol{J} \cdot \omega \tag{4.19b}$$

Here, $\{\mathrm{d}\omega/\mathrm{d}t\}_B = \{\mathrm{d}\omega/\mathrm{d}t\}_N = \dot{\omega}$

Gravity gradient torque can be included in the expression derived in Equation (4.19). Details are not presented here, interested readers can find further information on inclusion of gravity gradient term in (Wie, 1998) (Chu, 2018). Equation (4.20) presents a compact notation of the general dynamics expression of the rigid body spacecraft (Chu, 2018). Here n is the SC mean motion, the gravity gradient torque about the SC CoM is simplified by selecting the first term of binomial expansion.

$$\boldsymbol{J}\dot{\omega} + \omega_s \boldsymbol{J}\omega = \boldsymbol{G}_{DCM}\,\mathbf{J}\,\mathbf{g}_{DCM} + \boldsymbol{t_u} + \boldsymbol{t_{dist}} \tag{4.20a}$$

Here $\boldsymbol{J}$ is the spacecraft inertia matrix estimated from the CoM. Angular rate in the SC body axis:

$$\omega = \begin{pmatrix} \omega_1 \\ \omega_2 \\ \omega_3 \end{pmatrix} \tag{4.20b}$$

And, ω_s = Skew symmetric matrix of ω. $\mathbf{g_{DCM}}$ = DCM terms associated with gravity gradient torque.

$$\mathbf{g_{DCM}} = \begin{pmatrix} C_{13} \\ C_{23} \\ C_{33} \end{pmatrix} \tag{4.20c}$$

For a spacecraft in circular orbit, $\boldsymbol{G}_{DCM}$ is the skew symmetric matrix of $\mathbf{g_{DCM}}$ multiplied with $3n^2$

$$\boldsymbol{G}_{DCM} = 3n^2 \mathbf{g_{DCM}}_S \tag{4.20d}$$

$\boldsymbol{t_u}$ is the control torque at SC CoM. $\boldsymbol{t_{dist}}$ is the disturbance torque at SC CoM. SC mean motion can be expressed as:

$$n = \sqrt{\frac{\mu_\oplus}{r^3}} \tag{4.20e}$$

Gravitational parameter of Earth, $\mu_\oplus$ = 3.986004418·10^{14} [m^3 s^2], and r is the distance from O_{ECI} to CoM of SC [m] Expanded expression for rigid body rotational dynamics is presented with the aid of Equation (4.21).

$$\begin{bmatrix} J_{11} & J_{12} & J_{13} \\ J_{21} & J_{22} & J_{23} \\ J_{31} & J_{32} & J_{33} \end{bmatrix} \begin{pmatrix} \dot{\omega}_1 \\ \dot{\omega}_2 \\ \dot{\omega}_3 \end{pmatrix} + \begin{bmatrix} 0 & -\omega_3 & \omega_2 \\ \omega_3 & 0 & -\omega_1 \\ -\omega_2 & \omega_1 & 0 \end{bmatrix} \begin{bmatrix} J_{11} & J_{12} & J_{13} \\ J_{21} & J_{22} & J_{23} \\ J_{31} & J_{32} & J_{33} \end{bmatrix} \begin{pmatrix} \omega_1 \\ \omega_2 \\ \omega_3 \end{pmatrix} = \ldots$$
$$\ldots 3n^2 \begin{bmatrix} 0 & -C_{33} & C_{23} \\ C_{33} & 0 & -C_{13} \\ -C_{23} & C_{13} & 0 \end{bmatrix} \begin{bmatrix} J_{11} & J_{12} & J_{13} \\ J_{21} & J_{22} & J_{23} \\ J_{31} & J_{32} & J_{33} \end{bmatrix} \begin{pmatrix} C_{13} \\ C_{23} \\ C_{33} \end{pmatrix} + \boldsymbol{t_u} + \boldsymbol{t_{dist}} \tag{4.21a}$$

In Euler coordinates:

$$\begin{bmatrix} J_{11} & J_{12} & J_{13} \\ J_{21} & J_{22} & J_{23} \\ J_{31} & J_{32} & J_{33} \end{bmatrix} \begin{pmatrix} \dot{\omega}_1 \\ \dot{\omega}_2 \\ \dot{\omega}_3 \end{pmatrix} + \begin{pmatrix} 0 & -\omega_3 & \omega_2 \\ \omega_3 & 0 & -\omega_1 \\ -\omega_2 & \omega_1 & 0 \end{pmatrix} \begin{bmatrix} J_{11} & J_{12} & J_{13} \\ J_{21} & J_{22} & J_{23} \\ J_{31} & J_{32} & J_{33} \end{bmatrix} \begin{pmatrix} \omega_1 \\ \omega_2 \\ \omega_3 \end{pmatrix} = \ldots$$
$$3n^2 \begin{bmatrix} 0 & -\mathbf{c}\theta_1\mathbf{c}\theta_2 & \mathbf{s}\theta_1\mathbf{c}\theta_2 \\ \mathbf{c}\theta_1\mathbf{c}\theta_2 & 0 & \mathbf{s}\theta_2 \\ -\mathbf{s}\theta_1\mathbf{c}\theta_2 & -\mathbf{s}\theta_2 & 0 \end{bmatrix} \begin{bmatrix} J_{11} & J_{12} & J_{13} \\ J_{21} & J_{22} & J_{23} \\ J_{31} & J_{32} & J_{33} \end{bmatrix} \begin{pmatrix} -\mathbf{s}\theta_2 \\ \mathbf{s}\theta_1\mathbf{c}\theta_2 \\ \mathbf{c}\theta_1\mathbf{c}\theta_2 \end{pmatrix} + \boldsymbol{t_u} + \boldsymbol{t_{dist}} \tag{4.21b}$$

The above expressions are presented in DCM, since this will facilitate transformation of the problem to other coordinate systems.

Kinematics

Kinematics of spacecraft describe the attitude or orientation of the spacecraft in rotational equations of motion. First a general formation of kinematics is presented in terms of DCM. Later it is extended to an Euler formulation. Equation (4.22) outlines a DCM representation of the spacecraft kinematics without and with spacecraft mean motion term. General expression of kinematics without the influence of mean motion is:

$$\dot{C} + \omega_s \cdot C = 0 \tag{4.22a}$$

$$\dot{C}^T - C^T \omega_s = 0 \quad \text{And,} \ \omega_s^T = -\omega_s \tag{4.22b}$$

$$\begin{bmatrix} 0 & -\omega_3 & \omega_2 \\ \omega_3 & 0 & -\omega_1 \\ -\omega_2 & \omega_1 & 0 \end{bmatrix} = -\begin{bmatrix} \dot{C}_{11} & \dot{C}_{12} & \dot{C}_{13} \\ \dot{C}_{21} & \dot{C}_{22} & \dot{C}_{23} \\ \dot{C}_{31} & \dot{C}_{32} & \dot{C}_{33} \end{bmatrix}\begin{bmatrix} C_{11} & C_{21} & C_{31} \\ C_{12} & C_{22} & C_{32} \\ C_{13} & C_{23} & C_{33} \end{bmatrix} \tag{4.22c}$$

$$\omega_1 = \dot{C}_{21}C_{31} + \dot{C}_{22}C_{32} + \dot{C}_{23}C_{33} \tag{4.22d}$$

$$\omega_2 = \dot{C}_{31}C_{11} + \dot{C}_{32}C_{12} + \dot{C}_{33}C_{13} \tag{4.22e}$$

$$\omega_3 = \dot{C}_{11}C_{21} + \dot{C}_{12}C_{22} + \dot{C}_{13}C_{23} \tag{4.22f}$$

Constant orbital rate $\omega^{V/N} = -n\mathbf{Y}_{LVLH}$, leads to $\omega^{B/N} = \omega^{B/A} - n\mathbf{Y}_{LVLH}$.
A DCM conversion is implemented to augment this in kinematics.

$$\omega = \begin{bmatrix} \dot{C}_{21}C_{31} + \dot{C}_{22}C_{32} + \dot{C}_{23}C_{33} \\ \dot{C}_{31}C_{11} + \dot{C}_{32}C_{12} + \dot{C}_{33}C_{13} \\ \dot{C}_{11}C_{21} + \dot{C}_{12}C_{22} + \dot{C}_{13}C_{23} \end{bmatrix} - n\begin{pmatrix} C_{12} \\ C_{22} \\ C_{32} \end{pmatrix} \tag{4.22g}$$

Now that a general form of spacecraft rigid body kinematics is outlined, kinematics in terms of Euler 3-2-1 rotation, is presented in Equation (4.23). First kinematics without spacecraft mean motion is presented and later with mean motion term (Chu, 2018).

$$\begin{pmatrix} \omega_1 \\ \omega_2 \\ \omega_3 \end{pmatrix} = \begin{bmatrix} 1 & 0 & -\mathbf{s}\theta_2 \\ 0 & \mathbf{c}\theta_1 & \mathbf{s}\theta_1\mathbf{c}\theta_2 \\ 0 & -\mathbf{s}\theta_1 & \mathbf{c}\theta_1\mathbf{c}\theta_2 \end{bmatrix}\begin{pmatrix} \dot{\theta}_1 \\ \dot{\theta}_2 \\ \dot{\theta}_3 \end{pmatrix} \tag{4.23a}$$

$$\begin{pmatrix} \dot{\theta}_1 \\ \dot{\theta}_2 \\ \dot{\theta}_3 \end{pmatrix} = \frac{1}{\mathbf{c}\theta_2}\begin{bmatrix} \mathbf{c}\theta_2 & \mathbf{s}\theta_1\mathbf{s}\theta_2 & \mathbf{c}\theta_1\mathbf{s}\theta_2 \\ 0 & \mathbf{c}\theta_1\mathbf{c}\theta_2 & -\mathbf{s}\theta_1\mathbf{c}\theta_2 \\ 0 & \mathbf{s}\theta_1 & \mathbf{c}\theta_1 \end{bmatrix}\begin{pmatrix} \omega_1 \\ \omega_2 \\ \omega_3 \end{pmatrix} \tag{4.23b}$$

With mean motion the expressions can be extended to:

$$\begin{pmatrix} \omega_1 \\ \omega_2 \\ \omega_3 \end{pmatrix} = \begin{bmatrix} 1 & 0 & -\mathbf{s}\theta_2 \\ 0 & \mathbf{c}\theta_1 & \mathbf{s}\theta_1\mathbf{c}\theta_2 \\ 0 & -\mathbf{s}\theta_1 & \mathbf{c}\theta_1\mathbf{c}\theta_2 \end{bmatrix}\begin{pmatrix} \dot{\theta}_1 \\ \dot{\theta}_2 \\ \dot{\theta}_3 \end{pmatrix} - n\begin{pmatrix} \mathbf{c}\theta_2\mathbf{s}\theta_3 \\ \mathbf{s}\theta_1\mathbf{s}\theta_2\mathbf{s}\theta_3 + \mathbf{c}\theta_1\mathbf{c}\theta_3 \\ \mathbf{c}\theta_1\mathbf{s}\theta_2\mathbf{s}\theta_3 - \mathbf{s}\theta_1\mathbf{c}\theta_3 \end{pmatrix} \tag{4.23c}$$

$$\begin{pmatrix} \omega_1 \\ \omega_2 \\ \omega_3 \end{pmatrix} + n\begin{pmatrix} \mathbf{c}\theta_2\mathbf{s}\theta_3 \\ \mathbf{s}\theta_1\mathbf{s}\theta_2\mathbf{s}\theta_3 + \mathbf{c}\theta_1\mathbf{c}\theta_3 \\ \mathbf{c}\theta_1\mathbf{s}\theta_2\mathbf{s}\theta_3 - \mathbf{s}\theta_1\mathbf{c}\theta_3 \end{pmatrix} = \begin{bmatrix} 1 & 0 & -\mathbf{s}\theta_2 \\ 0 & \mathbf{c}\theta_1 & \mathbf{s}\theta_1\mathbf{c}\theta_2 \\ 0 & -\mathbf{s}\theta_1 & \mathbf{c}\theta_1\mathbf{c}\theta_2 \end{bmatrix}\begin{pmatrix} \dot{\theta}_1 \\ \dot{\theta}_2 \\ \dot{\theta}_3 \end{pmatrix} \tag{4.23d}$$

$$\begin{pmatrix} \dot{\theta}_1 \\ \dot{\theta}_2 \\ \dot{\theta}_3 \end{pmatrix} = \frac{1}{\mathbf{c}\theta_2}\begin{bmatrix} \mathbf{c}\theta_2 & \mathbf{s}\theta_1\mathbf{s}\theta_2 & \mathbf{c}\theta_1\mathbf{s}\theta_2 \\ 0 & \mathbf{c}\theta_1\mathbf{c}\theta_2 & -\mathbf{s}\theta_1\mathbf{c}\theta_2 \\ 0 & \mathbf{s}\theta_1 & \mathbf{c}\theta_1 \end{bmatrix}\begin{pmatrix} \omega_1 \\ \omega_2 \\ \omega_3 \end{pmatrix} + \frac{n}{\mathbf{c}\theta_2}\begin{pmatrix} \mathbf{s}\theta_3 \\ \mathbf{c}\theta_2\mathbf{c}\theta_3 \\ \mathbf{s}\theta_2\mathbf{s}\theta_3 \end{pmatrix} \tag{4.23e}$$

This concludes the kinematics and dynamics representation in Euler coordinate parametrisation.

4.3.2 | Quaternion

The analogy for Euler in the previous section can be extended to quaternion rigid body rotational kinematics and dynamics. For brevity, the final expressions are presented.

Dynamics

With the aid of quaternion DCM(**q**), the general dynamics expression in Equation (4.20) can be extended to quaternion representation as presented in Equation (4.24).

$$\boldsymbol{J}\dot{\omega} + \omega_s \boldsymbol{J}\omega = \boldsymbol{G}_{DCM}\,\mathbf{J}\,\mathbf{g}_{\mathrm{DCM}} + \boldsymbol{t_u} + \boldsymbol{t_{dist}} \tag{4.24a}$$

$$
\begin{bmatrix} J_{11} & J_{12} & J_{13} \\ J_{21} & J_{22} & J_{23} \\ J_{31} & J_{32} & J_{33} \end{bmatrix}
\begin{bmatrix} \dot{\omega}_1 \\ \dot{\omega}_2 \\ \dot{\omega}_3 \end{bmatrix}
+ \begin{pmatrix} 0 & -\omega_3 & \omega_2 \\ \omega_3 & 0 & -\omega_1 \\ -\omega_2 & \omega_1 & 0 \end{pmatrix}
\begin{bmatrix} J_{11} & J_{12} & J_{13} \\ J_{21} & J_{22} & J_{23} \\ J_{31} & J_{32} & J_{33} \end{bmatrix}
\begin{pmatrix} \omega_1 \\ \omega_2 \\ \omega_3 \end{pmatrix} = \ldots
$$

$$
\ldots 3n^2 \begin{bmatrix} 0 & -C_{33} & C_{23} \\ C_{33} & 0 & -C_{13} \\ -C_{23} & C_{13} & 0 \end{bmatrix}
\begin{bmatrix} J_{11} & J_{12} & J_{13} \\ J_{21} & J_{22} & J_{23} \\ J_{31} & J_{32} & J_{33} \end{bmatrix}
\begin{pmatrix} C_{13} \\ C_{23} \\ C_{33} \end{pmatrix} - \boldsymbol{t_u} - \boldsymbol{t_{dist}} \tag{4.24b}
$$

In quaternion parametrisation this can be expressed as:

$$
\begin{bmatrix} J_{11} & J_{12} & J_{13} \\ J_{21} & J_{22} & J_{23} \\ J_{31} & J_{32} & J_{33} \end{bmatrix}
\begin{pmatrix} \dot{\omega}_1 \\ \dot{\omega}_2 \\ \dot{\omega}_3 \end{pmatrix}
+ \begin{bmatrix} 0 & -\omega_3 & \omega_2 \\ \omega_3 & 0 & -\omega_1 \\ -\omega_2 & \omega_1 & 0 \end{bmatrix}
\begin{bmatrix} J_{11} & J_{12} & J_{13} \\ J_{21} & J_{22} & J_{23} \\ J_{31} & J_{32} & J_{33} \end{bmatrix}
\begin{pmatrix} \omega_1 \\ \omega_2 \\ \omega_3 \end{pmatrix} = \ldots
$$

$$
\ldots 3n^2 \begin{bmatrix} 0 & -(1 - 2\left(q_1^2 + q_2^2\right)) & 2\left(q_2 q_3 + q_1 q_4\right) \\ 1 - 2\left(q_1^2 + q_2^2\right) & 0 & -2\left(q_1 q_3 - q_2 q_4\right) \\ -2\left(q_2 q_3 + q_1 q_4\right) & 2\left(q_1 q_3 - q_2 q_4\right) & 0 \end{bmatrix}
\begin{bmatrix} J_{11} & J_{12} & J_{13} \\ J_{21} & J_{22} & J_{23} \\ J_{31} & J_{32} & J_{33} \end{bmatrix}
\begin{pmatrix} 2\left(q_1 q_3 - q_2 q_4\right) \\ 2\left(q_2 q_3 + q_1 q_4\right) \\ 1 - 2\left(q_1^2 + q_2^2\right) \end{pmatrix} \ldots
$$

$$
\ldots - \boldsymbol{t_u} - \boldsymbol{t_{dist}} \tag{4.24c}
$$

Kinematics

The kinematics of rigid body spacecraft can be extended to quaternions. The unit norm constraint is added to the expression. A summary of the quaternion kinematics is presented with the aid of Equation (4.25). Without the effect of mean motion of LVLH :

$$
\begin{pmatrix} \omega_1 \\ \omega_2 \\ \omega_3 \\ 0 \end{pmatrix} = 2
\begin{bmatrix} q_4 & q_3 & -q_2 & -q_1 \\ -q_3 & q_4 & q_1 & -q_2 \\ q_2 & -q_1 & q_4 & -q_3 \\ q_1 & q_2 & q_3 & q_4 \end{bmatrix}
\begin{pmatrix} \dot{q}_1 \\ \dot{q}_2 \\ \dot{q}_3 \\ \dot{q}_4 \end{pmatrix} \tag{4.25a}
$$

$$
\begin{pmatrix} \dot{q}_1 \\ \dot{q}_2 \\ \dot{q}_3 \\ \dot{q}_4 \end{pmatrix} = \frac{1}{2}
\begin{bmatrix} q_4 & -q_3 & q_2 & q_1 \\ q_3 & q_4 & -q_1 & q_2 \\ -q_2 & q_1 & q_4 & q_3 \\ -q_1 & -q_2 & -q_3 & q_4 \end{bmatrix}
\begin{pmatrix} \omega_1 \\ \omega_2 \\ \omega_3 \\ 0 \end{pmatrix} = \frac{1}{2}
\begin{bmatrix} 0 & \omega_3 & -\omega_2 & \omega_1 \\ -\omega_3 & 0 & \omega_1 & \omega_2 \\ \omega_2 & -\omega_1 & 0 & \omega_3 \\ -\omega_1 & -\omega_2 & -\omega_3 & 0 \end{bmatrix}
\begin{pmatrix} q_1 \\ q_2 \\ q_3 \\ q_4 \end{pmatrix} \tag{4.25b}
$$

Including the effect of mean motion of the LVLH frame:

$$
\begin{pmatrix} \omega_1 \\ \omega_2 \\ \omega_3 \\ 0 \end{pmatrix} = 2
\begin{bmatrix} q_4 & q_3 & -q_2 & -q_1 \\ -q_3 & q_4 & q_1 & -q_2 \\ q_2 & -q_1 & q_4 & -q_3 \\ q_1 & q_2 & q_3 & q_4 \end{bmatrix}
\begin{pmatrix} \dot{q}_1 \\ \dot{q}_2 \\ \dot{q}_3 \\ \dot{q}_4 \end{pmatrix}
- n \begin{pmatrix} 2\left(q_1 q_2 + q_3 q_4\right) \\ 1 - 2\left(q_1^2 + q_3^2\right) \\ 2\left(q_3 q_2 - q_1 q_4\right) \\ 0 \end{pmatrix} \tag{4.25c}
$$

$$
\begin{pmatrix} \dot{q}_1 \\ \dot{q}_2 \\ \dot{q}_3 \\ \dot{q}_4 \end{pmatrix} = \frac{1}{2}
\begin{bmatrix} q_4 & -q_3 & q_2 & q_1 \\ q_3 & q_4 & -q_1 & q_2 \\ -q_2 & q_1 & q_4 & q_3 \\ -q_1 & -q_2 & -q_3 & q_4 \end{bmatrix}
\left(\begin{pmatrix} \omega_1 \\ \omega_2 \\ \omega_3 \\ 0 \end{pmatrix} + n \begin{pmatrix} 2\left(q_1 q_2 + q_3 q_4\right) \\ 1 - 2\left(q_1^2 + q_3^2\right) \\ 2\left(q_3 q_2 - q_1 q_4\right) \\ 0 \end{pmatrix} \right) \tag{4.25d}
$$

This concludes the definition of kinematics and dynamics of rigid body rotational equations of motion in quaternion coordinates.

4.3.3 | Modified Rodrigues Parameters

This section aims at developing the rigid body rotational dynamics and kinematics expression in MRP coordinate system.

Dynamics

With the aid of DCM (σ) the general dynamics expression in Equation (4.20) can be extended to MRP representation as demonstrated in Equation (4.26)

$$J\dot{\omega} + \omega_s J\omega = G_{DCM}\,\mathbf{J}\,\mathbf{g}_{\mathrm{DCM}} + t_u + t_{dist} \tag{4.26a}$$

The general expression for rigid body spacecraft dynamics can be expressed as:

$$
\begin{bmatrix} J_{11} & J_{12} & J_{13} \\ J_{21} & J_{22} & J_{23} \\ J_{31} & J_{32} & J_{33} \end{bmatrix}
\begin{pmatrix} \dot{\omega}_1 \\ \dot{\omega}_2 \\ \dot{\omega}_3 \end{pmatrix}
+
\begin{bmatrix} 0 & -\omega_3 & \omega_2 \\ \omega_3 & 0 & -\omega_1 \\ -\omega_2 & \omega_1 & 0 \end{bmatrix}
\begin{bmatrix} J_{11} & J_{12} & J_{13} \\ J_{21} & J_{22} & J_{23} \\ J_{31} & J_{32} & J_{33} \end{bmatrix}
\begin{pmatrix} \omega_1 \\ \omega_2 \\ \omega_3 \end{pmatrix}
= \dots
$$
$$
\dots 3n^2
\begin{bmatrix} 0 & -C_{33} & C_{23} \\ C_{33} & 0 & -C_{13} \\ -C_{23} & C_{13} & 0 \end{bmatrix}
\begin{bmatrix} J_{11} & J_{12} & J_{13} \\ J_{21} & J_{22} & J_{23} \\ J_{31} & J_{32} & J_{33} \end{bmatrix}
\begin{pmatrix} C_{13} \\ C_{23} \\ C_{33} \end{pmatrix}
- t_u - t_{dist} \tag{4.26b}
$$

In MRP expressions this can be expanded as:

$$
\begin{bmatrix} J_{11} & J_{12} & J_{13} \\ J_{21} & J_{22} & J_{23} \\ J_{31} & J_{32} & J_{33} \end{bmatrix}
\begin{pmatrix} \dot{\omega}_1 \\ \dot{\omega}_2 \\ \dot{\omega}_3 \end{pmatrix}
+
\begin{bmatrix} 0 & -\omega_3 & \omega_2 \\ \omega_3 & 0 & -\omega_1 \\ -\omega_2 & \omega_1 & 0 \end{bmatrix}
\begin{bmatrix} J_{11} & J_{12} & J_{13} \\ J_{21} & J_{22} & J_{23} \\ J_{31} & J_{32} & J_{33} \end{bmatrix}
\begin{pmatrix} \omega_1 \\ \omega_2 \\ \omega_3 \end{pmatrix}
= \dots
$$
$$
\dots 3n^2 \frac{1}{\left(1+\sigma^2\right)^2}
\begin{bmatrix} 0 & -\left(\left(1+\sigma^2\right)^2 - 8\sigma_1^2 - 8\sigma_2^2\right) & 8\sigma_2\sigma_3 + 4\sigma_1\left(1-\sigma^2\right) \\ \left(1+\sigma^2\right)^2 - 8\sigma_1^2 - 8\sigma_2^2 & 0 & -\left(8\sigma_1\sigma_3 + 4\sigma_2\left(1-\sigma^2\right)\right) \\ -\left(8\sigma_2\sigma_3 + 4\sigma_1\left(1-\sigma^2\right)\right) & 8\sigma_1\sigma_3 + 4\sigma_2\left(1-\sigma^2\right) & 0 \end{bmatrix} \dots
$$
$$
\dots
\begin{bmatrix} J_{11} & J_{12} & J_{13} \\ J_{21} & J_{22} & J_{23} \\ J_{31} & J_{32} & J_{33} \end{bmatrix}
\frac{1}{\left(1+\sigma^2\right)^2}
\begin{pmatrix} 8\sigma_1\sigma_3 + 4\sigma_2\left(1-\sigma^2\right) \\ 8\sigma_2\sigma_3 + 4\sigma_1\left(1-\sigma^2\right) \\ \left(1+\sigma^2\right)^2 - 8\sigma_1^2 - 8\sigma_2^2 \end{pmatrix}
- t_u - t_{dist} \tag{4.26c}
$$

Kinematics

Following similar analogy of the rigid body rotational kinematics of Euler and quaternion presented earlier, kinematics expression in MRP paramterization is presented with the aid of Equation (4.27). Kinematics without the effect of mean motion of LVLH (Schaub and Junkins, 2002):

$$
\dot{\sigma} = \frac{1}{4}
\begin{bmatrix} 1 - \sigma^2 + 2\sigma_1^2 & 2\left(\sigma_1\sigma_2 - \sigma_3\right) & 2\left(\sigma_1\sigma_3 + \sigma_2\right) \\ 2\left(\sigma_2\sigma_1 + \sigma_3\right) & 1 - \sigma^2 + 2\sigma_2^2 & 2\left(\sigma_2\sigma_3 - \sigma_1\right) \\ 2\left(\sigma_3\sigma_1 - \sigma_2\right) & 2\left(\sigma_3\sigma_2 + \sigma_1\right) & 1 - \sigma^2 + 2\sigma_3^2 \end{bmatrix}
\begin{pmatrix} \omega_1 \\ \omega_2 \\ \omega_3 \end{pmatrix}
= \frac{1}{4}[B(\sigma)]\omega \tag{4.27a}
$$

$$[B]^{-1} = \frac{1}{\left(1+\sigma^2\right)^2}[B]^T \tag{4.27b}$$

$$\omega = \frac{4}{\left(1+\sigma^2\right)^2}[B]^T\dot{\sigma} \tag{4.27c}$$

Kinematics with the effect of mean motion of LVLH:

$$\omega = \frac{4}{\left(1+\sigma^2\right)^2}[B]^T\dot{\sigma} - n\begin{pmatrix} C_{12} \\ C_{22} \\ C_{32} \end{pmatrix} \tag{4.27d}$$

$$\omega = \frac{4}{\left(1+\sigma^2\right)^2}[B]^T\dot{\sigma} - n\frac{1}{\left(1+\sigma^2\right)^2}\begin{pmatrix} 8\sigma_1\sigma_2 + 4\sigma_3\left(1-\sigma^2\right) \\ \left(1+\sigma^2\right)^2 - 8\sigma_1^2 - 8\sigma_3^2 \\ 8\sigma_3\sigma_2 + 4\sigma_1\left(1-\sigma^2\right) \end{pmatrix} \tag{4.27e}$$

$$\dot{\sigma} = \frac{1}{4}[B(\sigma)]\left(\omega + n\frac{1}{\left(1+\sigma^2\right)^2}\begin{pmatrix} 8\sigma_1\sigma_2 + 4\sigma_3\left(1-\sigma^2\right) \\ \left(1+\sigma^2\right)^2 - 8\sigma_1^2 - 8\sigma_3^2 \\ 8\sigma_3\sigma_2 + 4\sigma_1\left(1-\sigma^2\right) \end{pmatrix}\right) \tag{4.27f}$$

ω is in $\mathcal{F}_\mathcal{B}$

4.4 | **Reaction Wheel Torque Input-Output Delay**

The objective of this section is to evaluate the input-output dynamic response of the reaction wheel, to check whether certain manoeuvres can be tracked. Typically Brush Less Direct Current (BLDC) motors are used for actuation of the reaction wheels. The actuator delay in reaching a set torque command, T_c must be included to capture how realistically the manoeuvres can be tracked. Figure 4.4 presents a simplified overview of the reaction wheel capturing most of the elements that are required for synthesizing attitude controllers considering actuator dynamics. A more detailed model is presented in (Bailke, 1998), however the model presented below captures the torque input output quite appropriately.
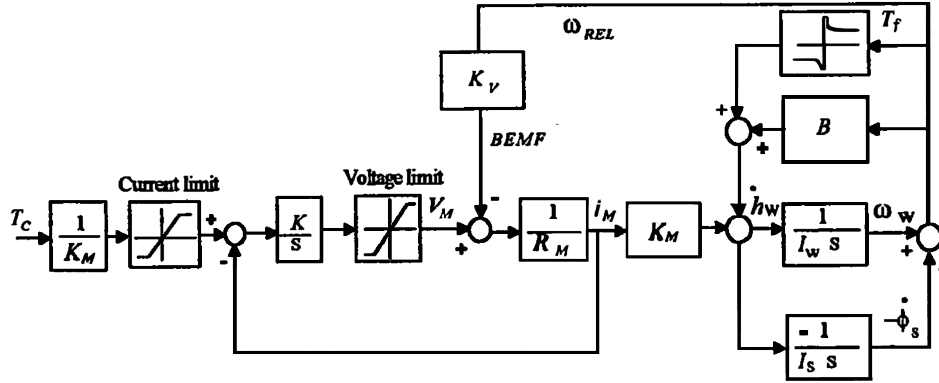
Figure 4.4: *Simplified architecture of reaction wheel set torque command to actual torque and wheel speed output (Sidi, 1997).*

Here, R_M is the armature resistance, K_M is the torque coefficient, I_w is the total moment of inertia of the rotor, i_M is the current in the motor, V_M is the voltage in the motor. I_s is the moment of inertia of the satellite. ω_{REL} is the angular velocity of the rotating part of the motor, relative to the stator and equivalent to the satellite body. Block B indicates viscosity damping co-efficient sensed by the rotor. The block describing coulomb and dry friction is omitted from the analysis to facilitate a linear transfer function of the complete dynamical model with satellite model included in the analysis. One of the advantages of the above presented model is its capability to generate reaction wheel disturbances, at a given wheel speed based on simple disturbance models. Alternatively, a worst case disturbance torque bound can be added this torque output, to capture the torque input/output behaviour. With the valid assumption that $I_w << I_s$ and B $\rightarrow$ 0, the transfer function between the torque command T_c and the achieved angular torque $\dot{h}_w$ is presented with the aid of Equation (4.28) (Sidi, 1997).

$$\frac{\dot{h}_w}{T_c} = \frac{\frac{K}{sR_M}}{1 + \frac{K}{sR_M}\left(1 + \frac{K_v K_M}{KI_w}\right)} \tag{4.28a}$$

In often cases K $>> \frac{K_V K_M}{KI_w}$. This leads to the first order system:

$$\frac{\dot{h}_w}{T_c} = \frac{1}{1 + s(R_M/K)} \tag{4.28b}$$

The basic equation presented in Equation (4.28) facilitates conversion of the complex electric motor expression into a simplified reaction wheel expression. The final expression resembles to a first order system, where τ is the time delay and k_{dc} is the ratio of the magnitude of the steady state step to the magnitude of the step input:

$$G(s) = \frac{b}{s+a} = \frac{k_{dc}}{\tau s + 1} \tag{4.29}$$

R_M/K is thus the characteristic delay parameter of a first order system. This is the delay for a reaction wheel to reach a given set point torque command value, it is often in the order of ms for a precision pointing mission (Sidi, 1997). However, it is unclear whether this is 1.) true for NanoSat class of reaction wheels 2.) whether this holds true for NanoSats under ground target tracking manoeuvres. The following will evaluate the worst case delay for a ground target tracking NanoSat.
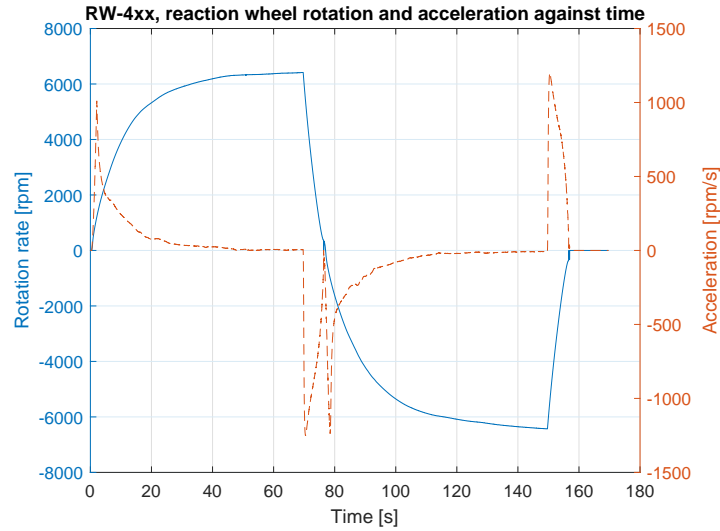
Figure 4.5: *Angular rate and angular acceleration profile for full torque ramp up/down with RW400. The measurements are taken by the hall-sensors on board of the reaction wheel.*

Table 4.3: *Torque delay behaviour for RW-4xx 50 mNms reaction wheels from Hyperion Technologies.*

Segment	Torque Range [mNm]	Initial Torque [mNm]	Final Torque [mNm]	Torque Difference [mNm]	Time Interval [s]	Time delay [s]	Time Delay/Torque Difference [s/mNm]	Time to reach 0.17 mNm [ms]
1	0.00 - 11.38	0	11.38	11.38	2.075 - 0.391	1.684	0.148	25.16
2	0.00 - 14.09	0	14.09	14.09	69.653 - 70.475	0.822	0.0583	9.91
3	3.08 - 13.89	3.08	13.89	10.81	77.029 - 78.514	1.485	0.1374	23.36
4	0.07 - 13.43	0.07	13.43	13.36	149.66 - 150.406	0.746	0.0558	9.49

4.4.1 | RW-400.50 Reaction Wheel Torque, and Response Time

In order to answer the two points posed in the previous paragraph, full torque ramp up to max rpm, and full torque ramp down to zero rpm, and eventually the negative maximum rpm is analysed. Before presenting the torque behaviour we need to analyse the torque required by the NanoSat and the reaction wheel under a terrestrial target tracking slew manoeuvres. The RW400-series of reaction wheel under consideration, is capable of providing ±12 mNm of Torque. Under certain conditions this can be pushed to ±14 mNm. Torque required by a satellite to track a ground station is related to the angular acceleration expected of it. Similarly, angular momentum is related to the angular rotation:

$$\mathbf{H} = \mathbf{I} \cdot \omega \tag{4.30a}$$

$$\mathbf{T} = \mathbf{I} \cdot \alpha \tag{4.30b}$$

As portrayed by the above expressions, torque requirements is dependent on the angular acceleration of the terrestrial target tracking manoeuvre. If the terrestrial target tracking manoeuvre presented in (Chen et al., 2000b) is utilised, a slew rate of $1°/s$ in 40s is expected, leading to an angular acceleration of $0.025°/s^2$. For this analysis we assume, 0 to 1.5 $°/s$ slew rate requirement in 20 s. This gives an angular acceleration of 0.075 $°/s^2$. For a 6U NanoSat (20cm x 30cm x 10cm) with a mass of 12 kg, the inertia is given by [I_{xx} = 0.130 $kg \cdot m^2$, I_{yy} = 0.100 $kg \cdot m^2$, I_{zz} = 0.050 $kg \cdot m^2$]. Thus the worst case expected torque of a single axis can be estimated to be:

$$\mathbf{T_{req}} = 0.130 \cdot 0.075 \cdot \frac{\pi}{180} = 0.00017 Nm = 0.17\, mNm \tag{4.31}$$

The above expected single axis torque is well within the 12 mNm torque capability of RW400. Figure 4.5 captures rpm and angular acceleration profile for a full torque ramp up and down with RW400. While Figure 4.6 captures the underlying torque behaviour. Here the the torque behaviour is split over four segments, where the time intervals indicate the time interval in Figure 4.5 from where the segment is chosen. For the presented segments, the torque range covered and underlying time interval to reach these torque ranges is summarized in Table 4.3. This captures the worst case torque delay to reach the maximum torque from 0 mNm. Clearly, the time required to reach a desired torque level

From this brief analysis, the worst case time delay to reach the max torque requirement of 0.17 mNm from 0 mNm is 25.16 ms. This worst case time delay will be utilised to model the reaction wheel torque input-output behaviour
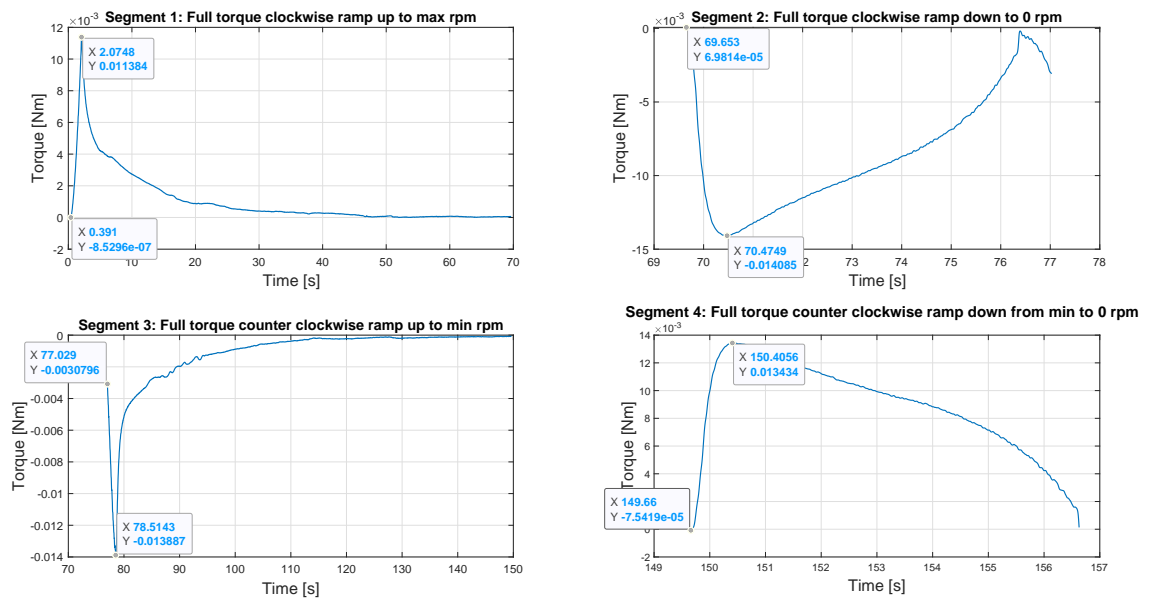
Figure 4.6: *Torque ramp up/down behaviour for four distinctive segments: 1. Clockwise full torque ramp-up to max rpm, 2. Full torque ramp-down/breaking to 0 rpm, wheel speed still in clockwise direction, 3. Full torque counter clockwise ramp up to min. rpm, 4. Full torque counter clockwise ramp down from min. rpm to zero rpm.*
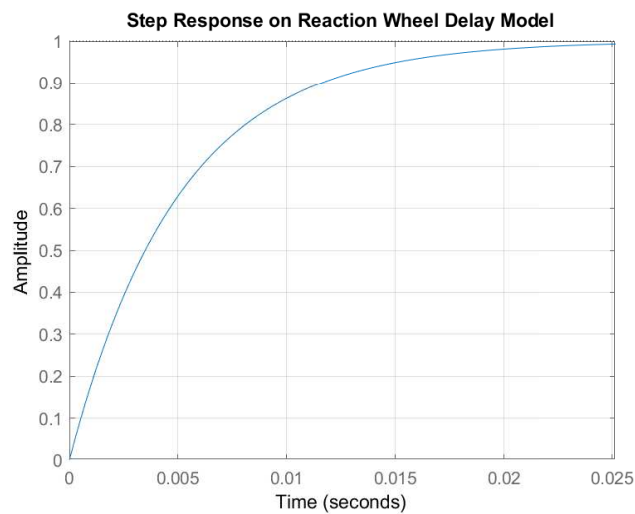
Figure 4.7: *Step response of the reaction wheel torque input-output delay model, utilised for tracking manoeuvres.*

as a first order system presented in Equation 4.28b. For a first order transfer function, the time constant τ is the time required to reach 63% of the DC gain. Alternatively, after four time constants a first order system reaches the DC gain provided by a step input. Thus the reaction wheel time delay is modelled by the following transfer function, and the maximum torque limits saturated to 0.17 mNm. Figure 4.7 captures the step response of the reaction wheel torque input-output delay model.

$$G(s) = \frac{1}{\tau s + 1} = \frac{1}{\frac{(25.16)\cdot 10^{-3}}{4}s + 1} \tag{4.32}$$

The output of the reference tracking controller is passed through an actuator limit of 0.17mNm, before adding a delay represented by Equation (4.32); the consequent output is fed in as torque to the rigid body dynamics.

4.5 | **Manoeuvres**

The manoeuvre sequences dealt within this thesis work is split into five general segments:

- ○ **Mission data acquisition phase :**   Preliminary steady state inertial pointing, with constant angular rate for 3600s. Inertial pointing with zero angular rate.
- ○ **Calibration phase:** Non-harmonic sinusoidal angular rate calibration manoeuvre for 7200s.
- ○ **Mission data transmission preparation:**   Pre-ground target tracking manoeuvre.
- ○ **Data transmission phase:** Agile terrestrial ground target tracking manoeuvre, for a NanoSat at a polar circular orbit at an altitude of 400 km, to an Optical Ground Station in Delft.
- ○ **Mission data acquisition phase:** Steady state inertial pointing with constant angular rate.

A simplified kinematics based simulator is used to generate the signals in data acquisition and calibration segment, denoted by phase A. While for the last three segments (denoted by phase B): pre-ground target tracking, ground target tracking, and steady state pointing after ground target tracking; kinematics and dynamics simulator, with flight controller and reaction wheel time delay model in the loop is utilised.

The calibration filter synthesized here is independent of the calibration manoeuvre and can operate with any arbitrary persistently exciting manoeuvre that a satellite might undergo during nominal operations. However, a calibration manoeuvre enables faster convergence of the calibration parameters. The filter by itself does not place any constraint on the calibration manoeuvres. With the aid of Equation (3.22c), it is observed that, gyro misalignment and scale factors are not observable when the spacecraft is not rotating. Furthermore for a constant angular rate vector the parameters are not independently observable and can be estimated as gyro bias. As noted by Pittelkau (2001), for angular rate constant in direction but variable in magnitude gyro scale factors are observable but the misalignments are not independently observable unless the angular rate is parallel to a gyro sense axis. This lack of observability indicates that some linear combination of states can be estimated while some other linear combinations cannot, other than their a priori estimate. For complete observability of parameters, the information matrix (which is a function of Ω_g from Equation (3.23)) shown below needs to be positive definite to satisfy the persistency of excitation condition:

$$\int_{t_1}^{t_2} \mathbf{\Omega_g}^T \mathbf{\Omega_g} \,\mathrm{d}t > 0 \quad \text{or} \quad \sum_k \mathbf{\Omega_{g_k}}^T \mathbf{\Omega_{g_k}} > 0 \tag{4.33}$$

For the interval of calibration manoeuvres synthesised here, the above information matrix was observed to be true. Furthermore, as discussed in (Pittelkau, 2007), increasing the frequency of sinusoidal manoeuvre improves the convergence time of calibration parameters by a factor of $\sqrt{2}$, while increasing the amplitude improves it by a factor of 2. As a consequence two different non-harmonic sinusoidal manoeuvres are investigated for this thesis work. The first one is a slow calibration manoeuvre, identical to the one utilised by (Lai et al., 2003):

$$\omega_x = 0.09 \cdot \sin(2 \cdot \pi \cdot 0.0006 \cdot t), \quad \omega_y = 0.09 \cdot \sin(2 \cdot \pi \cdot 0.0007 \cdot t), \quad \omega_z = 0.09 \cdot \sin(2 \cdot \pi \cdot 0.0008 \cdot t) \ \ [rad/s] \tag{4.34}$$

A faster calibration manoeuvre, with different amplitude (limited by the star tracker slew rate capability) and frequency of oscillation per axis is utilised:

$$\omega_x = 0.29 \cdot \sin(2 \cdot \pi \cdot 0.00318 \cdot t), \quad \omega_y = 0.2828 \cdot \sin(2 \cdot \pi \cdot 0.00212 \cdot t), \quad \omega_x = 0.2 \cdot \sin(2 \cdot \pi \cdot 0.00105 \cdot t) \ \ [rad/s] \tag{4.35}$$

Figure 4.8 captures the angular rate and attitude for slow calibration manoeuvre, while Figure 4.9 captures that for the faster calibration manoeuvre. A simple kinematics based simulator is utilised to generate the steady manoeuvre followed by the calibration manoeuvre. The boundary conditions are retained and fed into the simulator that generates phase B of the manoeuvre sequences.   Phase B, of the manoeuvre sequences (pre-ground target tracking, ground target tracking, steady state inertial pointing) is simulated with the aid of rigid body kinematics and dynamics. The flight controller constructed for reference tracking is constructed for MRP parameterisation and is presented with the aid of Appendix C.3. MRP based nonlinear kinematics and dynamics, presented earlier in Section 4.3.3, is utilised to capture the attitude motion of NanoSat in a circular orbit. Reaction wheel delay model and torque saturation limits discussed in Section 4.4.1 is utilised. Reference tracking error and the underlying control torque effort is presented in Appendix C.4. Pre-ground target tracking manoeuvre is generated with simplified trigonometry. While, the ground target tracking manoeuvre is a representation of the attitude motion required to track an OGS in Delft from a 400 km polar circular orbit. The manoeuvre presented here is an approximation of the ground target tracking manoeuvre generated with the aid of (Chen et al., 2000a). Three different segments of phase B attitude tracked with the rigid body simulator, is presented with the aid of Figures C.1 and C.2, for post slow and fast calibration manoeuvre respectively in Appendix C.4. Furthermore, the reference phase B attitude manoeuvre in Euler-321, and MRP that
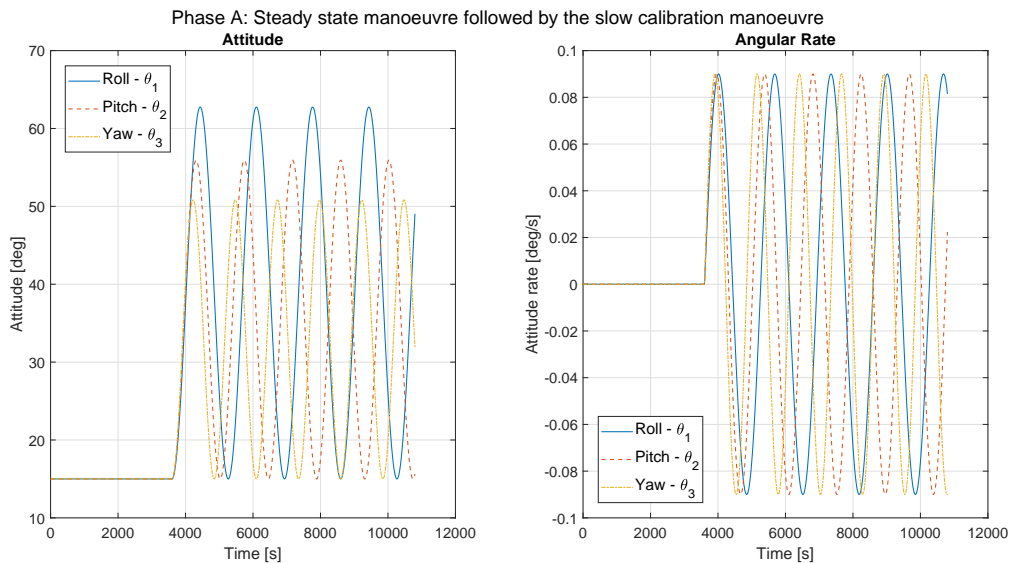
Figure 4.8: *Simulated Phase A (steady state followed by non-harmonic sinusoidal corkscrew calibration manoeuvre) tracking attitude and attitude rate for slow calibration manoeuvre manoeuvre.*
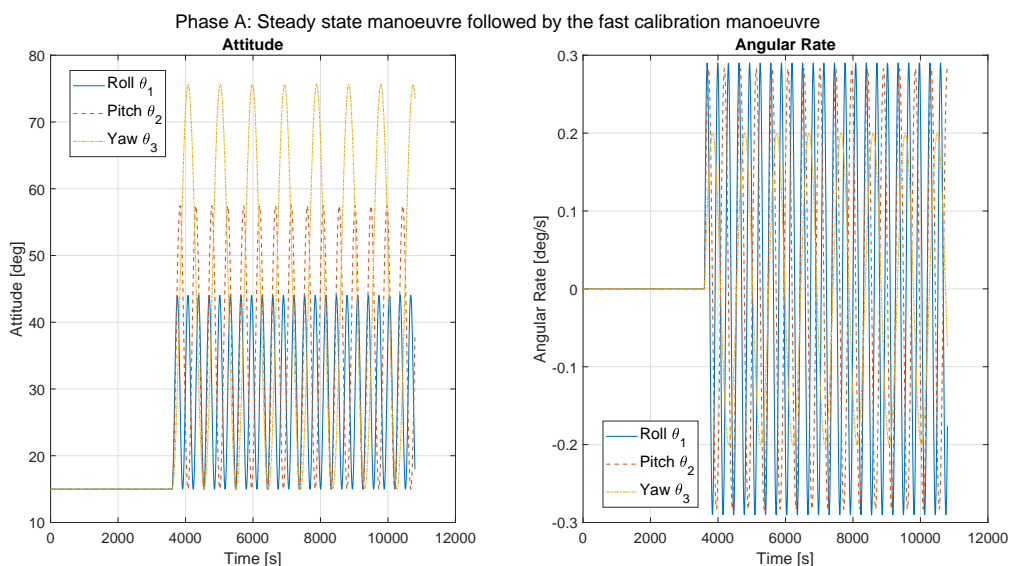
Figure 4.9: *Simulated Phase A (steady state followed by non-harmonic sinusoidal corkscrew calibration manoeuvre) tracking attitude and attitude rate manoeuvre for faster calibration manoeuvre.*

the controller requires tracking, (post slow and fast calibration manoeuvre) is presented with the aid of C.3 and C.4, in Appendix C.4. The error in tracking the reference, and the underlying absolute control torque effort is presented with the aid of Figures C.5 and C.6. A worst case absolute pointing error of 360 arcsec was observed, as captured with Figures C.5 and C.6. This preliminary analysis, indicated that the ceiling of 20.63 arcsec (1σ) attitude knowledge requirement is set rather low by the stakeholders, and can be increased by approximately 1400 arcsec (1σ). This suggests that a detailed pointing error source budgeting should be conducted before imposing such stringent attitude knowledge requirements.

The final attitude and attitude rate tracked by the NanoSat for the slow calibration manoeuvre is presented with the aid of Figures 4.10 and 4.11. These signals are fed into the star tracker and gyro simulator, and the objective of the synthesised filter is to track these attitude signals. Figure 4.11 further outlines the star tracker attitude acquisition limits, bounded by the slew rate limitation. Once the slew rate limit is reached on the roll axis, the star tracker stops generating attitude measurement. In such a case, only gyro measurements are available for attitude estimation.
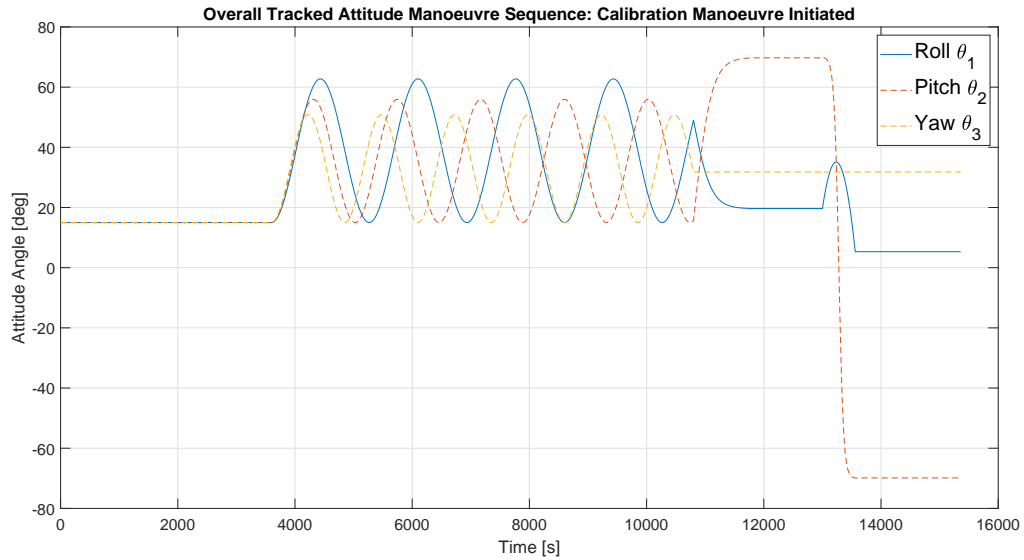
Figure 4.10: *Entire simulated attitude manoeuvre for the NanoSat under slow calibration manoeuvre. Phase A comprises of 1hr of steady state inertial pointing followed by non-harmonic sinusoidal corkscrew manoeuvre for the next 2hr. This is followed by Phase B, which comprises of a pre-ground target tracking manoeuvre, followed by ground target tracking, and eventually steady state inertial pointing.*
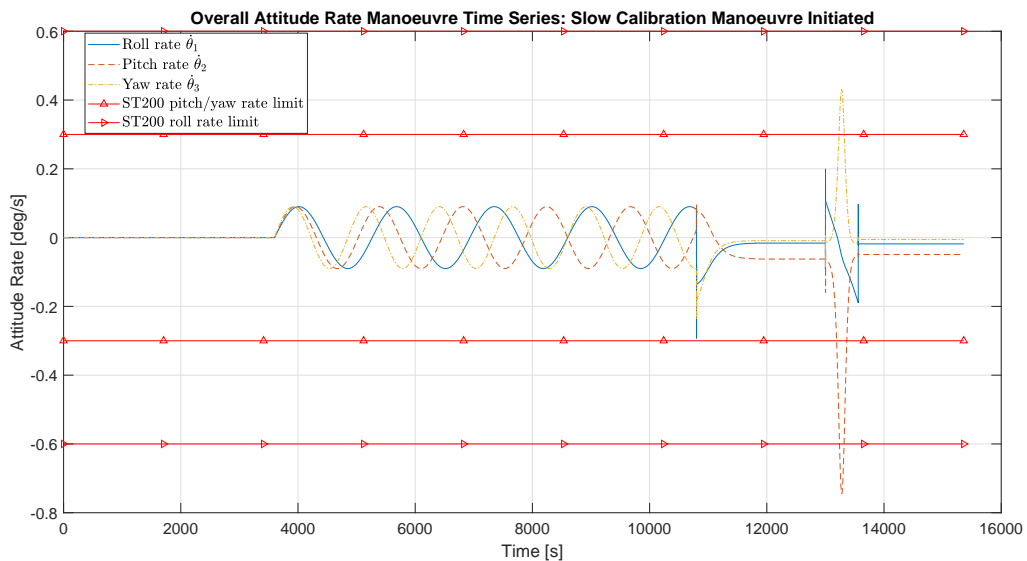
Figure 4.11: *Entire simulated angular rate manoeuvre for the NanoSat under slow calibration manoeuvre. Phase A comprises of 1hr of steady state inertial pointing followed by non-harmonic sinusoidal corkscrew manoeuvre for the next 2hr. This is followed by Phase B, which comprises of a pre-ground target tracking manoeuvre, followed by ground target tracking, and eventually steady state inertial pointing. Star tracker blinding limit under slewing conditions are further captured.*

Similarly, Figures 4.12 and 4.13 capture the attitude and attitude rate tracked by the NanoSat for the case of faster calibration manoeuvre. In both cases, it is observed that for ground target tracking ST200 would suffer from the loss of attitude knowledge acquisition capability due to operational slew rate limitations. It is important to note that the attitude and attitude rate, is in the NanoSat body frame with respect to the Earth inertial reference frame.
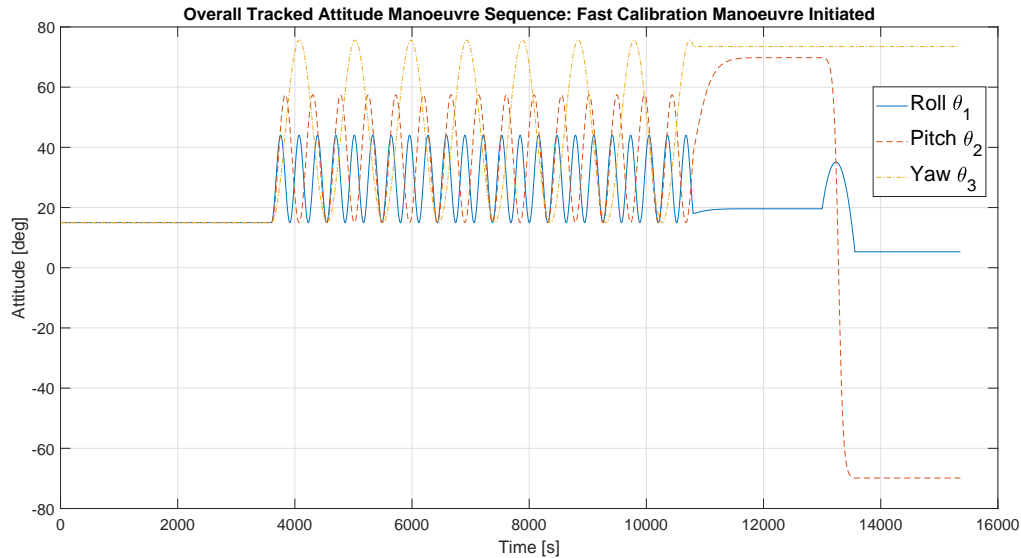
Figure 4.12: *Entire simulated attitude manoeuvre for the NanoSat under fast calibration manoeuvre. Phase A comprises of 1hr of steady state inertial pointing followed by non-harmonic sinusoidal corkscrew manoeuvre for the next 2hr. This is followed by Phase B, which comprises of a pre-ground target tracking manoeuvre, followed by ground target tracking, and eventually steady state inertial pointing.*
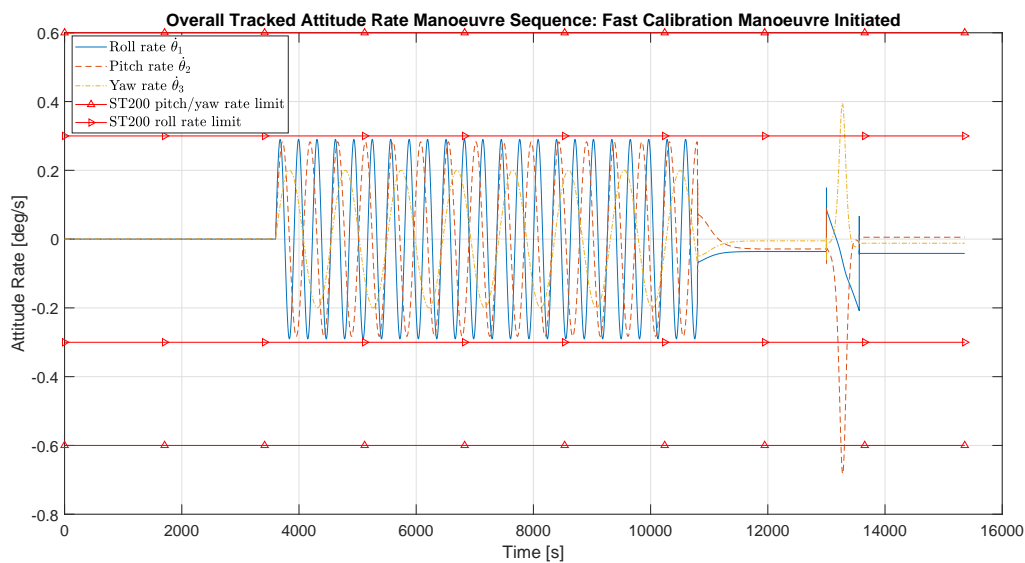
Figure 4.13: *Entire simulated angular rate manoeuvre for the NanoSat under fast calibration manoeuvre. Phase A comprises of 1hr of steady state inertial pointing followed by non-harmonic sinusoidal corkscrew manoeuvre for the next 2hr. This is followed by Phase B, which comprises of a pre-ground target tracking manoeuvre, followed by ground target tracking, and eventually steady state inertial pointing. Star tracker blinding limit under slewing conditions are further captured.*

4.6 | Rigid Body NanoSat Simulator Output and Filter Interface Overview

The objective of this section is to provide an insight into the role of the developed rigid body NanoSat simulator in the development of calibration filter. Figure 4.14 presents an overview of the interface of the rigid body simulator with the filters that are developed.

The rigid body simulator is divided into two main simulators. The first simulator generates the true attitude and attitude rate of a rigid body NanoSat for preliminary steady state and calibration manoeuvre. Simple quaternion
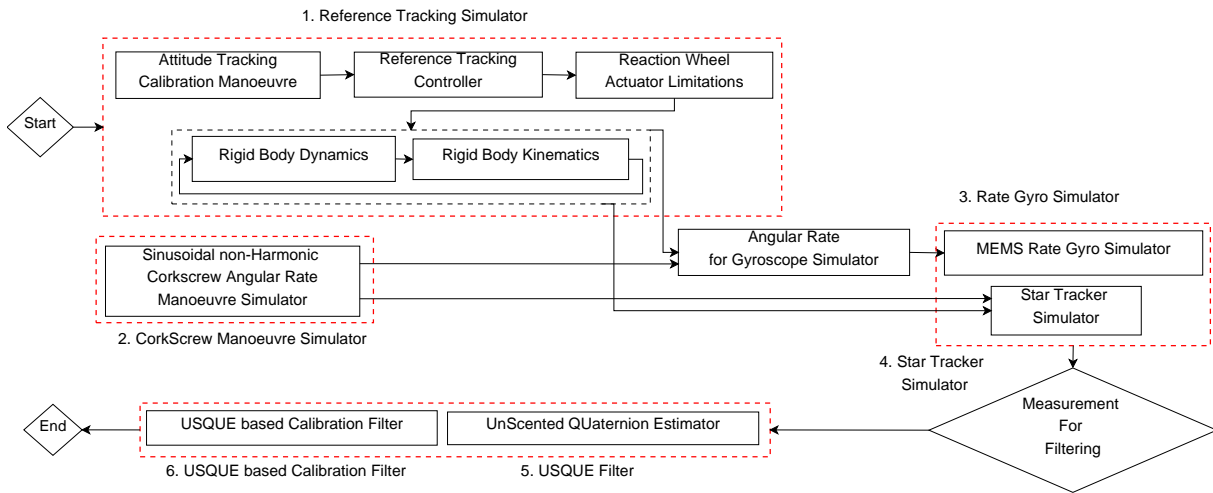
Figure 4.14: *Overview of the interconnection of different simulators to fully realise the calibration filter development process.*

attitude kinematics based simulator is utilised for this. Where the angular rate is integrated to provide the attitude knowledge. This is denoted by 2.) Corkscrew manoeuvre simulator in Figure 4.14. The second simulator generates the true attitude and attitude rate for a rigid body which undergoes pre-ground target tracking manoeuvre, followed by ground target tracking, followed by steady state inertial pointing. This is denoted by 1.) Reference tracking simulator in Figure 4.14. Appendix C provides a detailed overview of the working principles of the simulator. In light of that, first a stability analysis for the plant is conducted. This is followed by reference tracking controller synthesis, as presented in Appendix C.3. Where, first the reference tracking controller is synthesized in Euler-321 and later extended to MRP coordinate parametrisation. Different manoeuvres tracked by this simulator, and the underlying attitude tracking control effort, and reference tracking error is presented with the aid of Appendix C.4. Ideal attitude and attitude rate outputs are fed into the star tracker and gyro simulators, where the respective non-idealities are added. First the ideal attitude and attitude rate signal is passed through a simulator that adds misalignments and scale-factors. The process of misalignment and scale factor addition is discussed further in Section 4.7. Misalignment, and scale factor output results and verification is discussed in Section 4.7.4. The signal distorted with these deterministic errors, is later passed to the star tracker and gyro stochastic noise simulator discussed earlier in Chapter 3. Attitude and attitude rate outputs from this simulator is later fed into the filters developed as part of this thesis work.

4.7 | Sensor Configuration, Noise, Misalignment and Scale Factor Induced Measurement Models

The objective of this section is dive deeper into star tracker and gyro measurement models presented earlier in Figure 4.14. The choice of sensor configuration was justified earlier in Section 3.3, by virtue of steady state noise PSD analysis. Corresponding gyro and star tracker noise models were developed and verified, in depth, in Sections 3.4 and 3.6. A brief overview of gyro misalignment and scale factor model was presented earlier in Section 3.2.4, with a brief discussion on how it can be extended for utilisation in calibration filter in Section 3.2.5.

The objective of this section is to first define the gyro-stellar sensor configuration orientation used to measure the attitude and attitude rate output provided by the rigid body simulator. Section 4.7.1 defines the NanoSat body frame in combination with the star tracker and gyro sense axis. QR decomposition on nominal gyro rotational sense axis is utilised, to determine the non-orthogonal nominal sense axis, which is later utilised for parameterisation of the unknown true gyro sense axis.

Section 4.7.2 aims at deriving the gyro misalignment and scale factor model used to distort the ideal attitude rate before feeding into the gyro noise simulator. A linearised variant that can be utilised for the gyro model in the calibration filter is further derived. While Section 4.7.3 aims at deriving the star tracker misalignment measurement model. A linearised model used to estimate the star tracker misalignment calibration parameters is further discussed.
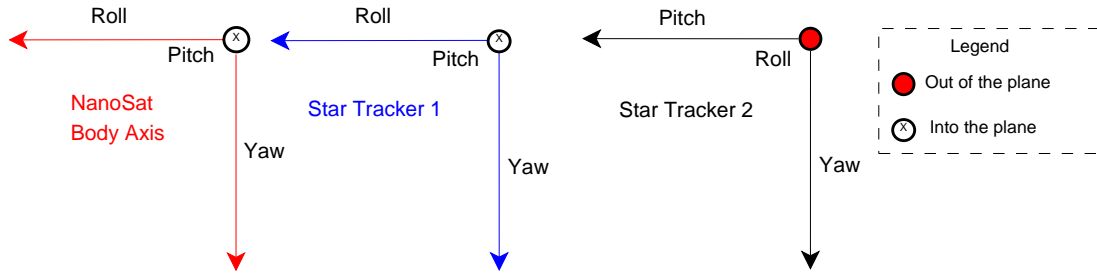
Figure 4.15: *Orientation of the star trackers with respect to the NanoSat body axis.*
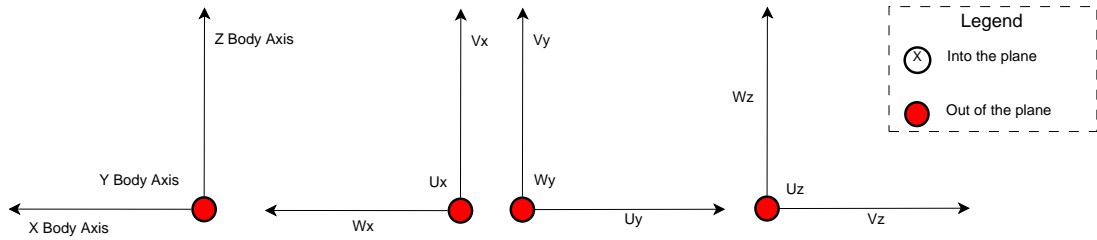
Figure 4.16: *Orientation of the rate gyro rotational sense axes, and the corresponding non-orthonormal sense axes.*

4.7.1 | Gyro-Stellar Configuration Orientation

The orientation of the star trackers with respect to the body axis is presented with the aid of Figure 4.15. Star tracker 1 is oriented with the NanoSat body axis, while star tracker 2 is oriented such that the yaw axis of both the star trackers remain unchanged, the roll axis of body aligned star tracker aligns with the pitch axis of the other star tracker, and the pitch and roll axis of the star trackers are pointed in anti-parallel orientation. This is done so to compensate for the low attitude knowledge performance of the star tracker roll axis, with high attitude knowledge performance of the pitch axis.

Calibration filter developed as part of this thesis work relies upon three gyro sense axis. The three gyro sense axes are oriented in parallel fashion as presented earlier in Figure 3.4. As discussed previously in Section 3.2.4, the misalignment around the gyro sense axis does not influence the gyro output, however the influence of misalignment along the non-orthogonal sense axes cannot be ignored. This leads to the minimal misalignment parametrisation expressed with the aid of Equations (3.7)-(3.10d). Gyro misalignment for each of the gyro sense axis can be visualised with the aid of Figure 3.5, and the relations between the nominal gyro sense axis, $\boldsymbol{w}_i$, and the true gyro sense axis, $\overline{\boldsymbol{w}}_i$, is outlined with the aid of Equations (3.7) - (3.9). The nominal gyro sense axis for each of the axis is ideally aligned with the NanoSat body axis. However, due to misalignment this is not the case in practice. Nominal gyro sense axis is known, however the true gyro sense axis is unknown. A calibration filter aims at estimating the rotational elements that facilitate this rotation from the known nominal sense axis to the unknown true sense axis. With the aid of Q factor in QR decomposition of $\begin{bmatrix} \boldsymbol{w}_i & 0 & 0 \end{bmatrix}$, the corresponding nominal non-orthogonal sense axes $\boldsymbol{u}_i$ and $\boldsymbol{v}_i$ can be expressed as:

$$\boldsymbol{w}_x = \begin{pmatrix} 1 \\ 0 \\ 0 \end{pmatrix}, \quad \begin{bmatrix} 1 & 0 & 0 \\ 0 & 0 & 0 \\ 0 & 0 & 0 \end{bmatrix} = \mathbf{QR} = \begin{bmatrix} 1 & 0 & 0 \\ 0 & 1 & 0 \\ 0 & 0 & 1 \end{bmatrix} \begin{bmatrix} 1 & 0 & 0 \\ 0 & 0 & 0 \\ 0 & 0 & 0 \end{bmatrix}, \quad \boldsymbol{u}_x = \begin{pmatrix} 0 \\ 1 \\ 0 \end{pmatrix}, \quad \boldsymbol{v}_x = \begin{pmatrix} 0 \\ 0 \\ 1 \end{pmatrix} \tag{4.36a}$$

$$\boldsymbol{w}_y = \begin{pmatrix} 0 \\ 1 \\ 0 \end{pmatrix}, \quad \begin{bmatrix} 0 & 0 & 0 \\ 1 & 0 & 0 \\ 0 & 0 & 0 \end{bmatrix} = \mathbf{QR} = \begin{bmatrix} 0 & -1 & 0 \\ -1 & 0 & 0 \\ 0 & 0 & 1 \end{bmatrix} \begin{bmatrix} -1 & 0 & 0 \\ 0 & 0 & 0 \\ 0 & 0 & 0 \end{bmatrix}, \quad \boldsymbol{u}_y = \begin{pmatrix} -1 \\ 0 \\ 0 \end{pmatrix}, \quad \boldsymbol{v}_y = \begin{pmatrix} 0 \\ 0 \\ 1 \end{pmatrix} \tag{4.36b}$$

$$\boldsymbol{w}_z = \begin{pmatrix} 0 \\ 0 \\ 1 \end{pmatrix}, \quad \begin{bmatrix} 0 & 0 & 0 \\ 0 & 0 & 0 \\ 1 & 0 & 0 \end{bmatrix} = \mathbf{QR} = \begin{bmatrix} 0 & 0 & -1 \\ 0 & 1 & 0 \\ -1 & 0 & 0 \end{bmatrix} \begin{bmatrix} -1 & 0 & 0 \\ 0 & 0 & 0 \\ 0 & 0 & 0 \end{bmatrix}, \quad \boldsymbol{u}_z = \begin{pmatrix} 0 \\ 1 \\ 0 \end{pmatrix}, \quad \boldsymbol{v}_z = \begin{pmatrix} -1 \\ 0 \\ 0 \end{pmatrix} \tag{4.36c}$$

Cross product of u and v, results in w, which provides a verification for the right handed triad that's being aimed for. A visual overview of the nominal rotational gyro sense axes and the corresponding nominal non-orthonormal gyro sense axes are outlined with the aid of Figure 4.16.
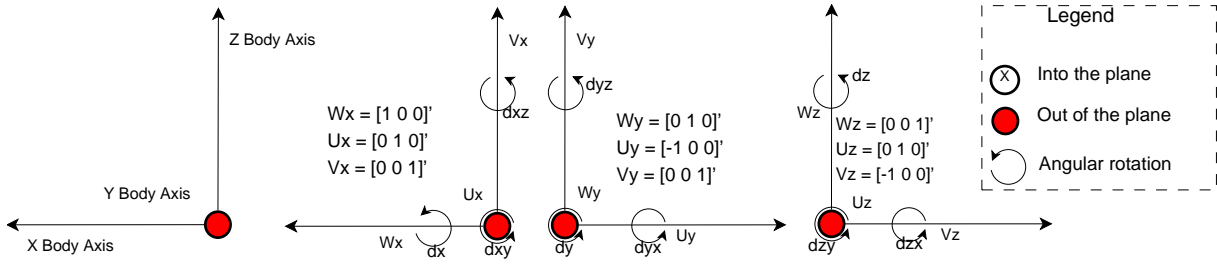
Figure 4.17: *NanoSat rigid body axis in combination with the gyro nominal rotational sense axes along with the corresponding orthogonal sense axes obtained via QR decomposition on the nominal sense axis.*

For the above extracted non-orthonormal gyro sense axis, the expressions in Equation (3.10) can be defined as:

$$
\begin{aligned}
\boldsymbol{\omega}^{\mathbf{g}} &= \boldsymbol{W}^T \boldsymbol{\omega}^{\mathrm{b}} - \boldsymbol{C}_{\boldsymbol{v}}\left(\boldsymbol{\omega}^{\mathrm{b}}\right)\boldsymbol{\delta}_{\boldsymbol{u}} - \boldsymbol{C}_{\boldsymbol{u}}\left(\boldsymbol{\omega}^{\mathrm{b}}\right)\boldsymbol{\delta}_{\boldsymbol{v}} \\
&= \boldsymbol{W}^T \boldsymbol{\omega}^{\mathrm{b}} - \boldsymbol{C}_{\mathrm{g}}\left(\boldsymbol{\omega}^{\mathrm{b}}\right)\boldsymbol{\delta}_{\mathrm{g}}
\end{aligned}
\tag{4.37a}
$$

$$
\begin{pmatrix} \omega_x^{\mathrm{g}} \\ \omega_y^{\mathrm{g}} \\ \omega_z^{\mathrm{g}} \end{pmatrix} = \begin{pmatrix} \omega_1^{\mathrm{g}} \\ \omega_2^{\mathrm{g}} \\ \omega_3^{\mathrm{g}} \end{pmatrix} = \begin{bmatrix} \boldsymbol{w}_1^T \\ \boldsymbol{w}_2^T \\ \boldsymbol{w}_3^T \end{bmatrix} \boldsymbol{\omega}^{\mathrm{b}} - \begin{bmatrix} \omega^{\mathrm{b}}\cdot\boldsymbol{v}_1 & 0 & 0 \\ 0 & \omega^{\mathrm{b}}\cdot\boldsymbol{v}_2 & 0 \\ 0 & 0 & \omega^{\mathrm{b}}\cdot\boldsymbol{v}_3 \end{bmatrix} \begin{pmatrix} \delta_{u1} \\ \delta_{u2} \\ \delta_{u3} \end{pmatrix} - \ldots
$$
$$
\ldots \begin{bmatrix} \omega^{\mathrm{b}}\cdot u_1 & 0 & 0 \\ 0 & \omega^{\mathrm{b}}\cdot u_2 & 0 \\ 0 & 0 & \omega^{\mathrm{b}}\cdot u_3 \end{bmatrix} \begin{pmatrix} \delta_{v1} \\ \delta_{v2} \\ \delta_{v3} \end{pmatrix}
\tag{4.37b}
$$

In matrix notation the rotational gyro sense axes, and the corresponding orthogonal gyro sense axes can be expressed as:

$$
\boldsymbol{U} = \begin{bmatrix} \boldsymbol{u}_1 & \boldsymbol{u}_2 & \boldsymbol{u}_3 \end{bmatrix} = \begin{bmatrix} \boldsymbol{u}_x & \boldsymbol{u}_y & \boldsymbol{u}_z \end{bmatrix} = \begin{bmatrix} \begin{pmatrix} 0 \\ 1 \\ 0 \end{pmatrix} & \begin{pmatrix} -1 \\ 0 \\ 0 \end{pmatrix} & \begin{pmatrix} 0 \\ 1 \\ 0 \end{pmatrix} \end{bmatrix}
\tag{4.38a}
$$

$$
\boldsymbol{V} = \begin{bmatrix} \boldsymbol{v}_1 & \boldsymbol{v}_2 & \boldsymbol{v}_3 \end{bmatrix} = \begin{bmatrix} \boldsymbol{v}_x & \boldsymbol{v}_y & \boldsymbol{v}_z \end{bmatrix} = \begin{bmatrix} \begin{pmatrix} 0 \\ 0 \\ 1 \end{pmatrix} & \begin{pmatrix} 0 \\ 0 \\ 1 \end{pmatrix} & \begin{pmatrix} -1 \\ 0 \\ 0 \end{pmatrix} \end{bmatrix}
\tag{4.38b}
$$

$$
\boldsymbol{W} = \begin{bmatrix} \boldsymbol{w}_1 & \boldsymbol{w}_2 & \boldsymbol{w}_3 \end{bmatrix} = \begin{bmatrix} \boldsymbol{w}_x & \boldsymbol{w}_y & \boldsymbol{w}_z \end{bmatrix} = \begin{bmatrix} \begin{pmatrix} 1 \\ 0 \\ 0 \end{pmatrix} & \begin{pmatrix} 0 \\ 1 \\ 0 \end{pmatrix} & \begin{pmatrix} 0 \\ 0 \\ 1 \end{pmatrix} \end{bmatrix}
\tag{4.38c}
$$

$\boldsymbol{\delta_u}$ and $\boldsymbol{\delta_v}$ represent the ortho-normal misalignment rotation angle around the respective $\boldsymbol{u}$ and $\boldsymbol{v}$ axis. Rotational misalignment, $\boldsymbol{\delta_w}$, about the nominal gyro sense axis has no influence on the sensed angular rate.

4.7.2 | Misalignment and Scale Factor Error Induced Gyro Measurement Model

Gyro Misalignment Measurement Model

The general gyro misalignment model was presented earlier with the aid of Section 3.2.3. Relevant expressions are outlined again in the context of the nomenclature provided in Figure 4.16, to facilitate gyro readout in the presence of relevant misalignment and scale factors. The sensed gyro measurement, $\boldsymbol{\omega}^{\mathbf{g}}$, is related to the rigid body angular rate of the NanoSat, $\boldsymbol{\omega}^{\mathrm{b}}$, by virtue of the misalignment matrix $\boldsymbol{I} + \boldsymbol{\Delta}$. The following aims at deriving the misalignment matrix used for the gyro measurement model from the rotational matrix presented in Equation 4.1.

Figure 4.17 outlines the gyro sense axes with respect to the NanoSat body axis, along with the rotational misalignments of the gyro sense axis. When it comes to gyro misalignment, rotation about the gyro sense axis has no impact on gyro measurements, as a result misalignments along the non-orthonormal sense axis are utilised to transform the known nominal gyro sense axis to the unknown true gyro sense axis. This can be visualised with the aid of Figure 3.5.

When the nominal sense axis is along the Z axis, rotational misalignment matrix can be expressed with the aid of angular misalignment along X and Y axis. Rotation along the non-orthonormal sense axis X, followed by a rotation

around the non-orthonormal sense axis Y leads to the rotation matrix translating the known nominal gyro sense axis to the unknown true gyro sense axis:

$$R_X(\theta_1) = \begin{bmatrix} 1 & 0 & 0 \\ 0 & c\theta_1 & s\theta_1 \\ 0 & -s\theta_1 & c\theta_1 \end{bmatrix} \tag{4.39a}$$

$$R_Y(\theta_2) = \begin{bmatrix} c\theta_2 & 0 & -s\theta_2 \\ 0 & 1 & 0 \\ s\theta_2 & 0 & c\theta_2 \end{bmatrix} \tag{4.39b}$$

Transformation matrix from nominal to true gyro sense axis can be expressed as:

$$R_{TN} = R_Y \cdot R_X = \begin{bmatrix} c\theta_2 & 0 & -s\theta_2 \\ 0 & 1 & 0 \\ s\theta_2 & 0 & c\theta_2 \end{bmatrix} \cdot \begin{bmatrix} 1 & 0 & 0 \\ 0 & c\theta_1 & s\theta_1 \\ 0 & -s\theta_1 & c\theta_1 \end{bmatrix} = \begin{bmatrix} c\theta_2 & s\theta_1 s\theta_2 & -c\theta_1 s\theta_2 \\ 0 & c\theta_1 & s\theta_1 \\ s\theta_2 & -c\theta_2 s\theta_1 & c\theta_1 c\theta_2 \end{bmatrix} \tag{4.39c}$$

True gyro sense axis expressed in terms of nominal gyro sense axis the corresponding misalignment matrix:

$$\begin{pmatrix} \overline{u} \\ \overline{v} \\ \overline{w} \end{pmatrix} = \begin{bmatrix} c\theta_2 & s\theta_1 s\theta_2 & -c\theta_1 s\theta_2 \\ 0 & c\theta_1 & s\theta_1 \\ s\theta_2 & -c\theta_2 s\theta_1 & c\theta_1 c\theta_2 \end{bmatrix} \cdot \begin{pmatrix} u \\ v \\ w \end{pmatrix} \tag{4.39d}$$

True gyro sense axis of interest, can be obtained in terms of the nominal gyro sense axis,

$$\overline{w} = s\theta_2 \cdot u - c\theta_2 s\theta_1 \cdot v + c\theta_1 c\theta_2 \cdot w \tag{4.39e}$$

For convenience of linearisation and inversion, the above expression can be re-expressed as:

$$\overline{w} = -(-s\theta_2 \cdot u) - c\theta_2 s\theta_1 \cdot v + c\theta_1 c\theta_2 \cdot w \tag{4.39f}$$

For small angles of misalignment, the misalignment model can be simplified further:

$$\overline{w} = w - s\theta_1 \cdot v - (-s\theta_2 \cdot u) \tag{4.39g}$$

$$\overline{w} = w - \theta_1 \cdot v - (-\theta_2 \cdot u) \tag{4.39h}$$

The above presented expression is equivalent to the minimal parametrisation expression presented in Equation (3.9). This can be extended to n gyro sense axis with the aid of Equations (3.10). We now extend the above rotation matrix to the general case of Euler 3-2-1 rotation presented earlier with the aid of Equation (4.1).

$$\mathbf{C}(\theta) = \begin{bmatrix} c\theta_2 c\theta_3 & c\theta_2 s\theta_3 & -s\theta_2 \\ s\theta_1 s\theta_2 c\theta_3 - c\theta_1 s\theta_3 & s\theta_1 s\theta_2 s\theta_3 + c\theta_1 c\theta_3 & s\theta_1 c\theta_2 \\ c\theta_1 s\theta_2 c\theta_3 + s\theta_1 s\theta_3 & c\theta_1 s\theta_2 s\theta_3 - s\theta_1 c\theta_3 & c\theta_1 c\theta_2 \end{bmatrix} \tag{4.40a}$$

For small angles of misalignment this can be expressed as:

$$\mathbf{C}(\theta) = \begin{bmatrix} 1 & s\theta_3 & -s\theta_2 \\ -s\theta_3 & 1 & s\theta_1 \\ s\theta_2 & -s\theta_1 & 1 \end{bmatrix} \approx \begin{bmatrix} 1 & \theta_3 & -\theta_2 \\ -\theta_3 & 1 & \theta_1 \\ \theta_2 & -\theta_1 & 1 \end{bmatrix} = \begin{bmatrix} 1 & 0 & 0 \\ 0 & 1 & 0 \\ 0 & 0 & 1 \end{bmatrix} + \begin{bmatrix} 0 & \theta_3 & -\theta_2 \\ -\theta_3 & 0 & \theta_1 \\ \theta_2 & -\theta_1 & 0 \end{bmatrix} \tag{4.40b}$$

$$\mathbf{C}(\theta) \approx \begin{bmatrix} 1 & 0 & 0 \\ 0 & 1 & 0 \\ 0 & 0 & 1 \end{bmatrix} - \begin{bmatrix} 0 & -\theta_3 & +\theta_2 \\ +\theta_3 & 0 & -\theta_1 \\ -\theta_2 & +\theta_1 & 0 \end{bmatrix} \tag{4.40c}$$

Utilising the above expression, misalignment matrix for the configuration provided in Figure 4.17 can be derived for each of the gyro sense axis. For the gyro sensor axis aligned along the NanoSat body X-axis: Angular rotation vector is defined as:

$$\delta\mathbf{X} = \begin{pmatrix} 0 \\ \delta_{XY} \\ \delta_{XZ} \end{pmatrix} \tag{4.41a}$$

Corresponding misalignment rotation matrix is defined as:

$$\mathbf{C}(\delta\mathbf{X}) \approx \begin{bmatrix} 1 & \delta_{XZ} & -\delta_{XY} \\ -\delta_{XZ} & 1 & 0 \\ \delta_{XY} & 0 & 1 \end{bmatrix} = \mathbf{I} + \begin{bmatrix} 0 & \delta_{XZ} & -\delta_{XY} \\ -\delta_{XZ} & 0 & 0 \\ \delta_{XY} & 0 & 0 \end{bmatrix} = \mathbf{I} - \begin{bmatrix} 0 & -\delta_{XZ} & \delta_{XY} \\ \delta_{XZ} & 0 & 0 \\ -\delta_{XY} & 0 & 0 \end{bmatrix} = \mathbf{I} - \tilde{\mathbf{\Delta}}_\mathbf{X} \tag{4.41b}$$

For the gyro sensor axis aligned along the NanoSat body Y-axis: Angular rotation vector is defined as:

$$\delta_{\mathbf{Y}} = \begin{pmatrix} \delta_{YX} \\ 0 \\ \delta_{YZ} \end{pmatrix} \tag{4.42a}$$

Corresponding misalignment rotation matrix associated with the gyro sense axis is defined as:

$$\mathbf{C}(\delta_{\mathbf{Y}}) \approx \begin{bmatrix} 1 & \delta_{YZ} & 0 \\ -\delta_{YZ} & 1 & \delta_{YX} \\ 0 & -\delta_{YX} & 1 \end{bmatrix} = \mathbf{I} + \begin{bmatrix} 0 & \delta_{YZ} & 0 \\ -\delta_{YZ} & 0 & \delta_{YX} \\ 0 & -\delta_{YX} & 0 \end{bmatrix} = \mathbf{I} - \begin{bmatrix} 0 & -\delta_{YZ} & 0 \\ \delta_{YZ} & 0 & -\delta_{YX} \\ 0 & \delta_{YX} & 0 \end{bmatrix} = \mathbf{I} - \tilde{\mathbf{\Delta}}_{\mathbf{Y}} \tag{4.42b}$$

For the gyro sensor axis aligned along the NanoSat body Z-axis: Angular rotation vector is defined as:

$$\delta_{\mathbf{Z}} = \begin{pmatrix} \delta_{ZX} \\ \delta_{ZY} \\ 0 \end{pmatrix} \tag{4.43a}$$

Corresponding misalignment rotation matrix associated with the gyro sense axis is defined as:

$$\mathbf{C}(\delta_{\mathbf{Z}}) \approx \begin{bmatrix} 1 & 0 & -\delta_{ZY} \\ 0 & 1 & \delta_{ZX} \\ \delta_{ZY} & -\delta_{ZX} & 1 \end{bmatrix} = \mathbf{I} + \begin{bmatrix} 0 & 0 & -\delta_{ZY} \\ 0 & 0 & \delta_{ZX} \\ \delta_{ZY} & -\delta_{ZX} & 0 \end{bmatrix} = \mathbf{I} - \begin{bmatrix} 0 & 0 & \delta_{ZY} \\ 0 & 0 & -\delta_{ZX} \\ -\delta_{ZY} & \delta_{ZX} & 0 \end{bmatrix} = \mathbf{I} - \tilde{\mathbf{\Delta}}_{\mathbf{Z}} \tag{4.43b}$$

The corresponding misaligned gyro measurement can be expressed as:

$$\tilde{\boldsymbol{\omega}} = \left(\boldsymbol{I} - \tilde{\boldsymbol{\Delta}} \right) \boldsymbol{\omega_b} \tag{4.44a}$$

$$\tilde{\boldsymbol{\omega}} = \left(\boldsymbol{I} - \tilde{\boldsymbol{\Delta}}_{\boldsymbol{X}} \right) \begin{pmatrix} \omega_{bx} \\ 0 \\ 0 \end{pmatrix} + \left(\boldsymbol{I} - \tilde{\boldsymbol{\Delta}}_{\boldsymbol{Y}} \right) \begin{pmatrix} 0 \\ \omega_{by} \\ 0 \end{pmatrix} + \left(\boldsymbol{I} - \tilde{\boldsymbol{\Delta}}_{\boldsymbol{Z}} \right) \begin{pmatrix} 0 \\ 0 \\ \omega_{bz} \end{pmatrix} \tag{4.44b}$$

Above expressions lead to the core elements of misalignment matrix:

$$\tilde{\boldsymbol{\Delta}} = \begin{bmatrix} 0 & -\delta_{YZ} & \delta_{ZY} \\ \delta_{XZ} & 0 & -\delta_{ZX} \\ -\delta_{XY} & \delta_{YX} & 0 \end{bmatrix} \tag{4.44c}$$

For the rate gyro sense axis configuration provided in Figure 4.17, the gyro misalignment measurement model can be expressed as the perception of the body angular rate by virtue of misalignments:

$$\boldsymbol{\omega_{g\ misalignment}} = \boldsymbol{\omega^g} = \tilde{\boldsymbol{\omega}} = \left[\boldsymbol{I} - \begin{bmatrix} 0 & -\delta_{YZ} & \delta_{ZY} \\ \delta_{XZ} & 0 & -\delta_{ZX} \\ -\delta_{XY} & \delta_{YX} & 0 \end{bmatrix} \right] \boldsymbol{\omega_b} \tag{4.44d}$$

In practice, one only knows the nominal gyro axis, the true gyro axis is unknown, and estimated by virtue of the calibration filter. True gyro sense axis, $\overline{\boldsymbol{w}}_i$, is related to the nominal gyro sense axis, $\boldsymbol{w}_i$, by the misalignment matrix as presented with the aid of Equations (4.44). Misalignment matrix captures the body angular rate, as perceived by the gyro sense axis due to misaligned placement of the sensor.

Gyro Measurement Model with Misalignment, Scale Factor, Noise, and Bias

Equation (4.44) captures the angular rate perceived by the rate gyros in the presence of misalignments. As presented earlier with the aid of Equations (3.11), the misaligned body angular rates are further aberrated with symmetric and asymmetric scale factors before being distorted by the gyro noise sources. Full gyro measurement model used to aberrate the ideal rigid body angular rate signal can be expressed as:

$$\boldsymbol{\omega_{gm}} = \tilde{\boldsymbol{\omega}} = (\mathbf{I} - \tilde{\mathbf{\Lambda}} - \tilde{\mathbf{U}})\boldsymbol{\omega^g} + \mathbf{b} + \boldsymbol{\eta_v} \tag{4.45a}$$

$$\boldsymbol{\omega_{gm}} = \tilde{\boldsymbol{\omega}} = (\mathbf{I} - \tilde{\mathbf{\Lambda}} - \tilde{\mathbf{U}}) \left(\boldsymbol{W}^T \boldsymbol{\omega}^{\mathrm{b}} - \boldsymbol{C_v} \left(\boldsymbol{\omega}^{\mathrm{b}} \right) \boldsymbol{\delta_u} - \boldsymbol{C_u} \left(\boldsymbol{\omega}^{\mathrm{b}} \right) \boldsymbol{\delta_v} \right) + \mathbf{b} + \boldsymbol{\eta_v} \tag{4.45b}$$

In the above presented case $\boldsymbol{W}^T$ is identity matrix, thus in compact form combining all the misalignment, scale factor, noise, and bias sources the gyro measurement model can be expressed as:

$$\boldsymbol{\omega_{gm}} = \tilde{\boldsymbol{\omega}} = (\mathbf{I} - \tilde{\mathbf{\Lambda}} - \tilde{\mathbf{U}}) \left(I - \tilde{\mathbf{\Delta}} \right) \boldsymbol{T_{go}^b} \boldsymbol{\omega}^{\mathrm{b}} + \mathbf{b} + \boldsymbol{\eta_v} \tag{4.45c}$$
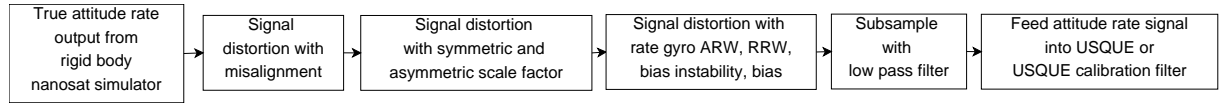
Figure 4.18: *Schematic overview outlining the process of measuring true attitude rate signal, which is later distorted by misalignment, symmetric and asymmetric scale factors, and gyro noise parameters before being subsampled into the USQUE/USQUE based calibration filter.*

$$\boldsymbol{\omega_{gm}} = \tilde{\boldsymbol{\omega}} = (\mathbf{I} - \tilde{\boldsymbol{\Lambda}} - \tilde{\mathbf{U}}) \left[\mathbf{I} - \begin{bmatrix} 0 & -\delta_{YZ} & \delta_{ZY} \\ \delta_{XZ} & 0 & -\delta_{ZX} \\ -\delta_{XY} & \delta_{YX} & 0 \end{bmatrix} \right] \boldsymbol{T_{g_o}^b} \boldsymbol{\omega}^{\mathrm{b}} + \mathbf{b} + \boldsymbol{\eta_v} \qquad (4.45\mathrm{d})$$

$\boldsymbol{T_{g_o}^b}$ is the transformation matrix describing the nominal orientation of the gyro reference $\boldsymbol{g_o}$ with respect to the body coordinate system b. Since all three gyro sense axes are perpendicular to the NanoSat body axis, $\boldsymbol{T_{g_o}^b}$ is equivalent to identity matrix. $\tilde{\boldsymbol{\Lambda}} = \mathrm{diag}\left[\lambda_x, \lambda_y, \lambda_z\right]$ is a matrix of symmetric scale factor errors. $\tilde{\mathbf{U}} = \mathrm{diag}\left[\mu_x \,\mathrm{sign}\left(\omega_x\right), \ldots \mu_y \,\mathrm{sign}\left(\omega_y\right), \mu_z \,\mathrm{sign}\left(\omega_z\right)\right]$ is a matrix of asymmetric scale factor errors. $\boldsymbol{I} - \tilde{\boldsymbol{\Delta}}$ is a non-orthogonal small angle misalignment matrix. An overview of interface between the rigid body NanoSat simulator, the above derived gyro measurement model, and the 6/7 state USQUE/USQUE calibration filter is presented with the aid of Figure 4.18.

4.7.3 | Misalignment Induced Star Tracker Measurement Model

One of the core objectives of this thesis work is to develop an absolute alignment calibration filter, which can be extended to a relative alignment calibration filter. Since rate gyros are used as reference sensors, misalignment of star trackers and any other optical payloads, if any, is estimated relative to the reference sensor. Misaligned star tracker measurement model, for use in calibration filter, presented here is similar to the star tracker misalignment model presented in (Pittelkau, 2001) or the payload alignment calibration model presented in (Pittelkau, 2002). The non-linear star tracker misalignment measurement model, which is used to misalign true attitude knowledge in the rigid body simulator can be expressed with the aid of rotational DCM presented earlier in Equation (4.1). The misalignment is modelled as rotational misalignment around the yaw-pitch-roll axis of the star tracker body frame (angle and axis nomenclature were presented earlier in Table 4.2):

$$\mathbf{C}(\theta) = R_X(\theta_1) \cdot R_Y(\theta_2) \cdot R_Z(\theta_3) \qquad (4.46\mathrm{a})$$

$$R_X(\theta_1) = \begin{bmatrix} 1 & 0 & 0 \\ 0 & \mathbf{c}\theta_1 & \mathbf{s}\theta_1 \\ 0 & -\mathbf{s}\theta_1 & \mathbf{c}\theta_1 \end{bmatrix} \qquad (4.46\mathrm{b})$$

$$R_Y(\theta_2) = \begin{bmatrix} \mathbf{c}\theta_2 & 0 & -\mathbf{s}\theta_2 \\ 0 & 1 & 0 \\ \mathbf{s}\theta_2 & 0 & \mathbf{c}\theta_2 \end{bmatrix} \qquad (4.46\mathrm{c})$$

$$R_Z(\theta_3) = \begin{bmatrix} \mathbf{c}\theta_3 & \mathbf{s}\theta_3 & 0 \\ -\mathbf{s}\theta_3 & \mathbf{c}\theta_3 & 0 \\ 0 & 0 & 1 \end{bmatrix} \qquad (4.46\mathrm{d})$$

Thus the DCM matrix for Euler 3-2-1 sequence is:

$$\mathbf{C}(\theta) = \begin{bmatrix} \mathbf{c}\theta_2\mathbf{c}\theta_3 & \mathbf{c}\theta_2\mathbf{s}\theta_3 & -\mathbf{s}\theta_2 \\ \mathbf{s}\theta_1\mathbf{s}\theta_2\mathbf{c}\theta_3 - \mathbf{c}\theta_1\mathbf{s}\theta_3 & \mathbf{s}\theta_1\mathbf{s}\theta_2\mathbf{s}\theta_3 + \mathbf{c}\theta_1\mathbf{c}\theta_3 & \mathbf{s}\theta_1\mathbf{c}\theta_2 \\ \mathbf{c}\theta_1\mathbf{s}\theta_2\mathbf{c}\theta_3 + \mathbf{s}\theta_1\mathbf{s}\theta_3 & \mathbf{c}\theta_1\mathbf{s}\theta_2\mathbf{s}\theta_3 - \mathbf{s}\theta_1\mathbf{c}\theta_3 & \mathbf{c}\theta_1\mathbf{c}\theta_2 \end{bmatrix} \qquad (4.46\mathrm{e})$$

The above presented nonlinear DCM is utilised to misalign the true Euler 3-2-1, before distorting it with the star tracker noise, and generating the expected star tracker quaternions. However, for the calibration filter this model can be simplified to a linear model for state estimation purposes. Since the misalignments around the yaw-pitch-roll axes are small angles, $\mathbf{c}\theta \approx 1$, $\mathbf{s}\theta \approx \theta$ and $\mathbf{s}\theta \cdot \mathbf{s}\theta \approx 0$,the above presented rotational DCM can be simplified to:

$$\mathbf{C}(\theta) = \begin{bmatrix} 1 & \mathbf{s}\theta_3 & -\mathbf{s}\theta_2 \\ -\mathbf{s}\theta_3 & 1 & \mathbf{s}\theta_1 \\ \mathbf{s}\theta_2 & -\mathbf{s}\theta_1 & 1 \end{bmatrix} \approx \begin{bmatrix} 1 & \theta_3 & -\theta_2 \\ -\theta_3 & 1 & \theta_1 \\ \theta_2 & -\theta_1 & 1 \end{bmatrix} = \begin{bmatrix} 1 & 0 & 0 \\ 0 & 1 & 0 \\ 0 & 0 & 1 \end{bmatrix} + \begin{bmatrix} 0 & \theta_3 & -\theta_2 \\ -\theta_3 & 0 & \theta_1 \\ \theta_2 & -\theta_1 & 0 \end{bmatrix} \qquad (4.46\mathrm{fa})$$

$$\mathbf{C}(\theta) \approx \begin{bmatrix} 1 & 0 & 0 \\ 0 & 1 & 0 \\ 0 & 0 & 1 \end{bmatrix} - \begin{bmatrix} 0 & -\theta_3 & +\theta_2 \\ +\theta_3 & 0 & -\theta_1 \\ -\theta_2 & +\theta_1 & 0 \end{bmatrix} \qquad (4.46\mathrm{fb})$$
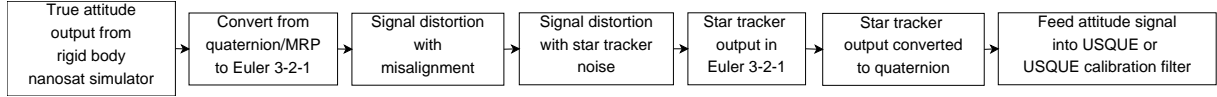
Figure 4.19: *Schematic overview outlining the process of measuring true attitude signal, which is later distorted by misalignment, and star tracker noise parameters before being fed into the USQUE/USQUE based calibration filter.*

This simplifies the nonlinear misalignment rotational matrix to a simple vector, capturing the misalignment around the roll(θ_1)-pitch(θ_2)-yaw(θ_3) axis, that can be estimated as three states with the calibration filter rather than nine DCM elements:

$$\zeta = \begin{pmatrix} \theta_1 \\ \theta_2 \\ \theta_3 \end{pmatrix} \tag{4.46g}$$

This leads to the following star tracker model that can be utilised by the calibration filter:

$$\mathbf{S} = \{I - [\zeta\times]\}T_{s_0,b}A(\mathbf{q})\mathbf{p}_s \tag{4.46h}$$

Here, $T_{s_0,b}$ is the transformation matrix from NanoSat body to star tracker. $A(\mathbf{q})$ is the attitude matrix associated with the star tracker output, and $\mathbf{p}_s$ is the star tracker measurement vector. $\{I - [\zeta\times]\}$ is the misalignment matrix associated with the star tracker. Where, ζ is essentially the vector of misalignment angles. In this case, the ζ represents the vector of misalignment angles around the measured yaw-pitch-roll axis attitude. An overview of interface between the rigid body NanoSat simulator, the above derived star tracker measurement model, and the 6/7 state USQUE/USQUE calibration filter is presented with the aid of Figure 4.19.

4.7.4 | Misalignment and Scale Factor Simulator Output Analysis and Assumption Verification

For the purpose of this section, the gyros misalignments ($\delta_{XY}, \delta_{XZ}, \delta_{YX}, \delta_{YZ}, \delta_{ZX}, \delta_{ZY}$) are set to: 5 deg; symmetric scale factors are set to: $\tilde{\mathbf{\Lambda}} = \mathrm{diag}\,[5000ppm,\ 5000ppm,\ 5000ppm]$; and asymmetric scale factors are set to:$\tilde{\mathbf{U}} = \mathrm{diag}\,[1000ppm,\ 1000ppm,\ 1000ppm]$. Full non-linear Euler-321 rotation matrices are utilised to generate the misaligned and scale factored angular rate. Misalignment and scale factor simulator developed takes in true body attitude rate as seen by the gyro reference frame and distorts it by misalignment and scale factor non-idealities. Figure 4.20a demonstrates the error in attitude rate, as observed by the gyros, for slow calibration manoeuvre in the presence of misalignment and scale factor. As expected, for agile slew rates the effect of misalignment and scale factor is significant, compared to slow manoeuvres. If the misalignment and scale factor is known identically, it is shown in Figure 4.20b, that the true signal can be reconstructed with minimal loss of precision. The effect of linearised misalignment and scale factor assumption, utilised by the calibration filter, on the reconstruction of true attitude signal is further presented in Figure 4.21a. In order to obtain observability of attitude and calibration states for all sensors, three rotational misalignment elements are discarded from the gyro misalignments in the calibration filter. The effect of this assumption, on the reconstructed attitude rate is demonstrated with the aid of Figure 4.21b. Similar observations with regards to the faster calibration manoeuvre is presented with the aid of Figure 4.23. Overall, as expected the effect of misalignment and scale factor is observed more under high slew rates. Simplification with regards to linearisation assumption, leads to increased error in reconstructing true angular rate from the distorted angular rate. Exclusion of rotational angle,for observability of calibration filter, leads to further increase in this attitude rate reconstruction error.

Similarly, Figure 4.24 captures the effect of misaligned star tracker under slow calibration manoeuvre. While Figure 4.25, captures that for fast calibration manoeuvre. This clearly demonstrates the need to calibrate for star tracker misalignment, as it significantly deteriorates the attitude knowledge acquisition capability of the system even in the presence of an ideal attitude sensor.
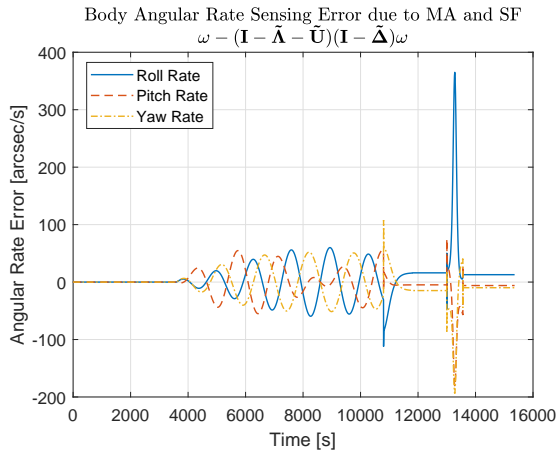
(a) *Error between the true attitude rate and that as seen by the gyro, due to the presence of misalignment and scale factor.*
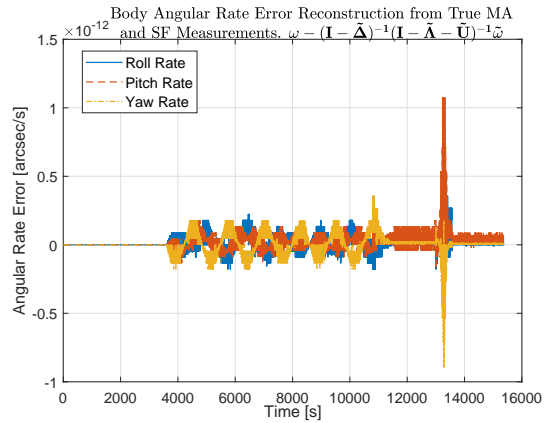
(b) *Reconstructing true attitude rate from the misaligned and scale factored attitude rate, utilising non-linear scale factor and misalignment inversions.*

Figure 4.20: *Effect of misalignment and scale factor addition on attitude rate, for slow calibration manoeuvre.*

(a) *Reconstructing true attitude rate from the misaligned and scale factored attitude rate, utilising simplified assumptions for scale factor and misalignment inversions.*
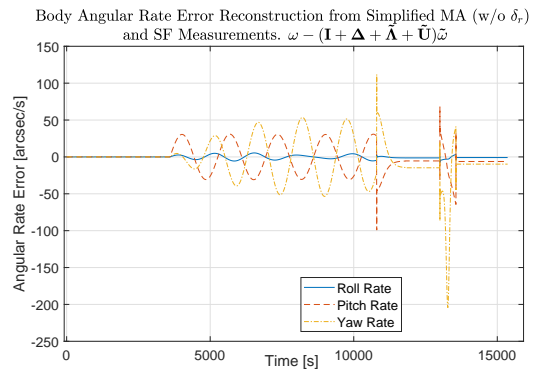
(b) *Reconstructing true attitude rate from the misaligned and scale factored attitude rate, utilising simplified assumptions (without gyro rotational misalignment) for scale factor and misalignment inversions.*

Figure 4.21: *Effect of misalignment and scale factor simplifications made by the filter on attitude rate reconstruction, for slow calibration manoeuvre.*
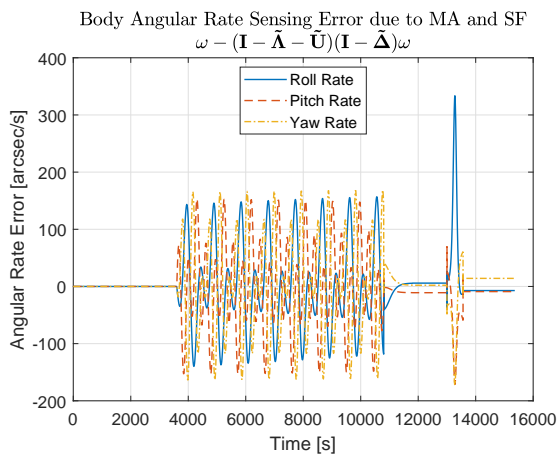
(a) *Error between the true attitude rate and that as seen by the gyro, due to the presence of misalignment and scale factor.*
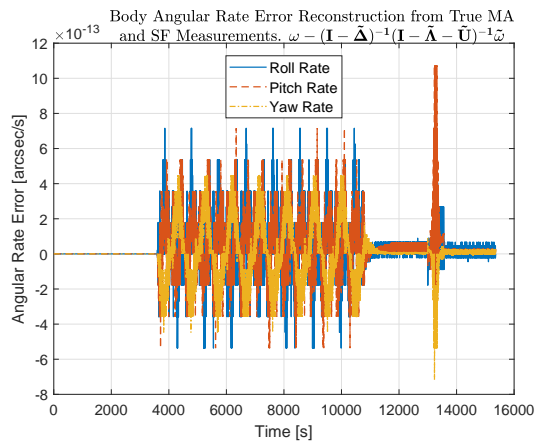
(b) *Reconstructing true attitude rate from the misaligned and scale factored attitude rate, utilising non-linear scale factor and misalignment inversions.*

Figure 4.22: *Effect of misalignment and scale factor addition on attitude rate, for fast calibration manoeuvre.*
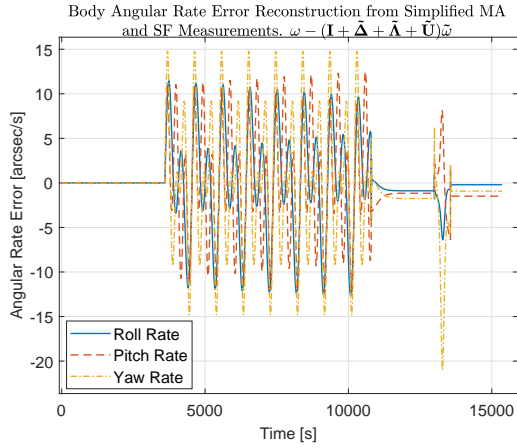
(a) *Reconstructing true attitude rate from the misaligned and scale factored attitude rate, utilising simplified assumptions for scale factor and misalignment inversions.*
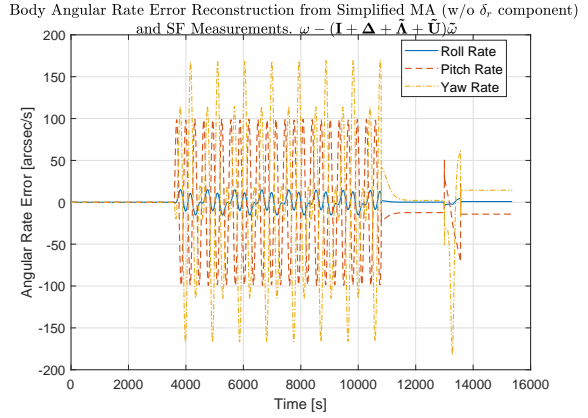
(b) *Reconstructing true attitude rate from the misaligned and scale factored attitude rate, utilising simplified assumptions (without gyro rotational misalignment) for scale factor and misalignment inversions.*

Figure 4.23: *Effect of misalignment and scale factor simplifications made by the filter on attitude rate reconstruction, for fast calibration manoeuvre.*
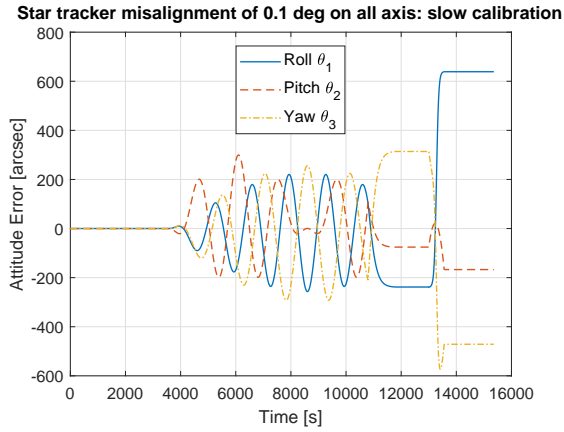
(a) *Effect of 0.1 deg star tracker misalignment on all axis, for slow calibration manoeuvre*
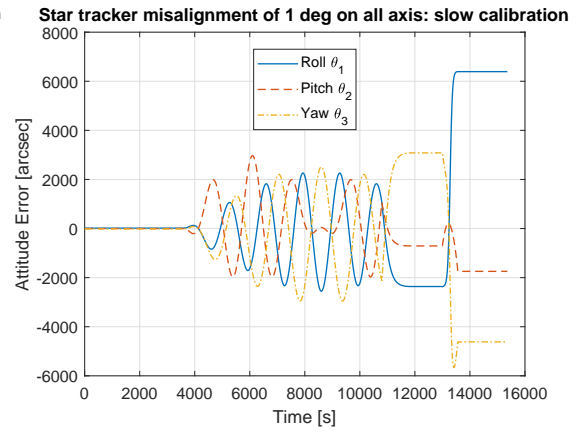
(b) *Effect of 1 deg star tracker misalignment on all axis, for slow calibration manoeuvre*

Figure 4.24: *Effect of star tracker misalignment for slow calibration manoeuvre.*
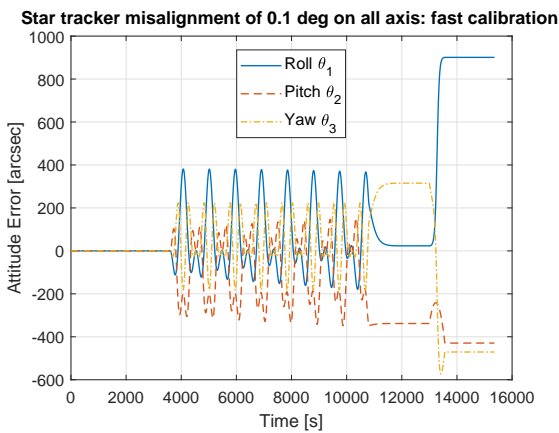
(a) *Effect of 0.1 deg star tracker misalignment on all axis, for fast calibration manoeuvre*
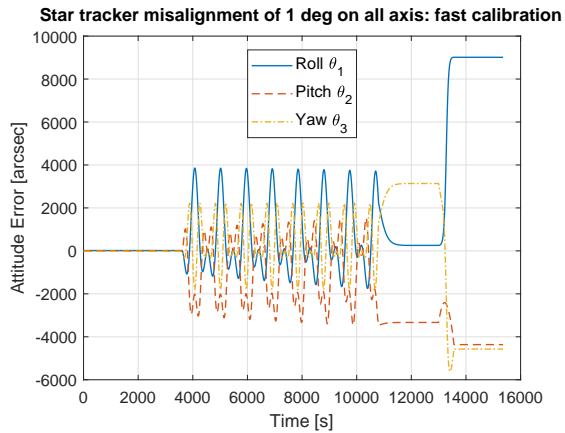
(b) *Effect of 1 deg star tracker misalignment on all axis, for fast calibration manoeuvre*

Figure 4.25: *Effect of star tracker misalignment for fast calibration manoeuvre.*
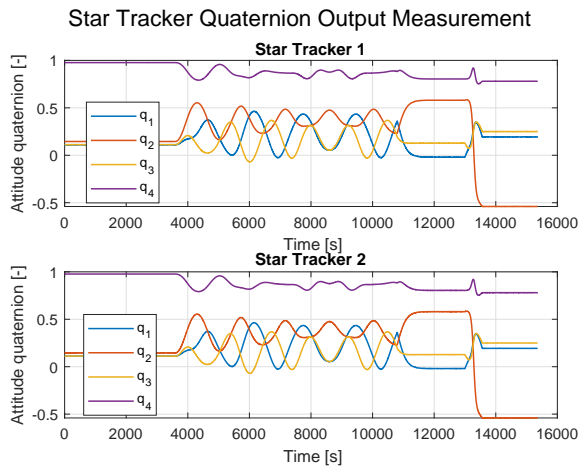
Figure 4.26: *Attitude quaternion measured at 5Hz by ST200 star trackers. Simulated for slow calibration manoeuvre sequences, with no MA.*
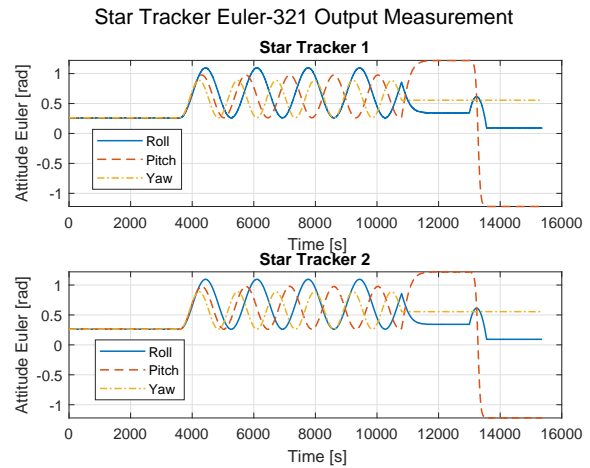
Figure 4.27: *Euler attitude measured at 5Hz by ST200 star trackers. Simulated for slow calibration manoeuvre sequences, with no MA.*

4.8 | **Rigid Body Simulator Sensor Output**

The objective of this section is to demonstrate the attitude and attitude rate signals generated by the rigid body sensor-integrated simulator. These signals are fed into the filters synthesized later on. The behaviour of the signals under different conditions related to configuration, subsampling, misalignment, scale factor and manoeuvres are discussed. Section 4.8.1 discusses the star tracker attitude output, while Section 4.8.2 discusses the gyro attitude rate output.

4.8.1 | Star Tracker Attitude Output

For the purpose of this section, the manoeuvre sequences captured by the slow calibration manoeuvre are utilised. 2 ST200 star trackers are utilised, with a sample rate of 5Hz. Alignment of the star trackers was discussed in Section 4.7.1. The star tracker output is transformed from star tracker to NanoSat sat body reference frame. The default quaternion output of the star trackers is presented with the aid of Figure 4.26. For ease of visualisation, the output is converted to Euler-321, and presented with the aid of Figure 4.27. Attitude error time series as seen by the star tracker through out the manoeuvre sequence is presented with the aid of Figure 4.28. To conclude this segment, attitude knowledge acquisition error of misaligned star tracker output is presented with the aid Figure 4.29. Here, both the star trackers are given a misalignment of 0.1 deg on all axis with the aid of non-linear rotational Euler-321 DCM. As expected, in the presence of misalignments the star tracker output degrades significantly, especially at larger angle readouts. This suggests that the star tracker misalignments must be calibrated, to improve the overall attitude knowledge performance of the system.
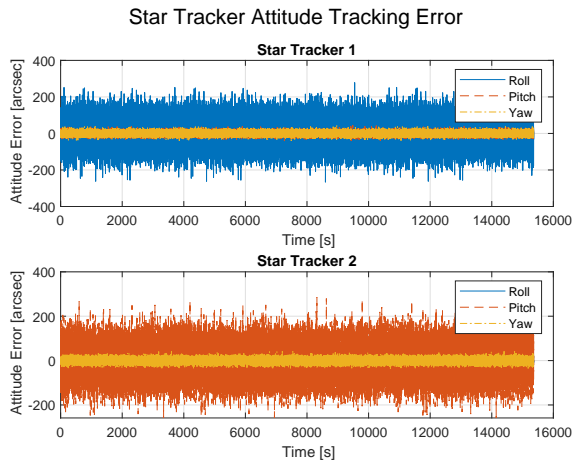
Figure 4.28: *ST200 attitude measurement error over the entire manoeuvre sequence. Simulated for slow calibration manoeuvre sequences, with no MA.*
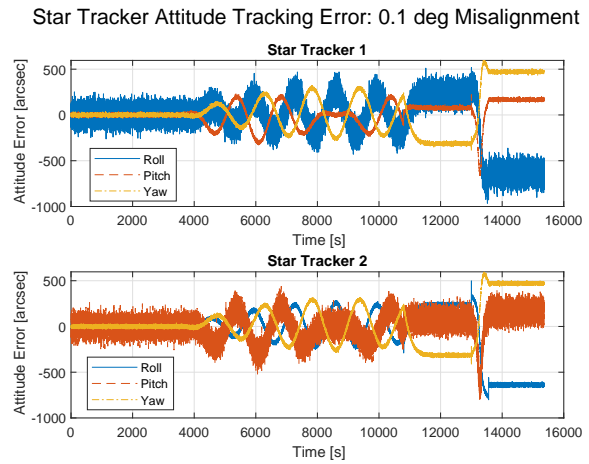
Figure 4.29: *ST200 attitude measurement error over the entire manoeuvre sequence. Simulated for slow calibration manoeuvre sequences, with MA of 0.1 deg on all axis.*
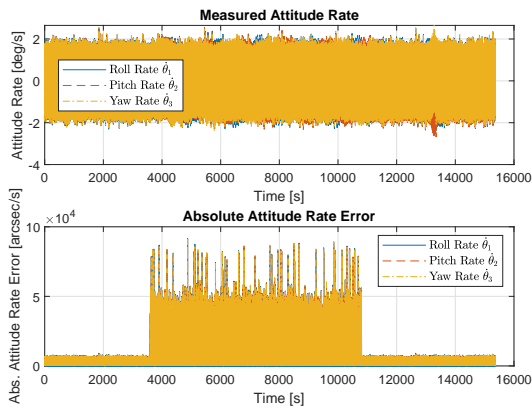
Figure 4.30: *MPSAG gyro attitude rate measurement error for the entire manoeuvre sequence when sampled at 2300Hz. Slow calibration manoeuvre sequences with no gyro MA and SF.*
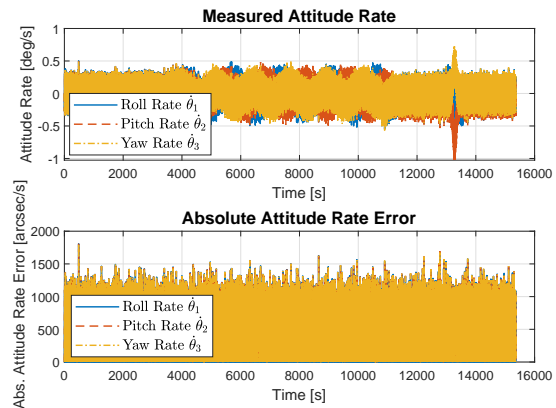
Figure 4.31: *MPSAG gyro attitude rate measurement error for the entire manoeuvre sequence when sampled at 100Hz. Slow calibration manoeuvre sequences with no gyro MA and SF.*

4.8.2 | Gyro Attitude Rate Output

The objective of this section is to demonstrate the behaviour of the attitude rate output generated by the rigid body simulator under different operational conditions. Four general root causes affecting the attitude rate are discussed: subsampling, sensor noise, manoeuvre,and misalignment and scale factor.

Effect of Subsampling

Samples from the MPSAG gyros are produced at 2300Hz, while that for HPTAG are produced at 2000Hz subsequently. The outputs are subsampled with the aid of a low pass filter, synthesized earlier in Section 3.5, to meet the desired filter update rate. The effect of subsampling is captured with MPSAG sensors, for the manoeuvre sequences involved with the slow calibration manoeuvre. Figure 4.30 captures the raw gyro sensor output at 2300 Hz, while Figure 4.31 captures the subsampled output at 100 Hz, consequently Figure 4.32 captures the attitude rate subsampled at 5 Hz. As expected, high sample rate comes at the expense of high noise injection onto the true attitude rate signal.
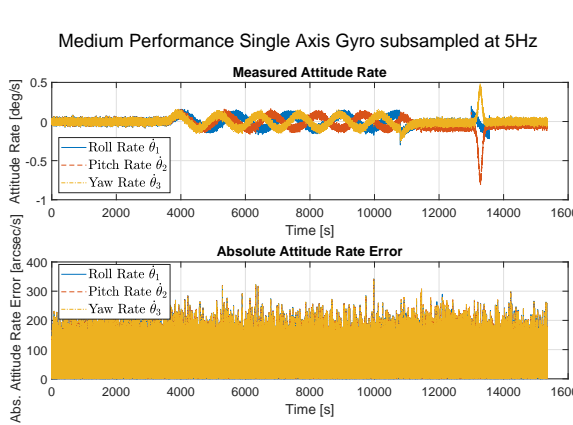
Figure 4.32: *MPSAG gyro attitude rate measurement error for the entire manoeuvre sequence when sampled at 5Hz. Slow calibration manoeuvre sequences with no gyro MA and SF.*
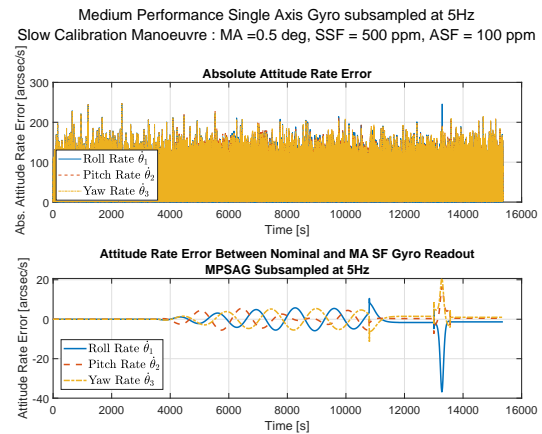
Figure 4.33: *MPSAG gyro attitude rate measurement error for the entire manoeuvre sequence when sampled at 5Hz. Slow calibration manoeuvre sequences with MA of 0.5 deg for all elements, SSF of 500 ppm and ASF of 100 ppm.*
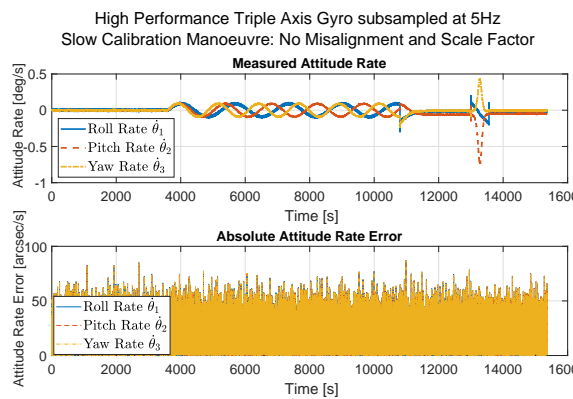
Figure 4.34: *HPTAG gyro attitude rate measurement and error for the entire manoeuvre sequence when sampled at 5Hz. Slow calibration manoeuvre sequences with no gyro MA and SF.*
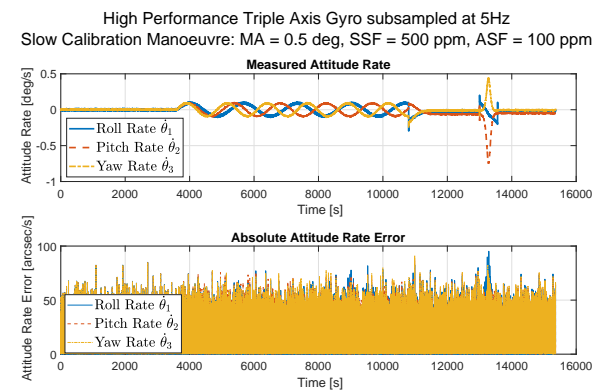
Figure 4.35: *HPTAG gyro attitude rate measurement and error for the entire manoeuvre sequence when sampled at 100Hz. Slow calibration manoeuvre sequences with MA of 0.5 deg for all elements, ASF of 500ppm, SSF of 100ppm.*

Effect of Improved Sensor

The effect of improved sensor, is captured with the aid of HPTAG sensors subsampled at 5Hz. This is presented with the aid of Figure 4.34 for manoeuvre sequences associated with the slow calibration manoeuvre phase. Clearly, the utilisation of HPTAG has an improvement on noise by a factor of 4 approximately, compared to MPSAG.

Effect of Misalignment and Scale Factor

The impact of misalignment and scale factor, on the true body rate observed by the gyro sensor was discussed earlier in Section 4.7.4, with the aid of Figure 4.20a for instance. The objective of this segment is to evaluate the differences in the gyro output, passed through a low pass filter, for sensors with and without misalignment and scale factor. Figure 4.33 captures the absolute attitude rate measurement error for MPSAG with MA (0.5 deg), SSF(500 ppm) and ASF(100 ppm). Comparing this with the absolute attitude rate measurement error, where the gyro is given no MA and SF, in Figure 4.32 one can hardly notice significant differences in the attitude rate measurement error. However, upon subtracting the gyro output with, and without MA and SF, the effect of SF and MA is observed as shown in Figure 4.33. Similar effects are observed for the HPTAG sensors utilised. Comparing Figures 4.34 and 4.35 for slow calibration manoeuvre, and Figures 4.36 and 4.37 for fast calibration manoeuvre the absolute attitude rate errors as observed by the gyros are rather similar. However, subtracting the gyro outputs with and without MA and SF effects, presents the underlying signal distortion introduced by virtue of MA and SF. This is captured with the aid of Figure 4.38. It is important to note that for slow calibration manoeuvre, the error introduced is lower than the star tracker
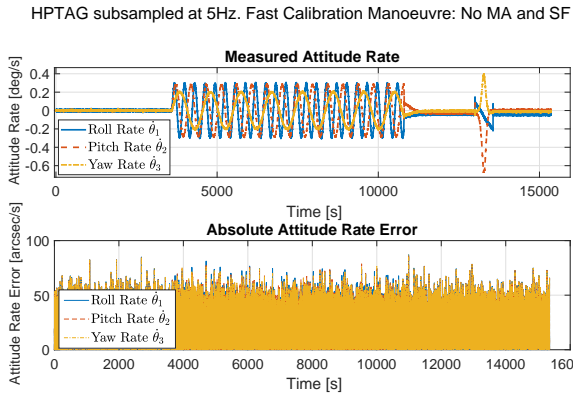
Figure 4.36: *HPTAG gyro attitude rate measurement and error for the entire manoeuvre sequence when sampled at 5Hz. Fast calibration manoeuvre sequences with no gyro MA and SF.*
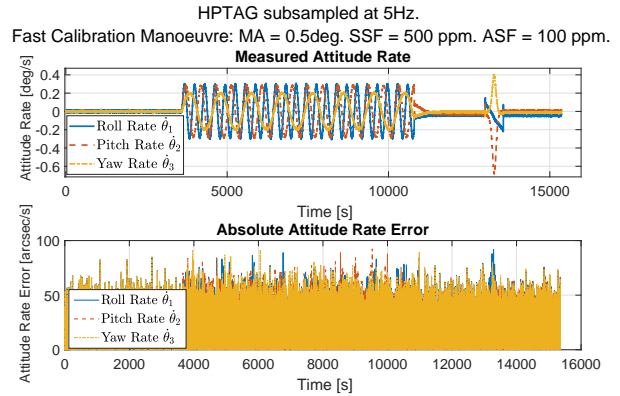
Figure 4.37: *HPTAG gyro attitude rate measurement and error for the entire manoeuvre sequence when sampled at 100Hz. Fast calibration manoeuvre sequences with MA of 0.5 deg for all elements, ASF of 500ppm, SSF of 100ppm.*
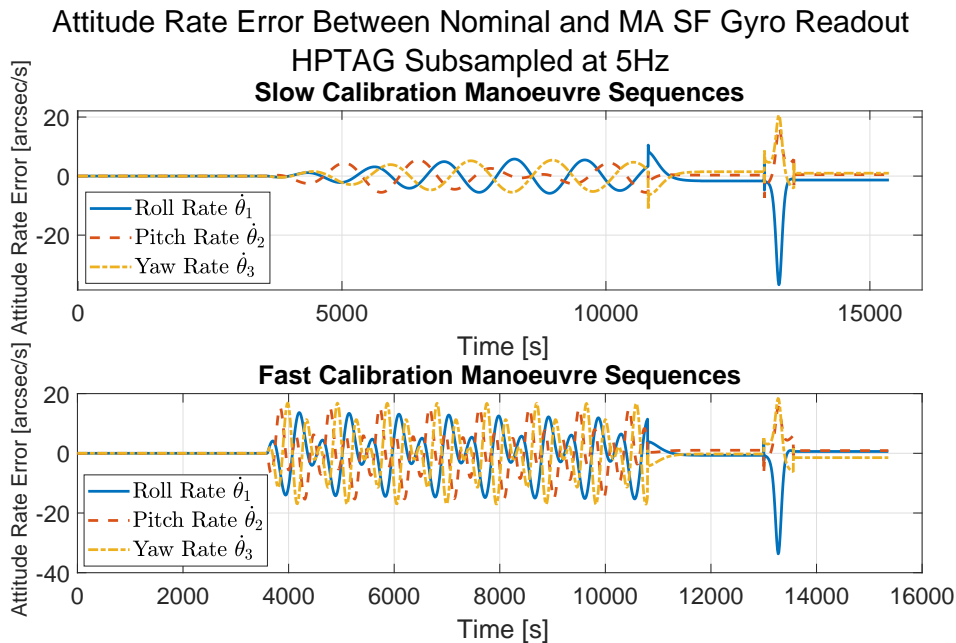
Figure 4.38: *Difference between ideal HPTAG read out and HPTAG read out under the influence of MA(0.5deg), ASF(500ppm), and SSF(100ppm). For slow and fast calibration manoeuvre sequences.*

attitude measurement capability. And in general, the error introduced is significantly lower than the error introduced by gyro output.

Effect of Calibration Manoeuvre on Misaligned and Scale Factored Sensor Output

From the discussions in the previous segments, it can be expected that higher the signal strength (i.e. higher the slew rate), higher the signal distortion introduced by misalignment and scale factor. Figure 4.35 captures the effect of misaligned and scale factored HPTAG output for slow calibration manoeuvre. While Figure 4.37 captures that for fast calibration manoeuvre. The impact of fast and slow calibration manoeuvre, for similar values of MA and SF is captured with the of Figure 4.38. Clearly, larger excitation leads to larger effect of MA and SF observed.

4.9 | **Summary and Conclusions**

The core objective of this chapter was to develop a simulator capable of generating attitude and attitude rate for different mission phases, considering sensor and actuator limitations, eventually leading to the signals that are later

utilised by the calibration filter for attitude estimation. In light of that, the underlying coordinate reference frames, parametrisations were presented in combination with the rotational dynamics and kinematics of the rigid body. Reaction wheel input-output torque limit and delay behaviour is analysed and included in the simulator. Flight controller is synthesised to track the respective reference signals. A worst case absolute pointing error of 360 arcsec was observed, as captured with Figures C.5 and C.6. This preliminary analysis, indicated that the ceiling of 20.63 arcsec (1σ) attitude knowledge requirement is set rather low by the stakeholders, and can be increased by approximately 1400 arcsec (1σ). This suggests that a detailed pointing error source budgeting should be conducted before imposing such stringent attitude knowledge requirements. Two different calibration manoeuvres are generated, and the subsequent steady state and agile ground-target tracking manoeuvres is further presented. An overview of the interface connecting manoeuvres, flight controller, actuator, rigid body simulator, sensors, and eventually the calibration filter is presented. Gyro-stellar configuration is defined, and the sensor noise, misalignment, and scale factor induced measurement models are derived. Effect of misalignment and scale factor on sensor output is discussed. Impact of the assumptions and simplifications utilised by the calibration filter regarding misalignment, and scale factor estimation on signal reconstruction is further discussed. The chapter is concluded with the sensor output under different operational conditions of sensor subsampling, sensor noise, manoeuvres, misalignment and scale factor.

This page is intentionally left blank.

Calibration Filter Algorithm Overview

The objective of this chapter is to present the algorithms utilised for the calibration filter. Since 6/7 state UnScented QUaternion Estimator (USQUE) forms the basis of the calibration filter developed as part of this thesis work; 6/7 state USQUE algorithm is first presented with the aid of Section 5.1. The filter was observed to encounter premature covariance convergence. As a consequence, a covariance convergence monitor is developed, and presented as part of this section. A schematic overview of the flow of algorithm, esp. in the event of star tracker drop out, is further presented. Section 5.2 is dedicated to the development of calibration filter, utilising the framework of USQUE. The section further outlines the sensor models utilised by the calibration filter. Unlike 6/7 state USQUE, an iterative process noise covariance matrix is derived, which is updated every time step.

5.1 | UnScented QUaternion Estimator USQUE

As discussed earlier, due to the favorable properties of fast convergence and robustness to large errors in initial conditions, a UKF based filter is preferred over an EKF variant for attitude estimation. In order to prevent the violation of the unity norm constraint of unit quaternion, UnScented QUaternion Estimator (USQUE) as presented in (Crassidis and Markley, 2003) is proposed. Internal to USQUE, error MRP is utilised as the attitude representation state to avoid this unity norm constraint violation.

The input and output attitude state for the 6/7 state USQUE filter is represented by quaternion. However, the state internal to the filter which facilitates attitude propagation is in error MRP. The internal filter state is comprised of the attitude error kinematics in MRP and bias:

$$\hat{\boldsymbol{x}}_{\boldsymbol{k}}^{+} \equiv \left(\begin{array}{c} \boldsymbol{\delta}\hat{\boldsymbol{p}}_{\boldsymbol{k}}^{+} \\ \boldsymbol{\beta}_{k}^{+} \end{array} \right) \tag{5.1}$$

General linear continuous time-varying state-variable system model is defined as:

$$\dot{\boldsymbol{x}}(t) = \boldsymbol{F}(t)\boldsymbol{x}(t) + \boldsymbol{B}(t)\boldsymbol{u}(t) + \boldsymbol{G}(t)\boldsymbol{w}(t) \tag{5.2a}$$

Corresponding discrete time equivalent expression is defined as:

$$\boldsymbol{x}_{k+1} = \boldsymbol{\Phi}_{k+1,k}\,\boldsymbol{x}_k + \boldsymbol{\Psi}_{k+1,k}\,\boldsymbol{u}_k + \boldsymbol{G}_k\boldsymbol{w}_k = \boldsymbol{f}(\boldsymbol{x}_k, k) + \boldsymbol{G}_k\boldsymbol{w}_k \tag{5.2b}$$

Here, $\boldsymbol{F}(t)$ is the system matrix, discrete time equivalent of which is defined as the state transition matrix, $\boldsymbol{\Phi}_{k+1}$. The system under consideration is an autonomous system, thus the input matrix $\boldsymbol{B} = \boldsymbol{0}$. $\boldsymbol{G}(t)$ is the system noise input matrix. $\boldsymbol{w}(t)$ is the process noise vector with covariance denoted by $\boldsymbol{Q}_k$. Similarly, the measurement equation can be expressed as:

$$\tilde{\boldsymbol{y}}(t) = \boldsymbol{H}(t)\boldsymbol{x}(t) + \boldsymbol{D}(t)\boldsymbol{u}(t) + \boldsymbol{v}(t) \tag{5.3a}$$

The corresponding, discrete time equivalent is defined as:

$$\tilde{\boldsymbol{y}}_{k+1} = \boldsymbol{H}_{k+1}\boldsymbol{x}_{k+1} + \boldsymbol{D}_{k+1}\boldsymbol{u}_{k+1} + \boldsymbol{v}_{k+1} = \boldsymbol{h}(\boldsymbol{x}_{k+1}, k) + \boldsymbol{v}_{k+1} \tag{5.3b}$$

Here, $\boldsymbol{H}$ is defined as the observation matrix $\boldsymbol{D}$ is defined as the feed forward matrix, which is $\boldsymbol{0}$ in this case. $\boldsymbol{v}(t)$ is the measurement noise vector, with covariance $\boldsymbol{R}_k$.

In continuous time, the attitude quaternion is propagated with the aid of the estimated error quaternion:

$$\boldsymbol{q}(t) = \boldsymbol{\delta}\boldsymbol{q}(\boldsymbol{\delta}\boldsymbol{p}(t)) \otimes \boldsymbol{q}_{\mathrm{ref}}(t) \tag{5.4}$$

Here, $\boldsymbol{q}_{\mathrm{ref}}(t)$ is some unit reference quaternion, and $\boldsymbol{\delta}\boldsymbol{q}(\boldsymbol{a}(t))$ is a unit quaternion representing the rotation from $\boldsymbol{q}_{\mathrm{ref}}(t)$ to the true attitude quaternion $\boldsymbol{q}(t)$. USQUE parametrises the error quaternion with regards to $\boldsymbol{\delta}\boldsymbol{p}$. It aims to compute an unconstrained estimate of the three component vector $\boldsymbol{\delta}\boldsymbol{p}$, while utilising the correctly normalised four

component $\boldsymbol{q}_{\text{ref}}$ to provide a globally non-singular attitude representation. $\boldsymbol{\delta q}(\boldsymbol{\delta p}(t))$ can be expressed as (Markley, 2003):

$$\boldsymbol{\delta q}\left(\boldsymbol{\delta p}\right) = \frac{1}{16 + \boldsymbol{\delta p}^2} \left(\begin{array}{c} 8\,\boldsymbol{\delta p} \\ 16 - \boldsymbol{\delta p}^2 \end{array} \right) \tag{5.5a}$$

A second order approximation of the error quaternion can be obtained with the aid of Taylor series expansion around $\boldsymbol{\delta p} = \boldsymbol{0}$:

$$\boldsymbol{\delta q}(\boldsymbol{\delta p}) \approx \left(\begin{array}{c} \boldsymbol{\delta p}/2 \\ 1 - \boldsymbol{\delta p}^2/8 \end{array} \right) \tag{5.5b}$$

Consequently, the rate of change of error MRP attitude kinematics can be expressed as:

$$\boldsymbol{\delta \dot{p}} = \left[\left(1 - \frac{1}{16}\boldsymbol{\delta p}^2 \right) I_{3\times 3} + \frac{1}{8}\boldsymbol{\delta p}\boldsymbol{\delta p}^T \right] (\tilde{\boldsymbol{\omega}} - \hat{\boldsymbol{\omega}}) - \frac{1}{2}(\tilde{\boldsymbol{\omega}} + \hat{\boldsymbol{\omega}}) \times \boldsymbol{\delta p} \equiv \boldsymbol{f}(\boldsymbol{x}, t) \tag{5.5c}$$

Utilising $\tilde{\boldsymbol{\omega}}(t) = \boldsymbol{\omega}(t) - \boldsymbol{b}(t) - \boldsymbol{\eta}_v(t)$, $\dot{\boldsymbol{b}}(t) = \boldsymbol{\eta}_u(t)$, $\hat{\boldsymbol{\omega}}(t) = \boldsymbol{\omega}(t) - \hat{\boldsymbol{b}}(t)$, and ignoring terms higher than first order in Equation 5.5c, leads to the following expression for system matrix $\boldsymbol{F}(t)$:

$$\boldsymbol{F}(t) \equiv \left[\begin{array}{cc} \frac{\partial \boldsymbol{f}}{\partial\,\boldsymbol{\delta p}} & \frac{\partial \boldsymbol{f}}{\partial \boldsymbol{b}} \\ \boldsymbol{0}_{3\times 3} & \boldsymbol{0}_{3\times 3} \end{array} \right] = \left[\begin{array}{cc} -\left[\ \hat{\boldsymbol{\omega}}\times\ \right] & -\boldsymbol{I}_{3\times 3} \\ \boldsymbol{0}_{3\times 3} & \boldsymbol{0}_{3\times 3} \end{array} \right] \tag{5.6}$$

Similarly, system noise input matrix $\boldsymbol{G}(t)$ is defined as:

$$\boldsymbol{G}(t) \equiv \left[\begin{array}{cc} \frac{\partial \boldsymbol{f}}{\partial \boldsymbol{\eta}_v} & \frac{\partial \boldsymbol{f}}{\partial \boldsymbol{\eta}_u} \\ \boldsymbol{0}_{3\times 3} & \boldsymbol{I}_{3\times 3} \end{array} \right] = \left[\begin{array}{cc} \boldsymbol{I}_{3\times 3} & \boldsymbol{0}_{3\times 3} \\ \boldsymbol{0}_{3\times 3} & \boldsymbol{I}_{3\times 3} \end{array} \right] \tag{5.7}$$

Utilising $\boldsymbol{F}(t)$ from above, corresponding discrete time $\boldsymbol{\Phi}$ can be obtained with the aid of power series expansion:

$$\boldsymbol{\Phi} = e^{\boldsymbol{F}\Delta t} = \boldsymbol{I} + \boldsymbol{F}\Delta t + \frac{\boldsymbol{F}^2 \Delta t^2}{2!} + \frac{\boldsymbol{F}^3 \Delta t^3}{3!} + \cdots \tag{5.8}$$

For small samples times, it is assumed that $\left\|\Delta t \hat{\boldsymbol{\omega}}_k^+\right\| \ll 1$. Substituting Equation (5.6) into Equation (5.8), the state transition matrix can be approximated as:

$$\boldsymbol{\Phi}(\Delta t) = \left[\begin{array}{cc} \boldsymbol{I}_{3\times 3} & -\Delta t \boldsymbol{I}_{3\times 3} \\ \boldsymbol{0}_{3\times 3} & \boldsymbol{I}_{3\times 3} \end{array} \right] \tag{5.9}$$

The above presented expression of state transition matrix, $\boldsymbol{\Phi}$, can now be used to derive discrete time process noise covariance matrix, $\mathbf{Q}_k$:

$$\boldsymbol{Q}(t) = diag\left[\sigma_v^2 \boldsymbol{I_{3\times 3}} \quad \sigma_u^2 \boldsymbol{I_{3\times 3}} \right] \tag{5.10a}$$

$$\boldsymbol{Q_k} = \int_0^{\Delta t} \boldsymbol{\Phi}(t)\boldsymbol{G}(t)\boldsymbol{Q}(t)\boldsymbol{G}^T(t)\boldsymbol{\Phi}^T(t)dt \tag{5.10b}$$

$$\mathbf{Q_k} = \left[\begin{array}{cc} \left(\sigma_v^2 \Delta t + \frac{1}{3}\sigma_u^2 \Delta t^3\right)\mathbf{I}_{3\times 3} & -\left(\frac{1}{2}\sigma_u^2 \Delta t^2\right)\mathbf{I}_{3\times 3} \\ -\left(\frac{1}{2}\sigma_u^2 \Delta t^2\right)\mathbf{I}_{3\times 3} & \left(\sigma_u^2 \Delta t\right)\mathbf{I}_{3\times 3} \end{array} \right] \tag{5.10c}$$

5.1.1 | USQUE Algorithm for Attitude and Rate Gyro Bias Estimation

The following will systematically present the USQUE algorithm, interested readers are referred to (Crassidis and Markley, 2003). The USQUE filter can be broadly split into five core steps:

1. Filter initialisation

2. Sigma point generation

3. Time update and model forecast

4. Data assimilation

5. Return filter output

The above steps are expanded further in the following:

1. **Filter Initialisation (External)**

(a) Initialise quaternion and gyro bias

Once the NanoSat is detumbled, the first state update from the star trackers can be used as an initial estimate of attitude for filter initialisation. This also ensures that the measurement corresponds to the measurement noise covariance statistics. Initial gyro bias is set to 0 deg/hr.

(b) Initialise the state vector.

○ For single star tracker:

$$\begin{pmatrix} \hat{\boldsymbol{q}}_0^+ \\ \hat{\boldsymbol{\beta}}_0^+ \end{pmatrix} \tag{5.11}$$

○ For two star trackers:
   ● If the star tracker measurements are stacked:

$$\begin{pmatrix} \hat{\boldsymbol{q}}_{s1,0}^+ \\ \hat{\boldsymbol{q}}_{s2,0}^+ \\ \hat{\boldsymbol{\beta}}_0^+ \end{pmatrix} \tag{5.12}$$

   ● If a quaternion is constructed by extracting pitch and yaw axis of each of the star tracker output (in other words, pre-selecting the best performing sense axis):

$$\begin{pmatrix} \hat{\boldsymbol{q}}_{s12,0}^+ \\ \hat{\boldsymbol{\beta}}_0^+ \end{pmatrix} \tag{5.13}$$

(c) Initialise state covariance $\boldsymbol{P}_0^+$, with expected variance of error MRP and gyro bias:

○ For single star tracker:

$$\mathrm{diag}\left(\begin{pmatrix} \sigma_{\bar{\sigma}_1}^2 & \sigma_{\bar{\sigma}_2}^2 & \sigma_{\bar{\sigma}_3}^2 & \sigma_{\beta_x}^2 & \sigma_{\beta_y}^2 & \sigma_{\beta_z}^2 \end{pmatrix}^T \right) \tag{5.14}$$

○ For two star trackers:

   ● If the star tracker outputs are stacked

$$\mathrm{diag}\left(\begin{pmatrix} \sigma_{\bar{\sigma}_{s1,1}}^2 & \sigma_{\bar{\sigma}_{s1,2}}^2 & \sigma_{\bar{\sigma}_{s1,3}}^2 & \sigma_{\bar{\sigma}_{s2,1}}^2 & \sigma_{\bar{\sigma}_{s2,2}}^2 & \sigma_{\bar{\sigma}_{s2,3}}^2 & \sigma_{\beta_x}^2 & \sigma_{\beta_y}^2 & \sigma_{\beta_z}^2 \end{pmatrix}^T \right) \tag{5.15}$$

   ● If a single quaternion is extracted by utilising the pitch and yaw axis of two star tracker quaternion outputs:

$$\mathrm{diag}\left(\begin{pmatrix} \sigma_{\bar{\sigma}_1}^2 & \sigma_{\bar{\sigma}_2}^2 & \sigma_{\bar{\sigma}_3}^2 & \sigma_{\beta_x}^2 & \sigma_{\beta_y}^2 & \sigma_{\beta_z}^2 \end{pmatrix}^T \right) \tag{5.16}$$

(d) Initialise process noise covariance matrix $\boldsymbol{Q}$

Total desired process noise follows as:

$$\boldsymbol{\Phi}(\Delta t)\bar{\boldsymbol{Q}}_k \boldsymbol{\Phi}^T(\Delta t) + \bar{\boldsymbol{Q}}_k = \boldsymbol{G}_k \boldsymbol{Q}_k \boldsymbol{G}_k^T \tag{5.17}$$

Where, $\boldsymbol{\Phi}(\Delta t)$ is the state transition matrix. Derivation of matrix $\bar{\boldsymbol{Q}}_k$ assumes that the approximation $\left\| \Delta t \hat{\boldsymbol{\omega}}_k^+ \right\| \ll 1$ is valid, this is generally adequate for computing process noise. The state transition matrix can then be approximated by:

$$\boldsymbol{\Phi}(\Delta t) = \begin{bmatrix} \boldsymbol{I}_{3\times3} & -\Delta t \boldsymbol{I}_{3\times3} \\ \boldsymbol{0}_{3\times3} & \boldsymbol{I}_{3\times3} \end{bmatrix} \tag{5.18}$$

The discrete process noise covariance is given by:

$$\boldsymbol{Q}_k = \begin{bmatrix} \left(\sigma_v^2 \Delta t + \frac{1}{3}\sigma_u^2 \Delta t^3 \right) \boldsymbol{I}_{3\times3} & -\left(\frac{1}{2}\sigma_u^2 \Delta t^2 \right) \boldsymbol{I}_{3\times3} \\ -\left(\frac{1}{2}\sigma_u^2 \Delta t^2 \right) \boldsymbol{I}_{3\times3} & \left(\sigma_u^2 \Delta t \right) \boldsymbol{I}_{3\times3} \end{bmatrix} \tag{5.19}$$

Where, σ_v is the standard deviation associated with the Angular Random Walk of the rate gyros and σ_u

is that associated with the Rate Random Walk of the rate gyros. While, Δt is the sample time internal to the gyros. Solving Equation (5.17) for $\bar{Q}_k$, results in:

$$\bar{Q}_k = \frac{\Delta t}{2} \left[\begin{array}{cc} \left(\sigma_v^2 - \frac{1}{6}\sigma_u^2 \Delta t^2\right) I_{3\times3} & 0_{3\times3} \\ 0_{3\times3} & \sigma_u^2 I_{3\times3} \end{array} \right] \tag{5.20}$$

(e) Initialise measurement error noise covariance matrix, R

This is taken from the worst case standard deviation of the star tracker output quaternion elements expected from the entire manoeuvre sequence.

  ○ For one star tracker, or when measurement axis from two star trackers are pre-selected and merged:

  •
$$\text{diag}\left(\left(\sigma_{q_1}^2 \quad \sigma_{q_2}^2 \quad \sigma_{q_3}^2 \quad \sigma_{q_4}^2\right)^T\right) \tag{5.21}$$

  ○ For two star trackers:

  • When the star tracker measurements are stacked:

$$\text{diag}\left(\left(\sigma_{q_{s1,1}}^2 \quad \sigma_{q_{s1,2}}^2 \quad \sigma_{q_{s1,3}}^2 \quad \sigma_{q_{s1,4}}^2 \quad \sigma_{q_{s2,1}}^2 \quad \sigma_{q_{s2,2}}^2 \quad \sigma_{q_{s2,3}}^2 \quad \sigma_{q_{s2,4}}^2\right)^T\right) \tag{5.22}$$

(f) Initialise a, λ, and n parameter. Set f = 2(a + 1). λ is a composite scaling factor that is used to define the spread of sigma points and exploit available knowledge about higher moments of a given distribution. Here a is a parameter between 0 and 1, and f is a scale factor. With a = 0 and f = 1, the following expression of error quaternion returns Gibbs vector, and with a = f = 1 it returns MRP from quaternion. n is the number of states, in this case 6. Error quaternion is defined as:

$$\delta q \equiv \left(\delta \varrho^T \quad \delta q_4\right)^T \tag{5.23a}$$

Corresponding generalised Rodrigues parameters as defined as:

$$\delta p \equiv f\left(\frac{\delta \varrho}{a + \delta q_4}\right) \tag{5.23b}$$

2. **Filter initialisation (Internal)**

  (a) Initialise filter state vector reset-ed error MRP, and bias vector from previous filter update. The attitude error for i = 0 is reset to zero after the previous update. This is used to move information from one part of the estimate to another part. This reset rotates the reference frame for the covariance matrix. However, the covariance depends on the assumed statistics of the measurements, and not on the actual measurements. The update is zero mean, the mean rotation caused by the reset is zero, thus the covariance is not affected by the reset:

$$\chi_k(0) = \hat{x}_k^+ \equiv \left(\begin{array}{c} \delta \hat{p}_k^+ \\ \hat{\beta}_k^+ \end{array} \right) \equiv \left(\begin{array}{c} 0 \\ \hat{\beta}_k^+ \end{array} \right) \tag{5.24}$$

3. **Sigma Point Generation**

  (a) Generate error MRP and gyro bias sigma points:
  First the sigma points are computed using:

$$\sigma_k \leftarrow 2n \text{ columns from } \pm \sqrt{(n + \lambda)\left[P_k^+ + \bar{Q}_k\right]} \tag{5.25a}$$

In practice, Cholesky decomposition is utilised to compute this matrix square root.

$$\chi_k(0) = \hat{x}_k^+ \tag{5.25b}$$

$$\chi_k(i) = \sigma_k(i) + \hat{x}_k^+ \tag{5.25c}$$

$$\chi_k(i) \equiv \left(\begin{array}{c} \chi_k^{\delta p}(i) \\ \chi_k^{\beta}(i) \end{array} \right), \quad i = 0, 1, \ldots, 12 \tag{5.25d}$$

(b) Estimate current quaternion based on the sigma points - Compute sigma point quaternion from the error quaternions. Corresponding error quaternions are calculated using:

$$\boldsymbol{\delta q}_k^+(i) \equiv \left(\boldsymbol{\delta \varrho}_k^{+T}(i) \quad \delta q_{4_k}^+(i)\right)^T \tag{5.26}$$

Where, the scalar error quaternion is given by:

$$\delta q_{4_k}^+(i) = \frac{-a \left\|\boldsymbol{\chi}_k^{\delta p}(i)\right\|^2 + f \sqrt{f^2 + (1 - a^2) \left\|\boldsymbol{\chi}_k^{\delta p}(i)\right\|^2}}{f^2 + \left\|\boldsymbol{\chi}_k^{\delta p}(i)\right\|^2}, \quad i = 1, 2, \ldots, 12 \tag{5.27}$$

And the vectorial error quaternion is given by:

$$\boldsymbol{\delta \varrho}_k^+(i) = f^{-1} \left(a + \delta q_{4_k}^+(i)\right) \boldsymbol{\chi}_k^{\delta p}(i), \quad i = 1, 2, \ldots, 12 \tag{5.28}$$

Since, $\boldsymbol{\chi}_k^{\delta p}(0)$ is set to $\boldsymbol{0}$

$$\boldsymbol{\delta q}_k^+(0) \equiv \left(\boldsymbol{\delta \varrho}_k^{+T}(0) \quad \delta q_{4_k}^+(0)\right)^T = \left(\begin{array}{cccc} 0 & 0 & 0 & 1 \end{array}\right)^T \tag{5.29}$$

Utilising this, the sigma point quaternions can be calculated as:

$$\hat{\boldsymbol{q}}_k^+(0) = \hat{\boldsymbol{q}}_k^+ \tag{5.30a}$$

$$\hat{\boldsymbol{q}}_k^+(i) = \boldsymbol{\delta q}_k^+(i) \otimes \hat{\boldsymbol{q}}_k^+, \quad i = 1, 2, \ldots, 12 \tag{5.30b}$$

4. **Time Update and Model Forecast**

(a) Quaternion vector is propagated forward in time step using :

$$\hat{\boldsymbol{q}}_{k+1}^-(i) = \Omega\left(\hat{\boldsymbol{\omega}}_k^+(i)\right) \hat{\boldsymbol{q}}_k^+(i), \quad i = 0, 1, \ldots, 12 \tag{5.31}$$

Where, the posteriori estimated angular velocities for k^{th} time step are given by:

$$\hat{\boldsymbol{\omega}}_k^+(i) = \tilde{\boldsymbol{\omega}}_k - \boldsymbol{\chi}_k^\beta(i), \quad i = 0, 1, \ldots, 12 \tag{5.32}$$

And, the discrete time equivalent of quaternion propagation is denoted by:

$$\boldsymbol{\Omega}\left(\hat{\boldsymbol{\omega}}_k^+\right) \equiv \left[\begin{array}{cc} \cos\left(0.5 \left\|\hat{\boldsymbol{\omega}}_k^+\right\| \Delta t\right) \boldsymbol{I}_{3\times3} - \left[\hat{\boldsymbol{\psi}}_k^+ \times\right] & \hat{\boldsymbol{\psi}}_k^+ \\ -\hat{\boldsymbol{\psi}}_k^{+T} & \cos\left(0.5 \left\|\hat{\boldsymbol{\omega}}_k^+\right\| \Delta t\right) \end{array}\right] \tag{5.33}$$

Where, Δt is the sampling interval of the gyro internal measurements used by the filter and $\hat{\boldsymbol{\psi}}_k^+$ is given by:

$$\hat{\boldsymbol{\psi}}_k^+ \equiv \sin\left(0.5 \left\|\hat{\boldsymbol{\omega}}_k^+\right\| \Delta t\right) \hat{\boldsymbol{\omega}}_k^+ / \left\|\hat{\boldsymbol{\omega}}_k^+\right\| \tag{5.34}$$

(b) Propagated error quaternions are then determined using:

$$\boldsymbol{\delta q}_{k+1}^-(i) = \hat{\boldsymbol{q}}_{k+1}^-(i) \otimes \left[\hat{\boldsymbol{q}}_{k+1}^-(0)\right]^{-1}, \quad i = 0, 1, \ldots, 12 \tag{5.35}$$

Where, $\boldsymbol{\delta q}_{k+1}^-(0)$ is the identity quaternion.

(c) Propagation of sigma points to the next time step

$$\boldsymbol{\chi}_{k+1}^{\delta p}(0) = \boldsymbol{0} \tag{5.36}$$

$$\boldsymbol{\chi}_{k+1}^{\delta p}(i) = f \frac{\boldsymbol{\delta \varrho}_{k+1}^-(i)}{a + \delta q_{4k+1}^-(i)}, \quad i = 1, 2, \ldots, 12 \tag{5.37}$$

Where,

$$\left(\boldsymbol{\delta \varrho}_{k+1}^{-T}(i) \quad \delta q_{4_{k+1}}^-(i)\right)^T = \delta q_{k+1}^-(i) \tag{5.38}$$

And,

$$\boldsymbol{\chi}_{k+1}^\beta(i) = \boldsymbol{\chi}_k^\beta(i), \quad i = 0, 1, \ldots, 12 \tag{5.39}$$

$$\boldsymbol{\chi}_{k+1}(i) \equiv \left(\begin{array}{c} \boldsymbol{\chi}_{k+1}^{\delta p}(i) \\ \boldsymbol{\chi}_{k+1}^\beta(i) \end{array}\right), \quad i = 0, 1, \ldots, 12 \tag{5.40}$$

(d) State propagation: Predicting mean of the state from propagated sigma points

$$\hat{\boldsymbol{x}}_{k+1}^{-} = \frac{1}{n+\lambda} \left\{ \lambda \boldsymbol{\chi}_{k+1}(0) + \frac{1}{2} \sum_{i=1}^{2n} \boldsymbol{\chi}_{k+1}(i) \right\}$$

(5.41)

(e) State covariance propagation: Predicting covariance of the state from propagated sigma points

$$\boldsymbol{P}_{k+1}^{-} = \frac{1}{n+\lambda} \left\{ \lambda \left(\boldsymbol{\chi}_{k+1}(0) - \hat{\boldsymbol{x}}_{k+1}^{-} \right) \left(\boldsymbol{\chi}_{k+1}(0) - \hat{\boldsymbol{x}}_{k+1}^{-} \right)^{T} \dots \right.$$
$$\left. \dots + \frac{1}{2} \sum_{i=1}^{2n} \left(\boldsymbol{\chi}_{k+1}(i) - \hat{\boldsymbol{x}}_{k+1}^{-} \right) \left(\boldsymbol{\chi}_{k+1}(i) - \hat{\boldsymbol{x}}_{k+1}^{-} \right)^{T} \right\} + \bar{\boldsymbol{Q}}_{k}$$

(5.42)

(f) Propagation of observation sigma points to the next time step using observation models

$$\boldsymbol{\gamma}_{k+1}(i) = \boldsymbol{h} \left(\boldsymbol{\chi}_{k+1}(i), k \right)$$

(5.43)

Since, the star tracker returns attitude knowledge in the spacecraft body frame with respect to inertial reference frame. Observation sigma points (gamma points) can be propagated using the following: When measurements are obtained from one star tracker:

- ○

$$\boldsymbol{\gamma}_{k+1}(i) = \left(\ \hat{\boldsymbol{q}}_{k+1}^{-}(i) \ \right)$$

(5.44)

When measurements are obtained from two star trackers:

- ○ If the star tracker measurements are stacked:

$$\boldsymbol{\gamma}_{k+1}(i) = \left(\begin{array}{c} \hat{\boldsymbol{q}}_{k+1}^{-}(i) \\ \hat{\boldsymbol{q}}_{k+1}^{-}(i) \end{array} \right)$$

(5.45)

- ○ If a single quaternion is extracted by utilising the pitch and yaw axes from the two star tracker quaternion outputs:

$$\boldsymbol{\gamma}_{k+1}(i) = \left(\ \hat{\boldsymbol{q}}_{k+1}^{-}(i) \ \right)$$

(5.46)

(g) Observation propagation: Predicting mean of the observation from propagated gamma points

$$\hat{\boldsymbol{y}}_{k+1}^{-} = \frac{1}{n+\lambda} \left\{ \lambda \boldsymbol{\gamma}_{k+1}(0) + \frac{1}{2} \sum_{i=1}^{2n} \boldsymbol{\gamma}_{k+1}(i) \right\}$$

(5.47)

(h) Observation covariance propagation: Propagating output covariance of the observation from propagated observation sigma points (gamma points) and mean of observation

$$\boldsymbol{P}_{k+1}^{yy} = \frac{1}{n+\lambda} \left\{ \lambda \left(\boldsymbol{\gamma}_{k+1}(0) - \hat{\boldsymbol{y}}_{k+1}^{-} \right) \left(\boldsymbol{\gamma}_{k+1}(0) - \hat{\boldsymbol{y}}_{k+1}^{-} \right)^{T} \dots \right.$$
$$\left. \dots + \frac{1}{2} \sum_{i=1}^{2n} \left(\boldsymbol{\gamma}_{k+1}(i) - \hat{\boldsymbol{y}}_{k+1}^{-} \right) \left(\boldsymbol{\gamma}_{k+1}(i) - \hat{\boldsymbol{y}}_{k+1}^{-} \right)^{T} \right\}$$

(5.48)

(i) Innovation covariance matrix propagation

$$\boldsymbol{R}_{k+1} = \boldsymbol{R}_{k}$$

(5.49)

$$\boldsymbol{P}_{k+1}^{vv} = \boldsymbol{P}_{k+1}^{yy} + \boldsymbol{R}_{k+1}$$

(5.50)

(j) Cross-correlation matrix propagation

$$\boldsymbol{P}_{k+1}^{xy} = \frac{1}{n+\lambda} \left\{ \lambda \left(\boldsymbol{\chi}_{k+1}(0) - \hat{\boldsymbol{x}}_{k+1}^{-} \right) \left(\boldsymbol{\gamma}_{k+1}(0) - \hat{\boldsymbol{y}}_{k+1}^{-} \right)^{T} \dots \right.$$
$$\left. \dots + \frac{1}{2} \sum_{i=1}^{2n} \left(\boldsymbol{\chi}_{k+1}(i) - \hat{\boldsymbol{x}}_{k+1}^{-} \right) \left(\boldsymbol{\gamma}_{k+1}(i) - \hat{\boldsymbol{y}}_{k+1}^{-} \right)^{T} \right\}$$

(5.51)

5. **Data Assimilation Step**

    (a) Filter gain update

$$K_{k+1} = P_{k+1}^{xy} \left[P_{k+1}^{vv} \right]^{-1}$$

    (5.52)

    (b) Innovation signal update

$$v_{k+1} \equiv \tilde{y}_{k+1} - \hat{y}_{k+1}^{-} = \tilde{y}_{k+1} - h\left(\hat{x}_{k+1}^{-}, k+1\right)$$

    (5.53)

    (c) State vector update

$$\hat{x}_{k+1}^{+} = \hat{x}_{k+1}^{-} + K_{k+1} v_{k+1}$$

    (5.54)

    (d) State covariance update

$$P_{k+1}^{+} = P_{k+1}^{-} - K_{k+1} P_{k+1}^{vv} K_{k+1}^{T}$$

    (5.55)

    (e) Post update error quaternion from post update error MRP

$$\hat{q}_{k+1}^{+} = \delta q_{k+1}^{+} \otimes \hat{q}_{k+1}^{-}(0)$$

    (5.56)

Where, $\delta q_{k+1}^{+} \equiv \left(\delta \varrho_{k+1}^{+T} \quad \delta q_{4_{k+1}}^{+} \right)^{T}$ is provided by the expressions:

$$\delta q_{4_{k+1}}^{+} = \frac{-a \left\| \delta \hat{p}_{k+1}^{+} \right\|^{2} + f \sqrt{f^{2} + (1 - a^{2}) \left\| \delta \hat{p}_{k+1}^{+} \right\|^{2}}}{f^{2} + \left\| \delta \hat{p}_{k+1}^{+} \right\|^{2}}$$

    (5.57a)

$$\delta \varrho_{k+1}^{+} = f^{-1} \left(a + \delta q_{4_{k+1}}^{+} \right) \delta \hat{p}_{k+1}^{+}$$

    (5.57b)

6. **Return filter output** :
    Here the attitude state is in quaternion
    $\hat{x}_{k+1}^{+}$ and P_{k+1}^{+}

5.1.2 | Covariance Convergence Monitor

For the 6/7 state USQUE filter, the attitude was observed to be estimated such that the attitude signals were tracked consistently, though gradual but early convergence of the state covariances was observed for both attitude and bias states. This is specially problematic, when the manoeuvre transitions from steady state to an agile tracking manoeuvre. To avoid this problem, spectral analysis based innovation signal monitor is utilised:

$$\sigma_{\vartheta}^{2} = \frac{1}{N-1} \sum_{k=1}^{N} (\vartheta(k) - \bar{\vartheta})^{2}$$

    (5.58a)

Here N is the number of samples in a moving window and:

$$\bar{\vartheta} = \frac{1}{N} \sum_{k=1}^{N} \vartheta(k)$$

    (5.58b)

And, $\vartheta(k)$ indicates the Euclidean 2-norm of the innovation signal in Euler-321:

$$\vartheta(k) = ||\vartheta_{Euler}(k)|| \equiv ||\tilde{y}_{Euler}(k) - \hat{y}_{Euler}^{-}(k)|| = ||\tilde{y}_{Euler}(k) - h_{Euler}\left(\hat{x}(k)^{-}, k\right)||$$

    (5.58c)

Spectral analysis presented above is simply the sample variance of the innovation signal for a given window size of N elements. The covariance convergence monitor σ_{ϑ}^{2} is the sample variance of the norm of the measurement innovation signal in Euler-321, for a time series comprising of N previous samples. When this sample variance, σ_{ϑ}^{2}, exceeds a given threshold, a forgetting or scaling factor is applied to the state covariance matrix initialized for the next iteration of the filter i.e. $P_{k+1}^{+} = \Pi^{-1} \cdot P_{k+1}^{+}$. The threshold is set to 1500 arcsec, for all the simulations conducted as part of this thesis. The performance of the 6/7 state USQUE with and without covariance convergence monitor is presented with the aid of Section 6.2.1.

5.1.3 | Schematic Overview: Attitude and Rate Gyro Bias Estimation

Figure 5.1 presents an overview of the filter algorithm, developed in the previous section. The schematic overview further outlines the flow of the filter algorithm, in the event of star tracker drop out. This routes is also followed when gyro sample rate and filter update rate is higher than the star tracker update rate. The influence of innovation signal monitor is further outlined.
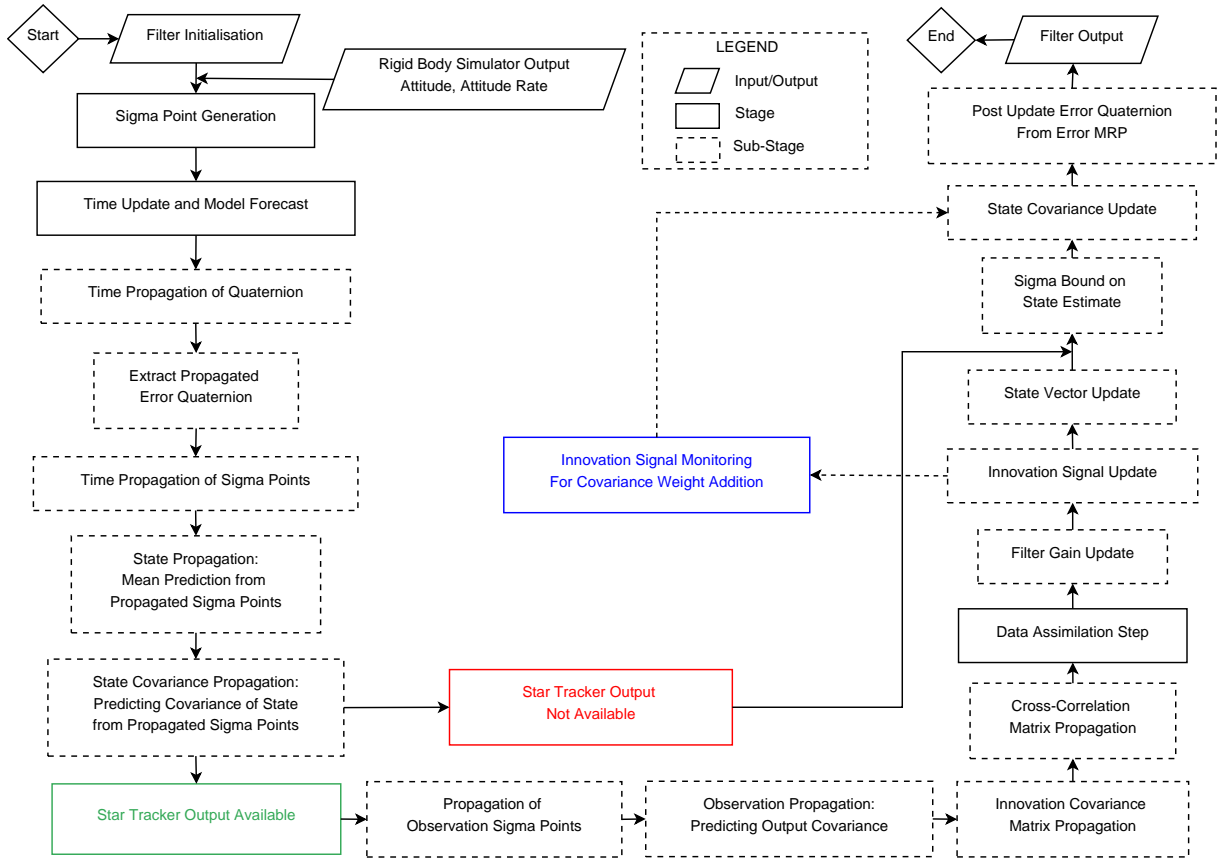
Figure 5.1: *USQUE filter algorithm overview outlining the flow of algorithm in the presence and absence of star tracker update. The implementation of the innovation signal monitor is further presented.*

5.2 | **USQUE based Spacecraft Relative Alignment Calibration Filter**

USQUE based calibration filter presented in this section, largely builds up on the USQUE filter developed earlier in Section 5.1, with some notable changes made to the gyro and star tracker models to accommodate relevant misalignment, and scale factor parameters. Section 5.2.1 aims at deconstructing the sensor models for utilisation in an USQUE based calibration filter framework. Section 5.2.2 derives the discrete process noise associated with the calibration filter. While Section 5.2.3 derives the underlying calibration filter algorithm.

5.2.1 | Sensor models utilised for calibration filter

Before USQUE based calibration filter is synthesized in Section 5.2.3, the objective of this Section is to outline the sensor models that is utilised by the calibration filter for attitude and calibration state estimation process. First the gyro sensor model utilised by the calibration filter is derived. This is followed by the star tracker model. The limitations imposed by the model assumptions were presented earlier with the aid of Section 4.7.4.

Gyro measurement model, with misalignment, symmetric and asymmetric scale factors, and the underlying noise sources, utilized to read out the angular rate measurements from the rigid body was presented earlier in Section 4.7.2. The relation between the gyro measurement model, and the rigid body angular rate was presented earlier with Equation 4.45. This model can be reorganised to estimate the misalignment, and scale factor parameters with the calibration filter.

$$\boldsymbol{\omega_{gm}} = \tilde{\boldsymbol{\omega}} = \left(\boldsymbol{I} - \tilde{\boldsymbol{\Lambda}} - \tilde{\boldsymbol{U}} \right) \left(I - \tilde{\boldsymbol{\Delta}} \right) \boldsymbol{T_{g_o}^b} \boldsymbol{\omega}^{\mathrm{b}} + \boldsymbol{\beta} + \boldsymbol{\eta_v} \tag{5.59a}$$

$$\boldsymbol{\omega_{gm}} = \tilde{\boldsymbol{\omega}} = \left(\boldsymbol{I} - \tilde{\boldsymbol{\Lambda}} - \tilde{\boldsymbol{U}} \right) \left[\boldsymbol{I} - \begin{bmatrix} 0 & -\delta_{YZ} & \delta_{ZY} \\ \delta_{XZ} & 0 & -\delta_{ZX} \\ -\delta_{XY} & \delta_{YX} & 0 \end{bmatrix} \right] \boldsymbol{T_{g_o}^b} \boldsymbol{\omega}^{\mathrm{b}} + \boldsymbol{\beta} + \boldsymbol{\eta_v} \tag{5.59b}$$

Measured angular rate from the rate gyro $\boldsymbol{\omega_{gm}} = \tilde{\boldsymbol{\omega}}$, is related to symmetric scale factor $\tilde{\boldsymbol{\Lambda}} = \mathrm{diag}\left[\lambda_x, \lambda_y, \lambda_z\right]$, asymmetric scale factor $\tilde{\boldsymbol{U}} = \mathrm{diag}\left[\mu_x \, \mathrm{sign}\left(\omega_x\right), \mu_y \, \mathrm{sign}\left(\omega_y\right), \mu_z \, \mathrm{sign}\left(\omega_z\right)\right]$, non-orthonormal small angle misalignment

matrix $\left(I - \tilde{\Delta}\right) T_{g_o}^b \omega^{\mathrm{b}} = \left(W^T \omega^{\mathrm{b}} - C_v\left(\omega^{\mathrm{b}}\right) \delta_u - C_u\left(\omega^{\mathrm{b}}\right) \delta_v\right)$, gyro frame to NanoSat body frame transformation $T_{g_o}^b$, body angular rate ω^{b}, bias β and noise parameters internal to the gyro η_v. Body angular rate can thus be expressed as:

$$\omega^b = T_{g_o}^b (I - \tilde{\Delta})^{-1}(I - \tilde{\Lambda} - \tilde{U})^{-1}(\tilde{\omega} - \beta - \eta_v) \tag{5.60}$$

As the nominal gyro sense axes are aligned with the body reference sense axes, $T_{g_o}^b$ is identity. Following expressions are derived with $T_{g_o}^b$, such that the model can be extended to cases where the gyro sense axes are not nominally aligned with the NanoSat body axes. Since the expected misalignments and scale factors are small, the above expressions can be simplified to:

$$\omega^b \simeq T_{g_o}^b (I + \Delta)(I + \Lambda + U)(\tilde{\omega} - \beta - \eta_v) \tag{5.61a}$$

$$\Delta \simeq \tilde{\Delta}, \Lambda \simeq \tilde{\Lambda} \text{ and } U \simeq \tilde{U} \tag{5.61b}$$

For symmetric scale factor of $\Lambda = \mathrm{diag}\,[5000ppm,\ 5000ppm,\ 5000ppm]$, asymmetric scale factor of $U = \mathrm{diag}\,[1000ppm,\ 1000ppm,\ 1000ppm]$, and misalignment of 3600 arcsec on all axis, the effect of this assumption is shown as follows:

For scale factor:

$$(I - \tilde{\Lambda} - \tilde{U})^{-1} = \left(\begin{bmatrix} 1 & 0 & 0 \\ 0 & 1 & 0 \\ 0 & 0 & 1 \end{bmatrix} - \begin{bmatrix} 5000 \cdot 10^{-6} & 0 & 0 \\ 0 & 5000 \cdot 10^{-6} & 0 \\ 0 & 0 & 5000 \cdot 10^{-6} \end{bmatrix} \dots \right.$$

$$\left. \dots - \begin{bmatrix} 1000 \cdot 10^{-6} & 0 & 0 \\ 0 & 1000 \cdot 10^{-6} & 0 \\ 0 & 0 & 1000 \cdot 10^{-6} \end{bmatrix} \right)^{-1} \tag{5.62a}$$

$$(I - \tilde{\Lambda} - \tilde{U})^{-1} = (I - \tilde{\Lambda} - \tilde{U})^{-1} = \begin{bmatrix} 1.00604 & 0 & 0 \\ 0 & 1.00604 & 0 \\ 0 & 0 & 1.00604 \end{bmatrix} \tag{5.62b}$$

$$(I + \tilde{\Lambda} + \tilde{U}) = \begin{bmatrix} 1.0060 & 0 & 0 \\ 0 & 1.0060 & 0 \\ 0 & 0 & 1.0060 \end{bmatrix} \approx (I - \tilde{\Lambda} - \tilde{U})^{-1} \approx (I + \Lambda + U) \tag{5.62c}$$

For misalignment:

$$\left[I - \tilde{\Delta} \right]^{-1} = \left[I - \begin{bmatrix} 0 & -\delta_{YZ} & \delta_{ZY} \\ \delta_{XZ} & 0 & -\delta_{ZX} \\ -\delta_{XY} & \delta_{YX} & 0 \end{bmatrix} \right]^{-1} \approx \left[I + \tilde{\Delta} \right] \approx [I + \Delta] \tag{5.62d}$$

$$\left[I - \begin{bmatrix} 0 & -0.01745 & 0.017453 \\ 0.017453 & 0 & -0.017453 \\ -0.017453 & 0.017453 & 0 \end{bmatrix} \right]^{-1} = \begin{bmatrix} 0.9994 & -0.01713 & 0.01774 \\ 0.01774 & 0.9994 & -0.01713 \\ -0.01713 & 0.01774 & 0.9994 \end{bmatrix} \tag{5.62e}$$

Corresponding eigenvalues of the matrix are $\left(0.9991 + 0.0302i \quad 0.9991 - 0.0302i \quad 1.0000 + 0.0000i \right)^T$

$$\left[I + \tilde{\Delta} \right] = \begin{bmatrix} 1 & -0.01745 & 0.01745 \\ 0.01745 & 1 & -0.01745 \\ -0.01745 & 0.01745 & 1 \end{bmatrix} \tag{5.62f}$$

Corresponding eigenvalues of the matrix are $\left(1.0000 + 0.0302i \quad 1.0000 - 0.0302i \quad 1.0000 + 0.0000i \right)^T$. Thus $\left[I - \tilde{\Delta} \right]^{-1} \approx \left[I + \tilde{\Delta} \right] \approx [I + \Delta]$

Let the scale factored gyro body rate be expressed as:

$$\bar{\omega} = (I + \Lambda + U)(\tilde{\omega} - \beta - \eta_v) \tag{5.63}$$

Corresponding body angular rate measurement from rate gyro measurement model, in Equation 5.61, can be expressed as:

$$(I + \Delta)\bar{\omega} = \begin{bmatrix} 1 & -\delta_{xz} & \delta_{xy} \\ \delta_{xz} & 1 & 0 \\ -\delta_{xy} & 0 & 1 \end{bmatrix} \begin{pmatrix} \bar{\omega}_x \\ 0 \\ 0 \end{pmatrix} + \begin{bmatrix} 1 & -\delta_{yz} & 0 \\ \delta_{yz} & 1 & -\delta_{yx} \\ 0 & \delta_{yx} & 1 \end{bmatrix} \begin{pmatrix} 0 \\ \bar{\omega}_y \\ 0 \end{pmatrix} + \dots$$

$$\dots \begin{bmatrix} 1 & 0 & \delta_{zy} \\ 0 & 1 & -\delta_{zx} \\ -\delta_{zy} & \delta_{zx} & 1 \end{bmatrix} \begin{pmatrix} 0 \\ 0 \\ \bar{\omega}_z \end{pmatrix} \tag{5.64a}$$

$$(I + \Delta)\bar{\omega} = \begin{bmatrix} 1 & -\delta_{yz} & \delta_{zy} \\ \delta_{xz} & 1 & -\delta_{zx} \\ -\delta_{xy} & \delta_{yx} & 1 \end{bmatrix} \bar{\omega} \tag{5.64b}$$

Performing QR factorization on the above presented misalignment matrix results in:

$$I + \Delta = QR = \quad \{I + [\boldsymbol{\delta} \times]\} R = \begin{bmatrix} 1 & -\delta_z & \delta_y \\ \delta_z & 1 & -\delta_x \\ -\delta_y & \delta_x & 1 \end{bmatrix} \begin{bmatrix} 1 & \xi_z & \xi_y \\ 0 & 1 & \xi_x \\ 0 & 0 & 1 \end{bmatrix} \dots$$

$$\simeq \begin{bmatrix} 1 & -(\delta_z - \xi_z) & \delta_y + \xi_y \\ \delta_z & 1 & -(\delta_x - \xi_x) \\ -\delta_y & \delta_x & 1 \end{bmatrix} \tag{5.65a}$$

Equating:

$$\begin{bmatrix} 1 & -\delta_{yz} & \delta_{zy} \\ \delta_{xz} & 1 & -\delta_{zx} \\ -\delta_{xy} & \delta_{yx} & 1 \end{bmatrix} \simeq \begin{bmatrix} 1 & -(\delta_z - \xi_z) & \delta_y + \xi_y \\ \delta_z & 1 & -(\delta_x - \xi_x) \\ -\delta_y & \delta_x & 1 \end{bmatrix} \tag{5.65b}$$

This leads to the following:

$$\begin{aligned} \delta_x &= \delta_{yx}, & \xi_x &= \delta_{yx} - \delta_{zx} \\ \delta_y &= \delta_{xy}, & \xi_y &= \delta_{zy} - \delta_{xy} \\ \delta_z &= \delta_{xz}, & \xi_z &= \delta_{xz} - \delta_{yz} \end{aligned} \tag{5.65c}$$

Since the gyros are used as reference sensors, to ensure observability the orthogonal components of the gyro misalignment are set to zero(Lai et al., 2003). This leads to:

$$\begin{aligned} \delta_x &= \delta_{yx} = 0, & \xi_x &= -\delta_{zx} \\ \delta_y &= \delta_{xy} = 0, & \xi_y &= \delta_{zy} \\ \delta_z &= \delta_{xz} = 0, & \xi_z &= -\delta_{yz} \end{aligned} \tag{5.66a}$$

$$I + \Delta = R = \begin{bmatrix} 1 & \xi_z & \xi_y \\ 0 & 1 & \xi_x \\ 0 & 0 & 1 \end{bmatrix} \tag{5.66b}$$

The gyro model expressed in Equation (5.61) can be simplified even further

$$\boldsymbol{\omega}^b \simeq \quad T_{g_o}^b (I + \Delta + \Lambda + U)(\tilde{\omega} - \beta - \eta_v) \tag{5.67}$$

$$\boldsymbol{\omega} = T_{g_o}^b (I + \Delta + \Lambda + U)(\breve{\omega} - \eta_v) \tag{5.68a}$$

$$= T_{g_o}^b \breve{\omega} - T_{g_o}^b (I + \Delta + \Lambda + U)\eta_v + T_{g_o}^b (\Delta + \Lambda + U)\breve{\omega} \tag{5.68b}$$

$$= T_{g_o}^b \breve{\omega} - T_{g_o}^b (I + \Delta + \Lambda + U)\eta_v + T_{g_o}^b \times \begin{bmatrix} 0 & \breve{\omega}_z & \breve{\omega}_y & \breve{\omega}_x & 0 & 0 & |\breve{\omega}_x| & 0 & 0 \\ \breve{\omega}_z & 0 & 0 & 0 & \breve{\omega}_y & 0 & 0 & |\breve{\omega}_y| & 0 \\ 0 & 0 & 0 & 0 & 0 & \breve{\omega}_z & 0 & 0 & |\breve{\omega}_z| \end{bmatrix} \times \begin{pmatrix} \xi_x \\ \xi_y \\ \xi_z \\ \lambda_x \\ \lambda_y \\ \lambda_z \\ \mu_x \\ \mu_y \\ \mu_z \end{pmatrix} \tag{5.68c}$$

$$= T_{g_o}^b \breve{\omega} + T_{g_o}^b \Omega_g \kappa - T_{g_o}^b (I + \Delta + \Lambda + U)\eta_v \tag{5.68d}$$

The above expression is similar to the one presented in (Lai et al., 2003). It is important to note that, a typo was found in the expression outlined by Equation 5.68c in Lai et al. (2003); where the first element in the second row should be $\breve{\omega}_z$ instead of $\breve{\omega}_x$. From Ω_g, it can be observed that if the direction of angular vector is constant but the magnitude varies, then the scale factors can be observed independently. However, gyro misalignments are not independently observable; unless a case where the angular rate is parallel to the gyro sense axis, in which case only the misalignment of that axis is observable. This indicates that a linear combination of the states can be estimated.

5.2.2 | Discrete Process Noise Covariance

Continuous time attitude kinematics, in combination with the calibration parameters can be expressed as (Lai et al., 2003):

$$\begin{pmatrix} \delta\dot{\varrho} \\ \delta\dot{\beta} \\ \delta\dot{\kappa} \\ \delta\dot{\zeta} \end{pmatrix} = F(t) \begin{pmatrix} \delta\varrho \\ \delta\beta \\ \delta\kappa \\ \delta\zeta \end{pmatrix} + G(t) \begin{pmatrix} \eta_v \\ \eta_u \\ \eta_\kappa \\ \eta_\zeta \end{pmatrix} \tag{5.69a}$$

$$\begin{pmatrix} \delta\dot{\varrho} \\ \delta\dot{\beta} \\ \delta\dot{\kappa} \\ \delta\dot{\zeta} \end{pmatrix} = \begin{bmatrix} -[\omega\times] & -\frac{1}{2}T_{b,g_0} & -\frac{1}{2}T_{b,g_0}\Omega_g & 0 \\ 0 & 0 & 0 & 0 \\ 0 & 0 & 0 & 0 \\ 0 & 0 & 0 & 0 \end{bmatrix} \begin{pmatrix} \delta\varrho \\ \delta\beta \\ \delta\kappa \\ \delta\zeta \end{pmatrix} \cdots$$

$$\cdots + \begin{bmatrix} -\frac{1}{2}T_{b,g_0}(I+M) & 0 & 0 & 0 \\ 0 & I & 0 & 0 \\ 0 & 0 & I & 0 \\ 0 & 0 & 0 & I \end{bmatrix} \begin{pmatrix} \eta_v \\ \eta_u \\ \eta_\kappa \\ \eta_\zeta \end{pmatrix} \tag{5.69b}$$

In the above expressions, $M = (\Delta + \Lambda + U)$. When misalignments for two star trackers are calibrated for $\delta_\zeta = \begin{pmatrix} \delta_{\zeta,s1} \\ \delta_{\zeta,s2} \end{pmatrix}$, and $\eta_\zeta = \begin{pmatrix} \eta_{\zeta,s1} \\ \eta_{\zeta,s2} \end{pmatrix}$. Continuous process noise covariance is given by:
For single star tracker misalignment calibration:

$$Q = diag \begin{bmatrix} \sigma_v^2 I_{3\times3} & \sigma_u^2 I_{3\times3} & \sigma_\kappa^2 I_{9\times9} & \sigma_\zeta^2 I_{3\times3} \end{bmatrix} \tag{5.70a}$$

For misalignment calibration of both star trackers:

$$Q = diag \begin{bmatrix} \sigma_v^2 I_{3\times3} & \sigma_u^2 I_{3\times3} & \sigma_\kappa^2 I_{9\times9} & \sigma_\zeta^2 I_{6\times6} \end{bmatrix} \tag{5.70b}$$

For small angles, $M \simeq 0$

$$\begin{bmatrix} \delta\varrho \\ \delta\beta \\ \delta\kappa \\ \delta\zeta \end{bmatrix}_{k+1} \simeq \begin{bmatrix} I & -\frac{1}{2}tT_{b,g_0} & -\frac{1}{2}tT_{b,g_0}\Omega_g & 0 \\ 0 & I & 0 & 0 \\ 0 & 0 & I & 0 \\ 0 & 0 & 0 & I \end{bmatrix} \times \begin{bmatrix} \delta\varrho \\ \delta\beta \\ \delta\kappa \\ \delta\zeta \end{bmatrix}_k + \Gamma_k\eta_k \tag{5.71}$$

Here, first matrix on the right hand side of the equation is referred to as the state transition matrix $\Phi(t)$. Γ is square root of the discrete process noise covariance matrix defined as:

$$Q_d = \int_0^{\Delta t} \Phi(t)G(t)Q(t)G^T(t)\Phi^T(t)dt \tag{5.72}$$

Since, both the gyros and star trackers are aligned with the NanoSat body axis, the transformation matrix from sensor frame to body frame is identity. The above expression leads to:

$$Q_d = \begin{bmatrix} \xi_{11} & \xi_{12} & \xi_{13} & 0 \\ \xi_{21} & \xi_{22} & 0 & 0 \\ \xi_{31} & \xi_{32} & \xi_{33} & 0 \\ 0 & 0 & 0 & \xi_{44} \end{bmatrix} \tag{5.73a}$$

Where,

$$\xi_{11} = \frac{1}{4}\Delta t\sigma_v^2(I+M)(I+M)^T + \frac{1}{12}\Delta t^3\sigma_u^2 + \frac{1}{12}\Delta t^3\Omega_g\sigma_\kappa^2\Omega_g^T \tag{5.73b}$$

For small angles, $(I+M)(I+M)^T \simeq I$, thus:

$$\xi_{11} = \frac{1}{4}\Delta t\sigma_v^2 + \frac{1}{12}\Delta t^3\sigma_u^2 + \frac{1}{12}\Delta t^3\Omega_g\sigma_\kappa^2\Omega_g^T \tag{5.73c}$$

$$\xi_{12} = -\frac{1}{4}\Delta t^2\sigma_u^2 \tag{5.73d}$$

$$\xi_{13} = -\frac{1}{4}\Delta t^2\Omega_g\sigma_\kappa^2 \tag{5.73e}$$

$$\xi_{21} = -\frac{1}{4}\Delta t^2 \sigma_u^2 \tag{5.73f}$$

$$\xi_{22} = \Delta t \sigma_u^2 \tag{5.73g}$$

$$\xi_{31} = -\frac{1}{4}\Delta t^2 \sigma_\kappa^2 \boldsymbol{\Omega_g}^T \tag{5.73h}$$

$$\xi_{33} = \Delta t \sigma_\kappa^2 \tag{5.73i}$$

$$\xi_{44} = \Delta t \sigma_\zeta^2 \tag{5.73j}$$

Here, Δt is the filter update interval. Unlike the 6/7 state USQUE, the process noise presented here is iterative and is updated for each filter update step.

5.2.3 | Calibration Filter Algorithm for Attitude, Rate Gyro Bias, Scale Factor, and Sensor Misalignment Estimation

USQUE based calibration filter alogrithm is largely the same as USQUE for attitude and rate gyro bias estimation, with additional calibration states and adaptations to models influenced by those states. In the event of star tracker drop out, approach similar to the one presented earlier with the aid of Figure 5.1 is utilised. Unlike 6/7 state USQUE, since the process noise covariance is updated every filter update step, no innovation signal monitor is utilised. USQUE based calibration filter algorithm (Lai et al., 2003), to estimate attitude, rate gyro bias, scale factor, and sensor misalignment is presented as follows:

1. ***Filter Initialisation (External)***

    (a) Initialise quaternion and gyro bias
    Once the NanoSat is detumbled, the first state update from the star trackers can be used as an initial estimate of attitude for filter initialisation. This also ensures that the measurement corresponds to the measurement noise covariance statistics. Initial gyro bias is set to 0 deg/hr. Furthermore, since it was observed that selectively picking the star tracker sense axis has no benefit over stacking the star tracker measurement, the star tracker measurements are stacked for the remnant of the filter algorithm.

    (b) Initialise the state vector.

    - ○ For two star trackers:
        - • When the star tracker measurements are stacked:

$$\left(\hat{\boldsymbol{q}}_{s1,0}^+ \quad \hat{\boldsymbol{q}}_{s2,0}^+ \quad \hat{\boldsymbol{\beta}}_0^+ \quad \hat{\boldsymbol{\kappa}}_0^+ \quad \hat{\boldsymbol{\zeta}}_0^+ \right)^T \tag{5.74}$$

    (c) Initialise state covariance $\boldsymbol{P}_0^+$, with expected variance of error MRP and gyro bias:

    - ○ For two star trackers:
        - • When the star tracker outputs are stacked

$$diag\left(\left(\sigma_{\bar{\sigma}s1,1}^2 \quad \sigma_{\bar{\sigma}s1,2}^2 \quad \sigma_{\bar{\sigma}s1,3}^2 \quad \sigma_{\bar{\sigma}s2,1}^2 \quad \sigma_{\bar{\sigma}s2,2}^2 \quad \sigma_{\bar{\sigma}s2,3}^2 \quad \sigma_{\beta_x}^2 \quad \sigma_{\beta_y}^2 \quad \sigma_{\beta_z}^2 \quad \sigma_\kappa^2 \quad \sigma_\zeta^2 \right)^T \right) \tag{5.75}$$

    (d) Initialise process noise covariance matrix $\boldsymbol{Q}_d$
    The process noise covariance matrix presented earlier via Equation (5.73) is utilised:

$$\boldsymbol{Q_d} = \begin{bmatrix} \xi_{11} & \xi_{12} & \xi_{13} & 0 \\ \xi_{21} & \xi_{22} & 0 & 0 \\ \xi_{31} & \xi_{32} & \xi_{33} & 0 \\ 0 & 0 & 0 & \xi_{44} \end{bmatrix} \tag{5.76}$$

    (e) Initialise measurement error noise covariance matrix, $\boldsymbol{R}$
    For two star trackers:

    - ○ When the star tracker measurements are stacked:

$$diag\left(\left(\sigma_{q s1,1}^2 \quad \sigma_{q s1,2}^2 \quad \sigma_{q s1,3}^2 \quad \sigma_{q s1,4}^2 \quad \sigma_{q s2,1}^2 \quad \sigma_{q s2,2}^2 \quad \sigma_{q s2,3}^2 \quad \sigma_{q s2,4}^2 \right)^T \right) \tag{5.77}$$

(f) Initialise a, λ parameter, n. Set f = 2(a + 1). λ is a composite scaling factor that is used to define the spread of sigma points and exploit available knowledge about higher moments of a given distribution. Here a is a parameter between 0 and 1, and f is a scale factor. With a = 0 and f = 1, the following expression of error quaternion returns Gibbs vector, and with a = f = 1 it returns MRP from quaternion. n is the number of states, in this case 18. Error quaternion is defined as:

$$\delta q \equiv \begin{pmatrix} \delta \varrho^T & \delta q_4 \end{pmatrix}^T \tag{5.78a}$$

Corresponding generalised Rodrigues parameters as defined as:

$$\delta p \equiv f \left(\delta \varrho / \left(a + \delta q_4 \right) \right) \tag{5.78b}$$

2. **Filter initialisation (Internal)**

(a) Initialise filter state vector: reset-ed error MRP, rate gyro bias, misalignment, symmetric and asymmetric scale factor, and star tracker misalignment vector from previous filter update. The attitude error for i = 0 is reset to zero after the previous update. This is used to move information from one part of the estimate to another part. This reset rotates the reference frame for the covariance matrix. However, the covariance depends on the assumed statistics of the measurements, and not on the actual measurements. The update is zero mean, the mean rotation caused by the reset is zero, thus the covariance is not affected by the reset:

$$\chi_k(0) = \hat{x}_k^+ \equiv \begin{pmatrix} \delta \hat{p}_k^+ & \hat{\beta}_k^+ & \hat{\kappa}_k^+ & \hat{\zeta}_k^+ \end{pmatrix}^T \equiv \begin{pmatrix} 0 & \hat{\beta}_k^+ & \hat{\kappa}_k^+ & \hat{\zeta}_k^+ \end{pmatrix}^T \quad i = 0, 1, \ldots, 36 \tag{5.79}$$

3. **Sigma Point Generation**

(a) Generate error MRP and gyro bias sigma points:
First the sigma points are computed using:

$$\sigma_k \leftarrow 2n \text{ columns from } \pm \sqrt{(n + \lambda) \left(P_k^+ + \bar{Q}_k \right)} \tag{5.80a}$$

In practice, Cholesky decomposition is utilised to compute this matrix square root.

$$\chi_k(0) = \hat{x}_k^+ \tag{5.80b}$$

$$\chi_k(i) = \sigma_k(i) + \hat{x}_k^+ \tag{5.80c}$$

$$\chi_k(i) \equiv \begin{pmatrix} \chi_k^{\delta p}(i) & \chi_k^{\beta}(i) & \chi_k^{\kappa}(i) & \chi_k^{\zeta}(i) \end{pmatrix}^T, \quad i = 0, 1, \ldots, 36 \tag{5.80d}$$

(b) Estimate current quaternion based on the sigma points - Calculate corresponding error quaternion, Compute sigma point quaternion from the error quaternions utilising
Corresponding error quaternions are calculated using:

$$\delta q_k^+(i) \equiv \begin{pmatrix} \delta \varrho_k^{+T}(i) & \delta q_{4_k}^+(i) \end{pmatrix}^T \tag{5.81}$$

Where, the scalar error quaternion is given by:

$$\delta q_{4_k}^+(i) = \frac{-a \left\| \chi_k^{\delta p}(i) \right\|^2 + f \sqrt{f^2 + (1 - a^2) \left\| \chi_k^{\delta p}(i) \right\|^2}}{f^2 + \left\| \chi_k^{\delta p}(i) \right\|^2}, \quad i = 1, 2, \ldots, 36 \tag{5.82}$$

And the vectorial error quaternion is given by:

$$\delta \varrho_k^+(i) = f^{-1} \left(a + \delta q_{4_k}^+(i) \right) \chi_k^{\delta p}(i), \quad i = 1, 2, \ldots, 36 \tag{5.83}$$

Since, $\chi_k^{\delta p}(0)$ is set to 0

$$\delta q_k^+(0) \equiv \begin{pmatrix} \delta \varrho_k^{+T}(0) & \delta q_{4_k}^+(0) \end{pmatrix}^T = \begin{pmatrix} 0 & 0 & 0 & 1 \end{pmatrix}^T \tag{5.84}$$

Utilising this, the sigma point quaternions can be calculated as:

$$\hat{q}_k^+(0) = \hat{q}_k^+ \tag{5.85a}$$

$$\hat{q}_k^+(i) = \delta q_k^+(i) \otimes \hat{q}_k^+, \quad i = 1, 2, \ldots, 36 \tag{5.85b}$$

4. **Time Update and Model Forecast**

(a) Quaternion propagated forward in time step using :

$$\hat{q}_{k+1}^-(i) = \Omega\left(\hat{\omega}_k^+(i)\right)\hat{q}_k^+(i), \quad i = 0, 1, \ldots, 36 \tag{5.86}$$

Where, the posteriori estimated angular velocities for k^{th} time step are given by:

$$\hat{\omega}_k^+(i) = T_{b,g0}\left[I_{3\times3} - \hat{M}(i)\right]\left(\tilde{\omega}_k - \chi_k^\beta(i)\right), \quad i = 0, 1, \ldots, 36 \tag{5.87}$$

Note that, $\hat{M} = \hat{\Delta} + \hat{\Lambda} + \hat{U}$, which comprises of the estimated rate gyro misalignment, symmetric and asymmetric scale factor parameters. The discrete time equivalent of quaternion propagation is denoted by:

$$\Omega\left(\hat{\omega}_k^+\right) \equiv \begin{bmatrix} \cos\left(0.5\left\|\hat{\omega}_k^+\right\|\Delta t\right)I_{3\times3} - \left[\hat{\psi}_k^+\times\right] & \hat{\psi}k^+ \\ -\hat{\psi}_k^{+T} & \cos\left(0.5\left\|\hat{\omega}_k^+\right\|\Delta t\right) \end{bmatrix} \tag{5.88}$$

Where, Δt is the sampling interval of the filter update and $\hat{\psi}_k^+$ is given by:

$$\hat{\psi}_k^+ \equiv \sin\left(0.5\left\|\hat{\omega}_k^+\right\|\Delta t\right)\hat{\omega}_k^+ / \left\|\hat{\omega}_k^+\right\| \tag{5.89}$$

(b) Propagated error quaternions are then determined using:

$$\delta q_{k+1}^-(i) = \hat{q}_{k+1}^-(i) \otimes \left(\hat{q}_{k+1}^-(0)\right)^{-1}, \quad i = 0, 1, \ldots, 36 \tag{5.90}$$

Where, $\delta q_{k+1}^-(0)$ is the identity quaternion.

(c) Propagation of sigma points to the next time step is conducted as follows:

$$\chi_{k+1}^{\delta p}(0) = 0 \tag{5.91}$$

$$\chi_{k+1}^{\delta p}(i) = f\frac{\delta\varrho_{k+1}^-(i)}{a + \delta q_{4k+1}^-(i)}, \quad i = 1, 2, \ldots, 36 \tag{5.92}$$

Where,

$$\left(\delta\varrho_{k+1}^{-T}(i) \quad \delta q_{4k+1}^-(i)\right)^T = \delta q_{k+1}^-(i) \tag{5.93}$$

And,

$$\chi_{k+1}^\beta(i) = \chi_k^\beta(i), \quad i = 0, 1, \ldots, 36 \tag{5.94}$$

$$\chi_{k+1}^\kappa(i) = \chi_k^\kappa(i), \quad i = 0, 1, \ldots, 36 \tag{5.95}$$

$$\chi_{k+1}^\zeta(i) = \chi_k^\zeta(i), \quad i = 0, 1, \ldots, 36 \tag{5.96}$$

$$\chi_{k+1}(i) \equiv \begin{pmatrix} \chi_{k+1}^{\delta p}(i) \\ \chi_{k+1}^\beta(i) \\ \chi_{k+1}^\kappa(i) \\ \chi_{k+1}^\zeta(i) \end{pmatrix}, \quad i = 0, 1, \ldots, 36 \tag{5.97}$$

(d) State propagation: Predicting mean of the state from propagated sigma points

$$\hat{x}_{k+1}^- = \frac{1}{n + \lambda}\left\{\lambda\chi_{k+1}(0) + \frac{1}{2}\sum_{i=1}^{2n}\chi_{k+1}(i)\right\} \tag{5.98}$$

(e) State covariance propagation: Predicting covariance of the state from propagated sigma points

$$P_{k+1}^- = \frac{1}{n + \lambda}\left\{\lambda\left(\chi_{k+1}(0) - \hat{x}_{k+1}^-\right)\left(\chi_{k+1}(0) - \hat{x}_{k+1}^-\right)^T \ldots \right.$$
$$\left. \ldots + \frac{1}{2}\sum_{i=1}^{2n}\left(\chi_{k+1}(i) - \hat{x}_{k+1}^-\right)\left(\chi_{k+1}(i) - \hat{x}_{k+1}^-\right)^T\right\} + \bar{Q}_k \tag{5.99}$$

(f) Propagation of observation sigma points to the next time step using observation models

$$\boldsymbol{\gamma}_{k+1}(i) = \boldsymbol{h}\left(\boldsymbol{\chi}_{k+1}(i), k\right) \tag{5.100}$$

Since, the star tracker returns attitude knowledge in the spacecraft body frame with respect to inertial reference frame. Observation sigma points (gamma points) can be propagated with the aid of general expression for gamma (observation sigma points) for a misaligned attitude sensor:

$$\boldsymbol{\gamma}_{k+1}(i) = \left[\boldsymbol{I} - \boldsymbol{\chi}_{k+1}^{\zeta}(i)\times\right]\boldsymbol{T}_{s_0,b}\hat{\boldsymbol{q}}_{k+1}^{-}(i), \quad i = 0, 1, \ldots, 36 \tag{5.101}$$

In the case of one misaligned star tracker and one nominal star tracker the gamma points can be expressed as:

$$\boldsymbol{\gamma}_{k+1}(i) = \left(\begin{array}{c}\left[\boldsymbol{I} - \boldsymbol{\chi}_{k+1}^{\zeta}(i)\times\right]\boldsymbol{T}_{s_0,b}\hat{\boldsymbol{q}}_{k+1}^{-}(i) \\ \boldsymbol{T}_{s_0,b}\hat{\boldsymbol{q}}_{k+1}^{-}(i)\end{array}\right), \quad i = 0, 1, \ldots, 36 \tag{5.102}$$

In the case of two misaligned star trackers:

$$\boldsymbol{\gamma}_{k+1}(i) = \left(\begin{array}{c}\left[\boldsymbol{I} - \boldsymbol{\chi}_{k+1}^{\zeta,\,s1}(i)\times\right]\boldsymbol{T}_{s_0,b}\hat{\boldsymbol{q}}_{k+1}^{-}(i) \\ \left[\boldsymbol{I} - \boldsymbol{\chi}_{k+1}^{\zeta,\,s2}(i)\times\right]\boldsymbol{T}_{s_0,b}\hat{\boldsymbol{q}}_{k+1}^{-}(i)\end{array}\right), \quad i = 0, 1, \ldots, 36 \tag{5.103}$$

(g) Observation propagation: Predicting mean of the observation from propagated gamma points

$$\hat{\boldsymbol{y}}_{k+1}^{-} = \frac{1}{n+\lambda}\left\{\lambda\boldsymbol{\gamma}_{k+1}(0) + \frac{1}{2}\sum_{i=1}^{2n}\boldsymbol{\gamma}_{k+1}(i)\right\} \tag{5.104}$$

(h) Observation covariance propagation: Propagating output covariance of the observation from propagated observation sigma points (gamma points) and mean of observation

$$\boldsymbol{P}_{k+1}^{yy} = \frac{1}{n+\lambda}\left\{\lambda\left(\boldsymbol{\gamma}_{k+1}(0) - \hat{\boldsymbol{y}}_{k+1}^{-}\right)\left(\boldsymbol{\gamma}_{k+1}(0) - \hat{\boldsymbol{y}}_{k+1}^{-}\right)^{T} \ldots \right.$$
$$\left. \ldots + \frac{1}{2}\sum_{i=1}^{2n}\left(\boldsymbol{\gamma}_{k+1}(i) - \hat{\boldsymbol{y}}_{k+1}^{-}\right)\left(\boldsymbol{\gamma}_{k+1}(i) - \hat{\boldsymbol{y}}_{k+1}^{-}\right)^{T}\right\} \tag{5.105}$$

(i) Innovation covariance matrix propagation

$$\boldsymbol{R}_{k+1} = \boldsymbol{R}_k \tag{5.106}$$

$$\boldsymbol{P}_{k+1}^{vv} = \boldsymbol{P}_{k+1}^{yy} + \boldsymbol{R}_{k+1} \tag{5.107}$$

(j) Cross-correlation matrix propagation

$$\boldsymbol{P}_{k+1}^{xy} = \frac{1}{n+\lambda}\left\{\lambda\left(\boldsymbol{\chi}_{k+1}(0) - \hat{\boldsymbol{x}}_{k+1}^{-}\right)\left(\boldsymbol{\gamma}_{k+1}(0) - \hat{\boldsymbol{y}}_{k+1}^{-}\right)^{T} \ldots \right.$$
$$\left. \ldots + \frac{1}{2}\sum_{i=1}^{2n}\left(\boldsymbol{\chi}_{k+1}(i) - \hat{\boldsymbol{x}}_{k+1}^{-}\right)\left(\boldsymbol{\gamma}_{k+1}(i) - \hat{\boldsymbol{y}}_{k+1}^{-}\right)^{T}\right\} \tag{5.108}$$

5. **Data Assimilation Step**

(a) Filter gain update

$$\boldsymbol{K}_{k+1} = \boldsymbol{P}_{k+1}^{xy}\left[\boldsymbol{P}_{k+1}^{vv}\right]^{-1} \tag{5.109}$$

(b) Innovation signal update

$$\boldsymbol{v}_{k+1} \equiv \tilde{\boldsymbol{y}}_{k+1} - \hat{\boldsymbol{y}}_{k+1}^{-} = \tilde{\boldsymbol{y}}_{k+1} - \boldsymbol{h}\left(\hat{\boldsymbol{x}}_{k+1}^{-}, k+1\right) \tag{5.110}$$

(c) State vector update

$$\hat{\boldsymbol{x}}_{k+1}^{+} = \hat{\boldsymbol{x}}_{k+1}^{-} + \boldsymbol{K}_{k+1}\boldsymbol{v}_{k+1} = \left(\begin{array}{cccc}\delta\hat{\boldsymbol{p}}_{k+1}^{+T} & \hat{\boldsymbol{\beta}}_{k+1}^{+T} & \hat{\boldsymbol{\kappa}}_{k+1}^{+T} & \hat{\boldsymbol{\zeta}}_{k+1}^{+T}\end{array}\right)^{T} \tag{5.111}$$

(d) State covariance update

$$P^+_{k+1} = P^-_{k+1} - K_{k+1} P^{vv}_{k+1} K^T_{k+1} \tag{5.112}$$

(e) Post update error quaternion from post update error MRP

$$\hat{q}^+_{k+1} = \delta q^+_{k+1} \otimes \hat{q}^-_{k+1}(0) \tag{5.113}$$

Where, $\delta q^+_{k+1} \equiv \left(\delta \varrho^{+T}_{k+1} \quad \delta q^+_{4_{k+1}} \right)^T$ is provided by the expressions:

$$\delta q^+_{4k+1} = \frac{-a \left\| \delta \hat{p}^+_{k+1} \right\|^2 + f \sqrt{f^2 + (1 - a^2) \left\| \delta \hat{p}^+_{k+1} \right\|^2}}{f^2 + \left\| \delta \hat{p}^+_{k+1} \right\|^2} \tag{5.114a}$$

$$\delta \varrho^+_{k+1} = f^{-1} \left(a + \delta q^+_{4_{k+1}} \right) \delta \hat{p}^+_{k+1} \tag{5.114b}$$

6. **_Return filter output_** :
   Here the attitude state is in quaternion:
   $\hat{x}^+_{k+1}, P^+_{k+1}$

This concludes the segment on USQUE (UnScented QUaternion Estimator) based filter development. First a 6/7 state UKF based unscented quaternion estimator was presented. This was followed by an innovation signal monitor for avoid premature convergence of the state covariance. A schematic outlining the flow of algorithm, esp. in the absence of star tracker was outlined. Finally, the USQUE based filter was adapted to include calibration states, and develop a calibration filter to calibrate for star tracker misalignment, and gyro misalignment, scale factor, and bias, in conjunction with the NanoSat body attitude knowledge. Results of the filters developed in this chapter are presented in Chapter 6.

Results and Sensitivity Analysis

The objective of this chapter is to present the results, and demonstrate the sensitivity of the filters synthesized with regards to different filter, sensor, and manoeuvre specific parameters. This is done so with the aid of three core segments. The simulation conditions used to simulate the filter performances presented here, is outlined with the aid of Section 6.1. First, Section 6.2 demonstrates the attitude knowledge estimation capability of the 6/7 state USQUE, in the absence of gyro-stellar misalignment and scale factors. The impact of covariance monitor, on the attitude knowledge estimation is demonstrated. Different ways of merging the available two star trackers is presented. Effect of gyro sampling rate on the filter output performance is demonstrated. Finally the effect of star tracker dropout, under agile terrestrial target tracking conditions, on the attitude knowledge output of the filter is discussed. Next, Section 6.3 aims at demonstrating the results in the presence of gyro-stellar misalignment and scale factors. The effect of gyro deterministic non-idealities on the observed attitude rate, was demonstrated earlier in Section 4.8.2 to be minimal; the impact of 6/7 USQUE filter with perfect knowledge of star tracker alignment but in the presence of gyro non-idealities is further investigated. Finally, Section 6.4 aims at investigating the attitude knowledge estimation and filter parameter calibration performance of the USQUE based calibration filter, for the manoeuvre sequences synthesised in Section 4.5. The effect of filter output performance in the event of sensor degradation, exclusion of rotational misalignment, star tracker drop out, and under different calibration manoeuvres is further investigated. The chapter concludes with a summary results obtained.

6.1 | Simulation Conditions

The initialisation conditions utilised for 6/7 state USQUE filter simulations, both in the absence and presence of deterministic sensors errors, are presented with the aid of Table 6.1. The table further outlines the additional simulation conditions utilised for the calibration filter. Initial quaternion is taken from the first raw star tracker output, irrespective of the misalignment condition. σ_u and σ_v, depends on the gyro sensor utilised. σ_u and σ_v were presented earlier in Table 3.3. The simulations presented as part Sections 6.2 and 6.3, rely on MPSAG for core analysis, while HPTAG is used to demonstrate the performance improvement. While Section 6.4 captures both MPSAG and HPTAG, and more emphasis is paid to the latter. Star tracker performance specifications were presented earlier with the aid of Table 2.3. While gyro specifications were presented earlier in Table 3.3. Star tracker and gyro configurations in the NanoSat body axis was presented earlier with the aid of Figures 4.15 and 4.17. Analytical process noise covariance, $\bar{\mathbf{Q}}_{\mathbf{k}}$, expressed earlier in Equation (5.20) is utilised for 6/7 state USQUE filter. However, for the calibration filter the time dependent process noise covariance $\boldsymbol{Q_d}$ as outlined previously with Equation 5.73 in Section 5.2.2 is utilised. For initial state covariance, $\mathbf{P}_{\mathbf{x,0}}$, it is assumed that the standard associated with the initial state attitude initialisation is 1 deg for pitch/yaw axis and 2 deg for roll axis. For small angles, MRP vector is approximately equivalent to Euler-321 angle. For MPSAG the manufacturer provides a bias instability of approximately 3 deg/hr, and for HPTAG a bias instability of 0.3 deg/hr. This is utilised to initialise the expected initial standard deviation of the bias in the state covariance matrix. $\mathbf{R_{s1}}$ is extracted by inferring the standard deviation of the difference in the real quaternion time series and that observed by star tracker aligned with the body axis. Similarly, $\mathbf{R_{s2}}$ is extracted from the standard deviation of the quaternion observation of two star trackers.

The gyros misalignment ($\delta_{XY}, \delta_{XZ}, \delta_{YX}, \delta_{YZ}, \delta_{ZX}, \delta_{ZY}$) are set to: 0.5 deg; symmetric scale factors are set to: $\tilde{\mathbf{\Lambda}}$ = [500 ppm, 500 ppm, 500 ppm] ; and asymmetric scale factors are set to: $\tilde{\mathbf{U}}$ =[100ppm, 100 ppm, 100 ppm]. Star tracker 1, which is aligned with the NanoSat body axis, is given a misalignment of 0.1 deg along the roll, pitch, and yaw axis. Star tracker 2, where the star tracker pitch axis is aligned with NanoSat body axis is assumed to be perfectly aligned.

Table 6.1: *Simulation initialisation conditions used for 6/7 state USQUE filter, and 18/19 state USQUE calibration filter.*

6/7 State USQUE Filter Initialisation Conditions		
Parameters	**Set Value**	**Units and Comments**
Initial attitude, q	First star tracker quaternion output	[-]
Initial bias, β	[0, 0, 0]	[rad/s]
Initial state covariance, $P_{x,0}$	$\text{diag}([(\frac{2\pi}{180})^2, (\frac{\pi}{180})^2, (\frac{\pi}{180})^2, \ldots$ $\ldots (3\frac{\pi}{180\cdot3600})^2, (3\frac{\pi}{180\cdot3600})^2, (3\frac{\pi}{180\cdot3600})^2])$	$[-^2, -^2, -^2, (\text{rad/s})^2, (\text{rad/s})^2, (\text{rad/s})^2]$
Standard deviation wrt RRW, σ_u for MPSAG	1.4605e-06	$[\text{rad/s}^{3/2}]$
Standard deviation wrt ARW, σ_v for MPSAG	1.1636e-04	$[\text{rad/s}^{1/2}]$
Standard deviation wrt RRW, σ_u for HPTAG	4.1985e-08	$[\text{rad/s}^{3/2}]$
Standard deviation wrt ARW, σ_v for HPTAG	4.3633e-05	$[\text{rad/s}^{1/2}]$
Sample time, dt_Q, for process noise covariance matrix, Q, MPSAG	1/2300	[s]
Sample time, dt_Q, for process noise covariance matrix, Q, HPTAG	1/2000	[s]
Measurement noise covariance R_{s1}, when one ST is utilised	$\text{diag}([\sigma^2_{q_{s1,1}}, \sigma^2_{q_{s1,2}}, \sigma^2_{q_{s1,3}}, \sigma^2_{q_{s1,4}}])$	[-]
Measurement noise covariance R_{s2}, when two ST are utilised	$\text{diag}([\sigma^2_{q_{s1,1}}, \sigma^2_{q_{s1,2}}, \sigma^2_{q_{s1,3}}, \sigma^2_{q_{s1,4}}, \ldots$ $\ldots \sigma^2_{q_{s2,1}}, \sigma^2_{q_{s2,2}}, \sigma^2_{q_{s2,3}}, \sigma^2_{q_{s2,4}}])$	[-]
Filter initialisation parameters	a = 1, λ = 1, f = 2·(a+1), n = 6	a = f = scale factor chosen for MRP conversion, n = number of states λ = composite scaling parameter to exploit knowledge of higher moments
Quaternion propagation sample time, dt	1/5 or 1/100	[s] depending on the filter update rate
Innovation signal ϑ, window size N	25	[-]
Covariance scaling factor, Π^{-1}	$1.5 I_{6\times6}$	[-]
USQUE Calibration Filter Initialisation Conditions		
Initial gyro MA, ξ_x, ξ_y, ξ_z	[0, 0, 0]	[rad]
Initial gyro ASF, $\lambda_x, \lambda_y, \lambda_z$	[0, 0, 0]	[ppm]
Initial gyro SSF, μ_x, μ_y, μ_z	[0, 0, 0]	[ppm]
Initial ST MA, $\zeta_1, \zeta_2, \zeta_3$	[0, 0, 0]	[rad]
Standard deviation wrt gyro MA and SF, σ_κ	[5, 5, 5, 5000, 5000, 5000, 5000, 5000, 5000]	[deg, deg, deg, ppm, ppm, ppm, ppm, ppm, ppm]
Standard deviation wrt ST MA, σ_ζ	[5, 5, 5]	[deg]
Initial state covariance, $P_{x,0_{calibration}}$	$\text{diag}([\ P_{x,0}, \sigma_\kappa{}^2, \sigma_\zeta{}^2\ ])$	$[-^2, -^2, -^2, (\text{rad/s})^2, (\text{rad/s})^2, (\text{rad/s})^2, \ldots$ $\ldots \text{rad}^2, \text{rad}^2, \text{rad}^2, \text{ppm}^2, \text{ppm}^2, \text{ppm}^2, \ldots$ $\ldots \text{ppm}^2, \text{ppm}^2, \text{ppm}^2, \ldots$ $\ldots \text{rad}^2, \text{rad}^2, \text{rad}^2\ ]$

6.2 | USQUE Filter Performance in the Absence of Misalignment and Scale Factors

The objective of this Section is to investigate the attitude estimation performance of 6/7 state USQUE developed in Section 5.1, in the absence of misalignment and scale factors. This is done so with the aid of four core segments. First the influence of innovation signal monitor for covariance convergence, developed earlier in Section 5.1.2, on attitude knowledge estimation performance is investigated. Next, the effect of star tracker drop-out, under agile ground target tracking manoeuvre, on the filter output is investigated in Section 6.2.2. The effect of different ways of merging star tracker output, on the filter output is investigated in Section 6.2.3. The effect of higher filter and gyro update rate compared to the star tracker update rate is investigated in Section 6.2.4. Finally, attitude estimation performance of the filter output when HPTAG is utilised, is presented with the aid of Section 6.2.5. 1σ absolute attitude knowledge error (AKE) is used to evaluate the attitude estimation performance of a given time window. 1σ AKE is defined as the 1σ of the estimation error, added to its absolute mean.

6.2.1 | Effect of Covariance Convergence Monitor

For this segment, one star tracker is utilised in combination with three MPSAG. It is further assumed that there are no star tracker drop-outs under agile slewing conditions. Figures 6.1 and 6.2, demonstrate the Euler-321 and quaternion attitude tracking performance achieved with, and without an innovation signal based covariance monitor. Primarily from these attitude tracking plots, not much difference is observed.
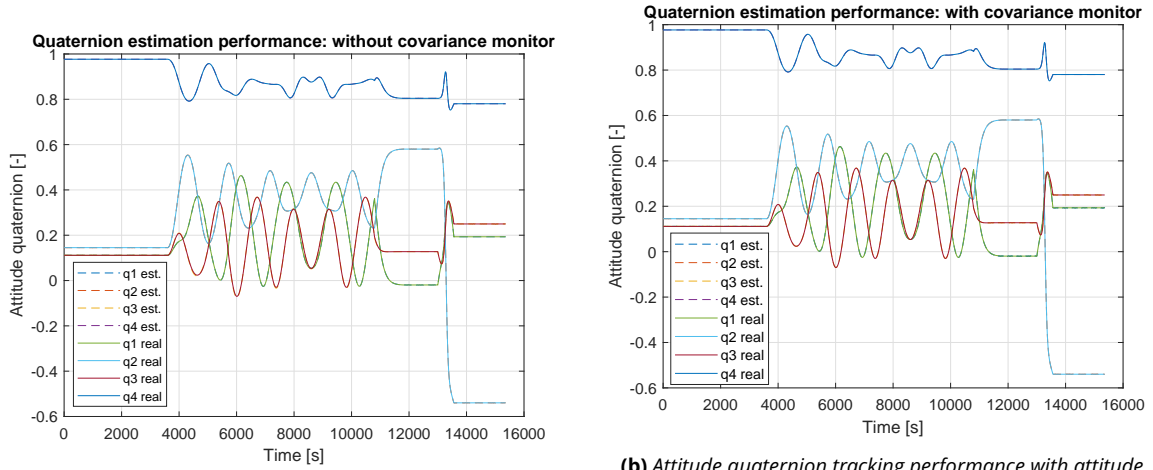
(a) *Attitude quaternion tracking performance without covariance monitor.*

(b) *Attitude quaternion tracking performance with attitude innovation signal monitor to avoid premature state covariance convergence.*

Figure 6.1: *Attitude quaternion tracking performance with and without an innovation signal monitor. One star tracker and three MPSAG utilised, with filter and sensor update rate set to 5Hz. No slew-rate induced star tracker dropouts are considered.*
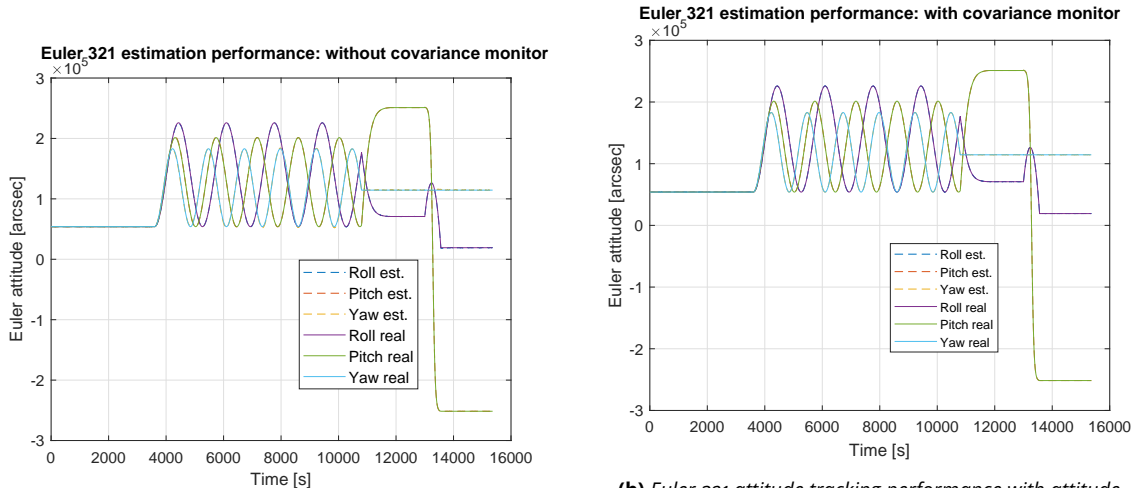
(a) *Euler-321 attitude tracking performance without covariance monitor.*

(b) *Euler-321 attitude tracking performance with attitude innovation signal monitor to avoid premature state covariance convergence.*

Figure 6.2: *Euler-321 attitude tracking performance with and without an innovation signal monitor. One star tracker, and three MPSAG, with filter and sensor update rate set to 5Hz. No slew-rate induced star tracker dropouts are considered.*
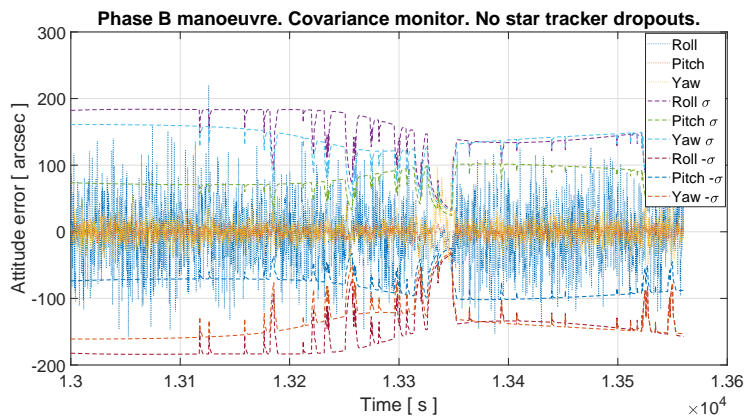
Figure 6.3: *Phase B manoeuvre attitude estimation performance with covariance monitor. One star tracker, and three MPSAG, with filter and sensor update rate set to 5Hz.*
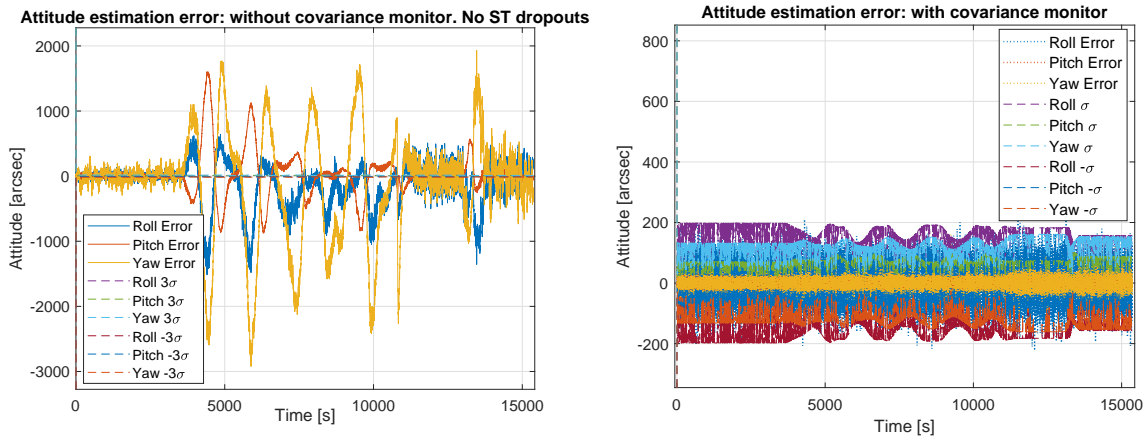
(a) *Euler-321 attitude estimation error, and 3σ bounds for USQUE without covariance monitor.*

(b) *Euler-321 attitude estimation error, and 1σ bounds for USQUE with covariance monitor.*

Figure 6.4: *Euler-321 attitude estimation error with and without covariance monitor. One star tracker, and three MPSAG, with filter and sensor update rate set to 5Hz. No slew-rate induced star tracker dropouts are considered.*
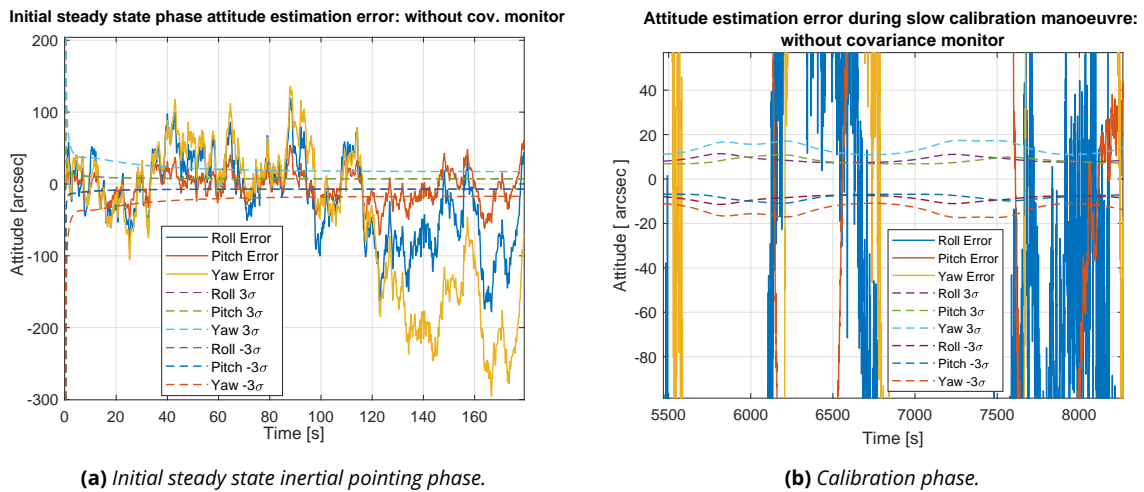
(a) *Initial steady state inertial pointing phase.*

(b) *Calibration phase.*

Figure 6.5: *Euler-321 attitude knowledge estimation error and 3σ-bound convergence behaviour for the initial inertial pointing phase and calibration manoeuvre, without covariance monitor. One ST, and three MPSAG, with filter and sensor update rate set to 5Hz. No slew-rate induced star tracker dropouts are considered.*

However, upon evaluating Figure 6.4a it is evident that the filter output 3σ bounds for the case without covariance monitor converges before the attitude error converges. This is especially problematic when the NanoSat starts slewing, when the state covariance is observed to be negligibly reactive to the growing attitude error. However, with a covariance monitor this problem is elevated as demonstrated by the 1σ bounds and the estimated attitude knowledge error in Figure 6.4b. Since manoeuvre specific behaviour of attitude estimation is harder to observe in Figure 6.4, the behaviour of initial inertial pointing with zero angular rate and during the slow calibration manoeuvre phase, without covariance monitor, is presented with the aid of Figure 6.5. Figure 6.6 captures the attitude estimation performance, with covariance monitor, for the initial inertial pointing manoeuvre. Similarly, Figure 6.7 captures the attitude estimation performance of the filter with covariance monitor for the slow calibration manoeuvre phase. While, Figure 6.3 captures the same for phase B manoeuvre associated with the slow calibration manoeuvre. This comprises of a pre-ground-target tracking segment, following by agile terrestrial target tracking manoeuvre, followed by inertial pointing with constant non-zero angular slew rate. For all the manoeuvres, no star tracker drop out is taken into account. The manoeuvres are simulated with one star tracker, and three MPSAG, with filter and sensor update rate set to 5Hz. The effect of covariance monitor on bias estimation with 6/7 state USQUE filter is presented with the aid of Appendix D.1.1. As demonstrated with Table 6.2, application of covariance monitor improves the attitude estimation performance across all mission phases.

(a) *Roll angle error for the initial steady state inertial pointing phase.*

(b) *Pitch and yaw angle error for the initial steady state inertial pointing phase.*
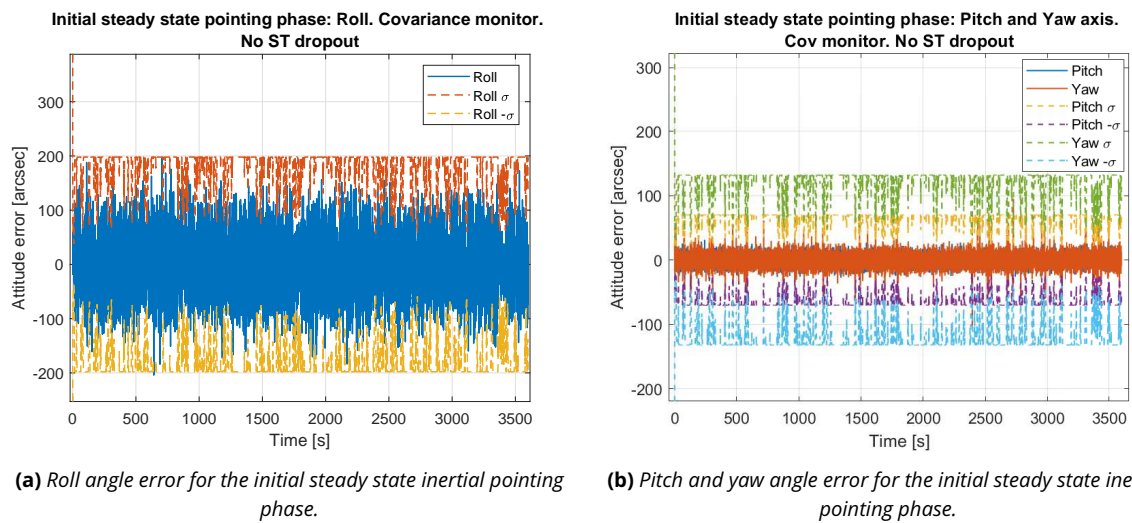
Figure 6.6: *Euler-321 attitude estimation error and σ-bound convergence behaviour for the initial inertial pointing phase, with covariance monitor. One star tracker, and three MPSAG, with filter and sensor update rate set to 5Hz. No slew-rate induced star tracker dropouts are considered.*

(a) *Roll angle error for the calibration phase.*

(b) *Pitch and yaw angle error for the calibration phase.*
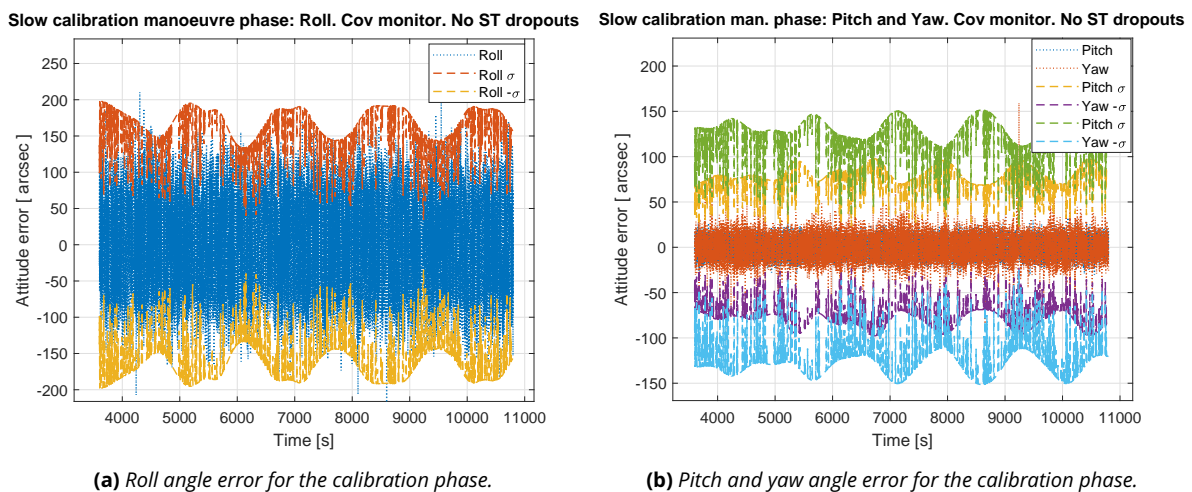
Figure 6.7: *Euler-321 attitude estimation error and σ-bound convergence behaviour for the calibration manoeuvre phase, with covariance monitor. One star tracker, and three MPSAG, with filter and sensor update rate set to 5Hz. No slew-rate induced star tracker dropouts are considered.*

Table 6.2: *Impact of covariance monitor on the attitude knowledge estimation performance of the 6/7 state USQUE filter.*

USQUE 6/7 state filter sensor and filter update rate set to 5 Hz	Time	[0, 3600)	[3600, 10800)	[10800, 13000)	[13000, 13560)	[13560, 15360]
	Mission manoeuvres without ST dropout:	Initial inertial pointing - Non-zero attitude - Zero angular rate	Slow calibration manoeuvre	Pre-ground target tracking	During agile target tracking	Target pointing, post calibration manoeuvre
Sensor configuration		Attitude error [arcsec]				
1 ST and 3 MPSAG at 5 Hz No MA SF. No covariance monitor	Mean [Roll, Pitch, Yaw]	[7.04, -0.07, 4.18]	[-1457.70, 368.72, -586.27]	[472.49, -436.83, 77.08]	[-2839.08, 896.10, 961.71]	[-694.60, -56.68, 713.60]
	Std. Dev (1 σ) [Roll, Pitch, Yaw]	[236.92, 67.23, 192.56]	[6017.62, 2912.07, 4312.28]	[1628.89, 875.79, 1837.31]	[994.90, 1808.95, 3259.92]	[1548.71, 306.39, 1654.31]
	Abs. AKE (1 σ) [Roll, Pitch, Yaw]	[243.96, 67.30, 196.74]	[7475.32, 3280.79, 4898.55]	[2101.38, 1312.62, 1914.39]	[3833.98, 2705.05, 4221.63]	[2243.31, 363.07, 2367.91]
1 ST and 3 MPSAG at 5 Hz No MA SF With covariance monitor	Mean [Roll, Pitch, Yaw]	[-0.55, -0.06, -0.12]	[-0.26, 0.048, 0.096]	[-0.64, 0.019, -0.18]	[-1.73, -0.39, 1.28]	[0.015, -0.033, 0.54]
	Std. Dev (1 σ) [Roll, Pitch, Yaw]	[46.87, 8.67, 11.59]	[48.49, 7.60, 12.56]	[51.93 7.76 15.78]	[48.09, 8.00, 17.45]	[48.20, 8.55, 18.69]
	Abs. AKE (1 σ) [Roll, Pitch, Yaw]	[47.42, 8.73, 11.71]	[48.75, 7.65, 12.66]	[52.57, 7.78, 15.96]	[49.82, 8.39, 18.73]	[48.22, 8.58, 19.23]

Table 6.3: *Attitude knowledge estimation performance of the 6/7 state USQUE filter with regards to different star tracker measurement mixing schemes.*

USQUE 6/7 state filter sensor and filter update rate set to 5 Hz	Time	[0, 3600)	[3600, 10800)	[10800, 13000)	[13000, 13560)	[13560, 15360]
	Mission manoeuvres without ST dropout:	Initial inertial pointing - Non-zero attitude - Zero angular rate	Slow calibration manoeuvre	Pre-ground target tracking	During agile target tracking	Target pointing, post calibration manoeuvre
Sensor configuration		Attitude error [arcsec]				
2 ST and 3 MPSAG at 5 Hz No MA SF ST measurements stacked	Mean [Roll, Pitch, Yaw]	[-0.29, -0.22, -0.23]	[-0.38, -0.10, 0.15]	[-0.13, -0.10, 0.040]	[0.074, 0.40, -0.0093]	[1.02, -0.54, -1.16]
	Std. Dev (1 σ) [Roll, Pitch, Yaw]	[20.11, 11.88, 17.62]	[25.97, 14.39, 20.43]	[35.41, 14.40, 31.49]	[27.09, 14.34, 28.99]	[25.59, 13.27, 32.46]
	Abs. AKE (1 σ) [Roll, Pitch, Yaw]	[20.40, 12.10, 17.85]	[26.35, 14.49, 20.58]	[35.54, 14.50, 31.53]	[27.16, 14.74, 29.00]	[26.61, 13.81, 33.62]
2 ST and 3 MPSAG at 5 Hz No MA SF ST axis pre-selection	Mean [Roll, Pitch, Yaw]	[1.92, 0.86, 1.70]	[-5.02, -5.24, 6.82]	[-1.09, -0.69, -1.18]	[-6.13, 10.92, 6.88]	[-0.01, -0.17, -0.10]
	Std. Dev (1 σ) [Roll, Pitch, Yaw]	[36.09, 19.25, 34.36]	[52.82, 63.49, 57.85]	[34.81, 8.65, 30.37]	[40.97, 37.45, 44.95]	[27.34, 13.14, 43.13]
	Abs. AKE (1 σ) [Roll, Pitch, Yaw]	[38.01, 20.11, 36.06]	[57.84, 68.73, 64.67]	[35.90, 9.34, 31.55]	[47.10, 48.37, 51.83]	[27.35, 13.31, 43.23]

Table 6.4: *Attitude knowledge estimation performance of the 6/7 state USQUE filter with regards to ground target tracking manoeuvre sequences with and without star tracker dropout. This further outlines the impact of gyro sampling and gyro sensor noise degradation on attitude estimation performance. [P] = Partially (some axis) qualified, [UQ] = Unqualified.*

USQUE 6/7 state filter performance	Time	[13000 , 13197)	[13197 , 13354)	[13197, 13354)	[13354, 13560)	[13000,13560)	[13000,13560)
	Mission Phase	Before ST dropout	During ST dropout	No ST dropout	After ST recovery	During agile target tracking with ST dropout	During agile target tracking without ST dropout
Sensor Configuration					Attitude error [arcsec]		
1 ST, 3 MPSAG, and filter update rate set to 5 Hz	Mean [Roll, Pitch, Yaw]	[0.22, 0.13, -0.30]	[-4925.60, 3328.01, -1284.87]	[-4.65, -1.37, 3.03]	[-0.26, -0.50, 0.61]	[-1526.41, 1031.19, -398.06]	[-2.0, -0.33, 1.09]
	Std. Dev (1 σ) [Roll, Pitch, Yaw]	[52.25, 7.49, 15.20]	[3855.64, 2476.16, 1049.05]	[42.25, 8.43, 19.46]	[62.94, 18.99, 21.55]	[3129.82, 2066.01, 833.23]	[48.16, 7.86, 16.65]
	Abs. AKE (1 σ) [Roll, Pitch, Yaw]	[52.47, 7.62, 15.50] [P]	[8781.25, 5804.17, 2333.91] [UQ]	[46.90, 9.80, 22.49] [P]	[63.21, 19.49, 22.16] [P]	[4656.23, 3097.20, 1231.29] [UQ]	[50.16, 8.19, 17.74] [P]
2 ST, 3 MPSAG, and filter update rate set to 5 Hz	Mean [Roll, Pitch, Yaw]	[-0.26, 2.91, 3.26]	[-5379.59, 7608.73, -2797.16]	[-0.26, 2.91, 3.26]	[1.00, -1.67, -2.61]	[-1667.02, 2357.27, -867.75]	[-0.03, 0.32, -0.09]
	Std. Dev (1 σ) [Roll, Pitch, Yaw]	[20.73, 16.18, 25.14]	[3233.5960, 5997.39, 1029.85]	[20.73, 16.18, 25.14]	[20.80, 11.83, 29.22]	[3070.78, 4850.32, 1414.66]	[27.15, 14.41, 29.10]
	Abs. AKE (1 σ) [Roll, Pitch, Yaw]	[37.29, 14.78, 32.49] [P]	[8613.18, 13606.12, 3827.01] [UQ]	[20.99, 19.09, 28.39] [P]	[21.80, 13.51, 31.83] [P]	[4737.81, 7207.60, 2282.41] [UQ]	[27.18, 14.74, 29.19] [P]
2 ST, 1 HPTAG, and filter update rate set to 5 Hz	Mean [Roll, Pitch, Yaw]	[-0.034, 0.24, 0.12]	[-2579.72, 7245.36, -516.08]	[-6.67, 0.46, 2.77]	[-3.02, -8.03, 5.95]	[-800.49,2242.54,-157.82]	[-3.56, -3.43, 3.84]
	Std. Dev (1 σ) [Roll, Pitch, Yaw]	[30.43, 12.88, 26.49]	[2131.51, 6243.27, 673.69]	[17.57, 16.22, 20.44]	[18.63, 13.57, 26.69]	[1682.04, 4828.28, 445.74]	[23.79, 16.60, 26.96]
	Abs. AKE (1 σ) [Roll, Pitch, Yaw]	[30.47, 13.11, 26.60] [P]	[4711.23, 13488.62, 1189.77] [UQ]	[24.24, 16.69, 23.20] [P]	[21.66, 21.60, 32.64] [UQ]	[2482.53, 7070.82, 603.56] [UQ]	[27.35, 20.03, 30.80] [P]
1 ST at 5Hz 3 MPSAG, and filter update rate set to 100 Hz	Mean [Roll, Pitch, Yaw]	[-162.82, 145.55, -0.55]	[-1641.58, 5288.92, -2725.31]	[45.75, 1337.39, 1.091]	[262.05,167.74,-2.45]	[-473.61 ,1749.36 ,-846.75]	[51.53, 520.44, -0.04]
	Std. Dev (1 σ) [Roll, Pitch, Yaw]	[100.08, 169.96, 37.73]	[1707.60, 3173.65, 1563.41]	[74.67, 373.24, 21.12]	[200.09, 339.90, 100.58]	[1251.84, 2968.63 , 1533.08]	[199.62, 604.21, 30.51]
	Abs. AKE (1 σ) [Roll, Pitch, Yaw]	[262.90, 315.51, 38.27] [UQ]	[3349.18, 8462.57, 4288.73] [UQ]	[120.42, 1710.64, 22.21] [UQ]	[462.14, 507.64, 103.03] [UQ]	[1725.45, 4717.99, 2379.83] [UQ]	[251.15, 1124.64, 30.56] [UQ]
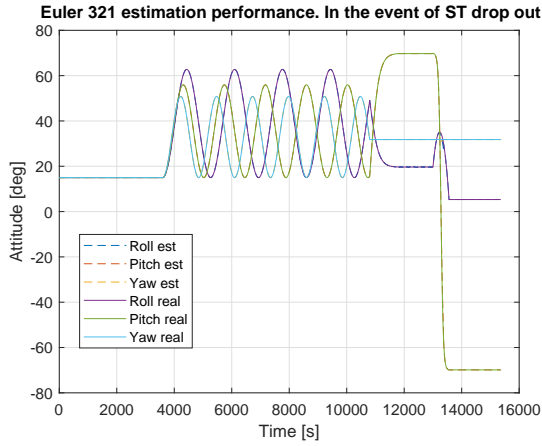
(a) *Tracked Euler-321 attitude in the event of ST drop out.*
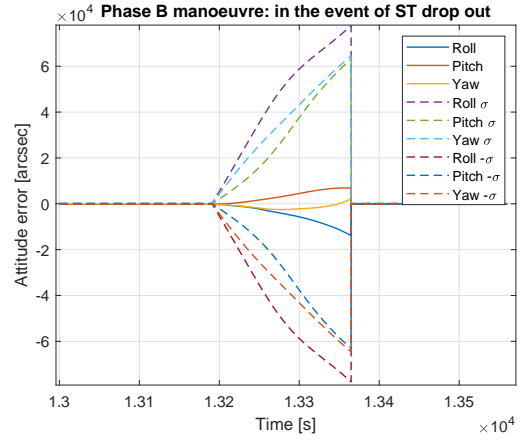
(b) *Impact of ST drop out, on attitude knowledge estimation performance, during agile slew rate.*

Figure 6.8: *Attitude estimation performance of 6/7 state USQUE filter, in the event of ST drop out. One ST, and three MPSAG, with filter and sensor update rate of 5Hz.*
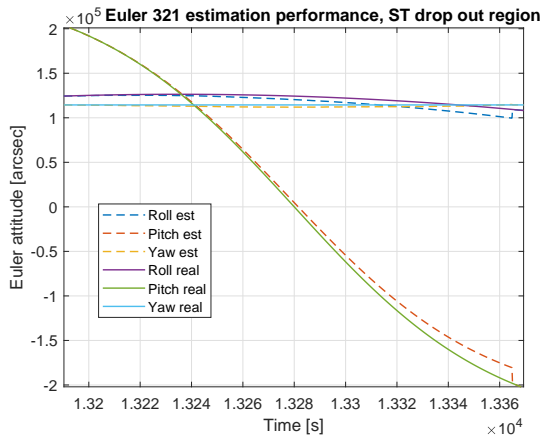
(c) *Offset in Euler-321 attitude tracking, due to gyro dead-reckoning, in the event of ST drop out.*
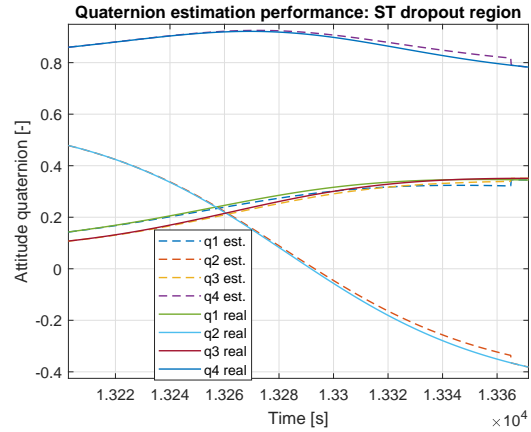
(d) *Offset in quaternion attitude tracking, due to gyro dead-reckoning, in the event of ST drop out.*

Figure 6.8: *Attitude estimation performance of 6/7 state USQUE filter, in the event of ST drop out. One ST, and three MPSAG, with filter and sensor update rate of 5Hz.*

6.2.2 | Effect of Slew Rate Induced Star Tracker Dropout

It was established earlier in Section 4.5, with the aid of Figures 4.11 and 4.13, that under terrestrial ground target tracking the slew rates encountered by the rigid body NanoSat leads to star tracker attitude knowledge acquisition dropout. The objective of this section is to evaluate the performance of filter supported gyro-only dead-reckoning in the event of star tracker dropout. Figure 6.8a demonstrates the overall Euler-321 attitude tracking performance in the event of star tracker dropout. While Figure 6.8b, demonstrates the attitude estimation error performance for the segment of Phase B manoeuvre, that undergoes star tracker blinding. Figures 6.8c and 6.8d demonstrates, the offset in Euler-321 and quaternion tracking in the event of gyro-only dead-reckoning. From the filter output it is evident that the system encounters degradation of attitude knowledge estimation performance in the event of star tracker dropout. The attitude estimation error, though deteriorating without star tracker input, is observed to be confined within the σ bounds. As soon as the star tracker input is available the filter output converges back to better accuracies, this is demonstrated with the aid of Figure 6.9a. The behaviour of the bias estimation before, during and after the star tracker dropout is captured with the aid of Figure 6.9b. During the star tracker drop out, bias values are held to near-constant values by the filter with regards to the bias values before the star tracker dropout. Table 6.4 summarises the attitude estimation performance, with and without star tracker dropout, for different sensor configurations and sampling rates. Star tracker dropout significantly worsens the attitude estimation performance.

(a) *Attitude knowledge estimation performance, before and after the ST drop out.*

(b) *Bias estimation error in the event of ST drop out.*
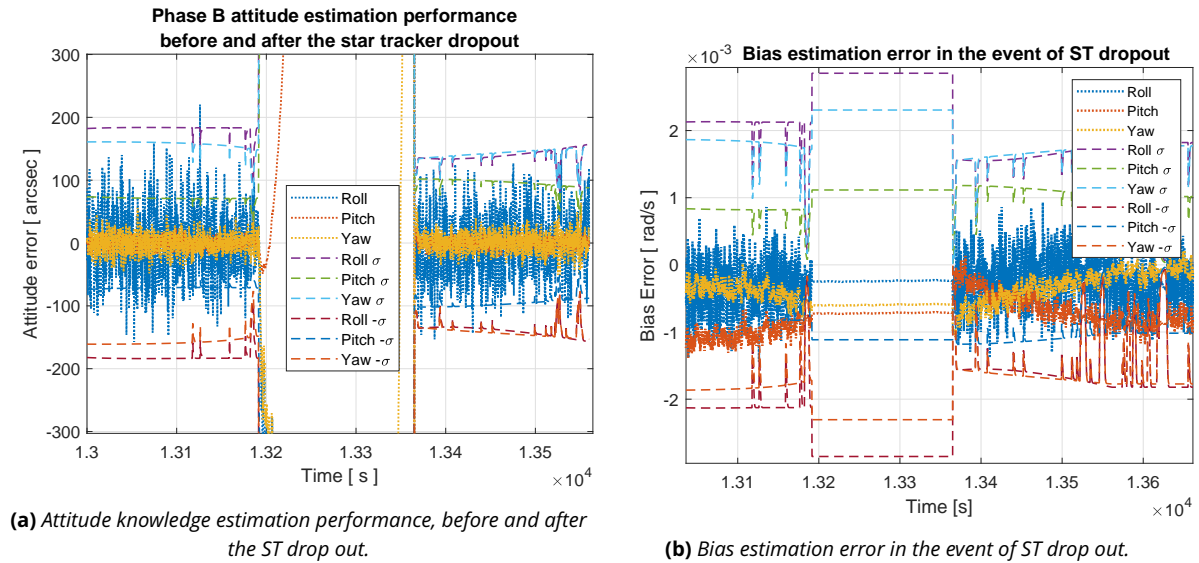
Figure 6.9: *Attitude estimation performance of 6/7 state USQUE filter, in the event of ST drop out. One ST, and three MPSAG, with filter and sensor update rate of 5Hz.*

6.2.3 | Merging Two Star Trackers

Now that the impact of covariance monitor and star tracker dropout is evaluated for the case with one star tracker and three MPSAG, the objective of this section is to evaluate the performance of the filter in the presence of two star trackers. Two star trackers are important, not only to improve the attitude knowledge performance, but also to prevent total occultation of the star tracker facilitated attitude knowledge which is very common to satellites of all classes, for instance occultation due to Sun/Moon/Earth limb in the FoV. When it comes to NanoSat star trackers, it is generally observed that the pitch/yaw axis (cross-axis) attitude knowledge acquisition performance is significantly better than that for roll axis (boresight-axis). For two orthogonal star trackers, as represented earlier in Figure 4.15, one can pre-select the star tracker sense axis such that the pitch/yaw axis for one star-tracker represents the roll axis of another star tracker. Thereby, combining the output of two star trackers into a signal star tracker quaternion output, which has a performance of pitch/yaw axis also for the roll axis. In such a case, the filter sees input from a single good star tracker. An alternative, to this strategy is to simply stack the star tracker measurements, and allow the filter to do the sorting. The objective of the following segments, is to analyse which of the above two strategies will lead to better filter output in terms of attitude knowledge estimation.

Star Tracker Axis Pre-Selection

Figure 6.10a demonstrates the attitude knowledge estimation performance for the entire manoeuvre with star tracker pre-axis selection, where the filter is fed with one single attitude quaternion input. The filter output is observed to exceed the sigma bounds around the calibration manoeuvre. Figure 6.10b captures the filter output attitude knowledge error during the initial steady state inertial pointing phase. Figure 6.11a captures the attitude knowledge estimation performance during the calibration manoeuvre. Finally, Figure 6.11b captures the attitude knowledge estimation performance in the event of star tracker dropout. In all cases, instead of improving the roll axis performance, the pitch and yaw axis performance is observed to degrade. Furthermore, it is observed that the attitude knowledge estimate of the filter, exceeds the filter output sigma bounds in the event of star tracker dropout.

Two Star Tracker Measurements Stacked

Figure 6.12a captures the attitude knowledge estimation performance of the entire manoeuvre sequence, when the star tracker measurements are stacked. Figure 6.12b demonstrates the attitude knowledge estimation error, along with the sigma bounds for the initial steady steady inertial pointing phase. While, Figure 6.13a demonstrates the attitude knowledge in combination with the sigma bounds for calibration manoeuvre phase. Finally, Figure 6.13b captures the attitude knowledge error performance in the event of star tracker drop. Unlike the previous case, if the star tracker output quaternions are stacked as two separate measurement sensors, the attitude estimation stays within the sigma bounds in the event of star tracker dropout. Furthermore, the roll axis performance is brought down to pitch and yaw axis attitude estimation performance without significant degradation in the performance

(a) *Overview of attitude estimation error for the entire manoeuvre sequence and the corresponding 1σ bounds.*

(b) *Attitude estimation performance associated with the initial steady state inertial pointing phase.*
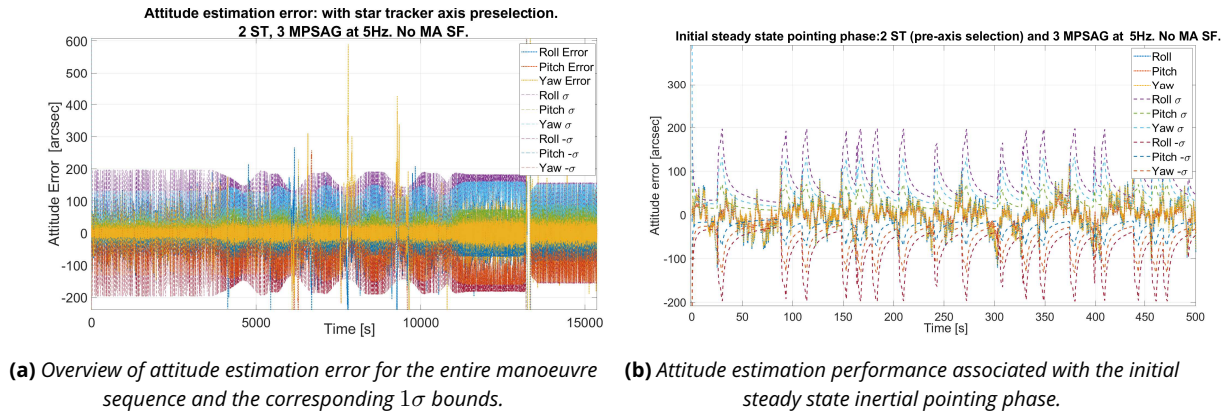
Figure 6.10: *Impact of ST pre-axis selection from two ST, on the attitude estimation performance of the 6/7 state USQUE filter. Filter, two ST, and three MPSAG update rate set to 5Hz. ST dropouts are considered.*

(a) *Attitude estimation performance associated with the calibration manoeuvre phase.*

(b) *Attitude estimation performance associated with phase B manoeuvre sequence.*
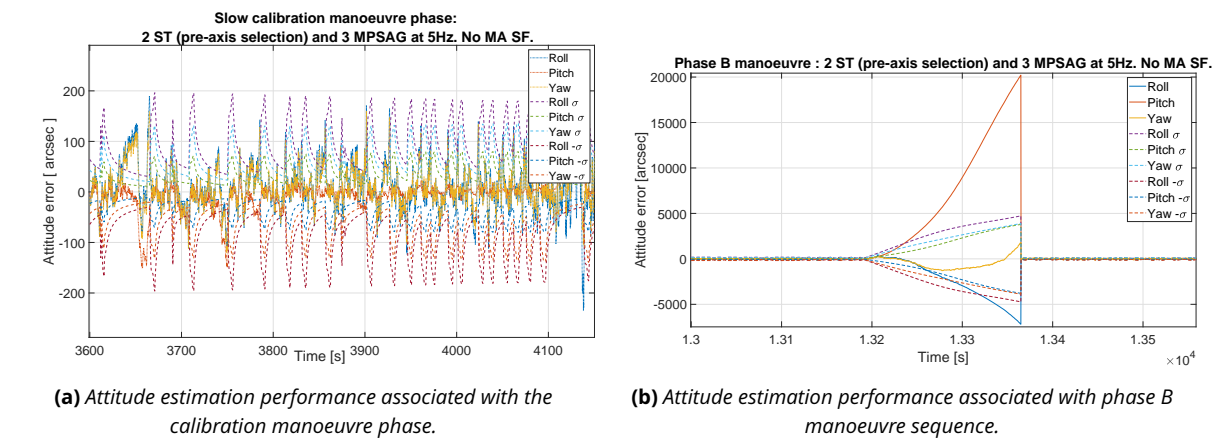
Figure 6.11: *Impact of ST pre-axis selection from two ST, on the attitude estimation performance of the 6/7 state USQUE filter. Filter, two ST, and three MPSAG update rate set to 5Hz. ST dropouts are considered.*

(a) *Overview of attitude estimation error for the entire manoeuvre sequence and the corresponding 1σ bounds.*

(b) *Attitude estimation performance associated with the initial steady state inertial pointing phase.*
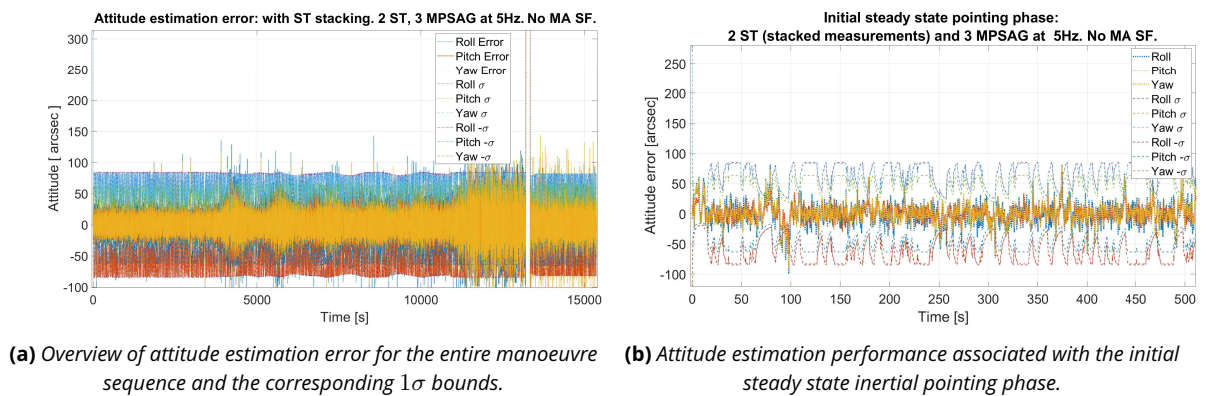
Figure 6.12: *Impact of ST measurement stacking from two ST, on the attitude estimation performance of the 6/7 state USQUE filter. Filter, two ST, and three MPSAG update rate set to 5Hz. ST dropouts are considered.*

thereof.

Choice of Star Tracker Measurement Merging Strategy

From the analysis presented above, it is evident that inclusion of one more star tracker measurement significantly improves the attitude knowledge estimation performance. Furthermore with the aid of Table 6.3, it can be deduced that stacking the star tracker output measurement, before feeding into the filter, leads to significant improvement in attitude estimation capability compared to the case where one low performing star tracker roll axis is replaced with

(a) *Attitude estimation performance associated with the calibration manoeuvre phase.*

(b) *Attitude estimation performance associated with phase B manoeuvre sequence.*
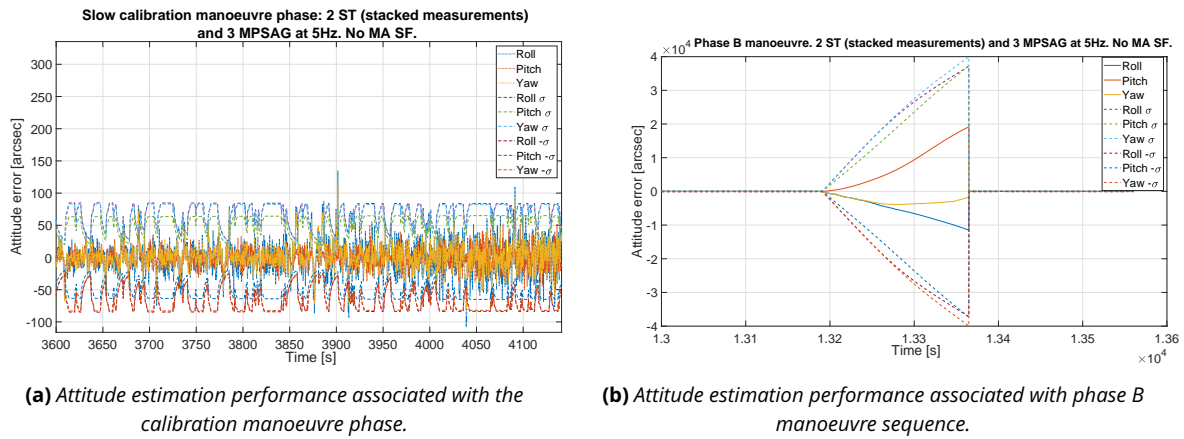
Figure 6.13: *Impact of ST measurement stacking from two ST, on the attitude estimation performance of the 6/7 state USQUE filter. Filter, two ST, and three MPSAG update rate set to 5Hz. ST dropouts are considered.*

(a) *Entire manoeuvre, with higher gyro sampling rate.*

(b) *Entire manoeuvre demonstrating sigma bound behaviour.*
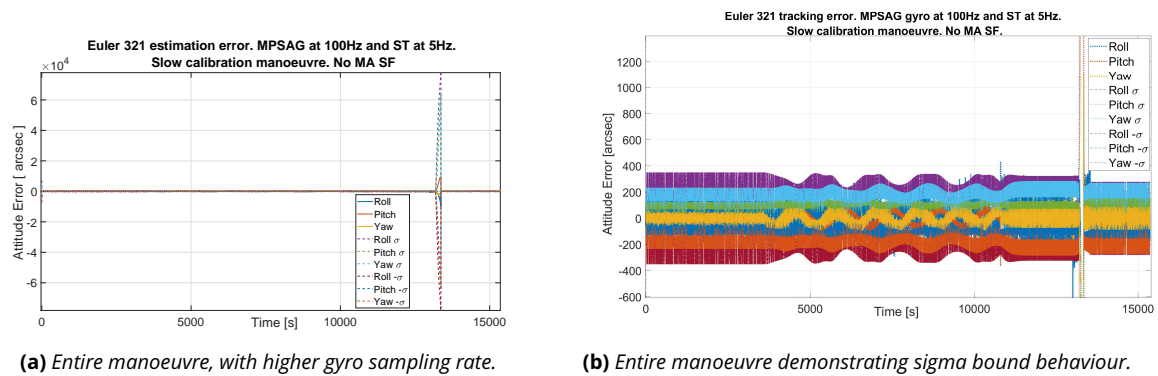
Figure 6.14: *Overall attitude error on phase A and B manoeuvre sequences associated with slow calibration manoeuvre, with three MPSAG at 100 Hz and one ST-200 ST at 5Hz. No misalignment and scale factors are considered.*

one high performing star tracker pitch/yaw axis. As a consequence, when two star trackers are utilised, the output measurement of both the star trackers shall be stacked before feeding into the filter.

6.2.4 | Effect of Gyro Sampling Rate

Though the star tracker update limit is bounded to 5Hz, it is not necessary that the gyro and filter update rate stays bounded to 5Hz. MPSAG gyro is capable of supporting upto 2.3kHz of sample rates while HPTAG is capable of supporting upto 2kHz of sample rate. The filter update rate is limited by the processing capabilities on board of the NanoSat. From the star tracker dropout scenario; it is observable that the absence of star tracker attitude measurement update leads to the loss of attitude estimation error performance when the filter relies on gyro measurement only. The objective of this section is to investigate whether surplus gyro and filter update rate, in between the star tracker update has any added benefit for attitude estimation error reduction. In order to investigate the impact of higher gyro and filter update rate on the attitude estimation error, the gyro and filter update rate is set to 100Hz and the star tracker update rate is set to 5Hz. One star tracker and three MPSAG is considered, star tracker dropouts under agile slewing conditions are considered to evaluate the impact of higher filter and gyro update rate in the event of star tracker drop out. Figure 6.15 demonstrates the attitude estimation performance for the initial steady state inertial pointing and calibration manoeuvre phase. Figure 6.15e captures the attitude estimation error performance in the event of star tracker dropout. Figure 6.15f demonstrates the impact of asynchronous star tracker and gyro/filter update rate, on the sigma bounds and the underlying attitude estimation performance for the initial inertial pointing phase. The thicker edges of sigma bounds, is observed as the sigma bounds moments momentarily diverge under gyro only dead-reckoning. Comparing the attitude knowledge estimation error against Figures 6.6 and 6.7, in combination with Table 6.4, it is observed that there is no added benefit in terms of the magnitude of attitude estimation error achieved with higher gyro sampling rates. The effect of gyro sample rate on bias estimation is presented with the aid of Appendix D.1.2. Furthermore comparing Figures 6.15e and 6.8b, no added benefit of higher gyro/filter update rate is observed for the gyro dead-reckoning phase of the manoeuvre in the event of ST drop out. As a consequence, for the remnant of this thesis work gyro, star tracker, and the filter update rate is set to 5Hz.
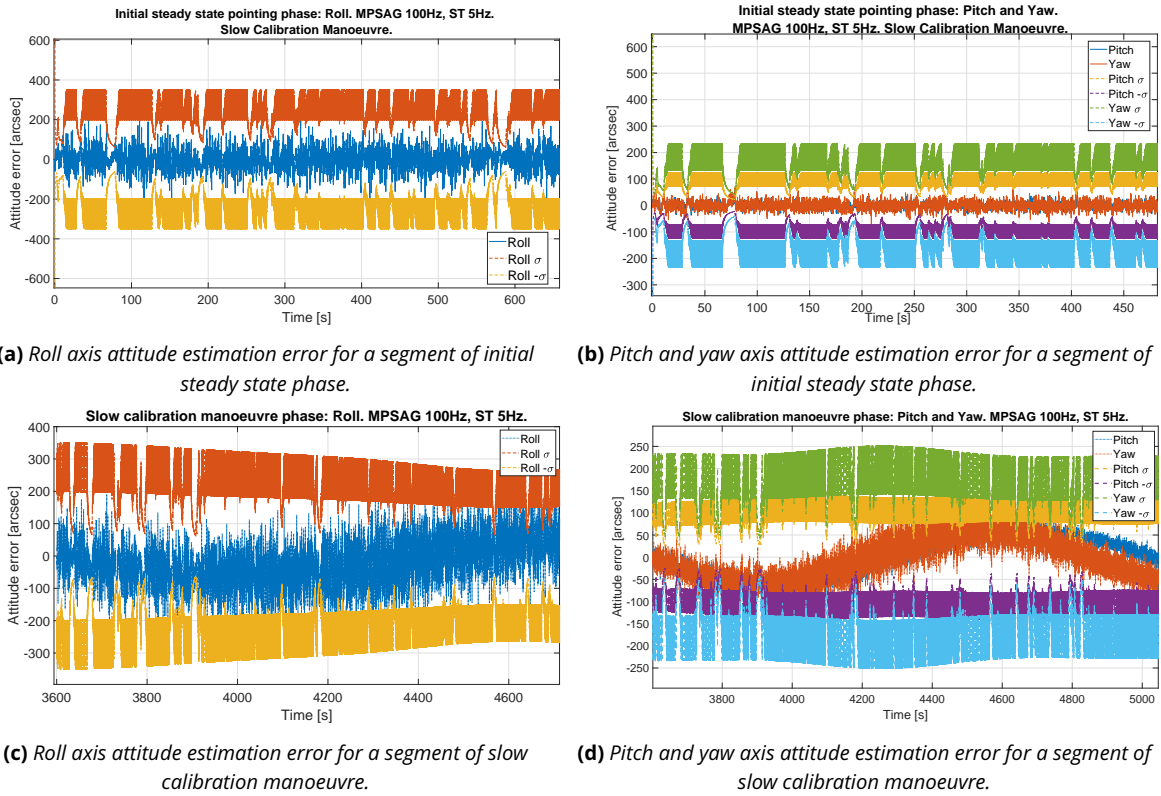
(a) *Roll axis attitude estimation error for a segment of initial steady state phase.*

(b) *Pitch and yaw axis attitude estimation error for a segment of initial steady state phase.*

(c) *Roll axis attitude estimation error for a segment of slow calibration manoeuvre.*

(d) *Pitch and yaw axis attitude estimation error for a segment of slow calibration manoeuvre.*

Figure 6.15: *Zoomed in overview, to demonstrate the impact of higher gyro sampling and filter update rate, on attitude estimation error. Slow calibration manoeuvre sequences, with three MPSAG and filter at 100 Hz and one ST at 5 Hz.*
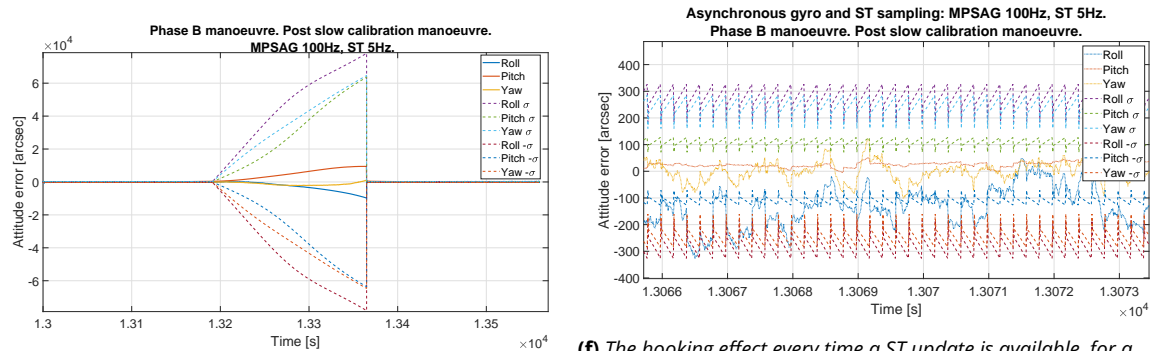
(e) *Effect of ST loss, during ground target tracking manoeuvre, on attitude estimation error.*

(f) *The hooking effect every time a ST update is available, for a segment of pre-ground target tracking manoeuvre, that leads to the thick sigma bounds when zoomed out.*

Figure 6.15: *Zoomed in overview, to demonstrate the impact of higher gyro sampling and filter update rate, on attitude estimation error. Slow calibration manoeuvre sequences, with three MPSAG and filter at 100 Hz and one ST at 5 Hz.*

6.2.5 | Performance with HPTAG

The analysis conducted in the previous subsections, relied upon MPSAG. However, it was demonstrated earlier in Table 3.8, that HPTAG has superior performance when compared against MPSAG. Thus, the objective of this section is to evaluate the performance of USQUE 6/7 state filter, with HPTAG and two star trackers. Figure 6.16 demonstrates the attitude knowledge estimation performance for phase A associated with slow calibration manoeuvre. While, Figure 6.17 demonstrates the attitude estimation performance with and without star tracker dropout for phase B associated with the slow calibration manoeuvre. Both MPSAG and HPTAG are observed to have near identical performance. HPTAG is observed to be less noisy, and performs better in the event of star tracker dropout, when compared with MPSAG. Tables 6.4 and 6.6, in combination with Table 6.3, demonstrates that utilising HPTAG improves the attitude knowledge estimation performance. However, this improvement is not significant when compared against MPSAG.

(a) *Attitude estimation performance associated with the initial inertial pointing phase.*

(b) *Attitude estimation performance associated with the calibration pointing phase.*
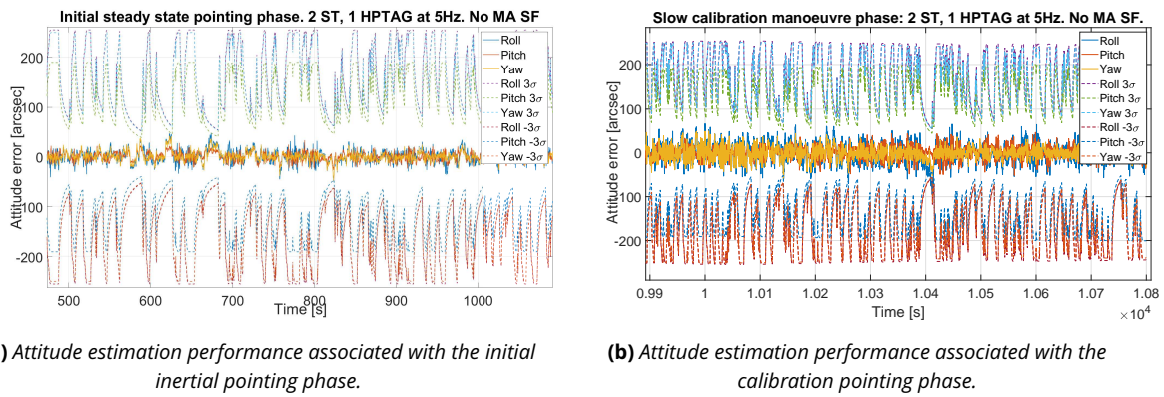
Figure 6.16: *Impact of HPTAG gyro on the attitude estimation performance of the 6/7 state USQUE filter, for initial inertial pointing and calibration manoeuvre. Filter with two ST, and one HPTAG update rate set to 5Hz.*

(a) *Attitude estimation performance associated with the phase B manoeuvre without ST dropout.*

(b) *Attitude estimation performance associated with the phase B manoeuvre with ST dropout*
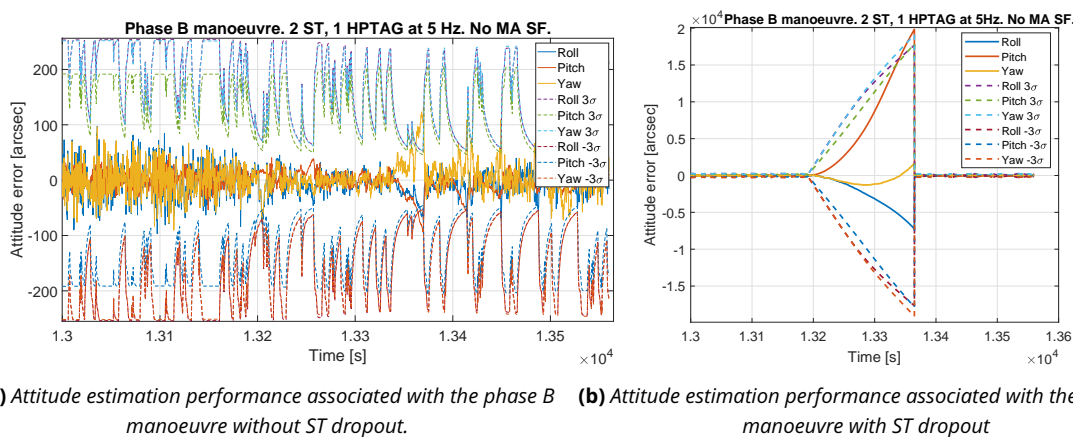
Figure 6.17: *Impact of HPTAG gyro on the attitude estimation performance of the 6/7 state USQUE filter, for phase B manoeuvre with and without ST dropout. Filter with two ST, and one HPTAG update rate set to 5Hz.*

6.3 | USQUE Filter Performance in the Presence of Misalignment and Scale Factors

Up until now, the 6/7 state USQUE filter utilised sensor outputs that were free of misalignment and scale factors. However, in reality misalignment and scale factors are common to gyro-stellar sensors of all satellites. Even when sensor alignments are calibrated optically with a Master Reference Cube (MRC) on ground, launch vibrations and thermal expansions can lead to sensor misalignment. Under inertial/steady pointing conditions, gyro misalignment and scale factor is captured as a linear combination under the estimated gyro bias. However under agile/target tracking conditions, performance of a steady state attitude estimation filter is expected to degrade significantly due to the presence of uncalibrated sensor misalignment and scale factors. This is especially true for NanoSats. Due to low volume, and low cost entry point to space, often times an MRC is not utilised for on ground calibration of sensor misalignment.

It was demonstrated earlier with the aid of Section 4.8 that the effect of misalignment and scale factor is not significant on gyro output, furthermore the additional error introduced is lower in magnitude than the gyro output noise floor magnitude. Under slow calibration manoeuvre, the error introduced by misalignment and scale factor on gyro output, is observed to be lower than the star tracker attitude acquisition capability. However, the presence of misalignment significantly deteriorates the star tracker output performance, esp. at large angles.

This section is aimed at investigating the effect gyro misalignment and scale factors on the attitude estimation error. Section 6.3.1 considers a misaligned star tracker, while Section 6.3.2 assumes that the knowledge of star tracker misalignment is available, by pre-calibration for instance.

(a) *Attitude estimation performance for the entire manoeuvre, signifying the loss of attitude knowledge performance during the availability of ST output.*

(b) *Attitude estimation performance associated with the phase B manoeuvre with ST drop out.*
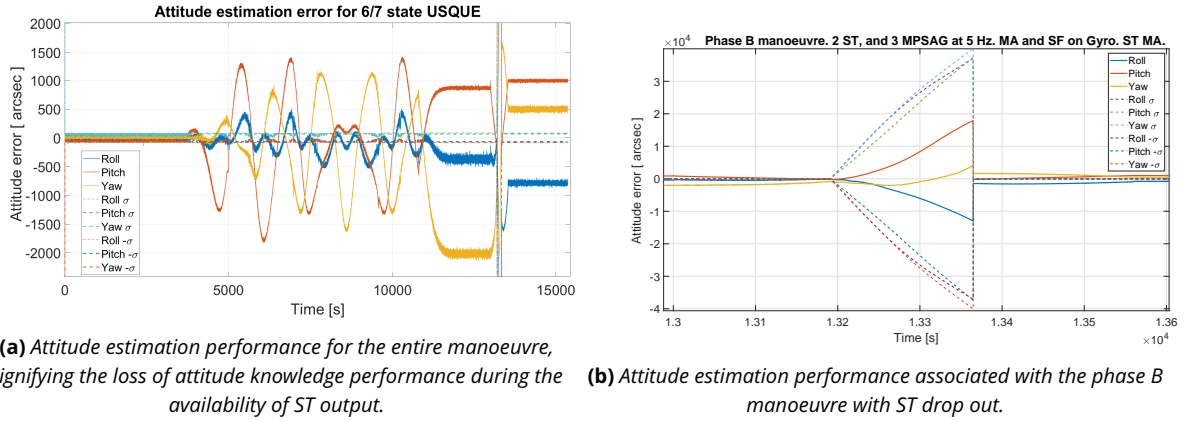
Figure 6.18: *The ST aligned with the body axis is given a misalignment of 0.1 deg on all axis. The second ST has no misalignment. All elements in the gyro misalignment matrix are set to 0.5 deg, while the symmetric and asymmetric scale factors are set to 500 ppm and 100 ppm. Two ST, three MPSAG, and the filter update rate is set to 5Hz.*

6.3.1 | Effect of No Knowledge of Star Tracker Misalignment

With MPSAG

Figure 6.18 captures the degradation in attitude estimation error performance observed with three MPSAG and 2 ST. Comparing this against Figures 6.12 and 6.13, the attitude knowledge estimation performance appears to have degraded significantly. The impact of gyro MA and SF is observed to lower than the impact of ST MA. This is visible by comparing the star tracker drop-out phase, in Figures 6.18 and 6.13. The attitude error reaches similar values, in the event of star tracker dropout. The significant error observed during, and after the calibration manoeuvre is mostly due to the presence of ST misalignment. This can be compared against Figure 4.29, which captures the error in ST output with 0.1 deg MA on roll, pitch and yaw axis. Corresponding impact on bias estimation is presented with the aid of Figure. The consequent impact on bias estimation is captured with the aid of Figure D.4 in Appendix D.1.3. Tables 6.3, 6.4, 6.5, and 6.6 capture the attitude knowledge estimation performance, in the presence and absence of gyro-stellar MA and SF, for different manoeuvre phases considered for this thesis work.

With HPTAG

Figure 6.19 captures the impact of attitude estimation error, when HPTAG is utilised. As observed in the case of MPSAG, the gyroscope seems to have very little effect on the attitude estimation performance, compared to the misaligned star tracker. In the event of star tracker dropout, the performance of gyro guided attitude estimation with and without misalignment and scale factor is near identical. This can be observed by comparing Figures 6.17b and 6.19. Clearly the impact of misaligned star tracker dominates in the case of HPTAG as well; resulting in no significant difference between attitude estimation performance with MPSAG and HPTAG. This further indicates that degradation of gyro sensor, from HPTAG to MPSAG for instance, has significantly less impact on the attitude estimation performance when compared to a misaligned star tracker. And calibration of star tracker misalignment alone, should improve the attitude knowledge estimation significantly. Tables 6.4, 6.5, and 6.6 capture the attitude knowledge estimation performance, in the presence and absence of gyro-stellar MA and SF, for different manoeuvre phases considered for this thesis work.

(a) *Attitude estimation performance associated with the entire manoeuvre.*

(b) *Attitude estimation performance associated with the phase B manoeuvre with ST dropout*
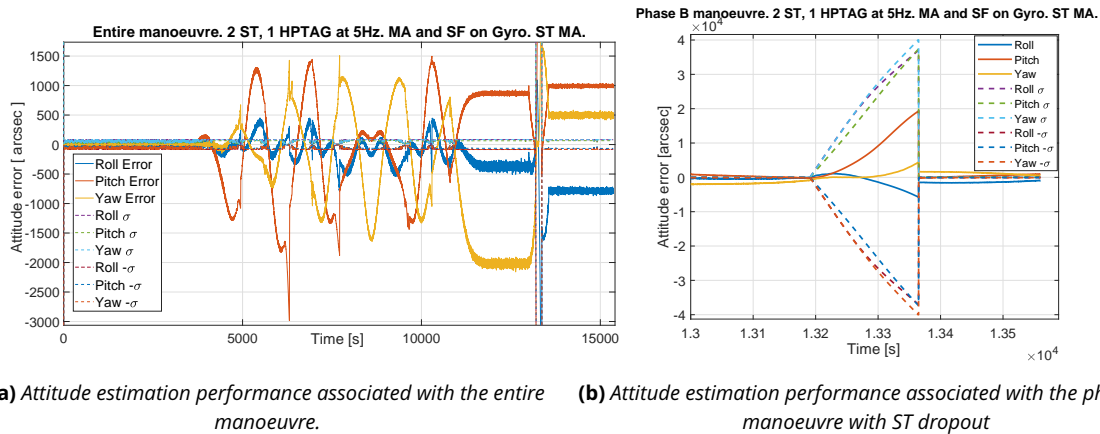
Figure 6.19: *Impact of HPTAG gyro on the attitude estimation performance of the 6/7 state USQUE filter. Filter with two ST (with misalignment), and one HPTAG (with misalignment and scale factors) update rate set to 5Hz.*

(a) *Attitude estimation performance for the entire manoeuvre, signifying the loss of attitude knowledge performance during the availability of ST output.*

(b) *Attitude estimation performance signifying the impact of ST drop out.*
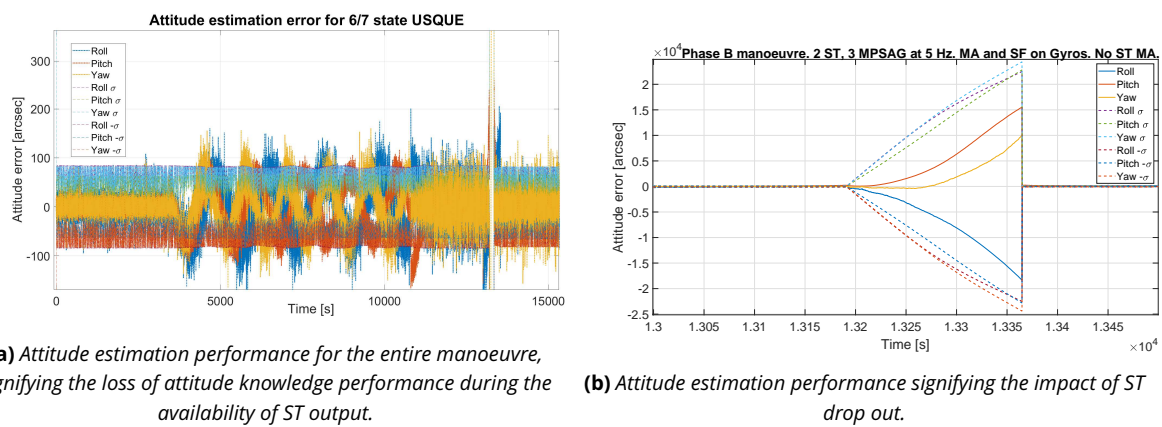
Figure 6.20: *Attitude estimation performance when both star trackers have no misalignment. All elements in the gyro misalignment matrix are set to 0.5 deg, while the symmetric and asymmetric scale factors are set to 500 ppm and 100 ppm. Three MPSAG gyro, along with two ST and filter update rate is set to 5Hz.*

6.3.2 | Effect of Perfect Knowledge of Star Tracker Misalignment

Previous section outlined the performance of the 6/7 states USQUE filter in the presence of gyro-stellar misalignment and scale factors. It was suggested that the impact of gyro misalignment and scale factors, have little impact on the attitude estimation performance when compared against a misaligned star tracker. The objective of this section is to verify this notion by assuming that the star trackers are perfectly aligned, while the gyros input signals are still distorted by misalignment and scale factors.

With MPSAG

Figure 6.20 demonstrates the attitude knowledge estimation performance for MPSAG, in the absence of star tracker misalignment. Comparing this against Figure 6.18, it can be observed that the attitude estimation knowledge performance is significantly better than the case where star tracker misalignment is presented. However, comparing Figure 6.20 against Figure 6.12a, it is evident that the attitude estimation performance degrades slightly in the presence of gyro misalignment and scale factor. However, the effect of star tracker misalignment on the attitude knowledge estimation process remains to be the significant source. Tables 6.3, 6.4, 6.5, and 6.6 capture the attitude knowledge estimation performance, in the presence and absence of gyro-stellar MA and SF, for different manoeuvre phases considered for this thesis work.

With HPTAG

Figure 6.21 captures the filter attitude estimation error in the absence of star tracker misalignment. Comparing Figures 6.16, 6.17, 6.19, and 6.21, it is evident that star tracker misalignment plays the most significant role in degrading
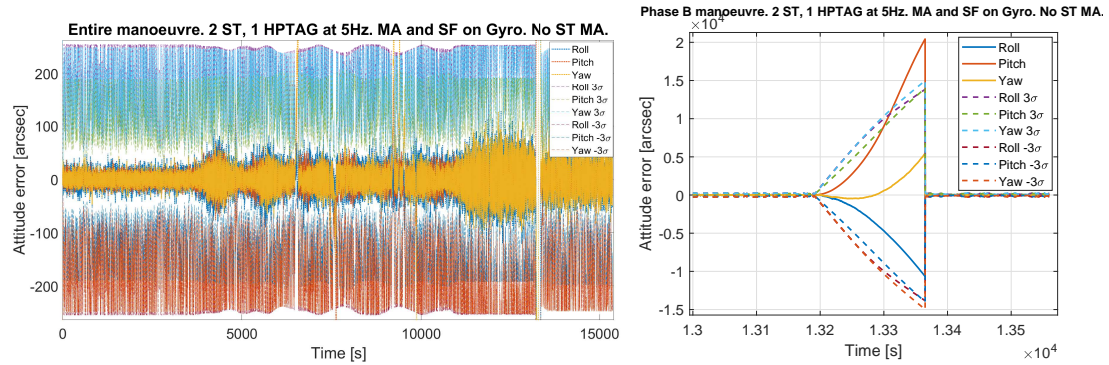
(a) *Attitude estimation performance associated with the entire manoeuvre.*

(b) *Attitude estimation performance associated with the phase B manoeuvre with ST dropout*

Figure 6.21: *Impact of HPTAG gyro on the attitude estimation performance of the 6/7 state USQUE filter. Filter with two star trackers (without misalignment), and one HPTAG (with misalignment and scale factors) update rate set to 5Hz.*

the attitude estimation performance. This is especially true when the star tracker reads out large angles. When perfect knowledge of star tracker alignment is available, the filter with misaligned and scale factored gyro input, returns near similar attitude output. In the event of star tracker drop out, gyro dead-reckoning performance in the presence of misalignment and scale factor is observed to provide higher attitude estimation error, when compared against a gyro with no deterministic errors. Performance gains in the event of star tracker dropout is expected, when the gyro deterministic errors are calibrated. Tables 6.4, 6.5, and 6.6 capture the attitude knowledge estimation performance, in the presence and absence of gyro-stellar MA and SF, for different manoeuvre phases considered for this thesis work.

Table 6.5: *Attitude knowledge estimation performance with 6/7 state USQUE for ground target tracking manoeuvre sequences, in the presence and absence of uncalibrated star tracker, and uncalibrated MEMS rate MPSAG and HPTAG gyro. [P] = Partially (some axis) qualified, [UQ] = Unqualified.*

USQUE 6/7 state filter performance. Sensor and filter at 5 Hz.	Time	[13000 - 13197)	[13197 - 13354)	[13197 - 13354)	[13354, 13560)	[13000,13560)	[13000,13560)
	Mission Phase	Before ST dropout	During ST dropout	No ST dropout	After ST recovery	During agile target tracking with ST dropout	During agile target tracking without ST dropout
Sensor Configuration				Attitude error [arcsec]			
2 ST, 3 MPSAG 1 ST - MA Gyro - MA and SF	Mean [Roll, Pitch, Yaw]	[-328.09, 311.71, -1678.12]	[-4957.58, 6759.06, -545.07]	[-536.07, -570.13, 628.37]	[-1405.37, 402.35, 1250.18]	[-2138.09, 2341.14, -306.45]	[-767.92, 70.02, 56.99]
	Std. Dev (1 σ) [Roll, Pitch, Yaw]	[105.04, 296.15, 319.91]	[3867.14, 5727.58, 1547.29]	[511.58, 190.26, 768.65]	[192.22, 333.26, 341.39]	[2901.47, 4358.39, 1524.12]	[567.53, 515.10, 1372.92]
	Abs. AKE (1 σ) [Roll, Pitch, Yaw]	[433.13, 607.86, 1998.03] [UQ]	[8824.72, 12486.64, 2092.36] [UQ]	[1047.65, 760.39, 1397.02] [UQ]	[1597.59, 735.61, 1591.57] [UQ]	[5039.56, 6699.54, 1830.56] [UQ]	[1335.45, 585.12, 1429.92] [UQ]
2 ST, 3 MPSAG ST - no MA Gyro - MA and SF	Mean [Roll, Pitch, Yaw]	[-56.14, 50.56, 0.11]	[-6871.41, 5326.32, 1995.84]	[16.65, 463.52, 0.71]	[92.89, 53.95, -1.20]	[-2116.19, 1686.71, 618.30]	[18.34, 179.72, -0.16]
	Std. Dev (1 σ) [Roll, Pitch, Yaw]	[44.64, 60.80, 32.11]	[5311.27, 4951.75, 2933.38]	[29.06, 132.03, 24.72]	[32.65, 62.46, 30.37]	[4347.09, 3680.42, 1875.49]	[71.74, 210.24, 29.38]
	Abs. AKE (1 σ) [Roll, Pitch, Yaw]	[100.78, 111.37, 32.22] [P]	[12182.67, 10278.07, 4929.22] [UQ]	[45.71, 595.55, 25.43] [UQ]	[125.54, 116.41, 31.57] [UQ]	[6463.28, 5367.14, 2493.80] [UQ]	[90.09, 389.96, 29.54] [UQ]
2 ST, 1 HPTAG 1 ST - MA Gyro - MA and SF	Mean [Roll, Pitch, Yaw]	[-328.15, 311.71, -1678.16]	[-1049.67, 7425.85, 699.11]	[-536.04, -570.13, 628.39]	[-1405.46, 401.98, 1250.66]	[-927.13, 2547.76, 79.07]	[-767.91, 70.02, 56.99]
	Std. Dev (1 σ) [Roll, Pitch, Yaw]	[104.27, 296.15, 319.63]	[2035.10, 6147.88, 1211.05]	[511.59, 190.26, 768.57]	[192.19, 334.10, 341.45]	[1227.20, 4739.49, 1477.38]	[567.44, 515.10, 1372.88]
	Abs. AKE (1 σ) [Roll, Pitch, Yaw]	[432.42, 607.86, 1997.79] [UQ]	[3084.77, 13573.73, 1910.16] [UQ]	[1047.63, 760.39, 1396.96] [UQ]	[1597.65, 736.08, 1592.11] [UQ]	[2154.33, 7287.25, 1556.45] [UQ]	[1335.35, 585.12, 1429.87] [UQ]
2 ST, 1 HPTAG ST - no MA Gyro - MA and SF	Mean [Roll, Pitch, Yaw]	[-56.29, 51.28, -0.19]	[-3875.11, 7928.13, 1032.61]	[12.60, 459.67, 3.99]	[82.32, 10.12, 28.48]	[-1191.40, 2477.89, 329.85]	[12.94, 162.08, 12.35]
	Std. Dev (1 σ) [Roll, Pitch, Yaw]	[40.55, 60.62, 27.07]	[3271.78, 6566.37, 1712.87]	[24.91, 136.19, 20.66]	[38.88, 105.44, 54.09]	[2560.13, 5167.20, 1063.83]	[67.66, 224.81, 41.32]
	Abs. AKE (1 σ) [Roll, Pitch, Yaw]	[96.85, 111.90, 27.26] [P]	[7146.89, 14494.50, 2745.48] [UQ]	[37.51, 595.87, 24.65] [UQ]	[121.20, 115.56, 82.57][UQ]	[3751.53, 7645.09, 1393.68] [UQ]	[80.60, 386.89, 53.67] [UQ]

Table 6.6: *Attitude knowledge estimation performance with 6/7 state USQUE for manoeuvre sequences excluding ground target tracking, in the presence and absence of uncalibrated star tracker, and uncalibrated MEMS rate MPSAG and HPTAG gyro. [P] = Partially (some axis) qualified, [UQ] = Unqualified.*

USQUE 6/7 state filter performance. Sensor and filter at 5 Hz.	Time	[0, 3600)	[3600, 10800)	[10800, 13000)	[13560, 15360]
	Mission Phase	Initial inertial pointing - Non-zero attitude - Zero angular rate	Slow calibration manoeuvre	Pre-ground target tracking	Target pointing, post calibration manoeuvre
Sensor Configuration	Attitude error [arcsec]				
2 ST, 3 MPSAG 1 ST - MA Gyro - MA and SF	Mean [Roll, Pitch, Yaw]	[-2.45, -0.46, 6.77]	[-57.30, -158.93, -69.29]	[-298.54, 717.34, -1682.80]	[-787.19, 993.12, 497.87]
	Std. Dev (1 σ) [Roll, Pitch, Yaw]	[19.83, 11.74, 17.13]	[200.91, 811.16, 672.80]	[124.15, 322.66, 661.05]	[23.17, 13.04, 24.23]
	Abs. AKE (1 σ) [Roll, Pitch, Yaw]	[22.28, 12.20, 23.90] [P]	[258.21, 970.09, 742.09] [UQ]	[422.69, 1040, 2343.85] [UQ]	[810.36, 1006.16, 522.10] [UQ]
2 ST, 3 MPSAG ST - no MA Gyro - MA and SF	Mean [Roll, Pitch, Yaw]	[0.11, -0.06, 0.10]	[-3.63, -0.25, -1.40]	[9.31, -17.79, -0.08]	[0.74, -0.41, -0.59]
	Std. Dev (1 σ) [Roll, Pitch, Yaw]	[19.54, 11.64, 16.95]	[53.00, 47.50, 50.50]	[40.06, 37.86, 31.46]	[25.04, 13.07, 31.60]
	Abs. AKE (1 σ) [Roll, Pitch, Yaw]	[19.65, 11.69, 17.04] [Q]	[56.63, 47.75, 51.90] [P]	[49.38, 55.64, 31.54] [Q]	[25.79, 13.48, 32.19] [P]
2 ST, 1 HPTAG 1 ST - MA Gyro - MA and SF	Mean [Roll, Pitch, Yaw]	[-2.38, -0.37, 6.85]	[-63.12, -186.73, -68.66]	[-298.02, 716.33, -1682.51]	[-787.18, 993.12, 497.87]
	Std. Dev (1 σ) [Roll, Pitch, Yaw]	[11.86, 8.11, 8.97]	[204.51, 859.41, 683.28]	[124.11, 325.59, 661.73]	[22.12, 12.60, 21.67]
	Abs. AKE (1 σ) [Roll, Pitch, Yaw]	[14.24, 8.48, 15.82] [Q]	[267.63, 1046.14, 751.94] [UQ]	[422.13, 1041.92, 2344.24] [UQ]	[809.30, 1005.72, 519.54] [UQ]
2 ST, 1 HPTAG ST - no MA Gyro - no MA and SF	Mean [Roll, Pitch, Yaw]	[0.46, 0.16, 0.47]	[-2.89, -3.17, 2.20]	[9.48, -17.90, -0.02]	[-0.17, 0.01, 0.95]
	Std. Dev (1 σ) [Roll, Pitch, Yaw]	[12.25, 8.16, 9.43]	[52.67, 54.23, 58.24]	[35.39, 37.37, 26.80]	[19.39, 10.30, 23.14]
	Abs. AKE (1 σ) [Roll, Pitch, Yaw]	[12.71, 8.32, 9.90] [Q]	[55.55, 57.41, 60.44] [UQ]	[44.87, 55.27, 26.82] [UQ]	[19.55, 10.31, 24.09] [P]
2 ST, 1 HPTAG ST - no MA Gyro - MA and SF	Mean [Roll, Pitch, Yaw]	[0.41, 0.13, 0.44]	[-0.33, -0.40,3.93]	[0.41,0.13,0.44]	[0.22, -0.21, 0.31]
	Std. Dev (1 σ) [Roll, Pitch, Yaw]	[12.08, 8.11, 9.25]	[21.58, 32.53, 38.89]	[19.58, 10.54, 24.12]	[12.08, 8.11, 9.25]
	Abs. AKE (1 σ) [Roll, Pitch, Yaw]	[12.49, 8.24, 9.69] [Q]	[21.91, 32.93, 42.82] [UQ]	[12.49, 8.24, 9.69] [P]	[19.80, 10.75, 24.43] [P]

(a) *Attitude estimation error for MPSAG.*

(b) *Attitude estimation error for HPTAG.*
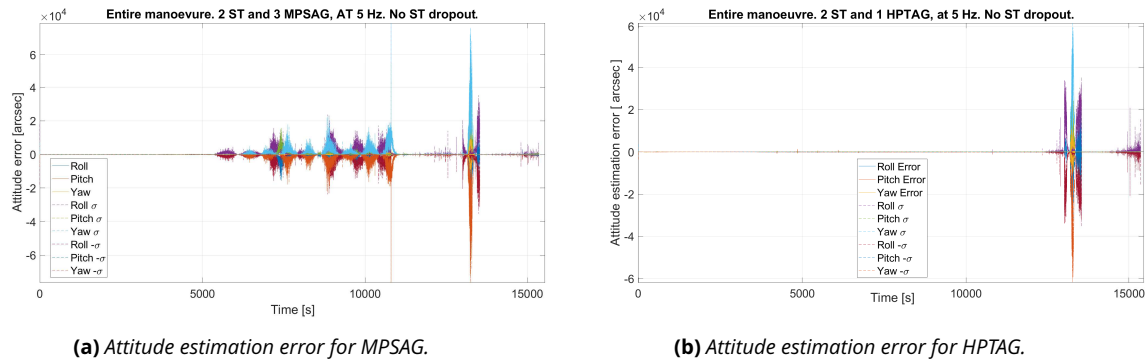
Figure 6.22: *Attitude estimation performance for the entire manoeuvre. Two ST, three MPSAG or one HPTAG, and filter at 5Hz, with no ST dropout. Gyro misalignment are set to 0.5 deg, ASF are set to 500 ppm, and SSF are set to 100 ppm.*

(a) *Attitude estimation error for MPSAG.*

(b) *Attitude estimation error for HPTAG.*
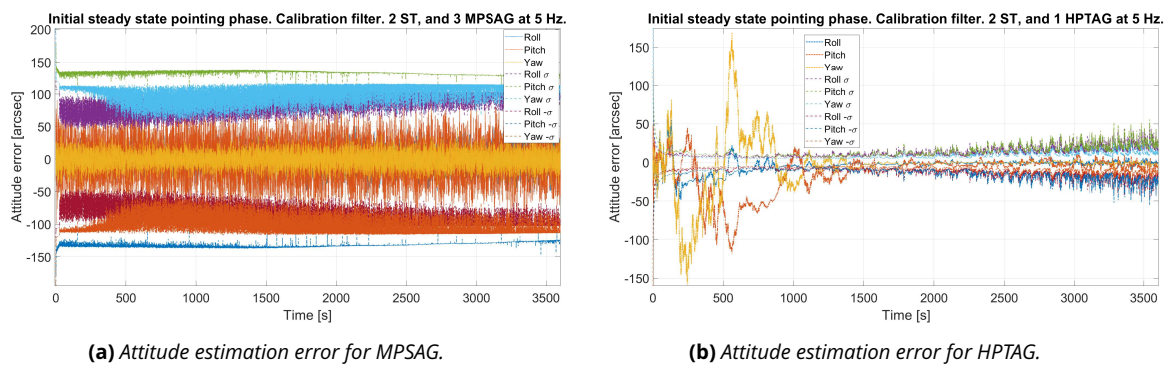
Figure 6.23: *Attitude estimation performance for the initial inertial pointing phase. Two ST, three MPSAG or one HPTAG, and filter at 5Hz, with no ST dropout. Gyro misalignment are set to 0.5 deg, ASF are set to 500ppm, and SSF are set to 100 ppm. ST misalignment is set to 0.1 deg.*

6.4 | USQUE Based Calibration Filter Performance in the Presence of Misalignment and Scale Factors

Section 6.3 demonstrated the loss of attitude estimation performance in the presence of gyro-stellar misalignment and scale factors. The objective of this section is, to utilise a USQUE based calibration filter developed earlier in Section 5.2, to estimate the deterministic error sources, and eventually improve the attitude estimation performance. This section focuses on three core segments. Section 6.4.1 is aimed at investigating the attitude estimation performance of USQUE based calibration filter, in the event of sensor degradation. This is done so, by evaluating the attitude estimation performance with HPTAG and MPSAG. Next the better performing sensor suite is excited through faster calibration manoeuvre in Section 6.4.2, to evaluate the impact of calibration manoeuvre on attitude estimation performance. Since the star tracker under consideration undergoes blinding under agile slewing motion, the objective of Section 6.4.4 is to demonstrate the filter performance in the event of star tracker drop out. Section 6.4.5, investigates the calibration parameter estimation capability of USQUE based calibration filter for the given set of sensors, under different calibration manoeuvres, and exclusion of rotational misalignment. A summary of the attitude estimation performance with 18/19 state USQUE based calibration filter, for different scenarios considered in the following Sections is presented with the aid of Table 6.7. Similarly, performance of the calibration filter for calibration parameter estimation is captured with the aid of Table 6.8.

6.4.1 | Performance with HPTAG and MPSAG

Figure 6.22 captures the overall attitude estimation performance obtained with the aid of USQUE based calibration filter, for MPSAG, HPTAG and two star trackers, during the manoeuvres associated with slow calibration manoeuvre. From a preliminary look it appears that overall a better gyro leads to a better attitude estimation performance, esp. during the calibration manoeuvre phase.

During the initial inertial pointing phase, as observed in Figure 6.23, though with HPTAG it takes the solution longer to converge; but the lower sigma bounds eventually reach 10 arcsec, compared to over 50 arcsec sigma bound observed

(a) *Attitude estimation error for MPSAG.*

(b) *Attitude estimation error for HPTAG.*

(c) *Attitude estimation error for HPTAG.*

(d) *Attitude estimation error for HPTAG.*
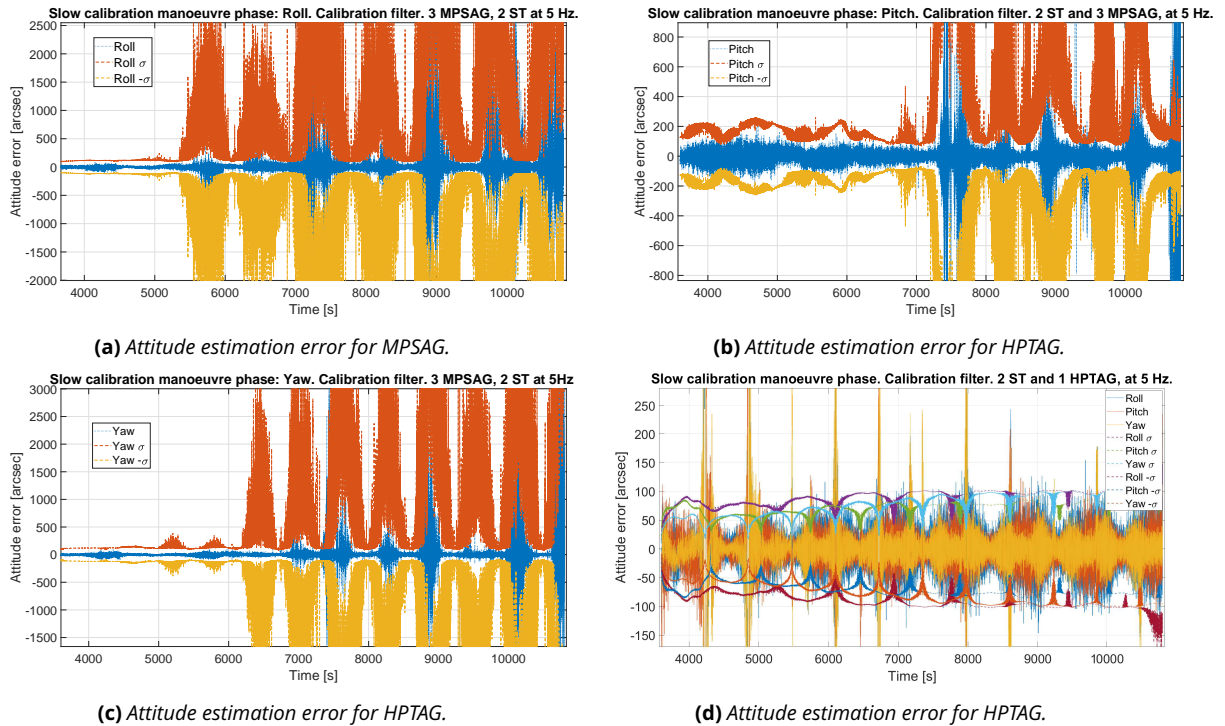
Figure 6.24: *Attitude estimation performance for the slow calibration manoeuvre phase. Two ST, three MPSAG or one HPTAG, and filter at 5Hz, with no ST dropout. Gyro misalignment are set to 0.5 deg, ASF are set to 500 ppm, and SSF are set to 100 ppm. ST misalignment is set to 0.1 deg.*

in the case of MPSAG. In either cases, the attitude knowledge estimation appears to be bounded.

When it comes to the slow calibration manoeuvre phase, as observed earlier with Figure 6.22, and now with Figure 6.24 the attitude estimation performance is observed to be significantly better with HPTAG. This can be partly explain with the aid of Figures 4.32-4.38, and the discussion presented earlier in Section 4.8.2. During the slow calibration manoeuvre sequence the impact of scale factor and misalignment on the gyro measurement is less than 10 arcsec/s (1σ), while the star tracker is capable of measuring with an accuracy of 10 arcsec (1σ) around the pitch/yaw axis, and 66.67 arcsec(1σ) around the roll axis. Figure 4.30 demonstrated earlier that for MPSAG raw sensor read out introduced a noise with a ceiling of 5×10^4 arcsec/s during the calibration manoeuvre phase, which after low pass filtering is brought down to around 200 arcsec/s as shown in Figure 4.32. For HPTAG this is 50 arcsec/s, as observed in Figure 4.34. Analysing Figures 4.32-4.35 it is observed that the impact of scale factor and misalignment is observed more on the raw sensor readout with HPTAG when compared against MPSAG. For the calibration manoeuvre phase, attitude estimation error obtained via USQUE based calibration filter is significantly better than the 6/7 state USQUE based attitude estimation error observed in Figures 6.18 and 6.19. Furthermore the attitude estimation error performance observed with HPTAG and calibration filter is quite comparable to the case where perfect knowledge of the star tracker is available, but the gyros are signals are still distorted with deterministic error sources.

For phase B manoeuvre, the results presented in Figure 6.25 consider that there is no star tracker dropout. The objective is to demonstrate the attitude estimation performance of the calibration filter, when slew rates significantly higher than the calibration manoeuvre is encountered. Figure 6.25 captures the attitude estimation performance of phase B, associated with MPSAG and HPTAG. Clearly, HPTAG performs better than MPSAG. Nevertheless, in both cases the attitude estimation performance degrades significantly around the agile slew manoeuvre, this is because such high slew rates haven't been calibration for before. For the given star tracker, there would be a blinding scenario during this phase. The results for this is captured later with the aid of Figure 6.28, in Section 6.4.4.

From this section it is clear that HPTAG assisted calibration filter performs better than the MPSAG assisted case. Overall attitude estimation performance improvement is observed, when compared against the regular 6/7 state USQUE filter. The filter is observed to have degraded attitude estimation performance, when slew rates higher than the ones utilised during calibration manoeuvre is used. This indicates that the underlying filter states require further calibration. A discussion on calibration states, with regards to gyro sensor choice is presented with the aid of Section

(a) *Attitude estimation error for MPSAG.*

(b) *Attitude estimation error for MPSAG.*

(c) *Attitude estimation error for HPTAG.*

(d) *Attitude estimation error for HPTAG.*
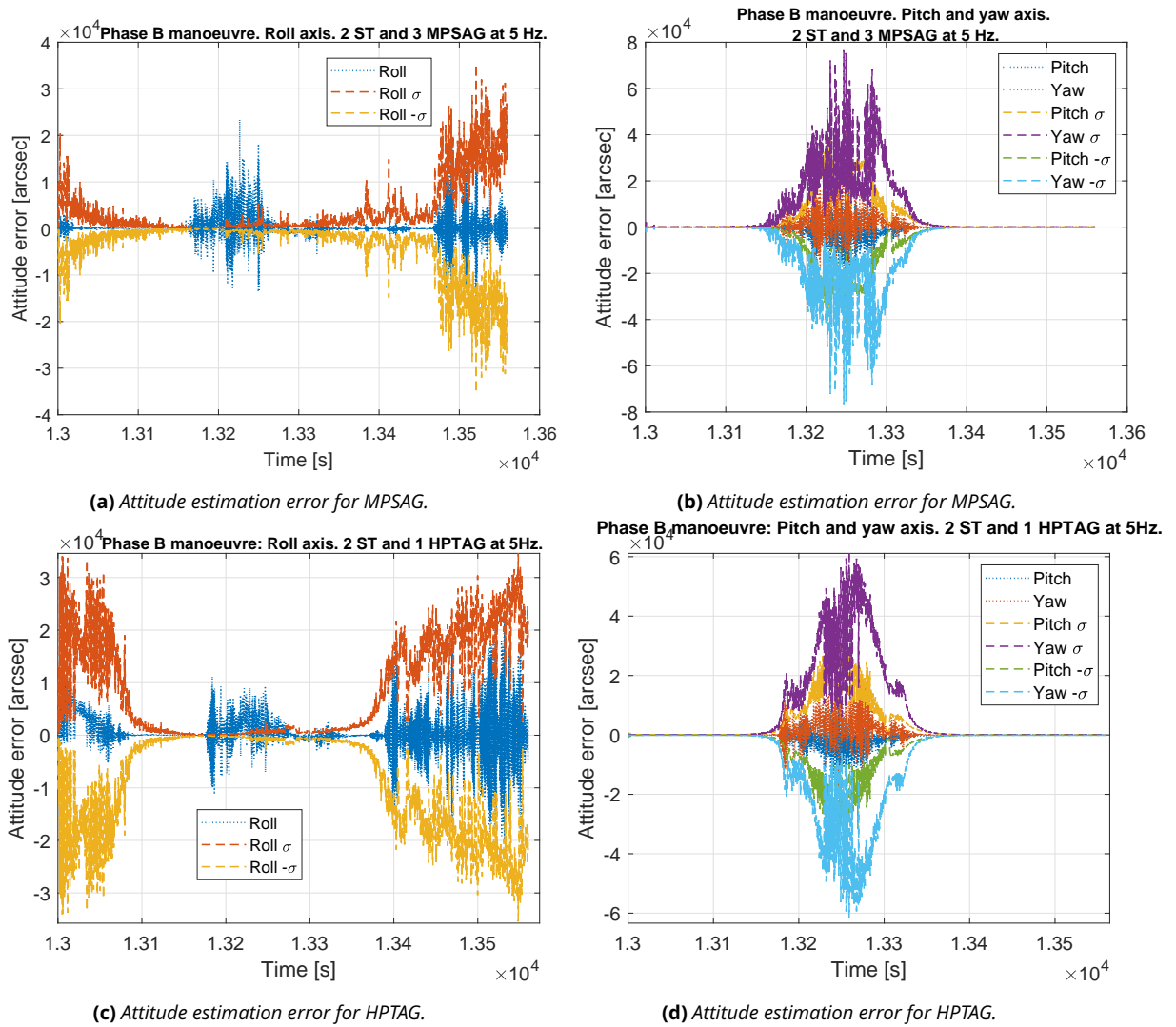
Figure 6.25: *Attitude estimation performance for phase B manoeuvre without ST dropout. Two ST, three MPSAG or one HPTAG, and filter at 5Hz. Gyro misalignment are set to 0.5 deg, ASF are set to 500ppm, and SSF are set to 100 ppm. ST misalignment is set to 0.1 deg.*

6.4.5. Attitude estimation performance with 18/19 state USQUE based calibration filter for different mission phases, with different choice of gyro sensors is presented with the aid of Table 6.7.

6.4.2 | Effect of Calibration Manoeuvre

The previous section demonstrated that HPTAG sensors have better attitude estimation performance, compared to the MPSAG sensors, for slow calibration manoeuvre sequences. It was further discussed in Section 4.8.2, that slow calibration manoeuvre leads to lower signal distortion associated with scale factor and misalignment. As a consequence, some of the calibration parameters associated with the gyro might not be observable as the effect of distortion is significantly below the attitude and attitude rate sensor noise floor. The objective of this section is to evaluate the influence of calibration manoeuvre on attitude estimation performance with HPTAG sensors. The impact of calibration manoeuvre, on the underlying calibration parameters is discussed later with the aid of Section 6.4.5. Table 6.7 captures the impact of calibration manoeuvre on the attitude estimation performance with calibration filter.

Figure 6.26, captures the attitude estimation performance for the manoeuvre sequences associated with the fast calibration calibration, for HPTAG sensor. Comparing the calibration manoeuvre phase with Figure 6.24d, the sigma bounds are observed to be more responsive, while very little to difference is observed in the attitude estimation performance. Similarly for the phase B manoeuvre, comparing Figure 6.26 against Figures 6.25c and 6.25d, the attitude estimation performance is observed to have very little difference. Nevertheless, the underlying gyro-stellar

(a) *Pitch and yaw axis attitude estimation error for fast calibration manoeuvre with HPTAG.*

(b) *Roll axis attitude estimation error for fast calibration manoeuvre with HPTAG.*

(c) *Pitch and yaw axis attitude estimation error for phase B maneoeuvre with HPTAG.*

(d) *Roll axis attitude estimation error for phase B maneoeuvre with HPTAG.*
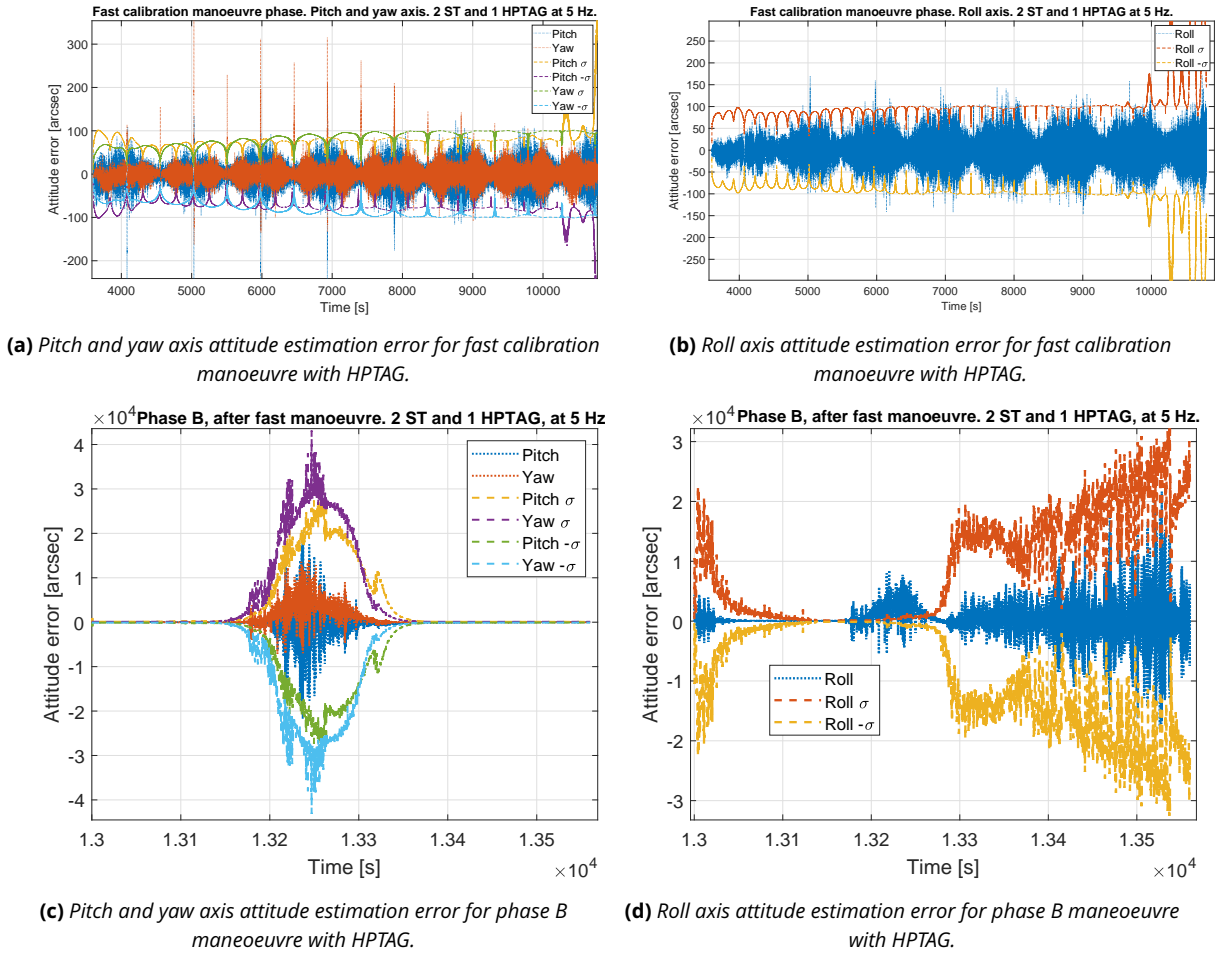
Figure 6.26: *Attitude estimation performance for fast calibration manoeuvre, and the following phase B manoeuvre without ST drop out. Two ST, one HPTAG, and filter at 5Hz. Gyro misalignment are set to 0.5 deg, ASF are set to 500ppm, and SSF are set to 100 ppm. ST misalignment is set to 0.1 deg.*

calibration parameters are influenced by faster calibration manoeuvre, as discussed later in Section 6.4.5.

6.4.3 | Effect of Gyro Rotational Misalignment Exclusion

It was discussed earlier in Section 5.2.1, to ensure the observability of calibration parameters three rotational gyro misalignment are discarded from the calibration filter. For the previous simulations, all gyro misalignment were set to 0.5 deg. While the rotational gyro misalignment is not estimated by the calibration filter. To evaluate the influence of this on the attitude estimation performance, the rotational gyro misalignment is set to 0 deg in the gyro simulator. This is similar to the results presented in (Lai et al., 2003), where rotational misalignment are set to zero for the gyro misalignment simulations to demonstrate the calibration parameter estimation capability of the filter with regards to the observable calibration parameters. The impact of this, on the calibration parameter estimation performance is discussed later in Section 6.4.5.

Figure 6.27 captures the attitude estimation performance of the calibration filter, when the rotational gyro misalignment are set to 0 deg, in the gyro misalignment simulator. Manoeuvre sequences associated with the fast calibration manoeuvre, in combination with HPTAG sensor is utilised for this segment. Comparing Figure 6.27 against Figures 6.26 and 6.23b, negligible change in attitude estimation performance is observed. This is very much in line with the observation presented earlier with the aid of Sections 4.8.2 and 6.3.2. For the chosen set of gyros, the effect of gyro misalignment and scale factor is so minimal on the gyro output compared to the noise of floor of attitude and attitude rate sensors; that very little change is observed in the overall attitude knowledge estimation performance in the presence/absence of rotational gyro misalignment. Table 6.7 captures the attitude knowledge estimation performance of the calibration filter when rotational gyro misalignment is excluded from the simulator.

(a) *Initial inertial pointing attitude estimation error for HPTAG.*

(b) *Calibration manoeuvre attitude estimation error for HPTAG.*

(c) *Phase B roll attitude estimation error for HPTAG.*

(d) *Phase B pitch yaw attitude estimation error for HPTAG.*
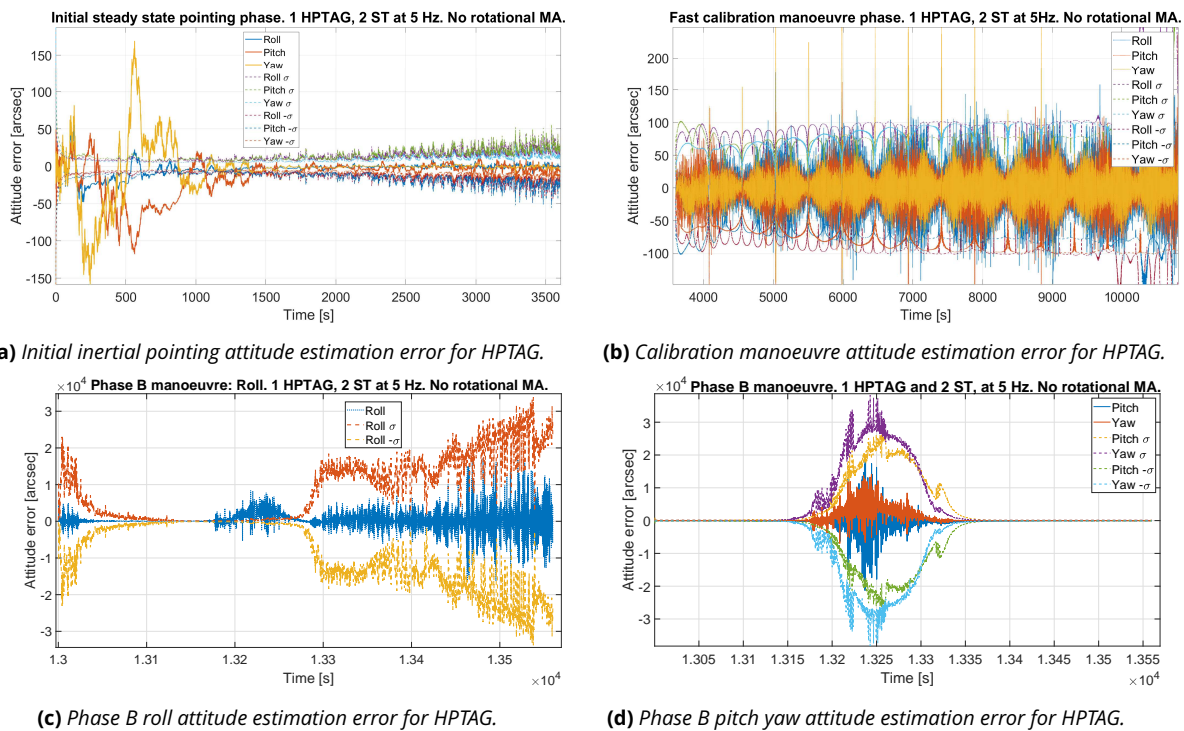
Figure 6.27: *Attitude estimation performance for fast calibration manoeuvre, and the following phase B manoeuvre without ST drop out. Two ST, one HPTAG, and filter at 5Hz. Rotational gyro misalignment are set to 0 deg, and the rest to 0.5 deg. ASF are set to 500ppm, and SSF are set to 100 ppm. ST misalignment is set to 0.1 deg.*

6.4.4 | Effect of Slew Rate Induced Star Tracker Drop Out

For the star tracker under consideration, one of the hard constraints involved is the loss of attitude acquisition capability under agile slew conditions exceeding 0.3 deg/s. We assume the loss of acquisition for one axis of the star tracker leads to the loss of acquisition capability along all other axis, and eventually the loss of both star trackers. Clearly this is problematic, since the calibration filter cannot be kept operational for all the manoeuvre sequences considered. Especially, not during the agile terrestrial target tracking phase.

Figure 6.28, demonstrates the loss of attitude estimation performance, and consequently the loss of overall attitude estimation performance of the filter even when the star tracker becomes active again. Since the filter states require calibrating again. This clearly demonstrates the need for two filters. A filter that calibrates the calibration parameters when the star tracker is available. And a secondary simple 6/7 state USQUE filter that utilises these pre-calibrated states, to pre-correct the sensor deterministic errors, and is kept operational during and after the agile mission manoeuvre. The significance of this approach was presented earlier with the aid of Section 6.3.2 earlier. Where it was demonstrated that calibration of star tracker alignment alone can significantly improve the attitude estimation capability of the regular 6/7 state USQUE filter through out the mission phases under consideration. Furthermore, it was demonstrated with the aid of Sections 4.8.1 and 4.8.2, that the overall impact of the deterministic gyro error sources on attitude estimation error is not significant compared to the stochastic gyro-stellar error sources. In addition, the attitude error is most significantly distorted by the star tracker misalignment. If this alone can be calibrated with good precision, a regular 6/7 state USQUE can be utilised for all the mission manoeuvres. This does not compensate for the degradation of attitude knowledge performance in the event of star tracker dropout. Since the gyro noise floor determines the performance of dead-reckoning, where the impact of gyro deterministic error sources in minimal in comparison to the overall error. However, this approach solves the attitude error convergence problem once the star tracker becomes available again. Star tracker alignment calibration capability of USQUE calibration filter is discussed later in Section 6.4.5. Attitude knowledge estimation performance with 18/19 state USQUE based calibration filter in the event of star tracker loss, and the subsequent mission phases is presented with the aid of Table 6.7.

(a) *Attitude estimation error for HPTAG, for pitch and yaw axis.*

(b) *Attitude estimation error for HPTAG, for roll axis.*
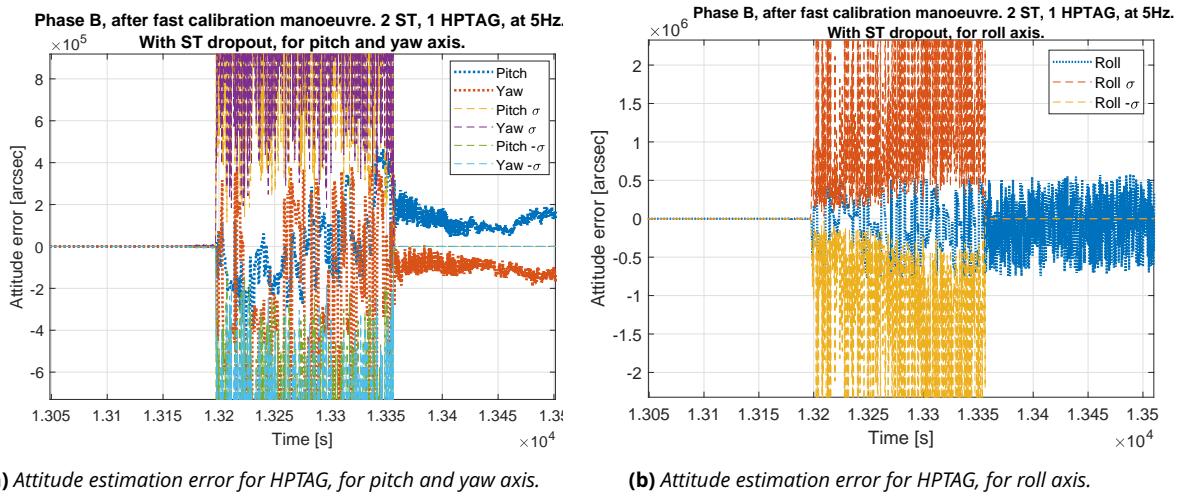
Figure 6.28: *Attitude estimation performance for phase B manoeuvre, post the fast calibration manoeuvre with ST drop out. Two ST, one HPTAG, and filter at 5Hz. Gyro misalignment are set to 0.5 deg, ASF are set to 500ppm, and SSF are set to 100 ppm. ST misalignment is set to 0.1 deg.*

6.4.5 | Calibration Parameter Estimation Performance

Previous section discussed the need to separate the calibration mission phase (Phase A), from the agile mission phase (Phase B). The objective of this section is to demonstrate the capability of the USQUE calibration filter to estimate the calibration parameters, under different conditions, for the chosen suite of sensors and simulation conditions. As a consequence only Phase A manoeuvre is considered, unless stated otherwise. This section is divided into three core, and an additional segment. First the choice of gyros on the calibration performance is investigated. This is followed by the choice of calibration manoeuvre, and the consequent impact on calibration performance. And finally the effect of rotational misalignment exclusion on the calibration parameter estimation is discussed. For all the cases it was observed that the gyro symmetric and asymmetric scale factors do not converge, and are thus discussed in a separate segment. Table 6.8 summarises the calibration parameter estimation performance for the cases considered in the following.

Effect of Gyro Choice

For the results presented in this segment, Phase A associated with the slow calibration manoeuvre is utilised. The calibration of star tracker alignment is the most significant one, in terms of attitude knowledge error contribution. Figures 6.29 and 6.30 capture the star tracker misalignment calibration for the case when MPSAG and HPTAG is utilised. In both cases, during the preliminary hypothetical steady state inertial pointing phase with zero angular rate and constant attitude, the filter sigma bounds are observed to diverge. Since gyros are used as reference sensors, this indicates that the filter needs non-zero angular rate vector input to calibrate for the star tracker misalignment. As soon as the calibration manoeuvre is initiated, in both cases the filter is observed to converge. Especially, for HPTAG the filter converges significantly faster compared to the case with MPSAG. At the end of the manoeuvre, the filter output for star tracker misalignment calibration parameter is observed to converge to below 5 arcsec of error, while for MPSAG this is observed to be 25 arcsec approximately. Clearly, low noise in reference gyro sensor leads a faster convergence and better estimation of star tracker alignment calibration parameter. This, in exchange, indicates the impact of reference gyro sensor degradation on star tracker alignment calibration performance.

Figure 6.31 captures the impact of sensor choice on the bias estimation performance of the calibration filter. In both cases the filter though detects that the bias with a much better accuracy than previously observed with the 6/7 state USQUE filter, the error is not contained within the sigma bounds for the entire manoeuvre. This is especially true for MPSAG. The sigma bounds diverge indicating the lack of confidence on the bias estimate. In both cases, calibration manoeuvre is observed to excite the bias estimation error out of the sigma bounds. Bias estimation error for HPTAG is observed to be significantly lower than that for MPSAG.

Figure 6.32 captures the impact of gyros on gyro misalignment calibration performance. In both cases, for the initial inertial pointing phase when the angular rate is zero, the sigma bounds are observed to diverge indicating the need for non-zero angular rate for persistency of excitation of gyro misalignment angle calibration. As soon
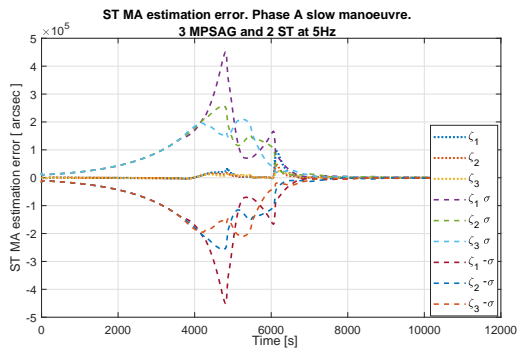
(a) ST misalignment estimation error for phase A of slow calibration manoeuvre.
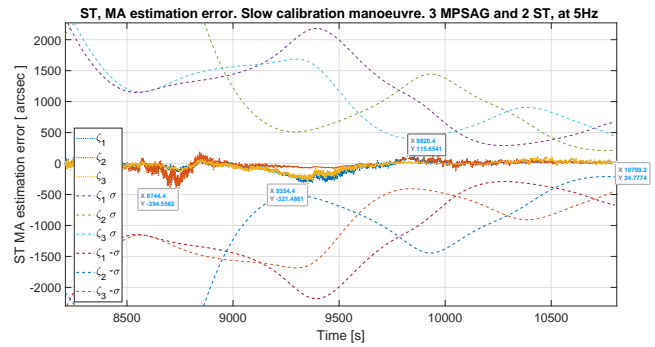
(b) ST misalignment estimation error for the slow calibration manoeuvre.

Figure 6.29: *ST misalignnment estimation error with USQUE calibration filter for slow phase A manoeuvre. Two ST, three MPSAG, and filter at 5Hz. Gyro misalignment are set to 0.5 deg, ASF are set to 500ppm, and SSF are set to 100 ppm. ST misalignment is set to 0.1 deg.*
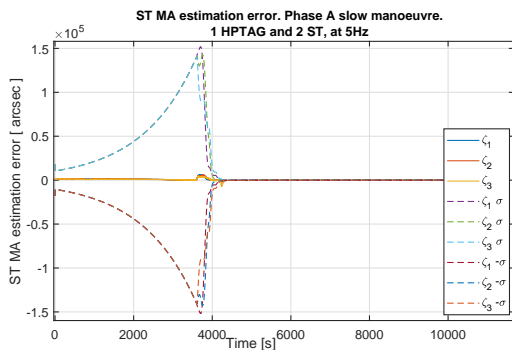
(a) ST misalignment estimation error for phase A of slow calibration manoeuvre.
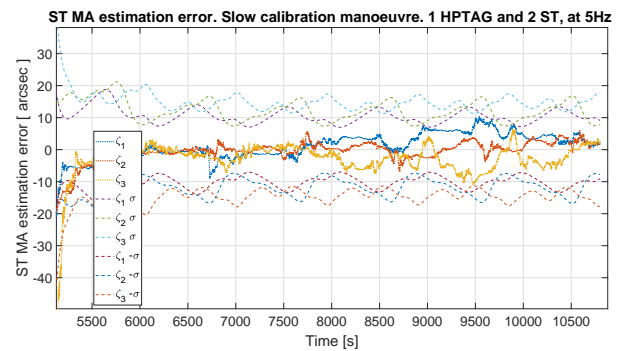
(b) ST misalignment estimation error for the slow calibration manoeuvre.

Figure 6.30: *ST misalignnment estimation error with USQUE calibration filter for slow phase A manoeuvre. Two ST, one HPTAG, and filter at 5Hz. Gyro misalignment are set to 0.5 deg, ASF are set to 500ppm, and SSF are set to 100 ppm. ST misalignment is set to 0.1 deg.*
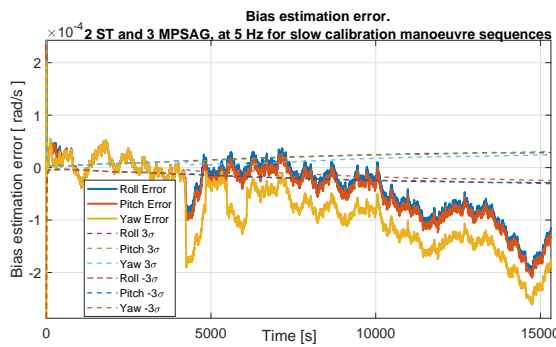
(a) Gyro bias estimation error for MPSAG.
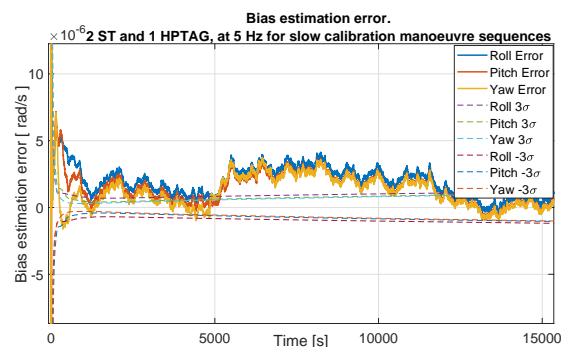
(b) Gyro bias estimation error for HPTAG.

Figure 6.31: *Bias estimation error for slow calibration manoeuvre phase sequences with USQUE calibration filter. Two ST, three MPSAG or one HPTAG, and filter at 5Hz. Gyro misalignment are set to 0.5 deg, ASF are set to 500ppm, and SSF are set to 100 ppm. ST misalignment is set to 0.1 ppm.*

as the calibration manoeuvre starts, the filter covariances are observed to converge and the calibration states are misalignment errors get closer to zero. However, in both cases the gyro misalignment did not converge entirely by the end of the calibration maneneuvre. A longer calibration manoeuvre, with higher frequency and amplitude of oscillation should be tested to evaluate the true performance of misalignment calibration. Misalignment error

(a) *Gyro misalignment estimation error for MPSAG.*

(b) *Gyro misalignment estimation error for HPTAG.*
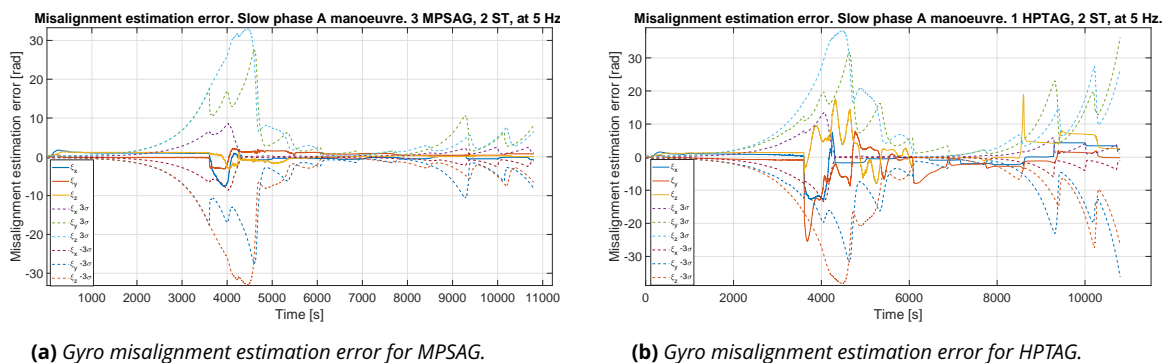
Figure 6.32: *Misalignment estimation error for slow calibration manoeuvre phase sequences with USQUE calibration filter. Two ST, three MPSAG or one HPTAG, and filter at 5Hz. Gyro misalignment are set to 0.5 deg or all elements, ASF are set to 500ppm, and SSF are set to 100 ppm. ST misalignment is set to 0.1 deg.*

(a) *ST misalignment estimation error for phase A of fast calibration manoeuvre.*

(b) *ST misalignment estimation error for the fast calibration manoeuvre.*
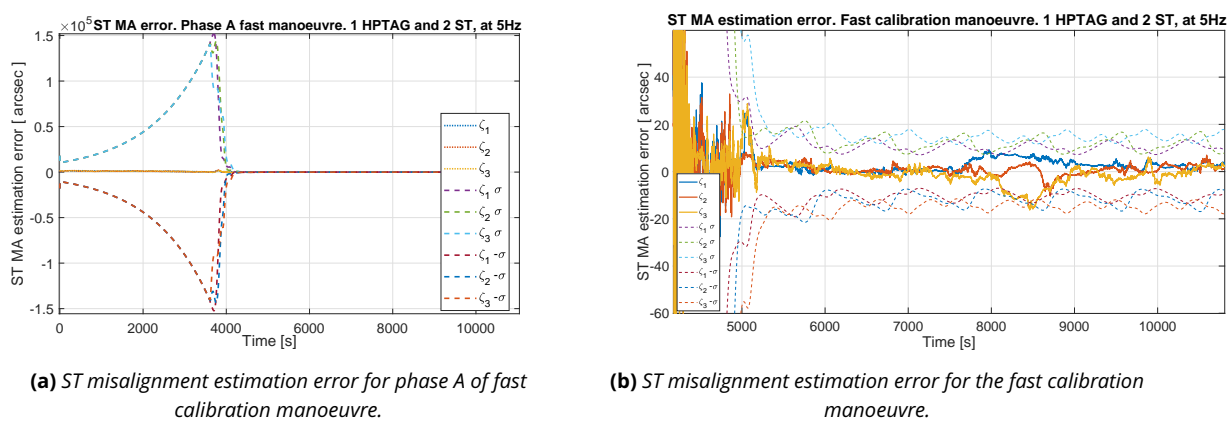
Figure 6.33: *ST misalignment estimation error with USQUE calibration filter for fast phase A manoeuvre. Two ST, one HPTAG, and filter at 5Hz. Gyro misalignment are set to 0.5 deg, ASF are set to 500ppm, and SSF are set to 100 ppm. ST misalignment is set to 0.1 deg.*

associated with HPTAG is observed to converge slower than that with MPSAG. This is improved with the aid of a calibration manoeuvre with higher amplitude and frequency of oscillation, as discussed later in this Section with the aid of Figure 6.34b. The overall gyro misalignment calibration performance is observed to be not as good as the star tracker misalignment calibration. The reason for this might be that the impact of misalignment on the gyro output, is significantly lower than the overall gyro-stellar noise floor as demonstrated earlier in Sections 4.8.1 and 4.8.2. Future work, should test the calibration filter with better performing star tracker and gyro, to localise the root cause of this behaviour. Table 6.8 summarises the calibration parameter estimation performance for the choice of gyro configuration.

Effect of Calibration Manoeuvre

This segment aims at exploring the impact of calibration manoeuvre on calibration parameter estimation convergence. For this, HPTAG sensor and the manoeuvre sequences associated with the fast calibration manoeuvre is considered. One HPTAG sensor, two star trackers, and the calibration filter are operated at 5 Hz.

Figure 6.33 captures the star tracker misalignment calibration performance, for a faster calibration manoeuvre. Compared to the slow calibration manoeuvre in Figure 6.30, no significant differences are observed in this case. As observed previously, fast convergence and low estimation error is observed. Table 6.8 summarises the calibration parameter estimation performance for the choice of calibration manoeuvre.

Figure 6.34 captures the bias and misalignment estimation error for fast calibration manoeuvre associated phase A manoeuvre. As observed, the bias estimation performance is not influenced by the calibration manoeuvre. This is in accordance with what is to be expected, since bias is driven by rate random walk of the gyro, and is not driven by the calibration manoeuvre. The gyro misalignment estimation performance and convergence behaviour gets

(a) *Bias estimation error.*

(b) *Misalignment estimation error.*
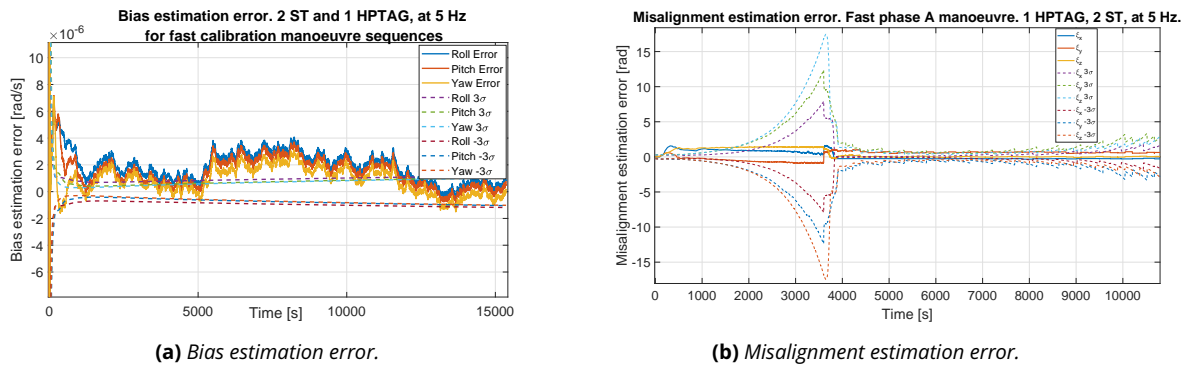
Figure 6.34: *Gyro bias and MA estimation error for fast calibration manoeuvre phase sequences with USQUE calibration filter. Two ST, one HPTAG, and filter at 5Hz. Gyro misalignment are set to 0.5 deg, ASF are set to 500ppm, and SSF are set to 100 ppm. ST misalignment is set to 0.1 deg.*

(a) *ST misalignment estimation error for phase A of fast calibration manoeuvre.*

(b) *ST misalignment estimation error for the fast calibration manoeuvre.*
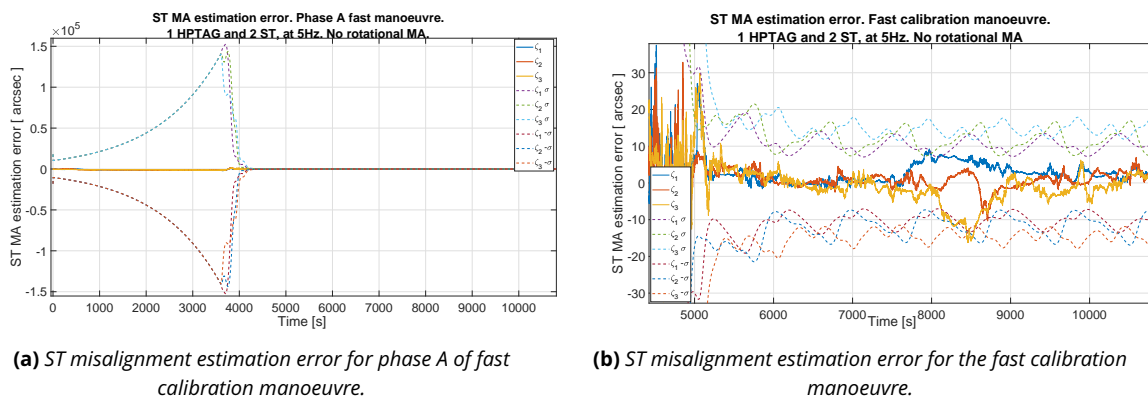
Figure 6.35: *ST misalignnment estimation error with USQUE calibration filter for slow phase A manoeuvre without gyro rotational misalignment. Two ST, one HPTAG, and filter at 5Hz. Rotational gyro misalignment are set to 0 deg, and the rest to 0.5 deg, ASF are set to 500ppm, and SSF are set to 100 ppm. ST misalignment is set to 0.1 deg.*

significantly better compared to the slow calibration manoeuvre sequence. This is in accordance with the observation made earlier in Section 4.8.2, that demonstrated that calibration manoeuvres with higher frequency and amplitude of oscillations leads to higher gyro signal distortion. As a consequence, the gyro misalignment calibration states are observed better by the filter.

Effect of Gyro Rotational Misalignment Exclusion

Three gyro rotational misalignment are excluded to ensure that the calibration filter is capable of observing the calibration states. All the previous simulation results, considered a 0.5 deg of misalignment for all the elements in gyro misalignment matrix. Here, rotational misalignment for simulating the gyro output from the rigid body simulator are set to zero, while the other elements are kept at 0.5 deg. This is to evaluate the impact of exclusion of rotational misalignment on the calibration parameter estimation process. Fast calibration manoeuvre and HPTAG sensor is utilised for the below presented results.

Figure 6.35 demonstrates the star tracker misalignment calibration performance. Comparing this against Figure 6.33, no differences are observed. It was discussed in the previous sections that gyro misalignment have very little impact on the overall attitude estimation performance, due to the higher gyro-stellar noise floor. This is observed here again.

Figure 6.36 presents the gyro bias and misalignment estimation performance, when the gyro rotational misalignment are initialised with zero rotational misalignment. Comparing this against Figure 6.34 no differences are observed for the case where rotational misalignment are set 0.5 deg for gyro output simulation. For bias estimation this is expected, as it is driven by rate random walk of the gyro. While, for gyro misalignment estimation, this demonstrates that exclusion of gyro rotational misalignment has no impact on the remnant gyro misalignment parameter cali-

(a) *Bias estimation error.*

(b) *Misalignment estimation error.*
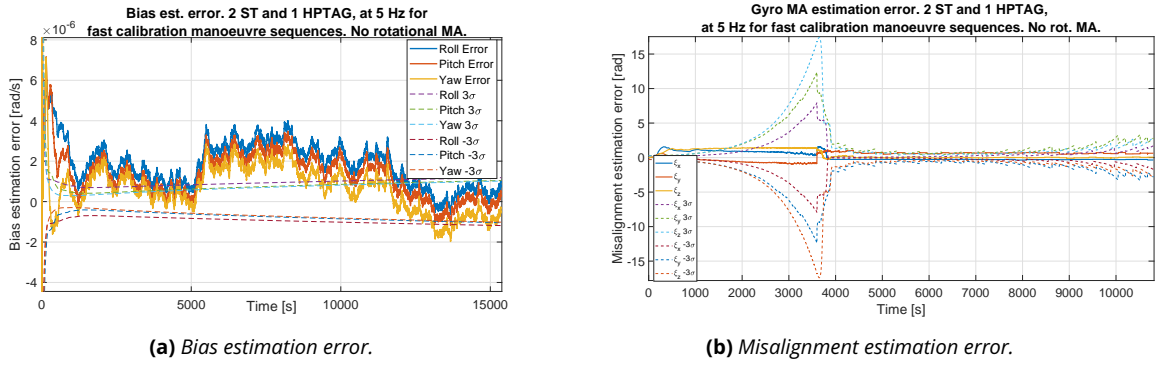
Figure 6.36: *Gyro bias and MA estimation error for fast calibration manoeuvre phase sequences with USQUE calibration filter. Two ST, one HPTAG, and filter at 5Hz. Rotational gyro misalignment are set to 0 deg, and the rest to 0.5 deg. ASF are set to 500ppm, and SSF are set to 100 ppm. ST misalignment is set to 0.1 deg.*

(a) *Asymmetric scale factor estimation*

(b) *Symmetric scale factor estimation*
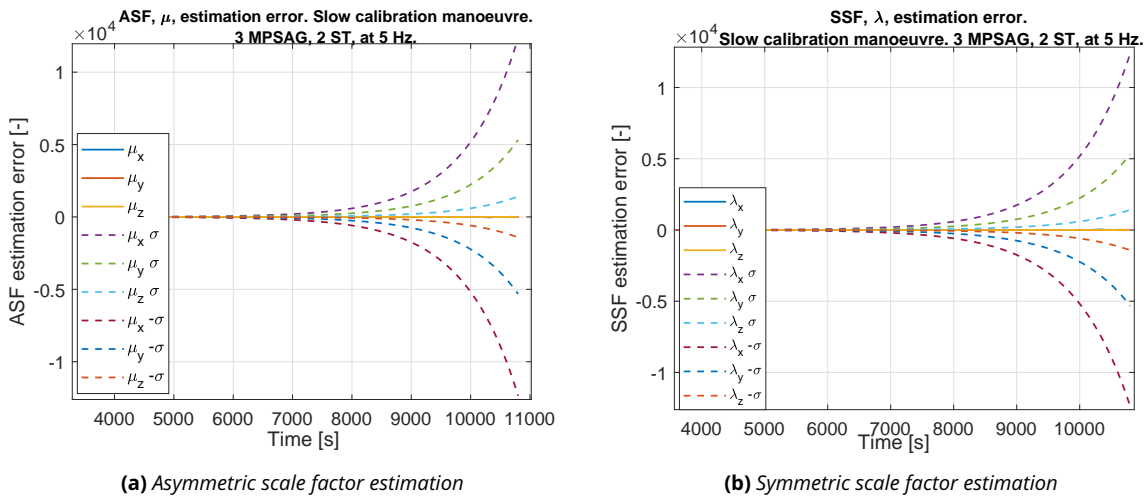
Figure 6.37: *Convergence behaviour of MPSAG for ASF and SSF, for slow calibration manoeuvre. Three MPSAG, 2 ST, and filter update rate of 5 Hz.*

bration, for the conditions considered as part of the thesis work. Table 6.8 summarises the calibration parameter estimation performance when gyro rotational misalignment is excluded from the simulator.

Symmetric and Asymmetric Scale Factor Estimation

In all cases, symmetric and asymmetric factors were not observed to converge. All gyro misalignment are initialised at 0.5 deg, with asymmetric scale factor at 500 ppm, symmetric scale factor at 100 ppm, unless stated otherwise. All star tracker misalignment angles are initialised at 0.1 deg. Figures 6.37, 6.38 and 6.39, demonstrate the scale factor estimation error associated with slow calibration manoeuvre for MPSAG and HPTAG, indicating the effect of gyro sensor choice on the estimation process. Similar performances are observed in both cases.

Figure 6.40 indicates the impact of fast calibration manoeuvre on scale factor estimation process, when compared against Figure 6.39. The estimation error is observed to oscillation more around the zero line.

Figure 6.41 captures the impact of exclusion of rotational misalignment on the scale factor estimation performance, when compared against Figure 6.40. No significant performance difference is observed.

In all of the above cases the scale factor was observed to oscillate around the zero point, during calibration manoeuvre, with increasing sigma bounds indicating the lack of certainty on the filter output. Though the impact of scale factor on the gyro output is minimal compared to the gyro bias and output noise floor. Further investigation, with better attitude and attitude rate sensors, where the impact of scale factor and misalignment is more prominent should be investigated in future works to identify the root cause of this anomaly. Table 6.8 summarises the scale factor calibration parameter estimation performances for the different cases discussed here.

(a) *Asymmetric scale factor estimation*   **(b)** *Symmetric scale factor estimation*
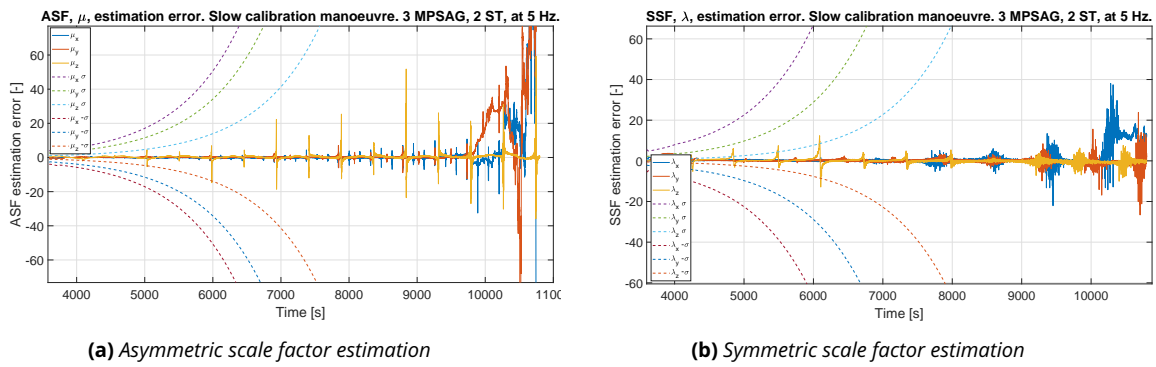
Figure 6.38: *Convergence behaviour of MPSAG for ASF and SSF, for slow calibration manoeuvre. Three MPSAG, 2 ST, and filter update rate of 5 Hz. Zoomed in to demonstrate the filter output estimation error.*

(a) *Asymmetric scale factor estimation*   **(b)** *Symmetric scale factor estimation*
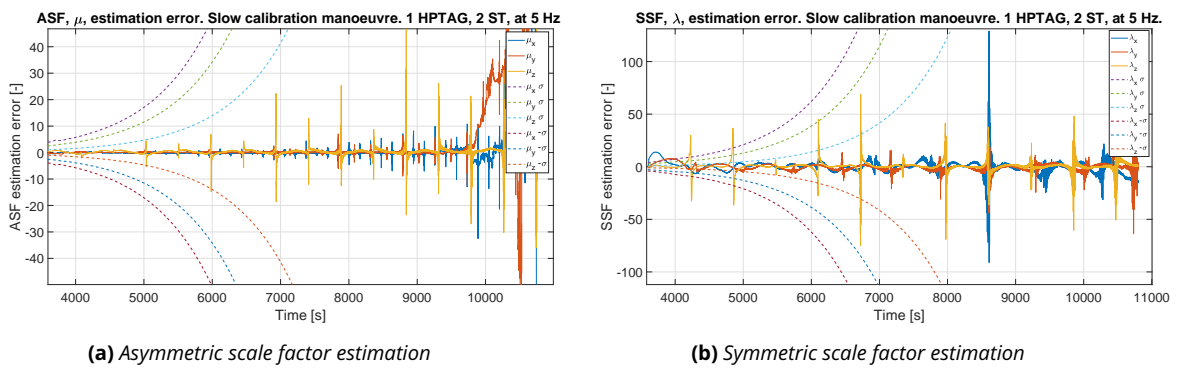
Figure 6.39: *Convergence behaviour of HPTAG for ASF and SSF, for slow calibration manoeuvre. One HPTAG, 2 ST, and filter update rate of 5 Hz.*

(a) *Asymmetric scale factor estimation*   **(b)** *Symmetric scale factor estimation*
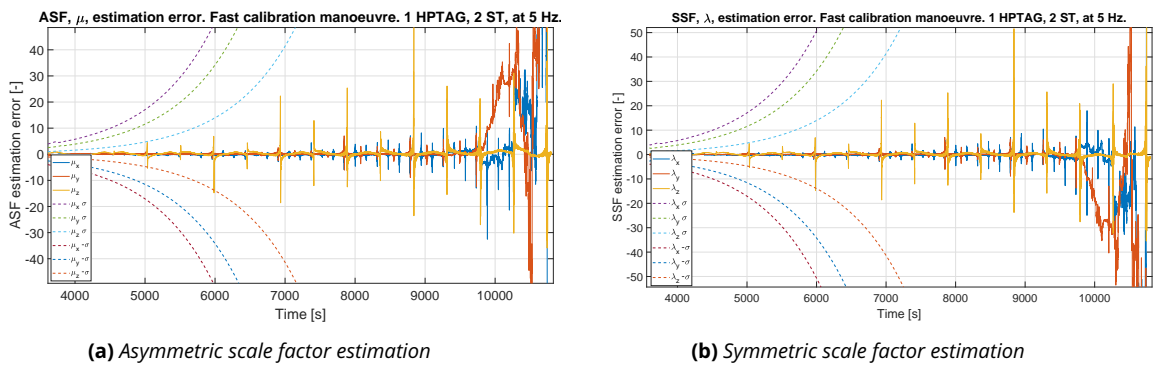
Figure 6.40: *Convergence behaviour of HPTAG for ASF and SSF, for fast calibration manoeuvre. One HPTAG, 2 ST, and filter update rate of 5 Hz.*

(a) *Asymmetric scale factor estimation*

(b) *Symmetric scale factor estimation*
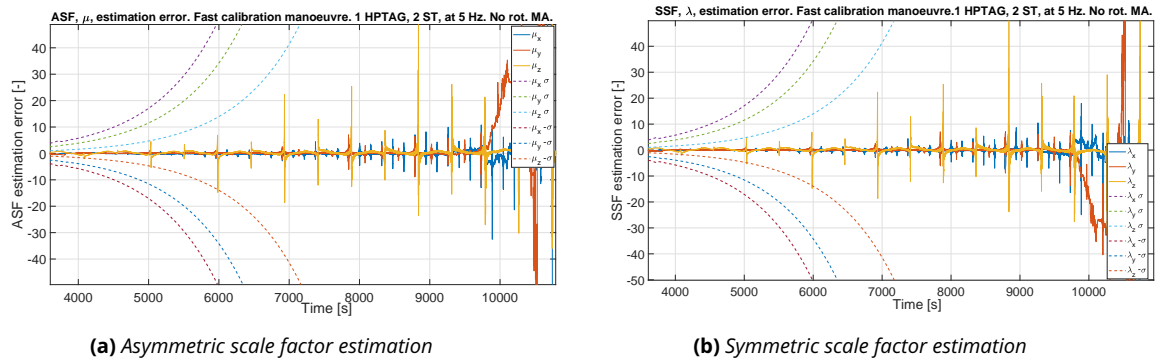
Figure 6.41: *Convergence behaviour of HPTAG for ASF and SSF, for fast calibration manoeuvre. One HPTAG, 2 ST, and filter update rate of 5 Hz. With exclusion of rotational misalignment by setting them to 0deg in gyro simulator.*

Table 6.7: *Attitude estimation performance with 18/19 state USQUE based calibration filter. Impact of gyro sensor choice, persistency of excitation of calibration manoeuvre, and exclusion of rotational misalignment on the attitude estimation performance is further outlined.*

		Impact of sensor choice on attitude estimation with 18/19 state USQUE calibration filter and sensor at 5Hz						
Sensor Configuration	Time [s]	[0, 3600)	[3600, 10800)	[10800, 13000)	[13000, 13197)	[13197, 13354)	[13354, 13560)	[13560, 15360]
	Mission manoeuvre	Initial inertial pointing - Non-zero attitude - Zero angular rate	Slow calibration manoeuvre	Pre-ground target tracking manoeuvre	Before ST dropout	No ST dropout	After ST recovery - No ST dropout	Target pointing, post slow calibration manoeuvre - Non-zero attitude - Non-zero angular rate
2ST, 3 MPSAG	Mean [arcsec] [Roll, Pitch, Yaw]	[-4.10, -1.03, -15.32]	[-1.66, -3.69, -0.77]	[-9.66, 16.96, -0.25]	[94.53, -38.41, 19.11]	[806.18, 2539.66, 3176.58]	[-52.65, -48.33, 2.19]	[1.78, 1.64, -1.49]
	Std. dev. (1 σ) [arcsec] [Roll, Pitch, Yaw]	[13.80, 36.66, 55.16]	[30.91, 68.59, 44.75]	[45.59, 40.66, 35.99]	[471.73, 91.01, 123.65]	[2124.32, 6000.31, 4145.44]	[1913.61, 69.24, 21.64]	[36.13, 20.67, 28.04]
1 MA ST, MA- SF Gyro	Abs. AKE (1 σ) [arcsec] [Roll, Pitch, Yaw]	[17.90, 37.69, 70.48] [P]	[32.57, 72.28, 45.52] [UQ]	[55.25, 57.62, 36.24] [P]	[566.26, 129.42, 142.76] [P]	[2930.50, 8539.97, 7322.02] [UQ]	[1966.26, 117.57, 23.83] [UQ]	[37.91, 22.31, 29.53] [UQ]
2ST, 1 HPTAG	Mean [arcsec] [Roll, Pitch, Yaw]	[-3.83, -13.49, -3.12]	[-2.79, -3.89, -0.77]	[-10.06, 17.10, -0.58]	[1085.41, -57.18, 15.91]	[628.34, -1548.51, 2114.66]	[174.36, -46.19, -4.39]	[2.24, 4.57, -2.16]
	Std. dev. (1 σ) [arcsec] [Roll, Pitch, Yaw]	[9.20, 24.11, 33.19]	[26.35, 56.26, 36.39]	[45.15, 41.01, 36.57]	[2788.25, 595.30, 1714.45]	[2457.01, 4786.64, 5088.86]	[6410.21, 69.00, 22.77]	[63.28, 31.46, 29.28]
1 MA ST, MA- SF Gyro	Abs. AKE (1 σ) [arcsec] [Roll, Pitch, Yaw]	[13.03, 37.60, 36.31] [P]	[29.14, 60.15, 37.16] [UQ]	[55.21, 58.11, 37.15] [UQ]	[3873.66, 652.48, 1730.36] [UQ]	[3085.35, 6335.15, 7203.52] [UQ]	[6584.57, 115.19, 27.16] [UQ]	[65.52, 36.03, 31.44] [UQ]
		Impact of fast calibration manoeuvre						
2ST, 1 HPTAG	Mean [arcsec] [Roll, Pitch, Yaw]	[-3.83, -13.49, -3.12]	[-0.70, -2.49, 0.50]	[3.14, 10.42, 2.54]	[76.06, -60.14, 7.73]	[1024.30, -476.58, 2197.02]	[215.45, -63.43, -14.09]	[37.67, 5.82, -18.65]
	Std. dev. (1 σ) [arcsec] [Roll, Pitch, Yaw]	[9.20, 24.11, 33.19]	[30.21, 27.16, 23.02]	[62.80, 38.07, 44.34]	[735.36, 204.81, 509.83]	[2039.02, 4675.87, 3047.98]	[5518.71, 83.35, 36.03]	[1910.75, 29.63, 42.61]
1 MA ST, MA- SF Gyro	Abs. AKE (1 σ) [arcsec] [Roll, Pitch, Yaw]	[13.03, 37.60, 36.31] [P]	[30.91, 29.65, 23.52] [UQ]	[65.94, 48.49, 46.88] [UQ]	[811.42, 264.95, 517.56] [UQ]	[3063.32, 5152.45, 5245] [UQ]	[5734.16, 146.78, 50.12] [UQ]	[1948.42, 35.45, 61.26] [UQ]
		Impact of rotational MA exclusion in the gyro-stellar attitude simulator						
2ST, 1 HPTAG 1 MA ST, MA- SF Gyro Excl. rot. MA	Mean [arcsec] [Roll, Pitch, Yaw]	[-3.83, -13.49, -3.12]	[-0.65, -2.68, 0.71]	[3.13, 10.40, 2.54]	[75.64, -59.68, 6.01]	[1036.08, -423.52, 2205.86]	[183.48, -63.59, -13.01]	[38.69, 5.61, -18.23]
	Std. dev. (1 σ) [arcsec] [Roll, Pitch, Yaw]	[9.20, 24.11, 33.19]	[30.31, 28.43, 24.66]	[62.87, 38.05, 44.37]	[776.23, 191.89, 467.41]	[2069.26, 4384.26, 3016.70]	[4942.17, 83.53, 35.75]	[1895.97, 29.53, 42.84]
	Abs. AKE (1 σ) [arcsec] [Roll, Pitch, Yaw]	[13.03, 37.60, 36.31] [P]	[30.96, 31.11, 25.37] [UQ]	[66.00, 48.45, 46.91] [UQ]	[851.87, 251.57, 473.42] [UQ]	[3105.34, 4807.78, 5222.56] [UQ]	[5125.65, 147.12, 48.76] [UQ]	[1934.66, 35.14, 61.07] [UQ]

Table 6.8: *Gyro-stellar misalignment and scale factor calibration parameter estimation performance. Attitude estimation performance with 18/19 state USQUE based calibration filter. Impact of gyro sensor choice, persistency of excitation of calibration manoeuvre, and exclusion of rotational misalignment on the attitude estimation performance is further outlined. [P] = Partially (some axis) qualified, [UQ] = Unqualified.*

18/19 state USQUE calibration filter at 5 Hz. Time = [10,700s - 10, 800s] -1 perfect ST and 1 ST - MA of 0.1 deg/axis - Gyro MA of 0.5 deg/axis. Gyro ASF of 500 ppm, Gyro SSF of 100 ppm		Impact of sensor choice. Slow calibration manoeuvre		Impact of more persistently exciting calibration manoeuvre	Impact of exclusion of rotational misalignment δ_r
Parameter estimation error	Metric	2 ST, and 3 MPSAG	2 ST, and 1 HPTAG	2 ST, and 1 HPTAG	2 ST, and 1 HPTAG
Bias [arcsec/s] $[\beta_x, \beta_y, \beta_z]$	Mean	[-14.06, -15.98, 26.42]	[0.37, 0.27, 0.26]	[0.36, 0.25, 0.17]	[0.35, 0.24, 0.08]
	Std. dev (1σ)	[10.73, 10.57, 10.78]	[0.23, 0.23, 0.23]	[0.23, 0.23, 0.23]	[0.23, 0.23, 0.24]
	Abs. bias error (1σ)	[24.79, 26.56, 37.19]	[0.61, 0.51, 0.49]	[0.59, 0.48, 0.41]	[0.58, 0.47, 0.32]
ST MA [arcsec] $[\zeta_x, \zeta_y, \zeta_z]$	Mean	[29.27, 12.18, 20.91]	[31.06, 13.05, 22.01]	[2.84, 1.51, 2.00]	[2.85, 1.51, 2.03]
	Std. dev (1σ)	[8.28, 3.81, 18.81]	[9.11, 4.19, 20.97]	[0.63, 0.45, 0.73]	[0.64, 0.45, 0.74]
	Abs. ST MA error (1σ)	[37.55, 15.99, 39.73]	[40.17, 17.23, 42.98]	[3.47, 1.96, 2.73]	[3.49, 1.96, 2.78]
Gyro MA [rad] $[\xi_x, \xi_y, \xi_z]$	Mean	[-0.69, 0.78, 0.08]	[-0.48, 0.70, -0.09]	[-0.28, 0.63, 0.07]	[-0.35, 0.63, 0.06]
	Std. dev (1σ)	[0.07, 8.24e-05, 3.13e-05]	[0.17, 0.002, 0.0005]	[2.29e-05, 2.47e-05, 4.17e-05]	[2.82e-05, 1.48e-05, 2.54e-05]
	Abs. Gyro MA error (1σ)	[0.76, 0.78, 0.08]	[0.65, 0.70, 0.09]	[0.28, 0.63, 0.07]	[0.35, 0.63, 0.06]
Gyro ASF [-] $[\mu_x, \mu_y, \mu_z]$	Mean	[-10.40, 1.28, 0.40]	[0.02, 2.79, -0.12]	[5.13, 228.21, 0.14]	[-38.83, 215.43, 0.04]
	Std. dev (1σ)	[1.89, 3.37, 0.28]	[0.81, 4.45, 0.24]	[60.44, 186.45, 6.18]	[95.50, 168.54, 6.75]
	Abs. ASF error (1σ)	[12.30, 4.65, 0.68]	[0.83, 7.24, 0.36]	[65.57, 414.66, 6.32]	[134.33, 383.97, 6.79]
Gyro SSF [-] $[\lambda_x, \lambda_y, \lambda_z]$	Mean	[10.90, -0.43, -0.19]	[0.43, -3.21, 0.40]	[-5.06, -228.10, -0.31]	[-0.35, 0.63, 0.06]
	Std. dev (1σ)	[1.90, 3.45, 0.28]	[0.82, 4.35, 0.24]	[60.41, 186.48, 6.50]	[2.82e-05, 1.48e-05, 2.54e-05]
	Abs. SSF error (1σ)	[12.79, 3.88, 0.47]	[1.25, 7.56, 0.64]	[65.48, 414.58, 6.81]	[0.35, 0.63, 0.06]

6.5 | Summary and Conclusions

This chapter is aimed at demonstrating the attitude estimation and calibration performance for the sensors characterised in Chapter 3, manoeuvres generated in Chapter 4, and the filters synthesised in Chapter 5. In that regard, the analysis presented as part of this chapter was broadly split into four distinctive segments.

The first segment aimed at demonstrating the attitude estimation performance of 6/7 state USQUE filter, synthesised in Section 5.1, in the absence of gyro-stellar deterministic error sources, namely misalignment and scale factor. In that regard, the significance of innovation signal monitor in preventing premature convergence of state covariance matrix was demonstrated. The effect of star tracker drop out, under agile terrestrial target tracking, on attitude and gyro bias estimation procedure, and the consequent effect of gyro dead reckoning on attitude knowledge estimation was demonstrated. The need for two star trackers to improve attitude knowledge, and retain attitude knowledge in the event of occultation of one of the star trackers was discussed. In that regard, two different strategies of merging star trackers were discussed: one where the better performing pitch/yaw axis of two star trackers are pre-selected to reconstruct a single attitude quaternion that is fed to the filter; second, where two star tracker quaternion measurements are stacked. The latter approach was observed to significantly improve the low performing roll axis attitude knowledge, and bring it to the performance level of high performing pitch and yaw axis. Feeding in stacked star tracker quaternion output is chosen for the rest of the filter development. The star tracker is limited to 5 Hz update rate, however MPSAG and HPTAG are capable of operating at 2.3 kHz and 2 kHz respectively. The effect of asynchronous gyro-stellar sensor fusion was investigated, by running the gyro and filter at 100Hz while acquiring the star tracker attitude solution at 5Hz. No improvement in attitude knowledge estimation is observed, neither during the nominal phase, nor during the star tracker dropout phase. As a consequence, the filter and sensor update rate are set to 5Hz. Attitude knowledge performance improvement with HPTAG is demonstrated, which in exchange, demonstrates the impact of gyro sensor degradation on the attitude knowledge estimation performance.

The second segment demonstrated the loss of attitude knowledge performance in the presence of gyro-stellar misalignment and scale factor. The impact of gyro misalignment and scale factor on the attitude estimation performance was observed to be minimal when compared against the impact of star tracker misalignment. This demonstrated to be in line with the observations presented earlier in Sections 4.8 and 4.7.4. It was further noted that calibration of star tracker misalignment alone, can lead to significant improvement in attitude knowledge estimation performance.

The third segment presented the attitude estimation performance of the USQUE based calibration filter, derived earlier in Chapter 5.2, in the presence of gyro sensor degradation, and varying amplitude and frequency of calibration manoeuvre oscillation. It further looks into the impact of exclusion of gyro rotational misalignment, and slew rate induced star tracker dropout on the attitude estimation performance. Both gyro sensors were observed to provide better attitude knowledge estimates for phase A manoeuvre, compared to the case where 6/7 state USQUE was used in conjunction with misaligned and scale factored gyro-stellar sensor suite. However, HPTAG is observed to demonstrate significantly better attitude estimation performance during the non-harmonic sinusoidal manoeuvre, compared to MPSAG. Similarly a calibration manoeuvre with higher amplitude and more frequent oscillation was observed to improve the attitude estimation performance during this non-harmonic sinusoidal corkscrew manoeuvre. This demonstrates that both low noise of a gyro and high angular rate acceleration make the effect of misalignment and scale factor more prominent on gyro output. This is in accordance with the observations in Sections 4.8 and 4.7.4. The exclusion of gyro rotational misalignment is observed to have minimal impact on the attitude estimation performance. As expected, the attitude estimation performance is demonstrated to degrade significantly in the event of star tracker drop out. When the star tracker measurements become active again, a re-calibration of the filter states is required. Calibration filter is proposed to calibrate for the calibration parameters. Since the most dominant source of error is star tracker misalignment, and it does not vary over shorter periods of time, it can be used to pre-calibrate the misaligned star tracker before feeding into the 6/7 state USQUE filter. This ensures that star tracker drop outs do not require re-calibration of the gyro-stellar configuration, and a single filter with pre-calibrated states can be used for all mission phases.

Finally, the fourth segment evaluated the calibration parameter estimation performance, and the sensitivity thereof, in the presence of gyro sensor degradation, varying amplitude and frequency of oscillation of calibration manoeuvre, and exclusion of gyro rotational misalignment. HPTAG is observed to facilitate faster and better convergence of star tracker misalignment. The star tracker misalignment is tracked to within 5 arcsec accuracy with HPTAG, for the manoeuvre under consideration. Gyro bias estimation performances are demonstrated. Gyro misalignment estimation is observed to improve under calibration manoeuvres with more frequent and higher amplitude of oscillation. No effect of exclusion of gyro rotational misalignment is observed on the calibration parameters. For the calibration manoeuvre phase the filter is observed to have convergence challenges associated with regards to the gyro symmetric

and asymmetric scale factors. Further analysis is required, to appropriately characterise the root cause of the lack of convergence of the scale factor. Nevertheless, calibration of star tracker misalignment alone, significantly improves the overall attitude estimation performance.

7
Conclusions and Recommendations

The purpose of this thesis work is to investigate the attitude estimation capabilities of NanoSats under agile terrestrial target tracking conditions. In doing so, we investigate the attitude estimation capability of NanoSats for chosen gyro-stellar configuration, and sensor fusion algorithm under nominal operational conditions. Under stringent agile tracking conditions, gyro-stellar misalignment and scale factors play a limiting role in the attitude knowledge estimation of NanoSats. Furthermore, the small aperture size of NanoSat class of star trackers require them to have a high integration time to deliver the required precision attitude knowledge. Under agile precision tracking conditions this leads to blurring of images, and eventual loss of star tracker knowledge. As a consequence, we investigate the attitude estimation performance of NanoSats in the presence of gyro-stellar misalignment and scale factors, and star tracker dropouts under agile slew manoeuvres. In order to improve the attitude estimation performance of the system, we extend the sensor fusion algorithm with calibration parameters, to calibrate for gyro-stellar misalignment and scale factor. The knowledge of which improves the attitude estimation performance of agile terrestrial target tracking NanoSats.

Research Methodology

Before outlining the concluding remarks regarding the research questions, and recommendations that follow; the underlying methodology used to enable answering these research questions are briefly outlined. In order to answer the research questions outlined in Chapter 1.3, we utilised CubeCAT NanoSat laser communication terminal as a reference payload, consequently top level mission and system requirements were derived from this. The payload required a top-level absolute attitude knowledge error requirement of 20.63 arcsec(1σ), and a pointing requirement of 1800 arcsec (1σ). Here, absolute attitude knowledge error is defined as the sum of the absolute mean of the error added to the 1σ standard deviation of the error. Based on these requirements, four different variants of MEMS rate gyros were selected and characterised. A steady state noise power spectral density (PSD) analysis was conducted on seven different gyro-stellar configurations, to select the configurations that meet the attitude knowledge requirement. Two different configurations were selected for answering the research questions: two NanoSat star trackers(ST) with three medium performance single axis gyros (MPSAG), and two NanoSat ST with one high performance triple axis gyros(HPTAG). Next, a rigid body NanoSat simulator was developed to enable the generation of desired attitude manoeuvres. Four core mission manoeuvres were generated 1. Inertial pointing with zero angular rate. 2. Non-harmonic sinusoidal manoeuvres for gyro stellar misalignment and scale factor calibration. 3. Agile ground target tracking manoeuvres with slew rate induced star tracker dropout. 4. And, target tracking manoeuvre with non-zero angular rate. The simulator was further extended to accommodate attitude and attitude rate output with misalignment and scale factors, and the characterised sensor noises. In order to evaluate the feasibility of the requirement provided by the stakeholders, reaction wheel time delay were characterised for RW-400 series of reaction wheels from Hyperion Technologies. Torque input-output response time delay, and torque saturation limits were introduced into the rigid body simulator to evaluate the pointing performance. A worst case absolute pointing error of 360 arcsec was observed, as captured with Figures C.5 and C.6. This preliminary analysis, indicated that the ceiling of 20.63 arcsec (1σ) attitude knowledge requirement is set rather low by the stakeholders, and can be increased by approximately 1400 arcsec (1σ). This suggests that a detailed pointing error source budgeting should be conducted before imposing such stringent attitude knowledge requirements. Attitude and attitude rate signals generated by this simulator was fed into the filters, for attitude and calibration parameter estimation purposes. Due to favourable properties of robustness to large initialisation errors, fast convergence, and preservation of attitude quaternion unity norm constraint; UnScented QUaternion Estimator (USQUE) variant of unscented Kalman filter (UKF) is synthesised for attitude estimation. This algorithm is extended to incorporate gyro-stellar misalignment and scale factors, with the aid of Chapter 5. The following conclusions are based on the results obtained following the above presented methodology.

Concluding Remarks and Recommendations for Research Questions

This thesis work was conducted to answer the following core research question:

> How can we extend the attitude knowledge estimation capabilities of agile precision target tracking NanoSats, by virtue of calibration filters utilising NanoSat MEMS rate gyro cluster and star trackers as sensing elements?

It was observed in Chapter 6, that calibrating for gyro-stellar misalignment and scale factors, with the calibration filter synthesised in Chapter 5 improves the overall attitude estimation performance. Chapter 5 demonstrated the performance of 6/7 state based USQUE filter under nominal conditions of no misalignment, scale factors and star tracker dropout. The best performing configurations and the corresponding 1σ absolute attitude knowledge performance error for different manoeuvre phases in roll, pitch, and yaw angles were: Inertial pointing with zero angular rate $[0s, 3600s)$: 2ST, 1 HPTAG $[12.71, 8.32, 9.90]$ arcsec. 2. Slow calibration manoeuvre $[3600s, 10800s)$: 2ST, 3 MPSAG $[26.35, 14.49, 20.58]$ arcsec. 3. Pre ground-target tracking $[10800s, 13000s)$: 2ST, 3 MPSAG $[35.54, 14.50, 31.53]$ arcsec. 4. Agile ground target tracking with no ST dropout $[13000s, 13560s)$: 2 ST, 3 MPSAG $[27.16, 14.74, 29.00]$ arcsec. 5. Target pointing, post calibration manoeuvre $[13560s, 15360s]$: 2ST, 1HPTAG $[19.55, 10.31, 24.09]$ arcsec. For inertial pointing with zero angular rate the AKE requirement of 20.63 arcsec 1σ is met for all axis. While for the rest, they were not met all sense axis. However, if the 1400 arcsec 1σ AKE budget space is made available as discussed above, the attitude knowledge requirements are met.

Later, non-idealities were added. Where, the gyro was given a misalignment of 0.5 deg along all axis, with symmetric scale factor of 500 pmm, and asymmetric scale factor of 100 ppm. One star tracker was given a misalignment of 0.1 deg on all sense axis, and both star tracker outputs were blinded when the slew rates exceeded 0.3 deg/s on any sense axis. Under such conditions, previously noted best performing sensor configurations, demonstrated the following degraded 1σ AKE across all mission phases: 1. Inertial pointing with zero angular rate $[0s, 3600s)$: 2 ST, 1 HPTAG $[14.24, 8.48, 15.82]$ arcsec. 2.Slow calibration manoeuvre $[3600s, 10800s)$: 2 ST, 3 MPSAG $[258.21, 970.09, 742.09]$ arcsec. 3. Pre ground-target tracking $[10800s, 13000s)$: 2 ST, 3 MPSAG $[422.69, 1040, 2343.85]$ arcsec. 4. Agile ground target tracking with and without ST dropout $[13000s, 13560s)$: 2 ST(w), 3 MPSAG $[5039.56, 6699.54, 1830.56]$ arcsec; 2 ST(w/o), 3 MPSAG $[1335.45, 585.12, 1429.92]$ arcsec. 5. Target pointing, post calibration manoeuvre $[13560s, 15360s]$: 2 ST, 1 HPTAG $[809.30, 1005.72, 519.54]$ arcsec. As expected under inertial pointing with non-zero angular rate, the requirements are still met. However, for the rest of the manoeuvres with non-zero angular rate the AKE performances degrade significantly. For some segments, this even exceeds the additional 1400 arcsec 1σ AKE budget space that might be available.

The calibration filter developed here was capable of calibrating for star tracker misalignments. Under the assumption that the star tracker misalignments are calibrated appropriately, while gyro non-idealities persist, the 1σ absolute AKE performance of the previously degraded configurations can be improved to: 1. Inertial pointing with zero angular rate $[0s, 3600s)$: 2 ST, 1 HPTAG $[12.49, 8.24, 9.69]$ arcsec. 2. Slow calibration manoeuvre $[3600s, 10800s)$: 2 ST, 3 MPSAG $[56.63, 47.75, 51.90]$ arcsec. 3. Pre ground-target tracking $[10800s, 13000s)$: 2ST, 3 MPSAG $[49.38, 55.64, 31.54]$ arcsec. 4. Agile ground target tracking with and without ST dropout $[13000s, 13560s)$: 2 ST(w), 3 MPSAG $[6463.28, 5367.14, 2493.80]$ arcsec; 2 ST(w/o), 3 MPSAG $[90.09, 389.96, 29.54]$ arcsec. 5. Target pointing, post calibration manoeuvre $[13560s, 15360s]$: 2 ST, 1 HPTAG $[19.80, 10.75, 24.43]$ arcsec. This demonstrates that utilising USQUE based calibration filter, can facilitate calibration of star trackers; which in turn improves the attitude estimation performance of $6/7$ state USQUE based filter when compared against the case where star tracker misalignments were uncalibrated. Attitude knowledge requirement is met for the inertial pointing phase, with non-zero angular rate. If the additional 1400 arcsec 1σ budget is made available, all mission phases meet the expected requirement. With the exception of the case with star tracker dropout. This further demonstrates that ST dropout has the most significant impact on attitude knowledge performance, followed by star tracker misalignment. In order to meet the agile AKE performances expected of NanoSat ADCS, it is strongly recommended to mitigate the star tracker dropout problem under agile slewing conditions.

Now that the core research question is answered; conclusions and recommendations corresponding to the sub-questions, that guided in answering the core research question, are reviewed:

Gyro-stellar sensor characterisation

- ○ How well can the relevant performance parameters of MEMS rate gyro clusters and NanoSat star tracker be characterised, and modelled?

Characteristic stochastic properties of MEMS rate gyros were captured with the aid of Allan-Variance analysis provided by the gyro manufacturers in Chapter 3. Gyro models constructed considered three main noise sources: angular random walk, rate random walk, and rate flicker noise. The noise parameters were modelled in continuous

time, where rate random walk was modelled with a bandlimited white noise shaped by an integrator, and rate flicker noise shaped by a pink noise shaping filter developed utilising Oustaloup's method of fractional integrators. 1σ standard deviation obtained from steady noise PSD of the gyro models had a factor offset of 1.000075 for MPSAG, and 1.000083 for HPTAG in the frequency range 10^{-4} Hz to 10^3 Hz, when compared against the Allan-Variance based noise PSD. Gyros were subsampled with a fourth order Optimum Legendre-Papoulis filter. Standard deviation of the subsampled steady-state gyro signal output noise PSD had a factor offset of 1.0016 when compared against the Allan-Variance based noise PSD for MPSAG. Star tracker noise was generated with bandlimited white noise, such that the standard deviation obtained from the output noise PSD, upto the Nyquist sampling freqeuncy, would match the 1σ accuracies provided by Hyperion Technologies. At steady-state conditions a factor offset of 1.0016 was observed between 1σ obtained from output noise PSD, and the values provided by the manufacturer for roll, pitch, and yaw axis. The gyro-stellar models were developed with sufficient details to meet the expected requirements outlined for gyro-stellar simulator in Chapter 2.1.

Gyro-stellar configuration, and sampling rate selection

○ What configuration and sampling rate of NanoSat star tracker, and MEMS rate gyro cluster will lead to minimal attitude estimation error from a steady state random noise power spectral density standpoint?

Preliminary choice of configuration was based on complementary filter based gyro-stellar hybridisation, utilising the steady state output noise PSD of gyro-stellar sensors. From the preliminary analysis it was observed that at 5 Hz sampling rate, one HPTAG and one star tracker was sufficient to achieve 17.78 arcsec AKE(absolute knowledge error) 1σ, meeting the expected attitude knowledge requirement of 20.63 arcsec (1σ). However, two star trackers were chosen, to facilitate attitude solution update in the event of occultation with Moon, Earth-limb, or Sun in the field-of-view. With two star trackers in place, and one HPTAG in combination, AKE was observed to be 6.75 arcsec 1σ. Similarly with three MPSAG in combination with two star trackers, demonstrated an AKE of 9.86 arcsec 1σ. The latter being 13 times cheaper and radiation hardened, was chosen along with the HPTAG variant to provide insight into the impact of gyro sensor degradation on the overall attitude estimation performance. From steady-state random noise PSD standpoint, increasing the gyro sampling rate had the effect of more noise addition. At 2 kHz of gyro sampling, two star trackers sampled at 5 Hz, with one HPTAG AKE increased to 6.93 arcsec 1σ, with three MPSAG AKE increased to 10.47 arcsec (1σ). Such high sampling rates are deemed unnecessary from angular rate sampling standpoint. At 1.5 deg/s NanoSat undergoes a kinematics motion at 0.0042 Hz, thereby a sample rate of 5 Hz is considered sufficient to capture kinematics motion. Though this method was favourable for preliminary gyro-stellar configuration selection, it was not observed to be an accurate representation of the final attitude estimation performance. Since, the above analysis is static both in terms of signal input and filter gain value, while the attitude estimator synthesised and the manoeuvres considered as part of the thesis work are dynamic. $6/7$ state USQUE filter developed here, was tested with asynchronous sampling rates with ST set to 5 Hz, and gyros set to 100 Hz in Chapter 6, this demonstrated loss of attitude knowledge performance at the expense of higher sample points.

Attitude knowledge performance with $6/7$ state USQUE filter

○ What is the attitude knowledge performance of a regular attitude and bias estimator, for steady state and agile manoeuvres in the presence of sensor misalignment, scale factors, and slew-rate induced star tracker drop out?

The $6/7$state USQUE filter was observed to have premature covariance convergence, to prevent this an innovation signal monitor was employed. The absolute 1σ AKE was observed to improve significantly as outlined in Table 6.2, where in the best case a factor of 386.93 improvement in the single axis AKE was observed. Two different ways of mixing star tracker solutions were investigated: 1. Stacking star tracker quaternion outputs 2. Selecting best performing Euler axis of each star tracker, and reconstructing a single quaternion attitude output. The former resulted in better performance. Manoeuvre specific 1σ AKE performances were outlined in Table 6.3. In the best case, a factor of 4.7 improvement in single axis AKE performance was observed when the star tracker quaternion outputs were stacked, in contrast with the case of pre-axis selection. As noted in the concluding remarks of the core question, presence of non-idealities degrade the attitude knowledge performance. Calibration of these parameters can mitigate the degraded performances. However, ST dropout under agile slewing conditions should be resolved at a hardware level, to facilitate the precision requirements expected under agile conditions.

Attitude estimation capability with $18/19$ state USQUE based calibration filter

○ How well can a calibration filter provide attitude knowledge, for steady state and agile manoeuvres in the presence of sensor misalignment, scale factors and slew-rate induced star tracker drop out?

The agile manoeuvre sequence considered here, involved slew rate induced star tracker dropout. Since the filter presented as part of this thesis work is a relative calibration filter; in the event of star tracker loss, all the calibration information is lost. Once the star tracker is acquired again, the system requires re-calibration. As a consequence, it is recommended to utilise two separate filters 1. Utilise $18/19$ state calibration filter to calibrate for the calibration states 2. Utilise the calibration information in combination with the regular $6/7$ state attitude and bias estimator, for nominal mission esp. during and after the agile manoeuvre sequence. Since the star tracker dropout was not observed during the initial steady state pointing, non-harmonic sinusoidal manoeuvre, and pre-ground target tracking manoeuvre, 1σ AKE performance of the best performing sensor configuration for these manoeuvre phases can still be considered: 1. Inertial pointing with zero angular rate $[0s, 3600s)$: 2 ST, 1 HPTAG $[13.03, 37.60, 36.31]$ arcsec. 2.a. Slow non-harmonic sinusoidal calibration manoeuvre $[3600s, 10800s)$: 2ST, 1 HPTAG $[29.14, 60.15, 37.16]$ arcsec. 2.b. Fast non-harmonic sinusoidal calibration manoeuvre $[3600s, 10800s)$: 2 ST, 1 HPTAG $[30.91, 29.65, 23.52]$ arcsec. 3. Pre-ground target tracking manoeuvre, post slow calibration maneouvre$[10800s, 13000s)$: 2 ST, 3 MPSAG $[55.25, 57.62, 36.24]$ arcsec. A detailed overview was presented in Table 6.7.

Calibration parameter estimation performance with USQUE based calibration filter

- How is the calibration filter parameter estimation and convergence performance impacted by degraded MEMS rate gyros?

- How do calibration manoeuvres impact the convergence of calibration parameters?

Before we make concluding remarks regarding the above two questions, we need to ask one further sub-question

- How well can the calibration filter, calibrate for gyro-stellar bias, misalignment and scale factors?

It was observed that the calibration filter is capable of estimating gyro bias, and star tracker misalignment appropriately. However, when it comes to gyro misalignment and scale factor, the synthesised calibration filter performed poorly. This can be demonstrated by considering the final $100s$ time window of slow calibration manoeuvre $[10, 700s, 10, 800s]$. For 2 ST and 3 MPSAG, the absolute 1σ calibration state estimation errors were: 1. Bias $[\beta_x, \beta_y, \beta_z]$: $[24.79, 26.56, 37.19]$ arcsec/s. 2. ST MA $[\zeta_x, \zeta_y, \zeta_z]$: $[37.55, 15.99, 39.73]$ arcsec. 3. Gyro MA $[\xi_x, \xi_y, \xi_z]$: $[0.76, 0.78, 0.08]$ rad. 4. Gyro ASF $[\mu_x, \mu_y, \mu_z]$: $[12.30, 4.65, 0.68]$. 5. Gyro SSF $[\lambda_x, \lambda_y, \lambda_z]$: $[12.79, 3.88, 0.47]$.

A preliminary root cause analysis was conducted in this regard in Chapter 4.8.2. For slow calibration manoeuvre readout with HPTAG subsampled at 5Hz, worst case absolute attitude rate error of 6 arcsec/s was observed, while for fast manoeuvre this was observed to be 17.1 arcsec/s. This error introduced by virtue of MA and SF, is significantly lower than the gyro noise bound of around 60 arcsec/s. Similarly, the star tracker sensor output has a worst case noise bound of 200 arcsec on the roll axis, and 20 arcsec on the pitch and yaw axis. This might be a contributing factor as to why gyro bias is estimated appropriately, but gyro misalignment and scale factor is not. Comparing this with literature (Lai et al., 2003), where the gyros were simulated with SSF of 500 ppm, and ASF of 100 ppm, and MA of $\delta_{xz} = \delta_{xy} = \delta_{yx} = 0$, $\delta_{zx} = 400$ arcsec, $\delta_{zy} = 300$ arcsec, $\delta_{yz} = 200$ arcsec and ST MA of 20 arcsec on each axis; one star tracker was allocated with an accuracy of 5 arcsec/axis, payload (which can be seen as a second ST in this case) was allocated with an accuracy of 0.5 arcsec/axis. While the gyro RRW was simulated with $1.3036 \times 10^{-3} \mu$rad/s$^{3/2}$, and ARW with 1.45444μrad/s$^{1/2}$. The thesis work presented here, considers ST 1σ accuracy of 10 arcsec along cross axis, and 66.67 arcsec along boresight. Consequently, MPSAG gyro considered RRW of 1.46×10^{-6} rad/s$^{3/2}$, and ARW of 1.16×10^{-4} rad/s$^{1/2}$. Similarly, HPTAG gyro considered RRW of 4.1985×10^{-8} rad/s$^{3/2}$, and ARW of 4.36×10^{-5} rad/s$^{1/2}$. Both gyro-stellar sensors considered here have a significantly higher noise floor. Thereby, it is recommended, to evaluate the calibration performance under reduced gyro-stellar noise conditions, to concretely localise whether this is indeed the source of this error. Alternatively, one might be tempted to increase the gyro-stellar misalignment instead to evaluate this hypothesis. The filter synthesised here relies on the assumption that the gyro-stellar MA and SF are considerably small. The impact of linearisation assumption made by the filter, has a considerable impact on the calibration state reconstruction accuracy as outlined in Chapter 4.7.4. As a consequence this approach is not recommended to investigate the convergence of gyro calibration parameters.

A better gyro and more persistently excited calibration manoeuvre was observed to improve the calibration parameter estimation and convergence performance. For the final 100s of faster calibration manoeuvre with 1 HPTAG, and 2 ST the absolute 1σ calibration state estimation errors improved significantly:1. Bias $[\beta_x, \beta_y, \beta_z]$: $[0.59, 0.48, 0.41]$ arcsec/s. 2. ST MA $[\zeta_x, \zeta_y, \zeta_z]$: $[3.47, 1.96, 2.73]$ arcsec. 3. Gyro MA $[\xi_x, \xi_y, \xi_z]$: $[0.28, 0.63, 0.07]$ rad. Similar to the slow calibration manoeuvre with higher gyro noise, ASF and SSF were not observed to converge.

Further Recommendations for Future Developments

This thesis work only considered, one misaligned star tracker which demonstrated to have a considerable impact on the attitude knowledge acquisition performance of the NanoSat. In practice both of the star trackers have mis-alignments, which are unknown. The filter states can simply be expanded with the misalignments associated with the second star tracker, without the loss of observability of other calibration parameters, as derived in Chapter 5.2. However, care must be taken in interpreting the filter output. The discarded rotational misalignment must be moved to the star tracker coordinate frame, and then should be subtracted from the star tracker misalignment as indicated in (Pittelkau, 2004) before comparing against the filter output.

Though it was concluded earlier, that gyro MA and SF have minimal impact on the filter output when compared against ST MA; it is still recommended to calibrate for SF. SF directly indicates gyro performance degradation, appropriate identification and tracking of which can facilitate early fault detection of gyros. For n independent uncorrelated homogeneous sensors characterised by noise σ, the noise behaviour can be improved by a factor of $\frac{\sigma}{\sqrt{n}}$ when averaged together. It was further demonstrated with Table 3.8, that with nine MPSAG (three per sense axis), performances similar to HPTAG can be achieved. This is not only attractive from a fault tolerance and risk mitigation standpoint, but it further leads to an overall cost reduction by a factor of ≈ 4.5. As a consequence 9 MPSAG cluster discussed as part of configuration 1, earlier in Chapter 3.3.4 should be considered for future developments. Since the impact of gyro misalignment and scale factor was observed to be minimal; it is uncertain whether calibrating for each of the gyro is a better option, or averaged virtual gyro output fed directly to the $6/7$ state USQUE filter(excluding misalignment and scale factor parameter estimation) would lead to overall improvement in the mission performance. This requires further analysis. Furthermore, in case of calibrating for n>6 gyro sense axis, the significance of null-space measurement update on the filter output performance, as outlined in (Pittelkau, 2005b) should be explored.

Often times the computational burden introduced by UKF, is used as an argument to opt for filter variants like extended or multiplicative extended Kalman filter. Lighter alternatives of UKF, for instance, single propogated UKF in (Biswas et al., 2018), have demonstrated equal robustness, faster convergence, and solution update rate, when applied for $6/7$ state filtering processes on CubeSats. These lighter alternatives are worth investigating for application to calibration filters. Since MEMS gyros introduce significantly more noise compared to larger class of satellite gyros, (Yoon et al., 2017) investigated a gyro-less method for attitude estimation and filter parameter calibration. In doing so the model replacement mode utilised here, where rotational dynamics are replaced directly by gyro angular rate output, is replaced with a differential form of the rigid-body rotational dynamics. Such that the body rate and the other attitude parameters can be updated directly by attitude measurements such that the gyro reading is not required. This approach is worth investigating, to include better attitude rate inputs based on star tracker output and rotational dynamics information, when the star tracker is available. Furthermore, extending the filter presented as part of the thesis, with additional filter states e.g. reaction wheel MoI, misalignment, NanoSat MoI, and reaction wheel speed by virtue of hall sensors, as captured earlier with the schematic in Figure 1.2, has the potential of improving the overall precision tracking performance of NanoSats. With the knowledge of these extended calibration parameters, uncertainties in the flight controller end can be reduced further, leading to overall improvement in precision tracking under agile conditions.

This page is intentionally left blank.

Bibliography

Asmar, S. W. and Matousek, S., "Mars Cube One (MarCO) Shifting the Paradigm in Relay Deep Space Operation," in *SpaceOps 2016 Conference*. American Institute of Aeronautics and Astronautics, May 2016.

Bailke, B., "High fidelity mathematical modeling of reaction wheel performance," *Advances in the Astronomical Sciences*, vol. 98, pp. 483–496, 1998. [Online]. Available: https://www.tib.eu/en/search/id/BLCP%3ACN026570298/High-Fidelity-Mathematical-Modeling-of-Reaction/

Bandyopadhyay, S., Chung, S.-J., and Hadaegh, F. Y., "Attitude control and stabilization of spacecraft with a captured asteroid," *AIAA Guidance, Navigation, and Control Conference.*, January 2015. [Online]. Available: https://authors.library.caltech.edu/72458/1/AsteroidAIAAPaperv17.pdf

Bayard, D. S., "High-precision three-axis pointing and control," *Jet Propulsion Laboratory, California Institute of Technology, Pasadena, CA, USA.*, December 2010. [Online]. Available: https://onlinelibrary.wiley.com/doi/10.1002/9780470686652.eae300

Biswas, S. K., Southwell, B., and Dempster, A. G., "Performance analysis of fast unscented kalman filters for attitude determination," *IFAC-PapersOnLine*, vol. 51, no. 1, pp. 697–701, 2018. [Online]. Available: https://doi.org/10.1016/j.ifacol.2018.05.117

Blanco, J.-L., "A tutorial on SE(3) transformation parameterizations and on-manifold optimization," Universidad de Málaga, Tech. Rep., 2013, citeseerx.ist.psu.edu/viewdoc/download?doi=10.1.1.468.5407&rep=rep1&type=pdf.

Bond, C., "Notes on "L" (Optimal) Filters," Tech. Rep., 2011, http://www.crbond.com/papers/lopt.pdf.

Cahoy, K., "Laser Communication with CubeSats," Massachusetts Institute of Technology. Space Telecommunications, Astronomy and Radiation (STAR) Laboratory. Presentation at Boston photonics., 2018, last visited 15/08/2019. [Online]. Available: http://www.bostonphotonics.org/files/seminars/KCahoy-2018.pdf

Chaturvedi, N. A., Sanyal, A. K., and McClamroch, N. H., "Rigid body attitude control using rotation matrices for continuous singularity free control laws," *IEEE control systems magazine*, pp. 34–36, June 2011. [Online]. Available: http://dx.doi.org/10.1109/MCS.2011.940459

Chen, X., Steyn, W., and Hashida, Y., "Ground-target tracking control of earth-pointing satellites," in *AIAA Guidance, Navigation, and Control Conference and Exhibit*. American Institute of Aeronautics and Astronautics, Aug. 2000. [Online]. Available: https://doi.org/10.2514/6.2000-4547

——, "Ground-target tracking control of earth-pointing satellites," in *AIAA Guidance, Navigation, and Control Conference and Exhibit*. American Institute of Aeronautics and Astronautics, Aug. 2000. [Online]. Available: https://doi.org/10.2514/6.2000-4547

Chen, Y., Vinagre, B. M., and Podlubny, I., "Using continued fraction expansion to discretize fractional order derivatives ," 2003.

Chu, Q., "TU Delft Course, AE4313, Spacecraft Attitude Dynamics and Control." 2018.

Cirillo, F., Winkler, S., Ott, T., Wiedermann, G., and Wilhelm, R., "Reaction wheel based aocs for high pointing accuracy and stability," *67th International Astronautical Congress(IAC)*, September 2016. [Online]. Available: https://www.researchgate.net/publication/308903298_Reaction-Wheels_Based_AOCS_For_High-Pointing_Accuracy_And_Stability_using_the_Euclid_Mission_as_Study-Case

Crassidis, J. L. and Markley, F. L., "Unscented filtering for spacecraft attitude estimation," *Journal of Guidance, Control, and Dynamics*, vol. 26, no. 4, pp. 536–542, July - August 2003. [Online]. Available: http://www.malcolmdshuster.com/Pub_1993h_J_Repsurv_scan.pdf

Diebel, J., "Representing Attitude: Euler Angles, Unit Quaternions, and Rotation Vectors," October 2006. [Online]. Available: https://www.astro.rug.nl/software/kapteyn-beta/_downloads/attitude.pdf

DoD WGS84, "World Geodetic System 1984 - Earth Centered, Earth Fixed (ECEF)," Local Geodetic Systems, NIMA TR8350.2, Third Edition, Amendment 1, 01 2000. [Online]. Available: https://web.archive.org/web/20110718215214/http://metadata.dod.mil/mdr/ns/GSIP/crs/WGS84C_3D

Engelen, S., "CTO at Hyperion Technologies B.V." July 2019, Personal Communication.

——, "Data collected at Hyperion Technologies B.V." February 2020.

——, "Hyperion Technologies online product portfolio and data sheets," 2020, Online, Last visited 31/01/2020, https://hyperiontechnologies.nl/products/ .

Goldstein, H., *Classical Mechanics - 2nd edition*. Addison-Wesley Series in Physics, 1980.

Grewal, M. S., Weill, L. R., and Andrews, A. P., *Global Positioning Systems, Inertial Navigation, and Integration*. John Wiley & Sons, Inc., Jan. 2007. [Online]. Available: https://doi.org/10.1002/0470099720

Hegel, D., "Blue Canyon Technologies Presentation at NASA Goddard Space Flight Center," 3rd Goddard Planetary CubeSat Symposium. Goddard Planetary CubeSat Science Institute (PCSI). Day 2, Subsystems-II., 2018, last visited 03/08/2019. [Online]. Available: https://cubesats.gsfc.nasa.gov/symposiums/2018/presentations/Day2/1115_Hegel.pdf

IEEE Std 647-2006, "IEEE Standard Specification Format Guide and Test Procedure for Single Axis Laser Gyros," Gyro and Accelerometer Panel of the IEEE Aerospace and Electronic Systems Society. Institute of Electrical and Electronics Engineers., Tech. Rep., 2006.

IEEE Std 952-1997, "Ieee standard specification format guide and test procedure for single axis interferometric fiber optic gyros," Gyro and Accelerometer Panel of the IEEE Aerospace and Electronic Systems Society. Institute of Electrical and Electronics Engineers., Tech. Rep., 2008.

Kasdin, N., "Discrete simulation of colored noise and stochastic processes and $1/f^\alpha$ power law noise generation," *Proceedings of the IEEE*, vol. 83, no. 5, pp. 802–827, May 1995. [Online]. Available: https://doi.org/10.1109/5.381848

Lai, K.-L., Crassidis, J., and Harman, R., "In-space spacecraft alignment calibration using the unscented filter," in *AIAA Guidance, Navigation, and Control Conference and Exhibit*. American Institute of Aeronautics and Astronautics, Aug. 2003. [Online]. Available: https://doi.org/10.2514/6.2003-5563

Lam, Q. M. and Crassidis, J. L., "Precision attitude determination using a multiple model adaptive estimation scheme," in *2007 IEEE Aerospace Conference*, 2007, pp. 1–20.

Lam, Q., Stamatakos, N., Woodruff, C., and Ashton, S., "Gyro modeling and estimation of its random noise sources," in *AIAA Guidance, Navigation, and Control Conference and Exhibit*. American Institute of Aeronautics and Astronautics, Aug. 2003. [Online]. Available: https://doi.org/10.2514/6.2003-5562

Lam, Q. M., Thomas Wilson, J., Contillo, R., and Buck, D., "Enhancing MEMS sensors accuracy via random noise characterization and calibration," in *Sensors, and Command, Control, Communications, and Intelligence (C3I) Technologies for Homeland Security and Homeland Defense III*, Carapezza, E. M., Ed. SPIE, Sep. 2004. [Online]. Available: https://doi.org/10.1117/12.538257

Magner, R. D. and Zee, D. R. E., "Extending Target Tracking Capabilities through Trajectory and Momentum Setpoint Optimization," *32nd Annual AIAA/USU Conference on Small Satellites*, 2018. [Online]. Available: https://digitalcommons.usu.edu/cgi/viewcontent.cgi?article=4112&context=smallsat

Markley, F. L., "Attitude error representations for kalman filtering," *Journal of Guidance, Control, and Dynamics*, vol. 26, no. 2, pp. 311–317, Mar. 2003. [Online]. Available: https://doi.org/10.2514/2.5048

Markley, F. L. and Crassidis, J. L., *Fundamentals of Spacecraft Attitude Determination and Control*. Springer - Space Technology Library, 2014, dOI: 10.1007/978-1-4939-0802-8.

Marlow, W. A. N. and Cahoy, P. K. L., "Improving Attitude Determination and Control of Resource-constrained CubeSats Using Unscented Kalman Filtering," Master Thesis, Aeronautics and Astronautics, Massachusetts Institute of Technology, June 2016.

Mazzini, L., *Flexible Spacecraft Dynamics, Control and Guidance.* Springer, 2016.

Meeus, J., *Astronomical Algorithms, 2nd edition*. Willmann Bell Inc., 1998.

Montenbruck, O., Gill, E., and Terzibaschian, T., "Note on the BIRD ACS Reference Frames, DLR-GSOC TN 00-01," 05 2000. [Online]. Available: https://web.archive.org/web/20110718231431/http://www.weblab.dlr.de/rbrt/pdf/TN_0001.pdf

Pittelkau, M., "RIMU misalignment vector decomposition," in *AIAA/AAS Astrodynamics Specialist Conference and Exhibit*. American Institute of Aeronautics and Astronautics, Aug. 2004. [Online]. Available: https://doi.org/10.2514/6.2004-4856

——, "Attitude determination kalman filter with a 1/f flicker noise gyro model," *26th International Technical Meeting of the Satellite Division of the Institute of Navigation, ION GNSS 2013*, vol. 3, pp. 2143–2160, 01 2013.

——, "Observability and calibration of a redundant inertial measurement unit (rimu)," *Advances in Astronautical Sciences/American Institute of Aeronautics and Astronautics, Astrodynamics Specialist Conference*, vol. 120, pp. 71–84, 01 2005.

——, "Survey of Calibration Algorithms for Spacecraft Attitude Sensors and Gyros," *Advances in Astronautical Sciences/American Institute of Aeronautics and Astronautics, Astrodynamics Specialist Conference*, vol. 129, pp. 651–705, 08 2007.

Pittelkau, M. E., *Sensors for Attitude Determination*. Wiley Online Library, 2010. [Online]. Available: https://onlinelibrary.wiley.com/doi/abs/10.1002/9780470686652.eae297

——, "Calibration and attitude determination with redundant inertial measurement units," *Journal of Guidance, Control, and Dynamics*, vol. 28, no. 4, pp. 743–752, Jul. 2005. [Online]. Available: https://doi.org/10.2514/1.7040

——, "Everything is relative in spacecraft system alignment calibration," *Journal of Spacecraft and Rockets*, vol. 39, no. 3, pp. 460–466, May 2002. [Online]. Available: https://doi.org/10.2514/2.3830

——, "Kalman filtering for spacecraft system alignment calibration," *Journal of Guidance, Control, and Dynamics*, vol. 24, no. 6, pp. 1187–1195, Nov. 2001. [Online]. Available: https://doi.org/10.2514/2.4834

Prof. Olivier de Weck, "MIT open courseware, 16.842, Fundamentals of Systems Engineering." 2009, last visited 18/11/2020. [Online]. Available: https://dspace.mit.edu/bitstream/handle/1721.1/103819/16-842-fall-2009/contents/index.htm

Robinson, B. S., Boroson, D. M., Schieler, C. M., Khatri, F. I., Guldner, O., Constantine, S., Burnside, J. W., Hakimi, F. Q., Bilyeu, B. C., Garg, A., Riesing, K., Chang, J., Brown, J., and Cornwell, D., "NASA's Terabyte Infrared Delivery (TBIRD) Program: Large-Volume Data Transfer from LEO," in *Free-Space Laser Communication and Atmospheric Propagation*. MIT Lincoln Laboratory. 33rd Small Satellite Conference, AIAA/ Utah State University, Feb. 2019. [Online]. Available: https://digitalcommons.usu.edu/cgi/viewcontent.cgi?article=4406&context=smallsat

Rose, T. S., Rowen, D. W., LaLumondiere, S., Werner, N. I., Linares, R., Faler, A., Wicker, J., Coffman, C. M., Maul, G. A., Chien, D. H., Utter, A., Welle, R. P., and Janson, S. W., "Optical communications downlink from a 1.5u cubesat: OCSD program," in *International Conference on Space Optics — ICSO 2018*, Karafolas, N., Sodnik, Z., and Cugny, B., Eds. SPIE, Jul. 2019. [Online]. Available: https://doi.org/10.1117/12.2535938

Saathof, R., Crowcombe, W., Kuiper, S., van der Valk, N., Pettazzi, F., de Lange, D., Kerkhof, P., van Riel, M., de Man, H., Truyens, N., and Ferrario, I., "Optical satellite communication space terminal technology at TNO," in *International Conference on Space Optics — ICSO 2018*, Karafolas, N., Sodnik, Z., and Cugny, B., Eds. SPIE, Jul. 2019. [Online]. Available: https://doi.org/10.1117/12.2535939

Sarda, K., Grant, C., Chaumont, M., Choi, S. Y., Johnston-Lemke, B., and Zee, R. R., "On-orbit performance of the bright target explorer (brite) nanosatellite astronomy constellation," 2014. [Online]. Available: https://bit.ly/2lxFxHu

Schaub, H. and Junkins, J., *Analytical Mechanics of Space Systems*, 2nd ed., ser. Education Series. American Institute of Aeronautics and Astronautics, 2002.

Shields, J., Pong, C., Lo, K., Jones, L., Mohan, S., Marom, C., McKinley, I., Wilson, W., and Andrade, L., "Characterization of cubesat reaction wheel assemblies," *Journal of Small Satellites*, vol. 06, no. 1, pp. 565–580, 2017.

Shoemake, K., "Quaternions." [Online]. Available: http://www.cs.ucr.edu/~vbz/resources/quatut.pdf

Shuster, M. D., "A survey of attitude representations," *The journal of astronauatical sciences*, pp. 439–517, October-December 1993. [Online]. Available: http://www.malcolmdshuster.com/Pub_1993h_J_Repsurv_scan.pdf

Sidi, M. J., *Spacecraft Dynamics and Control: A Practical Engineering Approach*. Cambridge University Press, 1997.

Smith, M. W., Donner, A., Knapp, M., Pong, C. M., Smith, C., Luu, J., Pasquale, P. D., Jr., R. L. B., Campuzano, B., Loveland, J., Colley, C., Babuscia, A., White, M., Krajewski, J., and Saeger, S., "On-orbit results and lessons learned from the asteria space telescope mission," *Jet Propulsion Laboratory, California Institute of Technology. Massachusetts Institute of Technology.*, 2018. [Online]. Available: https://digitalcommons.usu.edu/smallsat/2018/all2018/255/

Tanelli, S., Peral, E., Imken, T., Statham, S., Sauder, J., Price, D., Chahat, N., Joshi, S. S., and Williams, A., "RainCube, the First Spaceborne Precipitation Radar in a 6U CubeSat: From Concept to Mission," American Metrological Society 99th Annual Meeting, January 2019, last visited 12/08/2019. [Online]. Available: https://ams.confex.com/ams/2019Annual/webprogram/Paper355100.html

Tapley, B. D., Watkins, M. M., Ries, J. C., Davis, G. W., Eanes, R. J., Poole, S. R., Rim, H. J., Schutz, B. E., Shum, C. K., Nerem, R. S., Lerch, F. J., Marshall, J. A., Klosko, S. M., Pavlis, N. K., and Williamson, R. G., "The joint gravity model," *Journal of Geophysical Research*, vol. 101, pp. 28 029–28 049, 1996.

Trawny, N. and Roumeliotis, S. I., "Indirect kalman filter for 3d attitude estimation," MARS LAB: Multiple Autonomous Robotic Systems Laboratory. Department of Computer Science & Engineering, University of Minnesota., Tech. Rep., 2005.

Vallado, D. A., *Fundamentals of Astrodynamics and Applications - 4th edition*. Space Technology Library, 2013.

Verhaegen, M. and Verdult, V., *Filtering and System Identification: A Least Squares Approach*. Cambridge University Press, 2007.

Vinagre, B. M., Podlubny, I., and Feliu, V., "Some approximations of fractional order operators used in control theory and applications," *Journal of Fractional Calculus and Applied Analysis*, pp. 231–248, 2000.

Wertz, J. R., *Mission Geometry Orbit and Constellation Design and Management*. Microcosm Press, 2001, chapter 5 and Appendix C.

Wie, B., *Space Vehicle Dynamics and Control* . AIAA Education Series, 1998.

Winkler, S., "Observability of star tracker / gyro based attitude estimation considering time-variant sensor misalignment," in *Advances in Aerospace Guidance, Navigation and Control*. Springer Berlin Heidelberg, 2011, pp. 373–384. [Online]. Available: https://doi.org/10.1007/978-3-642-19817-5_29

Xue, L., Jiang, C.-Y., Chang, H.-L., Yang, Y., Qin, W., and Yuan, W.-Z., "A novel kalman filter for combining outputs of MEMS gyroscope array," *Journal of the International Measurement Confederation*, vol. 45, no. 4, pp. 745–754, May 2012. [Online]. Available: https://doi.org/10.1016/j.measurement.2011.12.016

Yoon, H., Riesing, K. M., and Cahoy, K., "Kalman filtering for attitude and parameter estimation of nanosatellites without gyroscopes," *Journal of Guidance, Control, and Dynamics*, vol. 40, no. 9, pp. 2272–2288, Sep. 2017. [Online]. Available: https://doi.org/10.2514/1.g002649

Ziemer, R. E., Tranter, W. H., and Fannin, D. R., *Instrumentation and Signals Continuous and Discrete, Fourth Edition.* Pearson Publishing, 2011.

Gyro Noise Simulink Block Overview

Figure A.1 demonstrates the gyro model utilised to readout the spacecraft body rates. Noise PSD of the output of this gyro model, was verified against the noise PSD of the MEMS gyro obtained via Allan-Variance analysis.
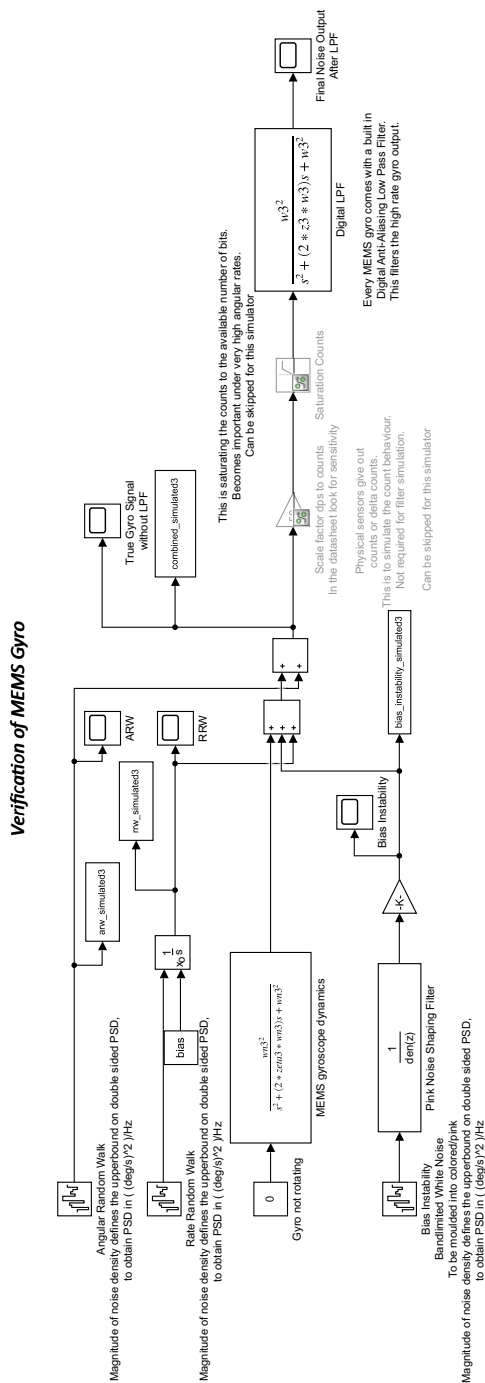
Figure A.1: *Gyro model used in Simulink to capture the MEMS gyro noise characteristics.*

This page is intentionally left blank.

Power Spectral Density

Frequency domain behavior of stationary or wide sense stationary processes are often captured with the aid of Power Spectral Densities (PSD). A requirement specified by its variance σ^2 can have several PSD magnitude shapes! Hindering the distinction of system error behaviour for low-frequency and high-frequency components. Physically power of a signal is equivalent to the area underneath the even double-sided PSD function. The following will provide a brief overview of the derivation of PSD:

Let, a continuous stationary random process be denoted as X(t). The autocorrelation function can be written as:

$$R_X(\tau) = E[X(t)X(t+\tau)] = \sigma_{XX}(\tau) + \mu_X^2 = \rho_{XX}(\tau)\sigma_X^2 + \mu_X^2 \tag{B.1}$$

Here, $\rho_{XX}(\tau)$ is a correlation coefficient, its value is always between $+1$ and -1, that is, $|\rho_{XX}(\tau)| \leq 1$. This makes the auto correlation function symmetric $R_X(\tau) = R_X(-\tau)$. μ_X is the mean of the process denoted as:

$$\mu_X(t) = E[X(t)] = \int_{-\infty}^{+\infty} x f_{X(t)}(x)dx \tag{B.2}$$

The variance at time t is denoted by

$$\sigma_X^2(t) = E\left[\{X(t) - \mu_X(t)\}^2\right] = \int_{-\infty}^{+\infty} [x - \mu_X(t)]^2 f_{X(t)}(x)dx. \tag{B.3}$$

And, $\sigma_{XX}(\tau)$ is the autocovariance function defined as:

$$\sigma_{XX}(t_1, t_2) = E\left[\{X(t_1) - \mu_X(t_1)\}\{X(t_2) - \mu_X(t_2)\}\right]. \tag{B.4}$$

The autocorrelation coefficient function is denoted by:

$$\rho_{XX}(t_1, t_2) = \frac{\sigma_{XX}(t_1, t_2)}{\sigma_X(t_1)\sigma_X(t_2)} \tag{B.5}$$

When $t_1 = t_2 = t$, $\sigma_{XX}(t,t) = E\left[\{X(t) - \mu_X(t)\}^2\right] = \sigma_X^2(t)$. And $\lim_{\tau \to \infty} R_X(\tau) = \mu_X^2$. Now, let X(t) and Y(t) be two different random processes. The cross correlation function is defined as follows. If both processes are stationary, the cross correlation function depends only upon the time lag between t_1 and t_2, $\tau = t_2 - t_1$:

$$R_{XY}(t_1, t_2) = E[X(t_1)Y(t_2)]$$
$$R_{XY}(\tau) = E[X(t)Y(t+\tau)] \tag{B.6}$$
$$R_{YX}(\tau) = E[Y(t)X(t+\tau)]$$

The two cross relation functions are not equal, for stationary processes they are reflections of one another about the origin:

$$R_{XY}(\tau) = E[X(t)Y(t+\tau)] = E[X(s-\tau)Y(s)] = E[Y(s)X(s-\tau)]$$
$$= R_{YX}(-\tau) \tag{B.7}$$

A very important Fourier transform relation between auto-correlation and double sided spectral density of a stationary random process is defined by the Wiener-Kinchin theorem as:

$$S_X(\omega) = \frac{1}{2\pi} \int_{-\infty}^{\infty} R_X(\tau)e^{-i\omega\tau}d\tau$$
$$R_X(\tau) = \int_{-\infty}^{\infty} S_X(\omega)e^{+i\omega\tau}d\omega \tag{B.8}$$

$S_X(\omega) = S_X(-\omega)$, as the auto-correlation function of real-valued stationary random process X(t) is real and symmetric, and Fourier tansform of such a function must be real valued and symmetric. Two sided power spectral density in the frequency domain can be expressed as:

$$S_X(f) = 2\pi S_X(\omega) \tag{B.9}$$

Discarding the negative frequencies, the density is multiplied by 2 to compensate and represent the one sided PSD in rad/s as:

$$G_x(\omega) = \begin{cases} 2S_x(\omega) & \omega \geq 0 \\ 0 & \omega < 0 \end{cases} \tag{B.10}$$

In frequency domain, one sided PSD is often called engineering spectral density. This can be expressed as:

$$W_X(f) = \begin{cases} 4\pi S_X(\omega) & \omega, f \geq 0 \\ 0 & \omega, f < 0 \end{cases} \tag{B.11}$$

Relation between cross spectral densities and cross correlation functions are defined as:

$$S_{XY}(\omega) = \frac{1}{2\pi} \int_{-\infty}^{\infty} R_{XY}(\tau)e^{-i\omega\tau}d\tau \tag{B.12a}$$

$$S_{YX}(\omega) = \frac{1}{2\pi} \int_{-\infty}^{\infty} R_{YX}(\tau)e^{-i\omega\tau}d\tau \tag{B.12b}$$

$$R_{XY}(\tau) = \int_{-\infty}^{\infty} S_{XY}(\omega)e^{i\omega\tau}d\omega \tag{B.13a}$$

$$R_{YX}(\tau) = \int_{-\infty}^{\infty} S_{YX}(\omega)e^{i\omega\tau}d\omega \tag{B.13b}$$

$S_{XY}(\omega) = S_{YX}(-\omega)$. If Z(t) is the sum of two processes X(t) and Y(t), the spectral densities can be expressed as:

$$S_{ZX}(\omega) = S_X(\omega) + S_{YX}(\omega) \tag{B.14a}$$

$$S_Z(\omega) = S_X(\omega) + S_{XY}(\omega) + S_{YX}(\omega) + S_Y(\omega) \tag{B.14b}$$

If X(t) and Y(t) are uncorrelated, these reduce to:

$$S_{ZX}(\tau) = S_X(\tau) \tag{B.14c}$$

$$S_Z(\omega) = S_X(\omega) + S_Y(\omega) \tag{B.14d}$$

Let x(t) be the response of a SISO system, F(t) the forcing input and h(t) the transfer relation. The corresponding Fourier transforms are denoted as: $X(\omega)$, $H(\omega)$ and $F(\omega)$. PSD of the response $X(\omega)$, can be expressed in terms of the forcing input PSD and the corresponding transfer function $H(\omega)$ as:

$$S_X(\omega) = H(-\omega)H(\omega)S_F(\omega) \tag{B.15}$$

For real $h(t)$, its Fourier transform has Hermitian symmetry (even real part and odd imaginary part), thus:

$$H(-\omega) = H^*(\omega) \tag{B.16}$$

$$S_X(\omega) = |H(\omega)|^2 S_F(\omega) \tag{B.17}$$

The variance of the response may be calculated as the area under the PSD function:

$$\sigma_X^2 = \int_{-\infty}^{\infty} S_X(\omega)d\omega \tag{B.18a}$$

$$\sigma_X^2 = \int_{-\infty}^{\infty} |H(\omega)|^2 S_F(\omega)d\omega \tag{B.18b}$$

The engineering spectral density of the response and the corresponding variance can be expressed as:

$$W_X(f) = |H(f)|^2 W_F(f) \tag{B.19}$$

$$\sigma_X^2 = \int_0^\infty |H(f)|^2 W_F(f) df \tag{B.20}$$

In practice, one does not have access to the time interval defined in the range $-\infty$ to ∞; but rather access to only a finite number of data samples. For a discrete signal x(k), with k = 1, 2, . . ., N the direct Discrete Fourier Transform pair is given by:

$$X_N(\omega_n) = \sum_{k=0}^{N-1} x(k) \mathrm{e}^{-\mathrm{j}\omega_n kT} \tag{B.21}$$

Where, $\omega_n = 2\pi n/(NT)$ radians per second, $n = 0, 1, 2, \ldots, N-1$, and sampling time $T \in \mathbb{R}$. Thus a time sequence of N samples is transformed by the DFT into a sequence of N complex numbers (Verhaegen and Verdult, 2007). The corresponding inverse transform pair of a sequence $X_N(\omega_n)$ with $\omega_n = \frac{2\pi n}{NT}$ and n = 0, 1, 2, . . ., N-1 is given by:

$$x(k) = \frac{1}{N} \sum_{n=0}^{N-1} X_N(\omega_n) \mathrm{e}^{\mathrm{j}\omega_n kT} \tag{B.22}$$

with time k = 0, 1, 2, . . ., N-1 and sampling time $T \in \mathbb{R}$. To derive DFT from continuous-time Fourier transform, the time-sampling interval was taken as T/N = Δt, where N is the total number of samples taken in a T-second interval (time window), and the frequency-sampling interval was taken as 1/T. Thus, both relationships imply periodicity, the first in frequency with period f_s = N/T = 1/ Δt and the second in time with period $T = N\Delta t = N/f_s$. For further details the reader is referred to (Verhaegen and Verdult, 2007, Ziemer et al., 2011).

Sampling the spectrum of a windowed time domain signal implies a periodic extension of the signal. Unless the signal is periodic with an integer number of periods within within the window or unless it smoothly approaches zero at each end of the interval , the resulting discontinuities can generate additional spectral components, leading to a noisy Power Spectral Density. This phenomenon is referred to as spectral leakage. In order to minimise this effect, the data samples are multiplied by non-rectangular windows which approach zero smoothly at the beginning and end of the window. Several window functions are presented in (Ziemer et al., 2011), of which Hamming window is utilised for windowing operation of gyro output. This is chosen to resolve closely space frequency components while minimising leakage from one component to another. The window function for Hamming window w(n) is defined as the following, with n = 0, 1, 2, . . ., N-1:

$$w(n) = 0.54 - 0.46 \cos \frac{2\pi n}{N} \tag{B.23}$$

Kaiser-Bessel window is a good alternative if suppression of leakage is the primary concern, the corresponding window function is defined as:

$$w(n) = \frac{I_0(\pi\alpha\beta)}{I_0(\pi\alpha)} \tag{B.24}$$

Here, $\beta = \sqrt{1 - (\frac{2n+1}{N} - 1)^2}$. n = 0, 1, 2, . . ., N - 1. $I_0(x)$ is the modified Bessel function of order zero. Windowing effectively reduces the variance of the PSD, however it comes at the expense of frequency resolution which is directly related to the number of data-points in the window. Most window functions drop to zero near the window edges, to reduce the negative effect of loss of information due to windowing, overlapping is often conducted.

For implementation purposes, the `[pxx,f] = pwelch (x, window, noverlap,nfft, fs, ...
'onesided','psd')` function from Matlab. This choice was verified against conduct an FFT and later converting it into a single sided PSD. $x$ is the dataset upon which FFT is is conducted. The function input variable `window` defines the number of window segments that should be created out of the dataset, for noise smoothing process. `noverlap` specifies the %-overlap among the windowed segments of dataset. `nfft` defined the number of discrete Fourier transform (DFT) to be utilised in the PSD estimate. The default is the greater of 256 or the next power of 2 greater than the length of the segments. `fs` is the sampling frequency that spans the interval $[0, \mathtt{fs}/2]$ when `nfft` is even, and $[0, \mathtt{fs}/2)$ when `nfft` is odd.

This page is intentionally left blank.

NanoSat Rigid Body Plant and Controller

C.1 | NanoSat Inertia

For a Rigid body 6U (3U × 2U × 1U = a × b × c) NanoSat of mass, m = 6 kg, the inertia can be expressed as:

$$\boldsymbol{J} = \begin{bmatrix} J_{11} & 0 & 0 \\ 0 & J_{22} & 0 \\ 0 & 0 & J_{33} \end{bmatrix} = \begin{bmatrix} \frac{1}{12} \cdot m \cdot (b^2 + c^2) & 0 & 0 \\ 0 & \frac{1}{12} \cdot m \cdot (c^2 + a^2) & 0 \\ 0 & 0 & \frac{1}{12} \cdot m \cdot (a^2 + b^2) \end{bmatrix} \tag{C.1a}$$

$$\boldsymbol{J} = \begin{bmatrix} \frac{1}{12} \cdot 6 \cdot ((0.20)^2 + (0.10)^2) & 0 & 0 \\ 0 & \frac{1}{12} \cdot 6 \cdot ((0.10)^2 + (0.30)^2) & 0 \\ 0 & 0 & \frac{1}{12} \cdot 6 \cdot ((0.30)^2 + (0.20)^2) \end{bmatrix} \tag{C.1b}$$

C.2 | Rigid Body Plant Stability Analysis

This section summarizes an overview of the stability analysis of the plant. Before stability analysis is conducted, the dynamics and kinematics expressions in Euler, presented earlier in Section 4.3.1, are linearized and simplified. Considering only the principal moment of inertia, Euler dynamics can be simplified as:

$$J_{11}\dot{\omega}_1 - (J_{22} - J_{33})\,\omega_2\omega_3 = -3n^2\,(J_{22} - J_{33})\,C_{23}C_{33} \tag{C.2a}$$

$$J_{22}\omega_2 - (J_{33} - J_{11})\,\omega_3\omega_1 = -3n^2\,(J_{33} - J_{11})\,C_{33}C_{13} \tag{C.2b}$$

$$J_{33}\omega_3 - (J_{11} - J_{22})\,\omega_1\omega_2 = -3n^2\,(J_{11} - J_{22})\,C_{13}C_{23} \tag{C.2c}$$

With small angle approximation, $\sin(\theta) \approx \theta$, $\cos(\theta) \approx 1$, $\omega_2 \approx n$, the linearized expressions are:

$$J_{11}\dot{\omega}_1 + (J_{22} - J_{33})\,n\omega_3 = -3n^2\,(J_{22} - J_{33})\,\theta_1 \tag{C.3a}$$

$$J_{22}\dot{\omega}_2 = 3n^2\,(J_{33} - J_{11})\,\theta_2 \tag{C.3b}$$

$$J_{33}\dot{\omega}_3 + (J_{11} - J_{22})\,n\omega_1 = 0 \tag{C.3c}$$

$$\omega_1 = \dot{\theta}_1 - n\theta_3 \tag{C.3d}$$

$$\omega_2 = \dot{\theta}_2 - n \tag{C.3e}$$

$$\omega_3 = \dot{\theta}_3 + n\theta_1 \tag{C.3f}$$

The linearised expressions can now be analysed for stability. First the pitch axis stability criterion is discussed, and later the roll and yaw axes stability criterion is discussed(Chu, 2018). The kinematics and dynamics can be combined to obtain the following expressions:

$$J_{11}\ddot{\theta}_1 - n\,(J_{11} - J_{22} + J_{33})\,\dot{\theta}_3 + 4n^2\,(J_{22} - J_{33})\,\theta_1 = 0 \tag{C.4a}$$

$$J_{22}\ddot{\theta}_2 + 3n^2\,(J_{11} - J_{33})\,\theta_2 = 0 \tag{C.4b}$$

$$J_{33}\ddot{\theta}_3 + n\,(J_{11} - J_{22} + J_{33})\,\dot{\theta}_1 + n^2\,(J_{22} - J_{11})\,\theta_3 = 0 \tag{C.4c}$$

It can be observed that the pitch axis is independent of the roll and yaw axes. Corresponding characteristic equation for the pitch axis after Laplace transform is:

$$s^2 + \frac{3n^2\,(J_{11} - J_{33})}{J_{22}} = 0 \tag{C.5}$$

The systems is Lyapunov stable, if $J_{11} > J_{33}$, the characteristic roots imaginary and Lyapunov stable. Otherwise the characteristic roots are positive real and unstable. This leads to the necessary and sufficient condition for pitch axis stability:

$$J_{11} > J_{33} \tag{C.6}$$

The roll and yaw stability criterion can now be derived:

$$\ddot{\theta}_1 + (k_1 - 1)\, n\dot{\theta}_3 + 4n^2 k_1 \theta_1 = 0, \quad k_1 = \frac{J_{22} - J_{33}}{J_{11}} \tag{C.7a}$$

$$\ddot{\theta}_3 + (1 - k_3)\, n\dot{\theta}_1 + n^2 k_3 \theta_3 = 0, \quad k_3 = \frac{J_{22} - J_{11}}{J_{33}} \tag{C.7b}$$

Laplace transform of the above expression results in:

$$s^2 \theta_1 + (k_1 - 1)\, ns\theta_3 + 4n^2 k_1 \theta_1 = 0 \tag{C.8a}$$

$$s^2 \theta_3 + (1 - k_3)\, ns\theta_1 + n^2 k_3 \theta_3 = 0 \tag{C.8b}$$

In matrix notation:

$$\begin{bmatrix} s^2 + 4n^2 k_1 & (k_1 - 1)\, ns \\ (1 - k_3)\, ns & s^2 + n^2 k_3 \end{bmatrix} \begin{bmatrix} \theta_1 \\ \theta_3 \end{bmatrix} = \begin{bmatrix} 0 \\ 0 \end{bmatrix} \tag{C.8c}$$

The corresponding characteristic equation of the above MIMO system is extracted by the determinant of the matrix:

$$\left(s^2 + 4n^2 k_1\right)\left(s^2 + n^2 k_3\right) - (k_1 - 1)(1 - k_3)\, n^2 s^2 = 0 \tag{C.9a}$$

$$s^4 + (1 + 3k_1 + k_1 k_3)\, n^2 s^2 + 4k_1 k_3 n^4 = 0 \tag{C.9b}$$

For stability, the right hand side of the characteristic equation should be negative:

$$s^2 n^2 = \frac{-(1 + 3k_1 + k_1 k_3) \pm \sqrt{(1 + 3k_1 + k_1 k_3)^2 - 4^2 k_1 k_3}}{2} \tag{C.10a}$$

$$1 + 3k_1 + k_1 k_3 > 0 \tag{C.10b}$$

$$1 + 3k_1 + k_1 k_3 > 0 \tag{C.10c}$$

$$1 + 3k_1 + k_1 k_3 > 4\sqrt{k_1 k_3} \tag{C.10d}$$

$$k_1 k_3 > 0 \tag{C.10e}$$

By definition, physical property of the moment of inertia follows the following definition:

$$J_{11} + J_{22} > J_{33} \tag{C.11a}$$

$$J_{22} + J_{33} > J_{11} \tag{C.11b}$$

$$J_{11} + J_{33} > J_{22} \tag{C.11c}$$

This indicates that $|k_1| \leq 1$ and $|k_3| \leq 1$, i.e. bounded by definition.

C.3 | Rigid Body Reference Tracking Controller

Linearised equations of rotational motion presented earlier in Equation (C.3) are expanded with disturbance and control torques, to facilitate the controller synthesis procedure. First a PD controller is synthesized for the pitch axis, and later for yaw and roll axis. The controllers are synthesized in Euler321 with the aid of (Chu, 2018), and later extended to MRP formulation by virtue of small angle relations. In the presence of disturbance and control torque:

$$J_{11}\dot{\omega}_1 + (J_{22} - J_{33})\, n\omega_3 + \dot{H}_{w1} + nH_{w1} = -3n^2 (J_{22} - J_{33})\, \theta_1 + M_{c1} + M_{d1} \tag{C.12a}$$

$$J_{22}\dot{\omega}_2 + \dot{H}_{w2} = 3n^2 (J_{33} - J_{11})\, \theta_2 + M_{c2} + M_{d2} \tag{C.12b}$$

$$J_{33}\dot{\omega}_3 + (J_{11} - J_{22})\, n\omega_1 + \dot{H}_{w3} - nH_{w1} = M_{c3} + M_{d3} \tag{C.12c}$$

$$\omega_1 = \dot{\theta}_1 - n\theta_3 \tag{C.12d}$$

$$\omega_2 = \dot{\theta}_2 - n \tag{C.12e}$$

$$\omega_3 = \dot{\theta}_3 + n\theta_1 \tag{C.12f}$$

Here, H_w and $\dot{H}_w$ represent the angular momentum and the rate of change of angular momentum of the reaction wheels. The rate of angular velocities can be expanded as follows:

$$\dot{\omega}_1 = \ddot{\theta}_1 - n\dot{\theta}_3 \tag{C.13a}$$

$$\dot{\omega}_2 = \ddot{\theta}_2 \dot{\omega}_3 \tag{C.13b}$$

$$\dot{\omega}_3 = \ddot{\theta}_3 + n\dot{\theta}_1 \tag{C.13c}$$

Utilising the above expressions, the control torque and disturbance moments can be expressed as:

$$M_{c1} + M_{d1} = J_{11}\ddot{\theta}_1 + 4n^2 \left(J_{22} - J_{33}\right)\theta_1 + n\left(J_{22} - J_{33} - J_{11}\right)\dot{\theta}_3 + \dot{H}_{w1} - nH_{w3} \tag{C.14a}$$

$$M_{c2} + M_{d2} = J_{22}\ddot{\theta}_2 + 3n^2 \left(J_{11} - J_{33}\right)\theta_2 + \dot{H}_{w2} \tag{C.14b}$$

$$M_{c3} + M_{d3} = J_{33}\ddot{\theta}_3 + n\left(J_{33} + J_{11} - J_{22}\right)\dot{\theta}_1 + n^2\left(J_{22} - J_{11}\right)\theta_3 + \dot{H}_{w3} + nH_{w1} \tag{C.14c}$$

Now that the equations of motions are simplified in terms of torques, first the pitch axis PD controller is synthesized. In the linearised system, the pitch axis is observed to be uncoupled from the roll and yaw axes. Using this analogy, H_w and $\dot{H}_w$ along other axes are ignored in derivation of the pitch axes controller. The following set of simplified expression can be obtained:

$$a = 4n^2 \left(J_{22} - J_{33}\right); \quad b = -n\left(J_{33} + J_{11} - J_{22}\right); \quad c = n^2\left(J_{22} - J_{11}\right); \quad d = 3n^2\left(J_{11} - J_{33}\right) \tag{C.15a}$$

$$M_{c1} + M_{d1} = J_{11}\ddot{\theta}_1 + (a)\,\theta_1 - (-b)\,\dot{\theta}_3 \tag{C.15b}$$

$$M_{c3} + M_{d3} = J_{33}\ddot{\theta}_3 + (-b)\,\dot{\theta}_1 + (c)\,\theta_3 \tag{C.15c}$$

$$M_{c2} + M_{d2} = J_{22}\ddot{\theta}_2 + d\theta_2 + \dot{H}_{w2} \tag{C.15d}$$

For a circular orbit at 400km, mean motion n = 1.1331559e-03 rad/s , while n^2 = 1.28404e-06 rad/s. The above expressions can be simplified further by eliminating a, b, c, and d. M_c is any other control torque apart from the reaction wheel, for instance magnetorquers. In the case of reaction wheel based control, this can be safely ignored in the the pitch axis control loop. This leads to the following PD law:

$$\dot{H}_{w2} = k_{p2}\theta_2 + k_{d2}\dot{\theta}_2 \tag{C.16}$$

Some I-action is further added to eliminate steady state oscillations. Pitch axis closed loop control system can be expressed as:

$$J_{22}\ddot{\theta}_2 + k_{d2}\dot{\theta}_2 + k_{p2}\theta_2 = M_{d2} \tag{C.17}$$

For disturbance rejection, considering M_d as the maximum bound of disturbance moment that can act on the system, with constant disturbance envelope the above expression can be expressed as:

$$\left(J_{22}s^2 + k_{d2}s + k_{p2}\right)\theta_2(s) = M_{d2}(s) \tag{C.18a}$$

$$M_{d2}(s) = \frac{M_{d20}}{s} \tag{C.18b}$$

Using the final value theorem, the steady state value pitch angle θ_2 can be expressed as:

$$\lim_{t\to\infty} \theta(t) = \lim_{s\to 0} \theta_2(s) \cdot s = \lim_{s\to 0} \frac{M_{d2}(s) \cdot s}{J_{22}s^2 + k_{d2}s + k_{p2}} == \lim_{s\to 0} \frac{M_{d2,0}}{J_{22}s^2 + k_{d2}s + k_{p2}} = \frac{M_{d2,0}}{k_{p2}} \tag{C.19}$$

Utilising the above leads to the following control law with regards to the pitch axis: Proportional gain for pitch axis is simply the maximum expected bound of the disturbance torque acting on the system, divided by the required steady state pointing accuracy.

$$k_{p2} = \frac{M_{d2,0}}{\theta_{ss2y}} \tag{C.20a}$$

For small angles $\theta \approx \sigma$

$$k_{p2} = \frac{M_{d20}}{\sigma_{ss2y}} \tag{C.20b}$$

The D-action is derived by comparing the closed loop pitch axis transfer function with a second order transfer function:

$$H(s) = \frac{\theta_2(s)}{M_{d2}(s)} = \frac{1}{J_{22}s^2 + k_{d2}s + k_{p2}} = \frac{\frac{1}{J_{22}}}{s^2 + \frac{k_{d2}}{J_{22}}s + \frac{k_{p2}}{J_{22}}} = \frac{\frac{1}{J_{22}}}{s^2 + 2\zeta\omega_n s + \omega_n^2} \tag{C.21a}$$

By comparison, the coefficients can be expressed as:

$$\frac{k_{d2}}{J_{22}} = 2\zeta\omega_n; \quad \frac{k_{p2}}{J_{22}} = \omega_n^2; \quad k_{d2} = 2\zeta\omega_n J_{22} = 2\zeta\sqrt{\frac{k_{p2}}{J_{22}}}J_{22} = 2\zeta\sqrt{k_{p2}J_{22}} \tag{C.21b}$$

Here, $\zeta = \sqrt{2}/2$ = 0.707. Similarly, yaw and roll axis can be synthesised. Let the control torque for roll and yaw axis be defined as:

$$M_{c1} = - \left(k_{p1}\theta_1 + k_{d1}\dot{\theta}_1 \right) \tag{C.22a}$$

$$M_{c3} = - \left(k_{p3}\theta_3 + k_{d3}\dot{\theta}_3 \right) \tag{C.22b}$$

Substituting the above into the equations of motions leads to:

$$M_{c1} + M_{d1} = J_{11}\ddot{\theta}_1 + (a)\theta_1 - (-b)\dot{\theta}_3 \tag{C.23a}$$

$$M_{d1} = J_{11}\ddot{\theta}_1 - nH_{w2,0}\theta_1 - H_{w2,0}\dot{\theta}_3 + k_{p1}\theta_1 + k_{d1}\dot{\theta}_1 \tag{C.23b}$$

$$M_{c3} + M_{d3} = J_{33}\ddot{\theta}_3 + (-b)\dot{\theta}_1 + (c)\theta_3 \tag{C.23c}$$

$$M_{d3} = J_{33}\ddot{\theta}_3 + H_{w2,0}\dot{\theta}_1 - nH_{w2,0}\theta_3 + k_{p3}\theta_3 + k_{d3}\dot{\theta}_3 \tag{C.23d}$$

Here, $H_{w2,0}$ illustrates a constant torque acting on the pitch axis:

$$\begin{bmatrix} \theta_1(s) \\ \theta_3(s) \end{bmatrix} = \frac{1}{\Delta(s)} \begin{bmatrix} s^2 + \frac{1}{J_{33}}\left(k_{p3} + k_{d3}s - nH_{w2,0}\right) & s\frac{H_{w2,0}}{J_{11}} \\ -s\frac{H_{w2,0}}{J_{33}} & s^2 + \frac{1}{J_{11}}\left(k_{p1} + k_{d1}s - nH_{w2,0}\right) \end{bmatrix}$$
$$\cdot \begin{bmatrix} \frac{M_{d1}(s)}{J_{11}} \\ \frac{M_{d3}(s)}{J_{33}} \end{bmatrix} \tag{C.23e}$$

Where,

$$\Delta(s)J_{11}J_{33} = s^4 J_{11}J_{33} + s^3\left(k_{d1}J_{33} + k_{d3}J_{11}\right)\dots$$
$$\dots + s^2\left[k_{d1}k_{d3} + H_{w2,0}^2 + J_{33}\left(k_{p1} - nH_{w2,0}\right) + J_{11}\left(k_{p3} - nH_{w2,0}\right)\right]\dots \tag{C.23f}$$
$$\dots + s\left[k_{d3}\left(k_{p1} - nH_{w2,0}\right) + k_{d1}\left(k_{p3} - nH_{w2,0}\right)\right] + k_{p1}k_{p3} + \left(nH_{w2,0}\right)^2 - nH_{w2,0}\left(k_{p1} + k_{p3}\right)$$

For a stable closed loop system the coefficients of characteristic equation needs to be positive. When the reaction wheel pitch axis is operational:

$$H_{w2,0} = -H \ , \quad H > 0 \tag{C.24a}$$

$$\Delta(s)J_{11}J_{33} = s^4 J_{11}J_{33} + s^3\left(k_{d1}J_{33} + k_{d3}J_{11}\right) + s^2\left[k_{d1}k_{d3} + H^2 + J_{33}\left(k_{p1} + nH\right) + J_{11}\left(k_{p3} + nH\right)\right]\dots$$
$$\dots + s\left[k_{d3}\left(k_{p1} + nH\right) + k_{d1}\left(k_{p3} + nH\right)\right] + k_{p1}k_{p3} + \left(nH\right)^2 + nH\left(k_{p1} + k_{p3}\right) \tag{C.24b}$$

Utilising the final value theorem, and steady state pointing accuracy expected of the system:

$$\frac{\theta_{ss1}}{M_{d1}} = \frac{k_{p3} + nH}{k_{p1}k_{p3} + (nH)^2 + nH\left(k_{p1} + k_{p3}\right)} = \theta_{ss1x} \tag{C.25a}$$

$$\frac{\theta_{ss3}}{M_{d3}} = \frac{k_{p1} + nH}{k_{p1}k_{p3} + (nH)^2 + nH\left(k_{p1} + k_{p3}\right)} = \theta_{ss3z} \tag{C.25b}$$

This leads to the roll and yaw axis pitch proportional gains:

$$k_{p1} = \frac{1 - nH\theta_{ss1x}}{\theta_{ss1x}} \tag{C.26a}$$

$$k_{p3} = \frac{1 - nH\theta_{ss3z}}{\theta_{ss3z}} \tag{C.26b}$$

For small angles $\theta \approx \sigma$

$$k_{p1} = \frac{1 - nH\sigma_{ss1x}}{\sigma_{ss1x}} \quad k_{p3} = \frac{1 - nH\sigma_{ss3z}}{\sigma_{ss3z}} \tag{C.26c}$$

In case of no constant torque acting along the pitch axis:

$$k_{p1} = \frac{1}{\theta_{ss1x}} \tag{C.26d}$$

$$k_{p3} = \frac{1}{\theta_{ss3z}} \tag{C.26e}$$

For small angles $\theta \approx \sigma$:

$$k_{p1} = \frac{1}{\sigma_{ss1x}} \tag{C.26f}$$

$$k_{p3} = \frac{1}{\sigma_{ss3z}} \tag{C.26g}$$

Similar to pitch axis D gain, the determinant $\Delta(s)$ can be expressed in terms of second order expression:

$$\Delta(s) = \left(s^2 + 2\zeta_1\omega_{n1}s + \omega_{n1}^2\right)\left(s^2 + 2\zeta_2\omega_{n2}s + \omega_{n2}^2\right) \tag{C.27a}$$

$$\Delta(s) = s^4 + s^3 2\left(\zeta_1\omega_{n1} + \zeta_2\omega_{n2}\right) + s^2\left(\omega_{n1}^2 + \omega_{n2}^2 + 4\zeta_1\zeta_2\omega_{n1}\omega_{n2}\right) + s2\omega_{n1}\omega_{n2}\left(\zeta_1\omega_{n2} + \zeta_2\omega_{n1}\right) + \omega_{n1}^2\omega_{n2}^2 \tag{C.27b}$$

The corresponding D-action for the roll and yaw axis can be expressed as:

$$\frac{k_{d1}J_{33} + k_{d3}J_{11}}{J_{11}J_{33}} = 2\left(\zeta_1\omega_{n1} + \zeta_2\omega_{n2}\right) \tag{C.28a}$$

$$\frac{k_{d1}k_{d3} + H^2 + J_{33}\left(k_{p1} + nH\right) + J_{11}\left(k_{p3} + nH\right)}{J_{11}J_{33}} = \omega_{n1}^2 + \omega_{n2}^2 + 4\zeta_1\zeta_2\omega_{n1}\omega_{n2} \tag{C.28b}$$

$$\frac{k_{d3}\left(k_{p1} + nH\right) + k_{d1}\left(k_{p3} + nH\right)}{J_{11}J_{33}} = 2\omega_{n1}\omega_{n2}\left(\zeta_1\omega_{n2} + \zeta_2\omega_{n1}\right) \tag{C.28c}$$

This leads to the derivative gains presented as follows:

$$k_{d1} = \sqrt{\frac{v - uJ_{11}J_{33}\left(4\zeta^2 - 2\right)}{\frac{J_{11}}{4\xi^2 J_{11}} + \frac{w}{2\zeta^2} + \frac{w^2 J_{11}}{4\zeta^2 J_{33}} - w}} \tag{C.28d}$$

The constants, u,v, and w in the above expressions are:

$$u = \sqrt{\frac{\left[k_{p1}k_{p3} + (nH)^2 + nH\left(k_{p1} + k_{p3}\right)\right]}{J_{11}J_{33}}} \tag{C.28e}$$

$$v = H^2 + J_{33}\left(k_{p1} + nH\right) + J_{11}\left(k_{p3} + nH\right) \tag{C.28f}$$

$$w = \frac{-k_{p3} - nH + uJ_{33}}{k_{p1} + nH - uJ_{11}} \tag{C.28g}$$

In case of no constant torque acting along the pitch axis, H is set to 0. This leads to the following constants:

$$u = \sqrt{\frac{\left[k_{p1}k_{p3}\right]}{J_{11}J_{33}}} \tag{C.28h}$$

$$v = J_{33}\left(k_{p1}\right) + J_{11}\left(k_{p3}\right) \tag{C.28i}$$

$$w = \frac{-k_{p3} + uJ_{33}}{k_{p1} - uJ_{11}} \tag{C.28j}$$

This concludes the segment on PD controller synthesis for disturbance rejection problem, outlining the PD gains utilised by the rigid body NanoSat simulator for reference ground target tracking. Some I action is added to eliminate the steady state oscillations.

C.4 | Rigid Body Reference Tracking Performance

Figures C.1 and C.2, capture the three sequences of reference phase B manoeuvres, post the respective slow and fast calibration manoeuvres, to be tracked utilising the rigid body controller presented in the previous section. All reference attitude signals are combined and presented in Figures C.3 and C.4, in Euler-321 and MRP coordinates.

Figure C.5 captures the reference tracking performance for the above presented controller, for tracking the manoeuvres subsequent to the slow calibration manoeuvre. While Figure C.6 captures that for tracking the manoeuvres subsequent to the faster calibration manoeuvre.
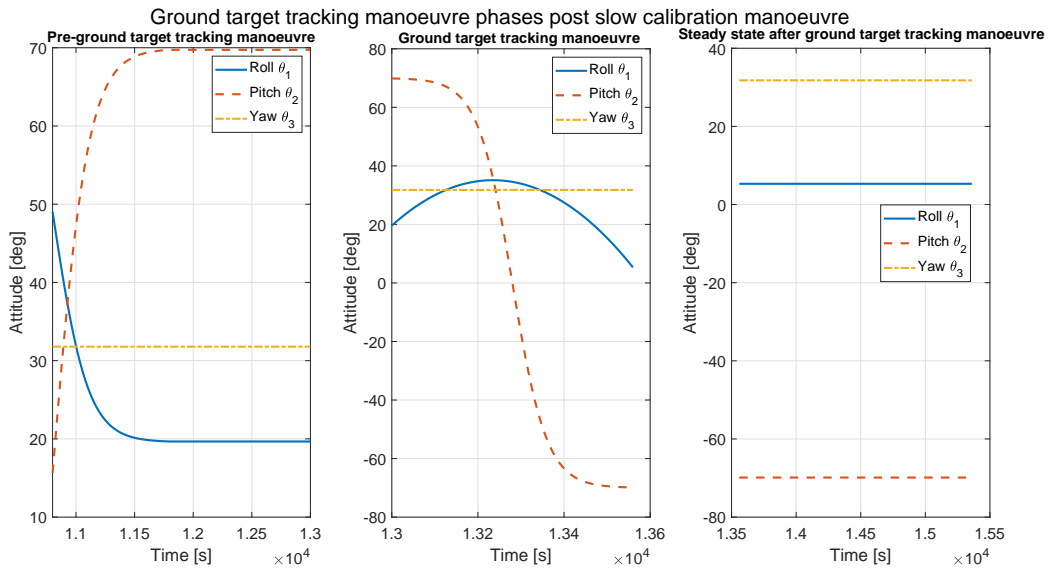
Figure C.1: *Three distinctive reference signals after slow calibration manoeuvre signifying 1.)pre-groundtarget tracking manoeuvre 2.) Ground target tracking of an Optical Ground Station in Delft from 400 km altitude polar orbit 3.) Steady state inertial pointing after ground target tracking manoeuvre.*
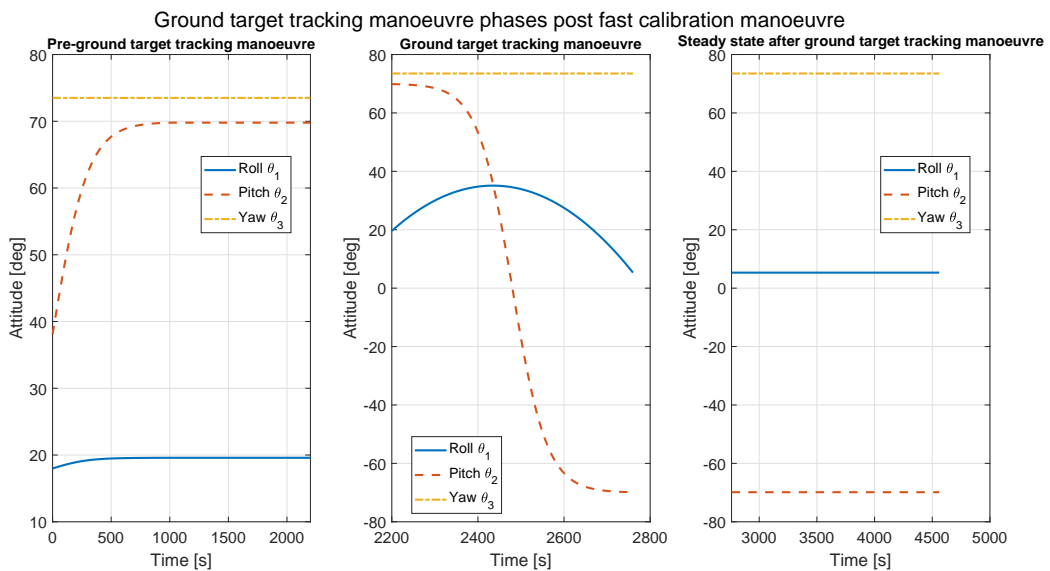
Figure C.2: *Three distinctive reference signals after fast calibration manoeuvre signifying 1.)pre-groundtarget tracking manoeuvre 2.) Ground target tracking of an Optical Ground Station in Delft from 400 km altitude polar orbit 3.) Steady state inertial pointing after ground target tracking manoeuvre.*

Phase B: Reference Euler 3-2-1 and corresponding MRP attitude after slow calibration manoeuvre
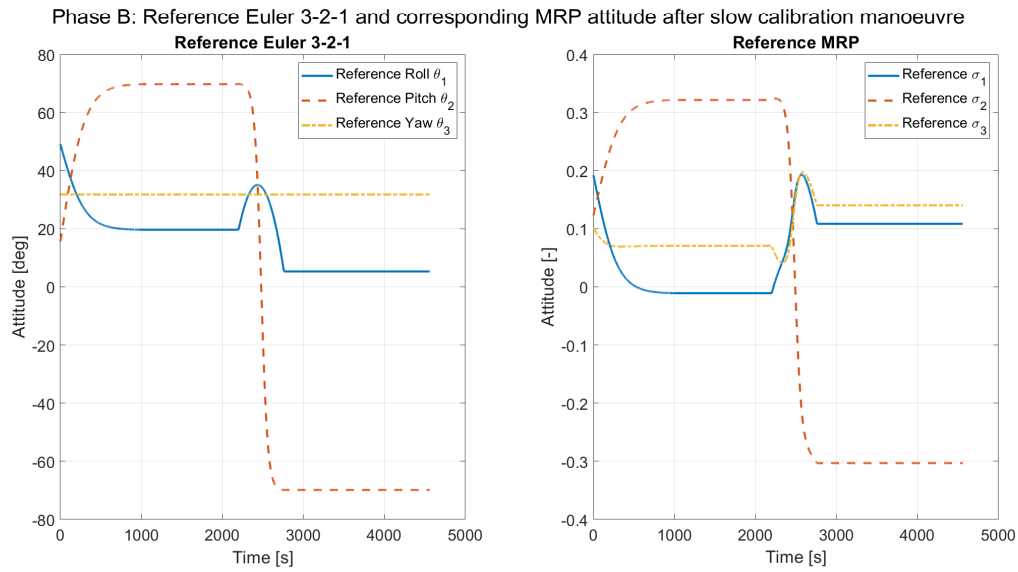
Figure C.3: *Phase B (pre-ground target tracking manoeuvre, followed by ground target tracking, followed by steady-state inertial pointing) reference attitude manoeuvre after slow calibration manoeuvre in Euler 3-2-1 and MRP, that is tracked by the synthesized rigid body controller.*

Phase B: Reference Euler 3-2-1 and corresponding MRP attitude after fast calibration manoeuvre
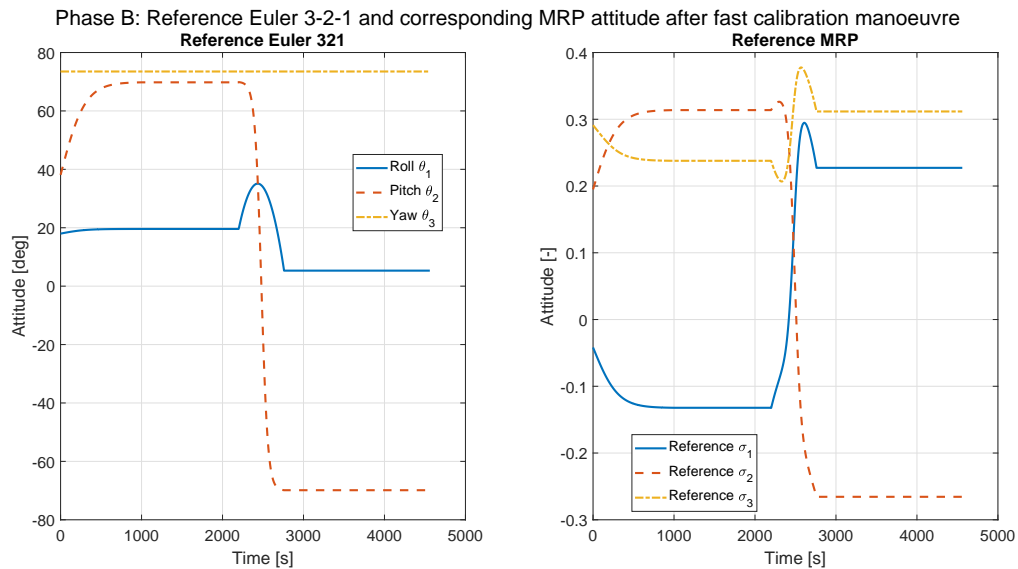
Figure C.4: *Phase B (pre-ground target tracking manoeuvre, followed by ground target tracking, followed by steady-state inertial pointing) reference attitude manoeuvre after faster calibration manoeuvre in Euler 3-2-1 and MRP, that is tracked by the synthesized rigid body controller.*
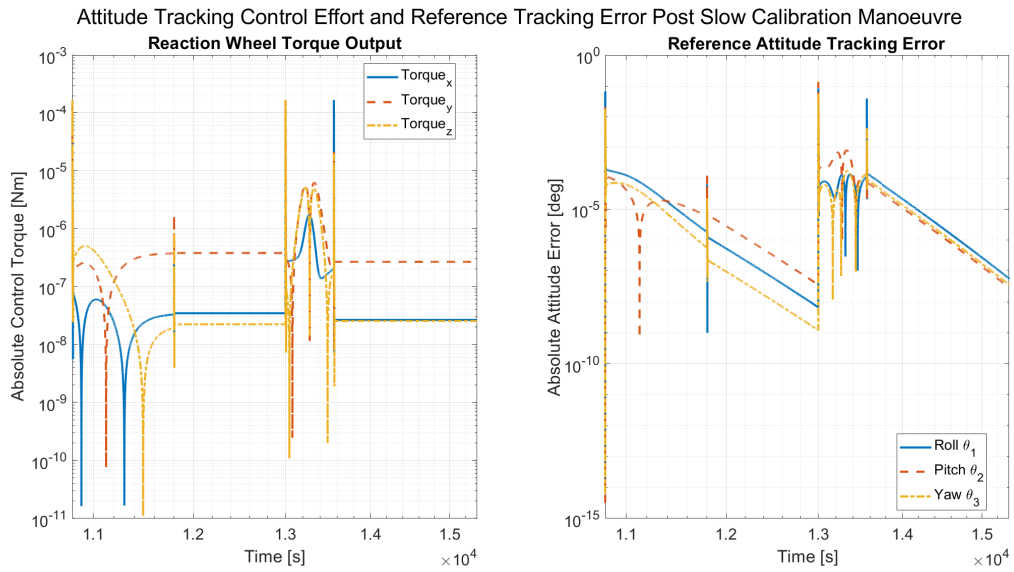
Figure C.5: *Phase B, reaction wheel control effort and corresponding reference tracking error, post slow calibration manoeuvre.*
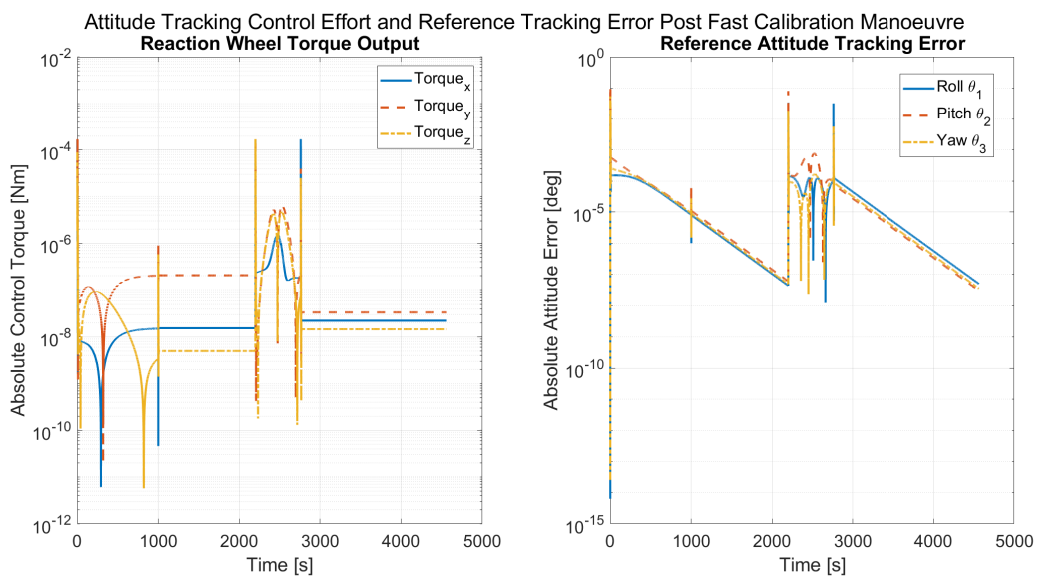
Figure C.6: *Phase B, reaction wheel control effort and corresponding reference tracking error, post faster calibration manoeuvre.*

Additional Figures: USQUE Filter Performance

This chapter is aimed at outlining additional figures associated with the 6/7 state USQUE filter and USQUE based alignment calibration filter synthesised as part of this thesis.

D.1 | USQUE Bias Estimation Performance

D.1.1 | Effect of Covariance Monitor

Figures D.1 and D.2 shows that due to premature state covariance convergence of the filter, the bias error is not confined within the sigma bounds. However, when covariance convergence monitor is utilised, the sigma bounds, bound the error of bias estimation. However, in general the filter is seen to estimate noise in combination with the bias, as a consequence a footprint of the tracked signal is observed in the bias estimate, where as the bias in general is driven by the rate random walk. This was not observed for the bias estimated with USQUE based calibration filter.
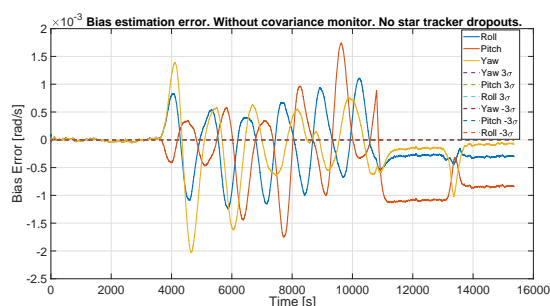
(a) *Overall bias estimation error with 3σ bounds, without covariance monitor.*
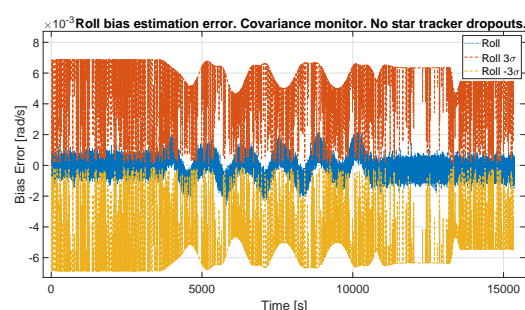
(b) *Bias estimation error for the roll axis with 3σ bounds, with covariance monitor.*
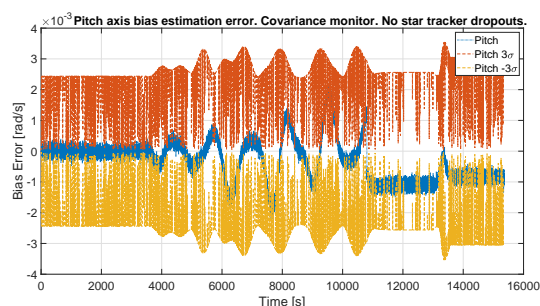
(c) *Bias estimation error for the pitch axis with 3σ bounds, with covariance monitor.*
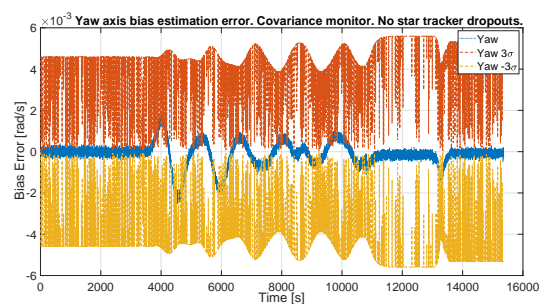
(d) *Bias estimation error for the yaw axis with 3σ bounds, with covariance monitor.*

Figure D.1: *Bias estimation error and state covariance convergence behaviour for the entire manoeuvre, with and without covariance monitor. One star tracker, and three MPSAG, with filter and sensor update rate set to 5Hz. No slew-rate induced star tracker dropouts are considered.*
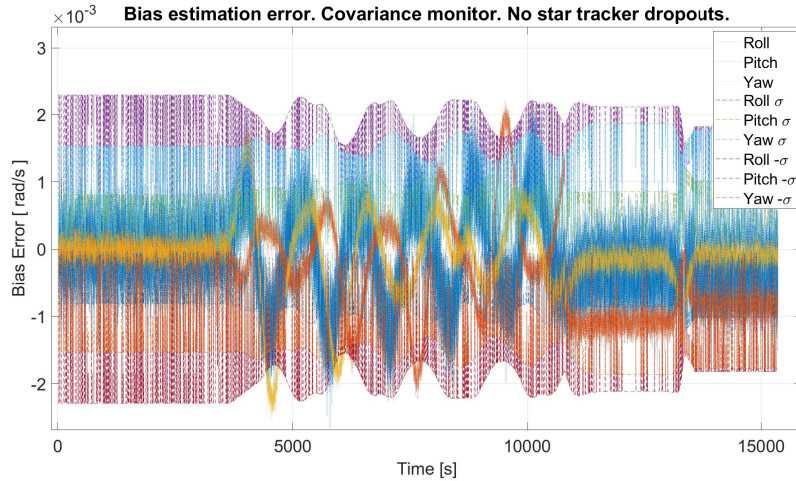
Figure D.2: *Overall bias estimation error, with covariance monitor. One star tracker, and three MPSAG, with filter and sensor update rate set to 5Hz. No slew-rate induced star tracker dropouts are considered.*
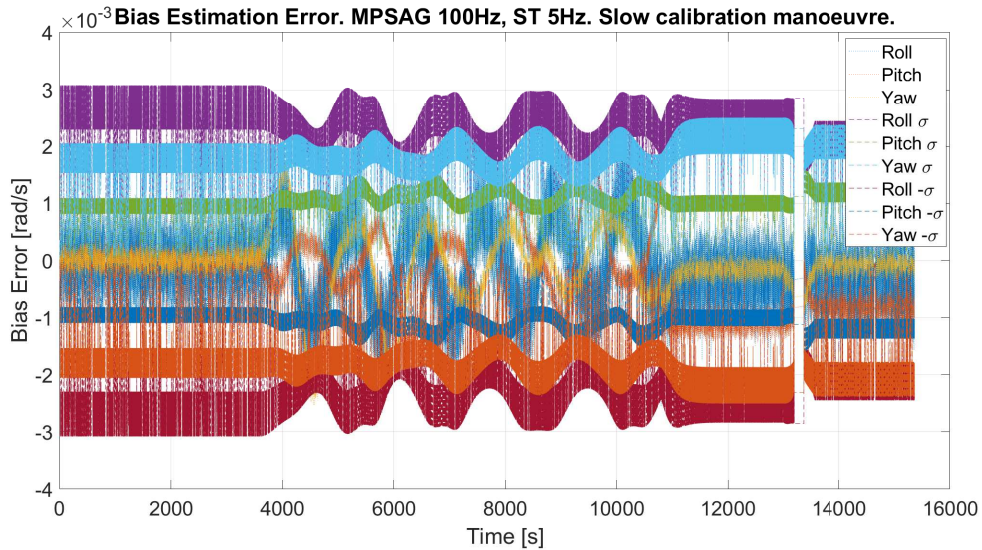
(a) *Overview of the impact of higher gyro sampling and filter update rate, on gyro bias estimation error for all axis.*
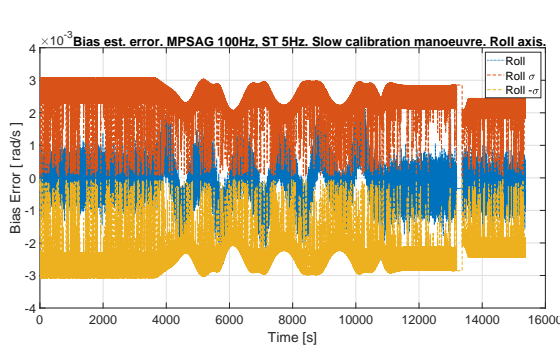
(b) *Overview of the impact of higher gyro sampling and filter update rate, on gyro bias estimation error for Roll axis.*
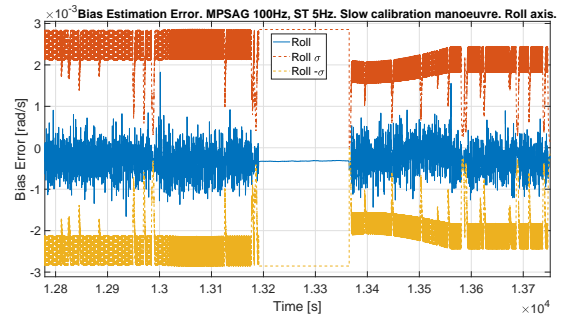
(c) *Overview of the impact of higher gyro sampling and filter update rate, on gyro bias estimation error during the star tracker drop out while tracking the ground station.*

Figure D.3: *Overview demonstrating the impact of higher gyro sampling and filter update rate, on bias estimation error. Slow calibration manoeuvre sequences, with three MPSAG and filter at 100 Hz and one ST at 5 Hz.*

D.1.2 | Effect of Gyro Sample Rate on Bias Estimation

Impact of gyro sample rate, and star tracker dropout is captured with the aid of Figure D.3.

D.1.3 | Effect of Gyro-Stellar Misalignment and Scale Factor on Bias Estimation

Figure D.4 captures the gyro bias estimated with 6/7 state USQUE, when gyro-stellar misalignment is unknown. While, Figure D.5 captures the gyro bias estimation performance of the 6/7 state USQUE filter, when star tracker misalignment is known, but gyro misalignment and scale factors are not calibrated for.

(a) Bias estimation performance, for roll axis.

(b) Bias estimation performance, for pitch and yaw axis.
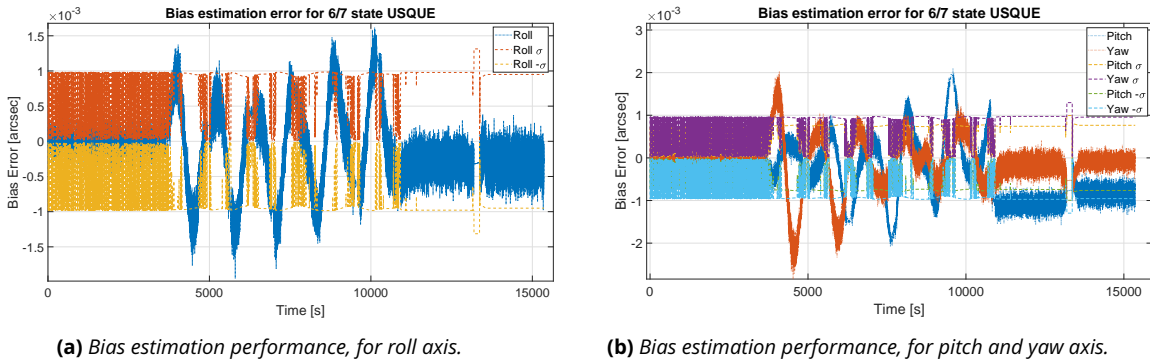
Figure D.4: *Effect of gyro-stellar misalignment and scale factor on bias estimtion. The star tracker aligned with the body axis is given a misalignment of 0.1 deg on all axis. The second star tracker has no misalignment. All elements in the gyro misalignment matrix are set to 0.5 deg, while the symmetric and asymmetric scale factors are set to 500 ppm and 100 ppm. Two ST, three MPSAG, and the filter update rate is set to 5Hz.*

(a) Bias estimation performance, for roll axis.

(b) Bias estimation performance, for pitch and yaw axis.
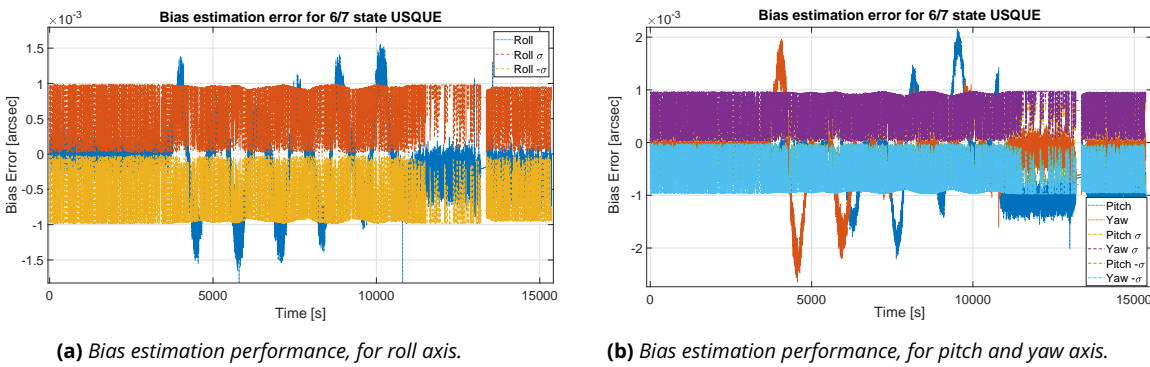
Figure D.5: *Both star trackers have no misalignments. All elements in the gyro misalignment matrix are set to 0.5 deg, while the symmetric and asymmetric scale factors are set to 500 ppm and 100 ppm.*